A-CR-72880) EVALUATION OF RANGE AND
-CRTION TOLERANCE FOR HIGH MACH NUMBER
SONIC FAN STAGES. TASK 2: PERFORMANCE
K.R. Bilwakesh, et al (General
=tric Co.) Jun. 1972 224 p CSCL 21E G3/28

N72-27818

Unclas
34066

NASA CR-72880

R71AEG195

Final Report on Task II: Performance of a 1500-Foot-Per-Second Tip Speed Transonic Fan Stage with Variable Geometry Inlet Guide Vanes and Stator.

EVALUATION OF RANGE AND DISTORTION TOLERANCE FOR HIGH MACH NUMBER TRANSONIC FAN STAGES

By

K.R. Bilwakesh, C.C. Koch, and D.C. Prince

GENERAL ELECTRIC COMPANY
Aircraft Engine Group
Cincinnati, Ohio 45215

Prepared For

NATIONAL AERONAUTICS AND SPACE ADMINISTRATION

June 1972

NASA-Lewis Research Center
Contract NAS3-11157
Charles H. Voit, Project Manager

1. Report No. NASA CR 72880	2. Government Accession No.	3. Recipient's Catalog No.
4. Title and Subtitle "Evaluation of Range and Distortion Tolerance for High Mach Number Transonic Fan Stages," Final Report on Task II: Performance of a 1500 feet per second Tip speed Transonic fan stage with variable Geometry Inlet Guide Vanes and Stator.		5. Report Date September 1971 6. Performing Organization Code
7. Author(s) K.R. Bilwakesh, C.C. Koch and D.C. Prince		8. Performing Organization Report No. 10. Work Unit No. GE R71-AEG195
9. Performing Organization Name and Address General Electric Company Aircraft Engine Group Cincinnati, Ohio 45215		11. Contract or Grant No. NAS3-11157 13. Type of Report and Period Covered Contractor Report
12. Sponsoring Agency Name and Address National Aeronautics and Space Administration Washington, D.C. 20546		14. Sponsoring Agency Code

15. Supplementary Notes

Project Manager, Charles H. Voit, Fluid Systems Component Division
NASA-Lewis Research Center
Cleveland, Ohio 44135

16. Abstract

A 0.5 hub/tip radius ratio compressor stage consisting of a 1500 ft/sec tip speed rotor, a variable camber inlet guide vane and a variable stagger stator was designed and tested with undistorted inlet flow, flow with tip radial distortion and flow with 90°, one-per-rev, circumferential distortion. At the design speed and design IGV and stator setting the design stage pressure ratio was achieved at a weight flow within 1% of the design flow. The rotor met its principal objective of achieving higher efficiencies at speeds above 1450 ft/sec than those achieved by a 1400 ft/sec design tip speed rotor tested under the same contract. Analytical results on rotor tip shock structure, deviation angle and part-span shroud losses at different operating conditions are presented. The variable geometry blading enabled efficient operation with adequate stall margin at the design condition and at 70% speed. Closing the inlet guide vanes to 40° changed the speed-versus-weight flow relationship along the stall line and thus provided the flexibility of operation at off-design conditions. A stage-matching analysis shows that the variable geometry IGV's can be used effectively to match a hypothetical second stage to the Task II Stage at off-design speeds with undistorted inlet flow. Inlet flow distortion caused considerable losses in peak efficiency, efficiency on a constant throttle line through design pressure ratio at design speed, stall pressure ratio, and stall margin at the 0° IGV setting and high rotative speeds. The use of the 40° inlet guide vane setting enabled partial recovery of the stall margin over the standard constant throttle line.

17. Key Words (Suggested by Author(s))	18. Distribution Statement
Transonic Fan Distortion Tolerance Compressor Variable Camber Inlet Guide Vanes Variable Stagger Stator	Unclassified - Unlimited

19. Security Classif. (of this report)	20. Security Classif. (of this page)	21. No. of Pages	22. Price*
Unclassified	Unclassified	224	$3.00

* For sale by the National Technical Information Service, Springfield, Virginia 22151

TABLE OF CONTENTS

TABLE OF CONTENTS (Concluded)

LIST OF TABLES

LIST OF ILLUSTRATIONS

LIST OF ILLUSTRATIONS (Continued)

LIST OF ILLUSTRATIONS (Continued)

LIST OF ILLUSTRATIONS (Continued)

LIST OF ILLUSTRATIONS (Continued)

LIST OF ILLUSTRATIONS (Continued)

LIST OF ILLUSTRATIONS (Continued)

LIST OF ILLUSTRATIONS (Continued)

LIST OF ILLUSTRATIONS (Continued)

LIST OF ILLUSTRATIONS (Concluded)

I. SUMMARY

A major objective of this program (Task II of Contract NAS3-11157) was to design a 1500 ft/sec tip speed stage capable of using the same rotor and consequently having weight flow, total-pressure ratio and stall margin at each tip speed that were nearly the same as the 1400 ft/sec tip speed stage tested in Task I. In addition, the Task II Stage was intended to operate at and above 1500 ft/sec tip speed with efficiency levels higher than could be achieved by the 1400 ft/sec design tip speed Task I Stage. Analysis of test results indicated that the high-speed efficiency objectives had been attained; the Task II Stage had higher efficiency than the Task I stage above a tip speed of approximately 1450 ft/sec. It was also determined that, although the Task I Stage had somewhat greater stall margin, both rotors reached essentially equal levels of tip static-pressure-rise coefficient at stall.

Results from tests with undistorted inlet flow of the 1500 ft/sec tip speed compressor were compared to design intent in order to determine the adequacy of the methods used in the design of this high speed fan. The design value of stage total-pressure ratio of 1.66 was achieved at a weight flow within 1% of the design flow, 226 lb/sec. The flow, however, was less than design intent in the rotor tip region because too low a suction surface incidence angle had been specified. The inlet guide vanes and stators performed nearly as estimated during design calculations, and neither vane row was responsible for any limitations in flow or unstalled weight flow range. Overall stage peak adiabatic efficiency was approximately 0.840, compared to a design value of 0.854, and the stall margin at the design point was 14%. Analytical results on rotor tip shock structure, deviation angles and part-span shroud losses were also obtained.

An additional major objective of Task II of this program was to develop a variable-camber inlet guide vane and a variable-stagger stator which would allow the stage to operate at 54% weight flow at 70% corrected speed with adequate stall margin and at high efficiency. Operation at this weight flow was not possible at 70% speed without the use of the variable-geometry blading, but the 70% corrected speed performance objectives were met by use of a 40° adjustment in inlet guide vane setting. An analysis to match a hypothetical second stage at 70% design speed to the Task II stage with undistorted inlet flow showed that the operating weight flow range (corrected to the IGV-inlet conditions) of the hypothetical two-stage fan increased 44% and 54% with IGV/Stator schedules of 20°/4° and 40°/8° respectively, as compared with the 0°/0° schedule. The variable geometry inlet guide vanes could be operated over a wide range of flow turning angles with a small increase in loss level over expectations from fixed camber, variable stagger inlet guide vanes of the same solidity. The added flexibility of operation made possible by use of the variable-camber blading was due to the ability to alter the flow-speed and pressure ratio-speed characteristics of the compressor. Guide vane adjustment, however, had little effect on the stalling pressure ratio-flow relationship. Guide vanes and stator losses were acceptably

low over wide ranges of setting angle and Mach number. A stage characteristic type of analysis was demonstrated to be capable of unifying the performance data obtained at various speeds and guide vane settings.

A final major objective of this program was to evaluate the effect of inlet flow distortions on stage performance and the effect of the variable-camber blading on distortion tolerance. A tip radial inlet flow distortion resulted in reductions in stage efficiency and stall margin that were more severe than those produced by a 90° one-per-rev circumferential distortion. Rotor tip aerodynamic loading at stall with radial distortion was approximately the same as that reached at stall with undistorted inlet flow. Distortion attenuation at the stage exit was better with radial distortion than with circumferential distortion; in the latter case attenuation was hampered at the hub because of a severe flow separation in the stator.

The effect of each type of inlet distortion on stall limits was less severe when the compressor was operated with an inlet guide vane setting of 40°. Use of the varible-camber blading, however, did not result in significant improvement in the ability to attenuate circumferential inlet flow distortions.

As in the case of undistorted inlet flow operation, the main advantage of the varible-camber blading was the ability to alter the flow-speed and pressure ratio-speed characteristics of this stage. With radial distortion, a 40° inlet guide vane setting also had the advantage of allowing a higher stalling total-pressure ratio to be achieved at a given flow than was possible with no guide vane adjustment.

II. INTRODUCTION

High tip speed fan and compressor stages are used in virtually all advanced aircraft engines. These stages must operate efficiently and stably not only at their design condition but also at part speed and with severe inlet flow distortions. The Task II of this contract was intended to investigate the efficiency and stall margin potential of a 1500 ft/sec tip speed stage, to develop design methods and criteria for stages of this type, to evaluate the effectiveness of variable-camber inlet guide vanes and stators in improving part-speed efficiency and weight flow range and to determine the effect of inlet flow distortions on stage performance plus the effect of the variable-camber blading on distortion tolerance.

The design of the Task II rotor was strongly influenced by the design and performance of the 1400 ft/sec tip speed NASA Rotor 1B (References 1-3), that was also tested in a compressor stage under Task I of this program (References 4 and 5). It was intended that the Task II rotor should have approximately the same weight flow and total-pressure ratio versus tip speed characteristics as Rotor 1B so that both stages could use the same stator vanes and test vehicle. Since Rotor 1B had a rapidly dropping efficiency level above its design tip speed of 1400 ft/sec, it was believed that by designing the Task II rotor with blades specifically selected for its higher tip speed, it would be possible to operate at and above 1500 ft/sec tip speed with a higher efficiency than could be attained by Rotor 1B in this speed range. Accordingly, the Task II rotor was designed with somewhat higher tip solidity, lower camber and with smaller throat areas than Rotor 1B. It was believed that using the common flowpath contours and aspect ratio would not compromise the performance of the Task II Stage. Additional details of the Task II rotor design are given in Reference 5 along with information on the design of the variable-stagger stator and variable-camber inlet guide vane.

In order to evaluate the effect of the variable-camber blading on off-design performance, a typical high Mach number cruise condition was selected as an objective operating point based on experience from several advanced engine systems under development for use in high Mach number aircraft. This experience indicated that the compressors of such engines typically operated at cruise at approximately 70 percent of their take-off corrected speed and 54 percent of take-off corrected weight flow. Rotor 1B could only be throttled to 54.5 percent of design weight flow at 70 percent design speed without stalling. By analogy then, it was anticipated that to operate at this cruising condition with adequate stall margin, it would be necessary to have a variable-camber blading for this new stage. Determining the influence of the variable-camber blading on stage performance with both undistorted and distorted inlet flows, and on the capability of matching a hypothetical Second Stage to the Task II Stage at off-design speeds were additional objectives of the program.

References 7 and 8 present detailed data obtained with the Task II Stage with undistorted inlet flows and distorted inlet flows, respectively. This final report summarizes the analytical and experimental results of the Task II program with specific reference to the design and off-design performance objectives.

III. APPARATUS AND PROCEDURE

1. TEST COMPRESSOR STAGE

a. INLET GUIDE VANE

The variable-camber IGV was designed to produce no turning of the flow at the 100 percent speed, 100 percent flow design point. At the 70 percent speed, 54 percent flow cruise condition, it was designed to impart up to 45 degrees of swirl to the flow at all radii. The design leading edge blade angle was 0 degrees at all conditions and the trailing edge blade angle could be varied from 0 degrees to 45 degrees. The discharge air angle could thus be varied without incurring excessive losses from high incidence angles. There were 24 inlet guide vanes, approximately half the number of stator vanes (46). With 24 IGV's, the stator exit wake rakes, which spanned two stator passages, also spanned approximately one IGV passage. Thus, the total pressure losses contributed by the IGV and stator wakes were measured in the proper proportion by the stage discharge instrumentation.

Figures 1 (a) and 1 (b) show pictures of IGV at zero degrees (nominal) and + 40 degrees respectively. The IGV airfoil sections were made geometrically similar at all radii by scaling a single master section. This master section was derived from an airfoil having an uncambered meanline with a NACA 65-008 thickness distribution scaled up to a maximum thickness/chord ratio of 10 percent. Leading and trailing edge thicknesses of the 65-series airfoil were 1.0 percent and 1.5 percent of chord respectively. The nose and flap sections were formed by dividing the 65-series airfoil into two parts. Contours around the rear part of the nose and the leading edge of the flap were chosen so that an aerodynamic slot would be formed when the vane was in a cambered configuration. The nose section moved circumferentially maintaining axial orientation when the rear flap was rotated to vary the trailing edge angle. Figure 1 (c) indicates the way in which the two parts of the guide vane were aligned in the uncambered position at the design point and in a cambered position at 30 degrees turning. Tables I and II list some of the IGV design parameters. Further details of aerodynamic design and actuation mechanism are discussed in Reference 6.

b. ROTOR

The 1500 ft/sec tip speed, 0.5 hub:tip radius ratio rotor consisted of 44 blades designed with fully arbitrary blade sections selected in order to better control throat areas and suction surface Mach numbers. The design point rotor inlet specific weight flow was 41.62 lbs/sec-ft^2 of annulus area and the relative inlet Mach number at the tip was 1.526 with zero inlet guide vane turning. Tip diffusion factor at design point was 0.368 with a tip solidity of 1.40. Chord length was varied slightly, increasing from hub to tip. A part-span shroud was used at approximately 63 percent span from the hub to insure aeromechanical stability. Table I contains some of the rotor design and performance specifications. Table III (a) gives the design values

of aerodynamic parameters and blading geometry on the design streamlines. In general, the design stream-surfaces were different from the blade element data measurement sections and, hence, the blading geometry parameters on the blade element data sections are presented in Table IV. Design values of incidence angle, deviation angle, diffusion factor, and loss coefficient on the blade element data sections are shown along with respective test data in the section on Results and Discussions. The principal conspicuous features of the new blading compared to the Task I rotor were higher solidity, some negative camber in the tip region to produce external compression, somewhat smaller throat areas and increased camber in the hub region.

A view of a portion of the assembled rotor appears in Figure 2. After manufacture, the blading was inspected by means of contour layouts at several sections and it was judged that the blading was adequate to achieve design intent.

c. STATOR

Design specifications for the stator vanes are contained in Tables III (b), and IV. The stator consisted of 46 vanes and was designed with variable-setting-angle capability. Mechanical limits of 15 degrees open to 20 degrees closed were provided. At the nominal design point setting, zero degrees, the exit air flow was designed to be axial. The outer half of the vane was made up of double-circular-arc airfoils. An arbitrary airfoil section was employed for the hub to obtain suction surface Mach numbers which were lower than those produced by a double-circular-arc hub section. The sections between the arbitrary hub and double-circular-arc pitch were selected to form a smooth transition. The design stator inlet Mach number was 0.61 at the tip, 0.66 at the pitch, and 0.77 at the hub. Figure 3 shows a picture of a typical stator vane. Additional design details are contained in Reference 6.

The stator blading was also inspected by means of contour layouts at several sections and was judged adequate to achieve design intent. Comparisons between the measured profiles and design intent are presented in Reference 4.

2. TEST FACILITY

Performance tests of this stage were conducted in General Electric's House Compressor Test Facility at Lynn, Massachusetts. This facility is an open cycle type with atmospheric inlet and discharge. A diagram and description of this test facility are contained in Reference 7.

3. INLET DISTORTION EQUIPMENT

The Task II inlet distortion screens were the same as those used in the Task I distortion testing performed under NASA Contract NAS3-11157 and reported in Reference 4. Both radial and circumferential distortions were tested. The radial distortion screen for Task II, shown in Figure 4, covered the outer 40% of the annulus area, while the circumferential screen, shown in Figure 5, spanned a 90° arc from hub to tip. Both screens were made of 20-mesh 0.016-inch diameter wire, giving a screen open area of 0.46. The screen material was selected to give a distortion parameter, $(P_{max} - P_{min})/P_{max}$, equal to 0.20 with a design flow of 226 lbs/sec at 100% design speed.

The support screen, which spanned the entire annulus and to which the distortion screens were attached, was designed to be rotated 360° past the instrumentation for the circumferential inlet distortion testing. The support screen material was one-inch-square mesh with 0.093-inch diameter wire, and gave an open area of 83.4%. The support screen was designed to separate into halves to facilitate installation.

The distortion screens were located one rotor diameter forward of the rotor leading edge, and were mounted in a cylindrical section approximately one-rotor diameter long which was inserted into the test vehicle only during distortion testing.

4. INSTRUMENTATION

A listing of major fixed and traverse instruments provided for the different phases of testing is given in Table V. The locations of these instruments and of the hub and casing static taps are shown in the instrumentation schematics, Figures 6 and 7. References 7 and 8 contain descriptions of the instrumentation arrangement used in each test configuration as well as photographs of the instruments used.

Overall performance data were calculated from fluid properties measured by fixed instruments at inlet and exit measuring stations. In general, measurements were obtained at seven radial immersions chosen to correspond to 5, 10, 30, 50, 70, 90 and 95 percent of annulus height from the tip at the rotor exit plane, 1.51. Immersions at each other instrumentation plane upstream and downstream of plane 1.51 were established to correspond to the radial locations at which design streamlines that passed through the selected immersions at plane 1.51 intersected the instrumentation plane. Blade element data were obtained from traverse probes at the respective indicated locations. During undistorted inlet flow shakedown testing only, a 14-element IGV wake rake was installed at each of the seven radial immersions to measure the pressure behind the IGV. The IGV loss coefficients obtained from these measurements were subsequently used in the rest of the program. During distortion testing only, the inlet total pressure aft of the distortion screen was obtained by two 7-element total-pressure distortion rakes located at Plane 0.18. For circumferential distortion testing, traverse data were recorded at the 10%, 50%, and 90% immersions by the 4-parameter probes instead of at the usual seven immersions. During all stall tests, three hot wire anemometers were used behind the rotor at 10%, 50%, and 90% immersions to detect the initiation of stall and the radial extent of stall cells.

Ten high-frequency-response static pressure sensing elements were located on the casing over the rotor tip to obtain data on pressure profiles and shock structure at the rotor tip. Two of these were located forward of the rotor leading edge and one aft of the trailing edge. The output signals from the ten transducers were displayed on two oscilloscopes. The oscilloscope traces were timed to record the static pressure history for four blade passages; the sweep rate superimposed the second pair of passages over the first pair. The reference static pressure level for each sensor was obtained from a casing static pressure tap located at the same axial position.

5. DATA REDUCTION

Three separate computer programs were used to reduce the test data. The Overall Performance Data Program computed average fluid properties at each measuring station from data measured by fixed instruments and calculated overall stage and rotor performance parameters such as total-pressure ratio and adiabatic efficiency. The Blade Element Data Program calculated vector diagram and blade element performance parameters for seven streamline sections. This program reduced data from both fixed and traversing instruments. These two computer programs were used primarily to reduce data obtained during undistorted and radial inlet flow distortion testing. A special Circumferential Distortion Data Program was used to calculate vector diagram data at numerous circumferential, radial and axial locations during circumferential inlet flow distortion testing. This data reduction computer program also calculated overall performance data from average fluid properties determined by special circumferential/radial mass-averaging methods. Input data were obtained from both fixed and traverse instruments at twelve different circumferential positions of the distortion screen. Additional details of these three data reduction methods used may be found in References 7 and 8.

In order to examine the static pressure profiles over the blade tips, to study the shock structure and starting, the static pressure versus time data from the photographs of the oscilloscope traces were input to another data reduction computer program. This program produced plots showing two adjacent rotor blade tip sections; superimposed upon this plot were data points representing the physical locations at which integer levels of static pressure occurred. Contours of constant static pressure were drawn in on these plots in order to reveal the rotor tip shock structure and other features of the flow relative to the rotor blades in the tip region. Plots of this type were produced for a number of high-speed operating conditions for the Task II Stage with the inlet guide vane in the design, zero-swirl, position with undistorted inlet. Detailed interpretation of these plots are presented in the section on Results and Discussions.

6. TEST PROCEDURE

A shakedown test was conducted in the initial phase of the testing with undistorted inlet flow during which the IGV wake losses for three principal IGV setting angles were determined at seven immersions with the IGV wake rakes immersed in the airstream. The optimum design and off-design IGV/Stator vane schedules were also chosen during this phase of the testing. This was followed by undistorted inlet flow performance testing during which blade element and overall performance data were obtained at 50%, 70%, 80%, 90%, 100%, and 110% speeds at the three IGV/Stator schedules of 0°/0°, 20°/4°, and 40°/8°. Testing with radial and circumferential inlet flow distortion was performed at 70%, 90% and 100% speeds at nominal (0°/0°) and 40°/8° IGV/Stator schedules. During radial distortion testing at nominal vane schedule, blade element traverses were performed at 100% speed at both maximum weight flow and near stalling flow and at 70% speed at an intermediate flow condition. For the 40°/8° IGV/Stator schedule, blade element data were obtained at 70% speed at maximum flow and near stalling flow and at 100% speed at an intermediate

flow condition. During circumferential distortion flow testing, detailed radial and circumferential flow surveys were made in addition to overall performance tests. These surveys were performed using the distortion screen rotation capability and the combination traverse probes. Screen rotation tests were performed at flow conditions similar to those used for the radial distortion blade element traverses. For each operating condition, at each of twelve circumferential distortion screen positions spaced every 30°, overall performance data were recorded and traverse data were obtained at immersion positions of 10%, 50%, and 90%. At each screen position, following the traverse test, the probes were retracted out of the airstream and overall performance data were recorded.

The Task II Stage was tested without the IGV as part of Task IV tests with solid casing and a blade angle slot casing treatment configuration. The results of these tests have been reported in detail in Reference 9. The cylindrical section and support screen used for mounting the distortion screens were retained during the undistorted flow testing in Task IV.

IV. RESULTS AND DISCUSSION

1. ANALYSIS OF PERFORMANCE AT NOMINAL VANE SCHEDULE WITH UNDISTORTED INLET FLOW

Testing with undistorted inlet flow for the Task II Stage was conducted during the shakedown tests and undistorted inlet flow performance tests. A complete listing of all the measured and calculated overall performance and blade element parameters from these tests is presented in Reference 7. The following sections present a discussion of the results.

a. EVALUATION OF ROTOR AND STAGE AERODYNAMIC DESIGN

The development of an efficient 1500 ft/sec tip speed rotor for use in a high speed fan stage with variable-camber inlet guide vanes was a major goal of the Task II program. It is, therefore, appropriate to evaluate the performance of the stage and of the rotor, on an absolute basis and in comparison with design intent.

The performance map for the entire Task II stage (inlet guide vanes, rotor and stator) is presented in Figure 8 for testing with the design geometry: the zero-swirl inlet guide vane setting and the nominal stator setting. At the test point closest to the 100% speed design rotor total pressure ratio of 1.686, the stage pressure ratio was 1.670, the corrected weight flow was 224.3 lbs/sec, 0.75% below the design value of 226.0 lbs/sec, and the stage efficiency was 0.838. Performance of the rotor alone is presented as Figure 9. At the same test point closest to design, the rotor adiabatic efficiency was 0.869, 0.014 below the design expectation of 0.883 (performance of the Task I rotor is given as background for Figure 9; the comparison will be discussed in a later section). The performance with respect to both weight flow and efficiency was gratifyingly close to the design expectation; the design expectation, of course, does not represent an upper limit to performance levels desired from future development.

Examination of radial profiles of significant thermodynamic and aerodynamic parameters at test points near design can measure conformity with design intent and provide clues to possible improvements. Radial profiles of measured rotor total pressure ratio and total temperature ratio at the test point closest to design and at the 100% speed test point nearest stall are presented as Figure 10. Reading numbers refer to tabulated data presented in References 7 and 8. At the particular test point chosen to match design pressure ratio, the work input (as measured by the temperature) in the hub region conforms to the design intent. A small excess of work input over the design in the tip region was produced. The profiles for the test point near stall show that the blading does have substantial excess capability over the design point requirement at all radii. Interpretation of the temperature and pressure profiles is presented in the form of efficiency as Figure 11 and as loss coefficient as Figure 12. Also included for comparison in Figure 11 are data from the Task IV tests using the Task II Stage without inlet guide vanes. Data from two comparable sets of readings from Task II and Task IV

tests are presented. It is apparent from these data that the presence of IGV's had very little effect on rotor efficiency, indicating that the IGV losses had been properly accounted for. This is also borne out from Figure 13 which presents the performance maps for the Task II Stage between rotor inlet and stator exit and for the Task IV Stage. It appears from Figure 12 that higher than expected losses were generated in the tip region and in the hub region. The design curve has no allowance for spreading of the wake from the mid-span shroud, which may well account for the higher level of measured loss in this region. Loss levels substantially higher than design expectation in both tip and hub regions would appear to be fruitful areas for subsequent development. Radial profiles of rotor diffusion factors are presented as Figure 14. This figure shows that the blading was capable of producing the design loading and substantially more. The profile of rotor relative deviation angle, shown as Figure 15, indicates that the blading was more than able to satisfy the design vector diagrams. In fact, these profiles suggest that at those radii where supersonic loading is the primary component, a significant adjustment should be made to Carter's Rule for predicting deviation angles. The relative leaving angles can be close to the trailing edge metal angle when the relative leaving velocity is close to sonic.

Some illumination on the small deficiency in measured weight flow below the design is given by Figures 16, 17, and 18. In Figure 16 the measured static pressure profile just upstream of the rotor is compared with the design intent; stagnation pressure variation is a negligible (0.002) factor in the dynamic pressure profile. This figure includes data taken from the testing without inlet guide vanes reported in Reference 9 as well as the earlier data from the complete stage test. The difference between the tests with and without IGV's is considered to be within experimental resolution. The high level of static pressure in the rotor tip region suggests that the velocity level is low there and that this region is the source of the flow deficiency. Figure 16 implies that the dynamic pressure for Reading 139 ahead of the rotor tip was about 5 percent below the design intent, and the dynamic pressure in the hub region equalled the design intent. Thus the entire flow deficiency appeared to be localized in the tip region. The impact of the low flow level in the tip region on the blading is a high incidence angle; the actual incidence angle distribution is presented in Figure 18 including comparison with the design intent.

The flow induction capacity of a supersonic cascade like the rotor tip sections depends upon interaction of the contributing effects of the suction surface shape in the leading edge region, the cascade passage inlet area, and the passage throat area. The flow induction surface sets an upper limit to the flow that can be sucked through the compressor. For each design, and for each speed for a given design, there is a minimum throat area which will pass the limit flow. Establishment of an oblique shock pattern at the leading edge implies that the throat area is large enough to pass the limit flow corresponding to the induction surface. On the other hand, a normal shock pattern, at or in front of the passage inlet suggests that the throat area is setting a flow limit below the limit set by the induction surface.

Contrary to previous practice, passage throat areas for the Task II rotor had deliberately been set small in the tip region in an effort to encourage some isentropic supersonic compression before attempting supersonic-subsonic transition. Passage inlet areas had not received direct attention, and the resulting cascade passage had a substantial convergence. More recent experience has suggested that the ratio of inlet to throat area may be an important design parameter. If the throat area is too small, or if the inlet area is too large in relation to the throat, it is expected that the flow in the cascade passage will be subsonic, after a strong normal shock standing some distance in front of the passage entrance. When this happens, an observer, looking at pressures on the leading edge plane of the rotor, will see a very high pressure region between the strong bow shock and the blade leading edge. The average static pressure which appears in a plot like Figure 16 would then be the resultant of this high pressure and whatever low pressure is generated along the suction surface forward of the shock. During the design process it was believed that throat areas (and inlet areas) had been chosen sufficiently large to pass the design flow. Static pressure isobar plots, given as Figures 19(a) - 19(g) and discussed in more detail later, show that the leading edge shock at 100% speed, for back pressures equal to or less than design, is an attached oblique shock. Thus, these provide evidence that the passage areas were large enough so as not to limit the flow. At the high back pressure, 100% speed condition, as shown in Figure 19(c), the strong shock was pushed forward of the passage entrance. In this case the flow induction was reduced, as indicated by the shape of the speed line on Figure 19(c) and on the overall performance map, Figure 8. The static pressure isobar plots for 90% speed, especially Figure 19(e) near stall, show the characteristic pattern when the passage throat area is not large enough to pass the desired flow.

The nature of the influence of the flow induction surface on the flow is suggested by the streamline section layouts presented as Figure 20. The presentation is done in a manner to emphasize the relation between the suction surface shape and the streamline that would be followed by air particles on a meridional stream surface in the absence of any blade force on that stream surface, the "free flow streamline". Free flow streamlines for the design flow level are shown on Figure 20; curvature of them reflects acceleration of the axial flow component in the converging annulus. Using linearized reasoning, any portion of the real surface with a negative angle of incidence to the free flow streamline will generate compression waves which will propagate upstream. Any portion of the surface with a positive angle of incidence will generate expansion waves. If the suction surface shape returns to the free flow streamline just in time to generate a wave that will intersect the leading edge of the next airfoil, the compression waves and expansion waves propagating upstream of the leading edge plane of the cascade will just cancel and the cascade should produce the desired flow induction. In practice, boundary layer growth along the suction surface gives an effective surface with 0.1° - 0.2° negative incidence with respect to the physical surface. Also some overexpansion on the majority of the surface is required to compensate for high local static pressures on the blunt leading edge. The cascade layouts showed that the actual blade surfaces had an average 0.5° negative incidence with respect to the free flow streamline. Thus, it should not have been surprising that the lowest

measured upstream flow angle was about 0.7° higher than the design level. This 0.7° difference is comparable to the difference between the design incidence and the lowest measured incidences at 100% and 110% rotor speeds as shown on the blade element data presentations, Figure 21.

In addition to the free flow streamline, the blade section layouts, Figure 20, show curves of cascade passage area, referenced to the flow area between stagnation streamlines upstream of the cascade, the cascade capture area. The area of a passage cross section is plotted on these curves at the axial position of the section midpoint. The minimum level on this curve is the throat area which had been carefully chosen in the original design process. The distribution of such areas may be used to examine the probable behavior of the cascade during acceleration to its design speed. In particular, this distribution may determine whether the cascade can reasonably be expected to develop its desired shock pattern at any speed below the design.

Figure 22 (a and b) summarize an analysis predicting the appearance of a design-type oblique shock structure attached to airfoil leading edges, or a lower speed normal shock structure standing forward of the cascade passage inlet, based on the passage area distribution. Development of the oblique shock structure is considered as essential to attainment of good efficiency at high Mach numbers.

The analysis assumes that the entire flow at radii greater than the mid-span shroud can be expressed in terms of linearized Method of Characteristics waves of one family, upstream of the cascade passage inlet, and in one-dimensional flow terms in the cascade passage and downstream. The flow analysis upstream of the cascade passage inlet consists of:

1) Axial acceleration in the converging annulus from the rotor inlet measurement plane to the blade leading edge (this effect was incorporated in the data reduction program for blade element data),

2) Expansion around the leading edge to the leading edge suction surface direction, and

3) Expansion and/or compression along the suction surface due to interaction of surface curvature and annulus convergence.

Results of the upstream analysis for three discharge throttle settings are presented on Figure 22(a). Upstream Mach numbers tend to decrease with increasing back pressure, reflecting flow roll-back. Flow induction surface Mach numbers increase as incidence angles and the resulting leading edge expansions increase.

The one-dimensional flow analysis downstream of the cascade passage inlet involves:

(a) Isentropic subsonic expansion from the cascade passage inlet to the throat, where the Mach number is the relative discharge Mach number (whenever that is subsonic) or unity.

(b) Isentropic deceleration from a normal shock downstream Mach number to the passage inlet Mach number (applicable when the shock stand-off distance is significant).

The conditions for leading edge shock swallowing and establishment of the oblique shock structure are presented on Figure 22(b). The leading edge shock may be a normal shock significantly upstream of the passage inlet, a normal shock at the passage inlet, or an oblique shock inside the passage. The normal shock will be observed at the passage inlet if normal shock relations are satisfied exactly by the supersonic Mach number in (3) and the subsonic Mach number in (a). If, however, the subsonic Mach number downstream of a normal shock after (3) is higher than the inlet Mach number in (a), some standoff and subsonic deceleration as in (b) is indicated. When the Mach number downstream of the normal shock after (3) is lower than the passage inlet Mach number in (a), shock swallowing should occur.

As shown by Figure 22(b), the forcing of the normal shock away from the passage entrance is predicted to occur below 89% rotative speed for discharge valve setting 15, at 91.5% speed for discharge valve setting 9, and at 95% speed for discharge valve setting 6. Thus this analysis predicts that the bow shock should be oblique in all three of the 100% speed pressure contour plots, Figures 19(a), 19(b) and 19(c) and in the low back pressure 90% speed plot, Figure 19(d). Since the actual transition from the normal shock structure to the oblique shock structure occurred at a throttle setting between those represented by Figures 19(b) and 19(c), this analysis appears to predict the transition at a speed about 6% too low. The respective speeds at which shock swallowing will occur would be raised if the effective passage contraction is more than that given by the section layouts, or if the effective Mach number approaching the cascade entrance is lowered through relative total pressure degradation through the bow shock at the previous leading edge. Both of these effects probably occur. If, for example, the effective ratio of passage throat area to inlet area is 0.94 rather than 0.96 as shown on Figure 20(b), the actual shock swallowing speeds are raised approximately 6% above those predicted by the analysis, as would be required to explain the oblique shock at the design point back pressure and the 100% speed low back pressure, and the normal shock appearing near 100% speed stall.

An intensive study of the static pressure isobar plots, Figures 19(a) to 19(g) was aimed at pinpointing the source and nature of cascade inefficiency in the tip region, and at correlating the flow behavior with design intent. It appeared that the study of the static pressure isobar plots was quite rewarding for insight into the flow behavior. Considerably better time and space resolution seemed to be required of the measuring system, if loss locations were to be identified. During this study, it became apparent that several features, common to more than one of the figures, could serve as quantitative measures of performance. Details are collected in Table VI.

(a) For oblique leading edge shocks, Figures 19(a), 19(b), 19(f) and 19(g), a wave angle was calculated using the relative total pressure upstream found from the blade element data, and static pressures upstream and downstream of the shock obtained from the isobar plots. This condition is designated as type A in Table VI. The shock wave angles determined in his manner near the pressure

surface, at mid-passage and near the suction surface have been laid out on the appropriate figures. The wave angles calculated for the two test points at 100% speed, Figures 19(a) and 19(b) are clearly about 5° smaller than the wave angles implied by the isobar plot. The wave angles calculated for the two 110% speed points, Figures 19(f) and 19(g), are quite similar to those on the isobar plots. A review of the original recorded pressures suggests that the response characteristics of the measurement system have cut off as much as 20% of the shock pressure rise. The wave angle, when the downstream Mach number is close to unity, as in the case for the test points at 100% speed, is quite sensitive to the pressure ratio. It seems likely that enough pressure rise could have been lost from the 100% speed measurements to account for 5° in wave angle. A similar analysis of the data at 110% speed suggests that an increase of 2° in wave angle might result, which would be compatible with the isobars.

(b) When the oblique leading edge shock was incident on the suction surface, no case showed a reflection at the location expected from inviscid theory. More commonly, the surface pressure rise starts upstream of the incident shock, suggestive of a shock-induced local flow separation. This early pressure rise may offset some of the expansion on the corner surface and permit a shock cancellation corner on the effective airfoil surface. Three of the cases, Figures 19(a), 19(b) and 19(f), showed an oblique shock compression originating at the trailing edge, whose strength increases with back pressure and provides the mechanism for the impact of back pressure on cascade loading. In the fourth case, Figure 19(g), an oblique-shock-like pressure rise appears substantially upstream of the appropriate location for either a trailing edge shock or a reflected shock. This pressure rise may be the coalescence of pressure waves generated by the induced separation. In this way the pressure rise equivalent of a reflected shock can appear well upstream of the usual position.

(c) The test conditions of Figures 19(c), 19(d) and 19(e) show normal leading edge shocks. Quantitative analysis on these may either use upstream data to deduce pressure rise expectations for comparison with the measurements (Type B in Table VI), or use measured pressure rise to deduce local upstream properties for comparison with far upstream properties (Type C in Table VI). If the upstream relative total pressure from the blade element data is used in conjunction with local static pressures from the isobar plot, a Mach number just upstream of the normal shock and a normal shock pressure ratio can be inferred. Static pressure downstream of the normal shock, expected on the basis of this procedure, are substantially higher than are shown on the isobar plots. A review of the pressure measurements for Figure 19(c) suggests that measurement response could have degraded the apparent shock pressure ratio near the pressure surface from 2.5 to 2.06, and that in mid-passage from 2.35 to 1.89. Thus the deficiency in measured pressure rise across the shock near the pressure surface may be attributed to the measurement system. In mid-passage, however, the value 2.35 is still substantially below the Type B expectations. Type C calculations suggest severe total pressure losses upstream of the passage inlet, and downstream total pressures near those obtained from the blade element data.

(d) Several cases, Figures 19(a), 19(b), 19(c) and 19(f) show abrupt pressure rises across a front perpendicular to the pressure surface, downstream of the cascade passage exit. Considered in two-dimensional terms, this front would represent a normal shock, and upstream and downstream Mach numbers and relative total pressure may be inferred from the pressure rise. In each case the downstream total pressure obtained in this way was substantially less than the average downstream total pressure taken from blade element data. An alternative interpretation supposes that the pressure front is the reflection line for an oblique shock with deflections in planes parallel to the pressure surface. This interpretation sets a minimum downstream Mach number level at 0.95, and suggests estimating total pressures based on unity downstream Mach number.

(e) The flow inside the passage may be entirely subsonic, shown primarily by the absence of sharp pressure fronts in Figures 19(c), 19(d), and 19(e). Then one-dimensional gas-flow seems to give a good description of the flow behavior throughout the region downstream of the passage inlet. In Figure 19(d), the flow appeared to accelerate through the sonic condition at the passage exit as far as a Mach number of unity and to require a secondary normal shock for transition back to the subsonic relative exit Mach number.

(f) Even though the flow downstream of the oblique shocks in Figures 19(a), 19(b), 19(e) and 19(f) appears to be supersonic, the pressure surface pressure increases when the back pressure is increased [19(b) vs. 19(a) and 19(f) vs. 19(e)]. This sort of back pressure influence violates the characteristics of two-dimensional supersonic flows. It seems clear, however, that subsonic passage flows which respond to back pressure must always be found in section stream surfaces at radii not far inside the blade tips. Since these subsonic flows will usually call for higher static pressures than the supersonic flows on the tip section stream surface, flow migration will be induced along the pressure surface toward the tip. The two-dimensional supersonic flow, flowing against the radial migration, sees a three-dimensional area contraction, which tends to lower its Mach number and raise its static pressure, relative to a simple two-dimensional situation. This type of effect should be expected to increase with increasing back pressure.

b. COMPARISON OF EFFICIENCIES AND STALL AERODYNAMIC LOADING OF TASK I ROTOR AND TASK II ROTOR

One of the major objectives of this program was to design a rotor to operate more efficiently than Rotor 1B at speeds of 1500 ft/sec and higher. A comparison of rotor performances from Task I and Task II Stages is presented here. The Task I and Task II Stages used the same flowpath, as shown in Figure 23, and the same stator. The performance maps of Task II rotor at the nominal vane schedule and of the Task I rotor, both with the undistorted inlet flow were presented in Figure 9. The Rotor 1B, designed to operate at 1400 ft/sec, showed sharply decreasing peak efficiency with increasing speed above 80% of its design speed. In order to evaluate performance at similar tip speeds, the peak efficiency achieved by the rotors is plotted versus tip speed in Figure 24(a). The Task II rotor attained a peak efficiency of 0.869 at 1500 ft/sec tip speed which is 0.01 higher than that attained by the Task I rotor. At speeds higher than 1500

ft/sec, the peak efficiency for Task I rotor dropped more rapidly; for example, at 1540 ft/sec, which is 110% speed for Task I rotor, its peak efficiency was 0.019 lower than that of Task II rotor. These data indicate that the Task II objective of obtaining improved efficiency at high speed was achieved. Although the Task II rotor demonstrated higher peak efficiency than the Task I rotor at 1500 ft/sec and above, the Task I rotor had superior performance at part speed.

Additional comparisons between the Task II Stage rotor and the Task I Stage rotor are shown in Figures 24 (b) and 24 (c). The data in these figures demonstrate that both stages had similar pressure-speed and flow-speed relationships. Achievement of this similarity in flow and pressure ratio capability, as well as the improved high-speed efficiency, was a goal of the Task II design, and is considered to have been achieved.

As seen in the rotor performance map comparison, Figure 9, the Task I rotor stall line fell higher on the performance map than that of the Task II rotor. The performance map also shows that the Task I rotor had a larger weight flow range between stall and maximum flow in the high-speed range of the map. Since the two rotors had identical flowpath contours and very similar distributions of solidity, camber, stagger and design aerodynamic loading, the differences in weight flow range and stalling loading were examined in some detail.

The variations of diffusion factor, static-pressure-rise coefficient, and work coefficient as the two rotors were throttled toward stall at design speed are compared in Figures 25, 26 and 27, respectively. Data are given at each blade element immersion, and data from Task IV testing (Reference 9) using the Task II Stage without inlet guide vanes are also shown. Radial variations of stalling values of diffusion factor, static-pressure rise coefficient and work coefficient, obtained by extrapolating the data to the stalling throttle valve setting, are compared in Figures 28, 29 and 30. Stalling values of diffusion factor and of work coefficient were somewhat less over the entire span with the Task II rotor than with the Task I rotor. The stalling values of static pressure rise coefficient also were lower in the outer span for Task II rotor compared to Task I rotor. Stalling values of rotor diffusion factors and static pressure rise coefficients obtained at 90% design speed for the Task II rotor are also presented in Figures 28 and 29 respectively which show no influence of tip speed on the observed trends.

c. EFFICIENCY LOSS DUE TO PART-SPAN SHROUD

The penalty in stage efficiency for the use of the part-span shroud has been evaluated by studying continuous traverse radial profiles of total pressure and temperature, and comparing these with the results of fixed discharge instrumentation used for overall performance data.

The shroud effects on efficiency are summarized in the following tabulation:

Reading Number	Percent Design Speed	DV Setting	Weight Flow lbs/sec	Shroud Efficiency Penalty (%) Based on Continuous Traverse	Shroud Efficiency Penalty (%) Included on Overall Perf. Data	Operating Condition
148	100	9	223.8	0.72	0.47	Near Design
149	100	6.5	215.95	0.4	0.19	Near Stall
147	110	8	234.24	1.1	0.51	Near CTL*

Continuous traverse data at the rotor exit measurement plane (Plane 1.5) were taken at 100% speed, near the design point and near stall, and at 110% speed near a constant throttle line through the design point; radial profiles of rotor adiabatic efficiency for these three data points are shown on Figures 31(a), 31(b) and 31(c), respectively. The profiles are shown plotted against stream-function to facilitate comparison with overall performance data taken at the stator exit measurement plane (Plane 2.0) with a different annulus area. Radial positions at the actual continuous traverse plane are also shown. The adiabatic efficiency profiles are derived from the total pressure and total temperature profiles presented in Figure 32.

The true efficiency penalty from the part span shroud was estimated by supposing profiles without the shroud to be given by the dashed lines on Figure 31. The difference between the solid line and the dashed line was mass-weighted. After comparing the results from fixed discharge instrumentation with the continuous traverse results, and making allowance for radial spreading of the shroud wakes, it seemed probable that the discharge instrumentation measured a fraction of the true shroud loss. That fraction has been estimated by the dashed line applied to the profile through the fixed discharge instrumentation data. It appears that the shroud effect was considerably more severe at 110% speed than at 100% speed. As a result of the fixed instrument locations, quoted overall efficiencies could be optimistic by 0.25% at 100% speed and 0.6% at 110% speed.

d. COMPARISON OF STATOR PERFORMANCE WITH DESIGN INTENT

The variable-stagger stator used in Task II was designed to accept the flow leaving the 1500 ft/sec tip speed Task II rotor and also to be compatible with the 1400 ft/sec tip speed Task I rotor. This section presents a comparison with design intent of the performance of the stator when used in the Task II Stage.

Figure 33 shows a comparison with design intent of the radial variation of stator incidence angle at 100% speed, near design condition at nominal vane schedule. The test values of incidence angles were slightly higher

* CTL condition refers to intersections with the respective speed lines of a constant throttle setting line through design stage pressure ratio at 100% design speed, nominal vane schedule with undistorted inlet flow. This constant throttle line has been kept fixed for both distorted and undistorted inlet flows at all the three vane schedules.

than design intent. The stator, at the nominal setting of 0°, was designed to return the flow leaving the rotor to the axial direction. A comparison with design intent of the radial profile of stator deviation angle at 100% speed, near design flow with undistorted inlet and nominal vane schedule, as shown in Figure 34 indicates that good agreement between design and test values was obtained. The test values of stator diffusion factor for the same condition as above, Figure 35, were slightly higher than design intent reflecting the slightly higher-than-design incidence angles. Except at the walls, the stator total pressure loss coefficient showed fair agreement with design, as seen in Figure 36. Plots of stator loss coefficient, loss parameter, diffusion factor and deviation angle versus stator incidence angle at nominal vane schedule, for 50, 70, 80, 90, 100 and 110% design rotor speeds with undistorted inlet flow were presented in the data report, Reference 7. The weight flow of the stage was not limited by the stator losses and the loss level was generally consistent with design prediction. A detailed discussion of stator loss characteristics and the influence of inlet guide vane turning on stator losses is presented in a later section.

2. USE OF VARIABLE CAMBER BLADING FOR OFF-DESIGN OPERATION WITH UNDISTORTED INLET FLOW

a. INFLUENCE OF VARIABLE CAMBER INLET GUIDE VANES ON ROTOR AND STAGE PERFORMANCE

It was shown in Reference 7 that in order to achieve the objective cruise condition weight flow of 122 lbs/sec at 70% design speed with sufficient stall margin, some IGV closure was required. Plots of stage inlet corrected weight flow and stage adiabatic efficiency versus IGV turning angle at 70% speed and stator setting angle of 8° were presented in Reference 7 to show that the optimum IGV/Stator schedule was 40°/8° to give reasonable adiabatic efficiency and stall margin at the cruise condition. An intermediate vane schedule of 20°/4° was also chosen for detailed testing with undistorted inlet flow.

A performance map for the Task II Stage with the IGV's at their nominal (axial) vane schedule and without IGV's was presented in Figure 13. For the case with IGV's, the performance shown is between rotor inlet and stator exit stations. The testing without IGV's was done under Task IV of this contract and is reported in detail in Reference 9. The close agreement of the two maps indicates that the IGV losses were properly accounted for in performance evaluation. Figure 13 shows about 4% greater stall margin at 100% corrected speed without IGV's and with them. This was surprising, as it was believed that the IGV's might help to suppress incipient instabilities. The IGV-rotor gap for the Task II was made generous to allow for a traverse station. The large gap may have made the IGV's ineffective as a stabilizing device.

Figure 37 presents a consolidated performance map for the Task II Stage at the three vane schedules with undistorted inlet flow. It is noticed from this figure that the stall lines for all the three vane schedules nearly coincided with each other indicating that turning the IGV did not change the pressure ratio-weight flow relationship along the stall line. However, the considerable decrease in weight flow at a fixed rotor speed with closed IGV settings resulted in an appreciable change in the speed-versus-weight flow relationship

along the stall line. A guide vane adjustment of 40° enabled achievement of the objective cruise condition of 54% weight flow (122 lbs/sec) at 70% corrected speed with 0.186 stall margin*.

The effect on key performance parameters of operating the stage at the three different vane schedules of 0°/0°, 20°/4°, and 40°/8° can be seen from Figures 38 through 41. The stage peak efficiency achieved at the six speeds tested are presented in Figure 38(a) for the three schedules. Figures 38(b), 39, 40, and 41 present the efficiency weight flow, pressure ratio and stall margin corresponding to the CTL condition. It is apparent from Figures 38 and 41 that at 100% design speed, considerations of efficiency and stall margin would favor the choice of either nominal or 20°/4° schedules. However, the weight flow and stage pressure ratio for the 20°/4° schedule were far below the design specification. At 70% corrected speed, in the absence of a specific requirement of the engine cycle cruise condition, several alternatives are available. If efficiency and stall margin at this speed were the main considerations, the vane schedule 20°/4° appears to be the most desirable. On the other hand, given the additional requirement of the assumed cruise weight flow of 122 lbs/sec without further speed reduction, it was found to be impossible to operate the compressor at the nominal schedule, and with the 20°/4° schedule, this flow is just barely within the stall limit. Turbine matching considerations, for example, might lead to this kind of specification. Both efficiency and stall margin at this weight flow were considerably higher with the 40°/8° schedule than with the 20°/4° schedule at a weight flow of 122 lbs/sec. At this assumed cruise weight flow and speed, the compressor operated very close to peak efficiency with the 40°/8° vane schedule. Figures 42 through 45 present the peak efficiency, and efficiency, weight flow, pressure ratio and stall margin at the CTL condition for the rotor at different speeds. Again, it is seen that at the chosen cruise condition of 122 lbs/sec weight flow at 70% speed, the rotor operated closer to peak efficiency and with higher stall margin at the CTL condition at 40°/8° vane schedule than at the two other schedules tested.

The use of variable geometry IGV's and stators thus enabled operation of the stage at both design speed and chosen part speed cruising condition at close to peak efficiency and with adequate stall margin.

b. USE OF VARIABLE GEOMETRY BLADING FOR MULTISTAGE MATCHING

Variable geometry inlet guide vanes and stators can be used to match the front stage to a second stage at off-design speeds. The capability of the Task II stage with the variable geometry IGV to match a hypothetical second stage at 70% design speed is investigated in Figure 46. The operating weight flow range (based on IGV inlet conditions) of the hypothetical two-stage

---

* Stall Margin = $\left[\left(\frac{P/P}{W\sqrt{\theta}/\delta} \right)_{\text{stall}} \Big/ \left(\frac{P/P}{W\sqrt{\theta}/\delta} \right)_{\substack{\text{operating} \\ \text{condition}}} \right]^{-1.0}$

fan is increased 44% and 54% with IGV/stator schedules of 20°/4° and 40°/8° respectively, relative to that at the 0°/0° nominal schedule. The sharp rise in IGV losses at 40° closure over the losses at 20° closure may account for the fact that the improvement in range at 40°/8° schedule is not considerably more than that at 20°/4° schedule.

A hypothetical second stage performance at 70% corrected speed was obtained for Figure 46 by scaling down the weight flow of first stage performance map using the 0°/0° IGV/stator schedule to the reduced annulus area appropriate for stage matching at 100% corrected speed. The scaling formula, chosen to maintain constant axial Mach number at the 100% speed design point, is

$$W^*_{\text{Stage 2}} = W^*_{\text{IGV inlet}} \left[\frac{\sqrt{T_{2.2}/T_{0.09}}}{(P_{2.2}/P_{0.09})} \right]$$ at 100% speed design point for Stage 1

The effect of the first stage temperature rise on the second stage corrected speed, which is quite small at 70% corrected speed, has been neglected.

The stage total pressure ratio at 70% speed at the three IGV/stator schedules is plotted versus weight flow corrected by IGV inlet conditions and by stage exit conditions. The pressure ratio versus inlet corrected weight flow speed line at 70% speed for a hypothetical second stage is also plotted in Figure 46. The operation of the two stages together was assumed to be represented by both stages operating at the same percent design speed at the same weight flow corrected to the inter-stage conditions. The second stage performance is assumed to be unaffected by the first stage stator setting. The operation would be bounded on the low side by stall of the first stage, and on the high side by choking of the second stage. This is shown on Figure 46. The first stage stalls at 118 lb/sec and 1.275 pressure ratio with the 20°/4° schedule. The discharge corrected flow from the first stage is 97 lb/sec. The second stage pressure ratio for this flow is 1.295. Therefore, the two stage stall pressure ratio is 1.65. Similarly the maximum flow for this schedule, set by second stage choke, is 136 lb/sec based on inlet conditions.

c. ROTOR BLADE ELEMENT WORK COEFFICIENT-FLOW COEFFICIENT CORRELATION IN UNDISTORTED INLET FLOW

As shown in the preceding section, the variable geometry inlet guide vanes and stators allowed the Task II Stage to operate with adequate stall margin and acceptable efficiency over a very broad range of flows at each speed. In order to condense the large amount of data obtained during testing, the 100% speed and 70% speed test data were used to calculate rotor work and flow coefficients for the pitchline blade element section. The basic data are shown in Figure 47, in which the large differences due to IGV turning angle can be seen and certain smaller effects of speed are still evident. The reduction in flow capacity and work input with increasing IGV turning shown in Figure 47 further demonstrates the wide range of operation possible with variable geometry blading.

The basic pitchline characteristic curves can be corrected to the same inlet swirl and axial velocity ratio in order to obtain a universal characteristic curve valid for all speeds and IGV setting angles. A flow coefficient, ϕ_o, derived in Reference 4, is corrected to zero inlet absolute swirl angle and thus becomes proportional only to rotor inlet relative air angle. A corrected work coefficient, $(\psi_{cor})_o$, is defined as the work coefficient that would exist at the same rotor inlet relative air angle as the actual data but at zero inlet swirl and an axial velocity ratio of unity. The data shown in Figure 47 have been reformulated into corrected characteristic data and are shown in Figure 48. It can be seen that all the data, which cover a wide range of speed and IGV turning are collapsed by this technique into a single band having a range of approximately ±5% from an average characteristic curve. This average corrected characteristic curve could be uncorrected so as to predict the performance of the rotor at operating conditions for which test data were not obtained thereby greatly expanding the usefulness of the data that were obtained.

d. PERFORMANCE OF THE VARIABLE CAMBER INLET GUIDE VANE

Variable camber inlet guide vanes were chosen for this stage to minimize losses while varying the swirl angle at the guide vane exit. This section presents the IGV blade element data obtained with undistorted inlet flow and compares the performance of these guide vanes with conventional rigid cambered guide vanes.

Figure 49 presents the IGV total pressure loss coefficients as a function of IGV inlet Mach number and IGV setting angle at seven radial immersions. These data were obtained by methods discussed in Reference 7. In the inlet Mach number range between 0.2 and 0.55, the variation of the loss coefficients with Mach number was very small at both the 0° and the 20° IGV setting angles, showing a slight tendency toward higher loss coefficients with increasing Mach number. The loss coefficients at the 20° IGV setting angle were nearly equal to those at the 0° setting angle in the midspan region. Near the walls, however, the loss coefficients at the 20° setting were nearly twice the values at the 0° setting angle. The loss coefficients at the 40° setting angle were considerably higher than those at the 0° and the 20° setting angles, especially near the walls, probably due to flow separation at the high turning angles. The variation with Mach number of the loss coefficients at the 40° setting angle was also considerably different from that at the 0° and 20° setting angles, showing a sharp increase with Mach number above M = 0.25 near the walls and above M = 0.3 - 0.35 in the midspan region. It is believed that this sharp rise in losses was caused by choking of the flow in the vane passage.

Radial profiles of IGV deviation angles at IGV setting angles of 0°, 20°, and 40° are presented in Figure 50. The deviation angles were less than 5° at practically all immersions for all IGV setting angles. Figure 51 shows rotor inlet swirl at 100% speed, intermediate flow with IGV from Task II tests at nominal vane schedule, and without IGV from Task IV tests reported in Reference 9. The non-zero rotor inlet swirl measured without IGV indicated that part of the deviation angles shown in Figure 50 could have resulted from slight error in flow angle measurement.

The total pressure loss coefficients at different flow turning angles obtained with the variable camber IGV of the present study are compared with those from rigid airfoil cascade tests of Dunavant (Reference 10) in Figure 52. Dunavant's data were obtained at low Mach numbers with guide vanes of solidity 1.5 and camber values given by $c_{\ell_o} = 0.6$ and 1.2. The data presented from the current study were obtained at the IGV inlet Mach number of 0.2 at 70% immersion from the tip, where the solidity is 1.5. From the data presented, it is apparent that at selected narrow ranges of flow turning angles between 0° and 40°, the conventional fixed camber inlet guide vanes suffered lower losses than the variable camber IGV of the present study. It appears probable that fixed camber, variable stagger IGV's, designed with a positive camber less than $c_{\ell_o} = 0.6$, would give a loss level at zero deflection no greater than was achieved with the variable camber IGV's. If, however, extrapolation of the fixed camber IGV loss data follows the dashed curve of Figure 52, as is suggested by experimental data from lower solidities, the variable-camber design may show clear benefits for extreme range requirements.

The capability of varying the IGV exit swirl over a range from 0° to 40° within acceptable loss levels was a principal objective in the choice of the variable camber IGV profiles over conventional rigid camber profiles. Figure 52 shows that these IGV's may have demonstrated a somewhat greater range within loss levels double the minimum than would be expected from rigid camber profiles, with a small increase in the minimum loss. If the variable camber principle permits simplification of the inlet structure, this increased loss may be acceptable.

e. CORRELATION OF STATOR LOSS CHARACTERISTICS

Stator loss data from all three standard vane schedules have been studied in an effort to confirm the general applicability of correlations such as those presented in Reference 11. The study led to conclusions about the influence of Mach number on minimum loss and on incidence range within twice minimum loss, which are summarized on Figures 53(a) and 53(b) for data at 50% immersion. Within the scatter of the data, the loss level [Figure 53(a)] is about 50% greater than would be predicted from Reference 11, independent of the Mach number below 0.7. For data at 110% corrected speed, the Mach number rises above 0.7 and the loss level appears to increase. The usable incidence angle range of approximately 25° in Figure 53(b) at low Mach numbers is typical of results quoted in Reference 11. Typical results in Reference 11 show that the low loss incidence angle range has decreased to 10° at 0.7 Mach number. The data of Figure 53(b) show substantially less Mach number sensitivity than that.

The results of Figure 53 were obtained with the assistance of correlation plots of data from the three vane schedules grouped according to speed, Figures 54(a) - 54(c). Since these data scattered enough to prevent resolution of the minimum loss coefficient within about ±0.01, a statistical type approach was used. A least square polynomial curvefit was made for the data of each vane schedule and each speed. A minimum loss was identified from the curvefit, and supplemented by the two lowest-loss test points, in arriving at the data plotted

in Figure 53(a). The "best estimate" of the loss level appropriate to the speed has been chosen as the arithmetic average. The standard deviation about that average has been taken as one-third of the extreme range. This procedure appears to allow an estimate of the minimum loss somewhat better than ±0.005. The incidence angle range of Figure 53(b) has been taken from the polynomial curvefits and checked for consistency with Figure 54.

Figure 55 presents the stator loss coefficients at 90% immersion for the three vane schedules together. At this immersion, it appears that there were three distinct levels of loss coefficient profiles for the three vane schedules. An examination of the stator wake profiles was made to determine if the impingement of IGV wakes on stator wake profiles could have caused erroneous evaluation of stator and rotor losses. Figure 56 shows the stator wake profiles at 50% and 90% immersions from three readings with IGV setting angles of 0°, 20°, and 40°. The three readings were obtained at 70% speed at a constant throttle valve setting, and the same 0° stator setting angle, with undistorted inlet flow. Each stator wake rake covered two stator passages. The two wakes for each reading at 50% immersions were of approximately equal depth, but the free-stream levels between wakes are different, as if an IGV wake had affected the lower free stream level. At 90% immersion, however, the depths of the wakes were distinctly unequal, particularly at non-zero IGV setting angles, indicating the likelihood of impingement of IGV wakes on the stator wake rakes. The shallower wake would more likely be the true stator wake. The rotor exit/stator inlet total pressure at each immersion was obtained from an arithmetical average of the three highest readings from the corresponding 14-element wake rake and the stator exit total pressure was obtained from a circumferential mass-average of the enthalpy and the change in entropy between compressor inlet and the stator exit planes. Impingement of IGV wakes on stator wake rakes thus would cause erroneous evaluation of rotor and stator total pressure loss coefficients. It is therefore believed that rotor losses have been underestimated and stator losses overestimated by small amounts, particularly at the hub, depending on the sizes of the IGV wakes at different IGV turning angles.

The influence of the closure of IGV and stator on rotor tip and stator hub loadings near stall can be observed from Figures 57 and 58. The rotor diffusion factor, static pressure rise coefficient and work coefficient at 5 and 10 percent immersions from tip are plotted versus weight flow from the readings closest to stall at each speed and vane schedule in Figures 57(a) and 57(b). Similar plots of stator diffusion factor and static pressure rise coefficient at 90 and 95 percent immersions from tip are presented in Figures 58(a) and 58(b). The weight flow was found to be a convenient parameter to spread the data at the different speeds and was not chosen with an implication of being the controlling variable. The rotor tip loading seemed to reach the same limiting value at all speeds before stall at nominal vane schedule. At off-design vane schedules, the maximum loading at the rotor tip before stage stall was less than the limit loading defined by the 0° vane schedule. The actual rotor tip loading near stall decreased considerably with increasing speed. The stator hub loading reached its highest values at the lower speeds near stall with the off-design vane schedules, suggesting that this loading could have been critical. However, the anemometer traces indicated stall to be initiated always in the outer span of the rotor, contrary to the expectation if the stator hub loading was the limiting parameter.

3. PERFORMANCE WITH INLET FLOW RADIALLY DISTORTED IN THE TIP REGION

a. OVERALL PERFORMANCE

Performance data from tests with a radial inlet distortion pattern covering the outer 40% of the annulus area were obtained at 70%, 90% and 100% of design corrected speed at the two IGV/stator schedules 0°/0° and 40°/8°.

The distortion screen used to produce the tip radial distortion was shown in Figure 4. At 100% design speed and with nominal vane schedule, the severity of the inlet distortion pattern is indicated by the distortion parameter $(P_{max.} - P_{min.}) / P_{max.}$, equal to 0.172. Figure 59 shows the variation of the distortion parameter for radial (and also circumferential) inlet distortions over the weight flow range at all speeds tested. These data were calculated from overall performance results with radial and circumferential inlet distortions.

Task II Stage performance maps with radial inlet flow distortion for the two IGV/stator schedules are presented in Figures 60 and 61 respectively. Performance of the stage with undistorted inlet flow is also included in these maps for comparison. Figure 60 also shows comparable data with the IGV's removed, taken from Reference 9. The distortion was responsible for significant deterioration in peak efficiency, stall pressure ratio, and stall margin at all speeds. The stall margin loss without the IGV's was slightly greater than with them. The efficiency for the intermediate flow, 70% speed point on Figure 61, is thought to be in error; the curve has been drawn for consistency with trends under other conditions. At design speed and nominal vane schedule, the radially distorted inlet flow caused a loss of 5.3 percentage points in peak efficiency compared to that attained with clean inlet flow and a drop in stall margin at the CTL condition from 0.135 with undistorted inlet flow to 0.034 with radially distorted flow. At 70% speed and IGV/stator schedule of 40°/8°, the stall margin at the CTL condition dropped from 0.203 with undistorted inlet flow to 0.181 with radial distortion.

b. COMPARISON OF STALL AERODYNAMIC LOADING IN RADIALLY DISTORTED INLET FLOW WITH THAT IN UNDISTORTED INLET FLOW

The stage was stalled at 70%, 90%, and 100% design speeds at 0°/0° and 40°/8° vane schedules with radially distorted inlet flow. Hot wire anemometer signals indicated that rotating stall initiated nearly simultaneously at the rotor tip and pitch and considerably later at the hub. This indicated that the limiting loading parameters should occur in the outer 50% of the rotor span.

Variation of aerodynamic loading, work input and total pressure ratio with throttle valve setting at 5% immersion from tip is shown in Figure 62 for 100% speed, nominal vane schedule with undistorted and radially distorted inlet flows. Figure 63 presents these parameters for the same cases at 10% immersion from tip. The tip diffusion factor, pressure ratio and work input

at stall obtained by extrapolating to stall DV setting were approximately the same for both undistorted and radially distorted inlet flows indicating that it was not a significantly different rotor tip behavior which led to the reduction in stalling pressure ratio with radially distorted inlet flow. Figure 64 shows radial profiles of diffusion factor, work input, static pressure rise coefficient and total pressure ratio near stall with undistorted inlet flow and radially distorted inlet flow at design speed and nominal vane schedule. It is seen that the low pressure ratios in the lower half of the span were responsible for the low average pressure ratio at stall with radial distortion. The tip radial distortion screen caused higher hub axial velocities and lower tip axial velocities than with undistorted inlet flow, resulting in high incidence angles at the tip and low incidence angles at the hub. This is seen from Figure 65 which shows the variation of rotor incidence angles with DV setting at 5, 10, 90, and 95% immersions from tip with undistorted inlet and radially distorted inlet flows at nominal vane schedule. Figure 66 shows radial profiles of rotor incidence angles for the near stall readings from undistorted and radially distorted inlet flows at design speed and nominal vane schedule. The considerable deviation of incidence angles from design value in the case of radial distortion can also account for the loss in efficiency over the entire speed line.

The variation of rotor diffusion factor, static pressure rise coefficient, work input and rotor pressure-ratio with DV setting at 5% and 10% immersions from tip is presented in Figures 67 and 68 for 70% speed, 40°/8° vane schedule with undistorted and radially distorted inlet flows. Figure 69 shows radial plots of rotor diffusion factor, static pressure rise coefficient and work input near stall for the two types of flows. The tip work input and diffusion factor at stall, obtained by extrapolating to DV setting at stall were approximately equal for both cases indicating that the tip diffusion factor was a reasonably consistent indicator of loading at stall. A comparison with nominal vane schedule cases also shows that the tip diffusion factor generally reached a value between 0.5 and 0.55 at stall for both undistorted and radially distorted inlet flows at both schedules tested.

c. INFLUENCE OF VARIABLE CAMBER INLET GUIDE VANES ON STAGE PERFORMANCE WITH TIP RADIAL DISTORTION

Consolidated stage performance maps for nominal and 40°/8° vane schedule with radial inlet flow distortion are presented in Figure 70. It is seen that with the 40°/8° vane schedule, both the pressure ratio-weight flow and the speed-weight flow relationships along the stall line were changed. This enabled achieving higher pressure ratio at stall than that attainable if the stall line had not changed as in the case of undistorted inlet flow. The objective cruise operating condition of 54% (122 lbs/sec) weight flow at 70% speed was achieved with the 40°/8° schedule with 18% stall margin while with the nominal schedule, the compressor stalled before being throttled to this condition.

The influence of the variable geometry features on the key performance parameters of the stage with radially distorted flow can be seen from Figures 71 through 74 which present the variation with speed and vane schedule of peak

efficiency and efficiency, weight flow, stage pressure ratio and stall margin at the CTL condition. The efficiency at the CTL condition and the corresponding weight flow and pressure ratio achieved are higher at all speeds at nominal vane schedule; however, turning the IGV to 40° appears to give a marked improvement in stall margin at all speeds up to 100% speed where the compressor stalled at peak efficiency for both vane schedules. This improvement in stall margin is also evident from the performance maps. The efficiency, pressure ratio and stall margin obtained from the chosen cruising condition of 122 lbs/sec flow at 70% speed are also shown in Figures 71 through 74.

The differences in efficiency and stall margin at the CTL condition between undistorted inlet flow and radially distorted inlet flow are plotted versus percent design rotor speed in Figure 75 for the two vane schedules. It is seen that the 40°/8° vane schedule permitted a significant recovery of the loss in the CTL efficiency and the stall margin that occurred at 90% and 100% corrected speeds at the 0°/0° vane schedule with radial distortion. The efficiency comparison at 70% is clouded by the uncertainty in distorted CTL efficiency discussed in connection with Figure 61.

d. TRANSFER OF RADIAL DISTORTION BETWEEN STAGE INLET AND STAGE EXIT WITH AND WITHOUT IGV/STATOR CLOSURE

The attenuation of the radially distorted inlet total pressure profile through the stage is shown in Figure 76 at maximum flow and near stall conditions at 100% speed with nominal vane schedule and at 70% speed with 40°/8° vane schedule. The inlet distortion at the tip appeared in all cases as a region of low pressure.

At 100% design speed and maximum flow with 0°/0° vane schedule, Figure 76(a), the ratio of the distortion parameter at the stage exit to that at IGV inlet was 0.68 indicating that the attenuation of the distortion was small. At the same speed and vane schedule, the distortion was attenuated more near stall, Figure 76(b); the distortion parameter at the stage exit was only 34% of that at stage inlet. The radial pressure profiles at the 40°/8° vane schedule at 70% speed maximum flow condition, Figure 76(c), showed that although the inlet radial distortion was strongly attenuated behind the rotor, the distortion at the stator exit appeared as a region of very low total pressure at the hub. The high deviation angles and significantly low axial velocities at the hub at this station, indicate that the distortion at the hub was caused by separated flow in the stator hub region. Near stall, at the 40°/8° vane schedule, 70% speed condition, the very high rotor incidence angles and consequent high rotor total pressure ratios at the outer span caused an amplification of the distortion parameters at rotor exit to 1.67 times the value at stage inlet. However, this distortion at rotor exit, Figure 76(b), appeared as a region of higher than average pressure at the outer span of the rotor. The distortion parameter at the stator exit was 1.27 times the value at stage inlet, the distortion still appearing as a region of higher than average pressure at the outer span. High deviation angles and low exit axial velocities were observed near the stator hub.

Radial profiles of total pressure at the inlet and exit planes to the blade rows for undistorted inlet flow are also included in Figure 76 for comparison. The data presented are at maximum flow and near stall flow at 100% speed with nominal vane schedule and at 70% speed with 40°/8° vane schedule for comparison with radial distortion data obtained at similar conditions. The values of the distortion parameters at the flow measurement stations are plotted for these cases in Figure 77. The similarity of the pressure profiles for both undistorted and radially distorted flows and the nearly equal values of the distortion parameters at the stage exit station except in the case of maximum flow at 70% speed, 40°/8° vane schedule indicates that the effect of radial distortion at the inlet to the front stage is minimal on the subsequent stages. However in the case of 70% speed, 40°/8° vane schedule, maximum flow, a flow separation at the stator hub resulted from inlet radial distortion; this can affect the performance of any subsequent fan stage or the core compressor.

4. PERFORMANCE IN FLOW WITH CIRCUMFERENTIAL INLET DISTORTION

Performance data from tests with circumferential inlet distortion were obtained at 70%, 90%, and 100% speeds at the two IGV/stator schedules of 0°/0° and 40°/8°. The distortion screen used to introduce the circumferential distortion was shown in Figure 5. The screen covered a 90° arc of the inlet annulus area at plane 0.10. Figure 59 shows the variation of the distortion parameter over the entire weight flow range tested based on maximum and minimum total pressures on the inlet disortion rakes with the center of the distortion screen in the nominal position, 195° from top center.

a. OVERALL PERFORMANCE

The stage performance maps with circumferential inlet flow distortion are shown on Figure 78 for the 0°/0° IGV/stator schedule and for an IGV-less configuration (data from Reference 9) and in Figure 79 for the 40°/8° schedule. Performance on the stage with undistorted inlet flow also is included for comparison. The stage suffered significant losses in efficiency at the CTL condition and stall margin from that condition at both vane schedules with inlet circumferential distortion. There is no systematic difference between the stall margin losses with and without the IGV's. Rotating stall was encountered at each speed and vane schedule. As in the case of radial distortion, the rotating stall originated in the outer 50 percent of span. For the nominal IGV/stator schedule at 100% design speed, the circumferential distortion caused a decrease in stalling total pressure ratio to 1.66 from 1.78 obtained with undistorted inlet flow. The peak efficiency was reduced 3.9 percent due to circumferential distortion. At 70% speed and 40°/8° schedule, the stall pressure ratio dropped from 1.22 with undistorted inlet flow to 1.21 with circumferential inlet flow distortion and the peak efficiency loss from clean inlet flow was less than 0.5 percent.

b. INFLUENCE OF VARIABLE CAMBER INLET GUIDE VANES ON STAGE PERFORMANCE IN FLOW WITH CIRCUMFERENTIAL DISTORTION

Comparison of Figures 78 and 79 shows that the weight flow and pressure ratio penalties suffered due to circumferential distortion were

less with the 40°/8° schedule than with the 0°/0° schedule. Consolidated stage performance maps for 0°/0° and 40°/8° vane schedules with circumferential inlet distortion are presented in Figure 80. As in the case of undistorted inlet flow, it is seen that the stall lines for the two vane schedules maintained nearly the same pressure ratio-weight flow relationship. The speed-weight flow relationships, however, were different along the stall lines enabling operation at lower weight flows at the same speed with 40°/8° schedule than with nominal schedule. The stage peak efficiency and efficiency, weight flow, stall pressure ratio and stall margin at the CTL condition at the two vane schedules with circumferential inlet distortion are plotted versus rotor percent design speed in Figures 81 through 84. The peak efficiencies were nearly equal at 70% design speed with both vane schedules. The 40°/8° vane schedule gave higher peak efficiencies at 90 and 100% speeds. At the CTL condition, the stage efficiencies were equal for both 0°/0° and 40°/8° vane schedules at 70% and 100% speeds. The considerable decreases in weight flow and pressure ratios at 40°/8° vane schedule should, however, be taken into account while weighing the performances at the two vane schedules. For example, although the 40°/8° schedule gave higher peak efficiency than the 0°/0° schedule at 100% speeds, the weight flow and pressure ratio at nominal schedule were much closer to design conditions.

The objective cruising weight flow of 122 lbs/sec at 70% design speed could not be achieved at nominal schedule before stall. However, at 40°/8° schedule, this condition was achieved at peak efficiency, Figure 81(a), indicating that, even with inlet circumferential distortion the use of variable geometry blading enabled operation at the cruising condition with 83.5% efficiency and 21% stall margin. It was mentioned in earlier sections that the 40°/8° vane schedule enabled efficient operation with adequate stall margin at cruising weight flow and speed with undistorted and radially distorted inlet flows also.

c. TRANSMISSION OF CIRCUMFERENTIAL DISTORTION THROUGH STAGE

Some analysis of the persistence of the circumferential distortion pattern through the stage is aimed at evaluating its suitability for use in front of another fan stage or a core compressor. The suitability is measured by the "distortion transfer"; stages giving substantial reduction in the distortion amplitude are desirable.

It has seemed valuable to examine distortion transfer in terms of the "distortion parameter"

$$DP = \frac{P_{max.} - P_{min.}}{P_{max.}}$$

and in terms of the "Index of Distortion, Circumferential"

$$IDC = \frac{P_{avg,\ immersion} - P_{min.,\ immersion}}{P_{avg,\ face}}$$

The use of DP is conventional; this quantity is easy to evaluate and explain. It does not, however, discriminate between local low pressure regions, which demand high pressure ratio output of the blading with susceptibility to local stalling, and local high pressure regions, which simply unload the following blading. The IDC attempts to concentrate attention on requirements for locally high performance of the blading.

Table VII summarizes distortion transfers, for the six test conditions under which detailed performance measurements with circumferential distortion were made. Using DP as the measure, substantial attenuation of the inlet distortion is observed, after both rotor and stator, for most of the test conditions. Two highly loaded test conditions showed preservation or amplification of the distortion through the rotor tip, and subsequent attenuation to a satisfactory level through the stator. The remaining test conditions showed substantial ttenuation through the rotor tip, with the reduced level maintained through the stator. The rotor hubs seem to have tried to eliminate the distortion: in the two test conditions where DP did not decrease substantially, the width of the low pressure zone is actually reduced. The stator hubs seem to have stalled, with a consequent high loss returning the distortion level close to the initial value.

Examination of the data in Table VII using IDC as the distortion measure shows that substantial attenuations of the harmful distortion occurred through the rotor in tip and mid span regions for all test conditions. The two cases where DP does not indicate attenuation are cases where the rotor has actually inverted the distortion, so that a potentially harmful pressure diffusion is turned into a pressure mountain. The IDC concept supposes that this pressure mountain will not produce adverse effects downstream. The message given by IDC data about the hub is the same as that inferred from DP data: that the rotor hubs generally try to eliminate the distortion and the stator hubs help regenerate it. There is no conspicuous evidence of significantly different distortion transfers as a result of the different variable geometry settings.

A closer examination of the data behind the distortion numbers, as found in Figures 21-26 of Reference 8, reveals a number of features about localized behavior of the blading, which are summarized quantitatively in Table VIII, and numerically in Table IX. Table X presents some undistorted data from the maximum-flow and near-stall ends of the appropriate speed lines, for convenient comparison with the local values.

The rotor tries to compensate for distorted pressure profiles under most of the operating conditions and at all immersions. The tip region is especially successful at this. The distortion profile is inverted. In the screen shadow the rotor tip pressure ratio is 2.09 at 100% corrected speed with the 0°/0° schedule, as compared with 1.85 maximum under undistorted conditions, and 1.60 at 100% corrected speed with the 40°/8° schedule, a. compared with 1.52 undistorted. The rotor hub pressure ratio is 1.97 in the screen shadow at 100% corrected speed with the 0°/0° schedule, as compared with 1.71 undistorted, and 1.48 in the screen shadow with the 40°/8° schedule as compared with 1.36

undistorted. Under the maximum flow conditions at 100% corrected speed, most of the inlet total pressure depression remains after the rotor. This appears to be a consequence of the back pressure, low enough so that stator passages choke over the entire annulus. Then the back pressures have no effect at equilizing rotor discharge pressures.

Among the test conditions, there are strong suggestions that either stator choke or stator stall may be the dominant effect in determining the distortion in the discharge pressure profile. Three of the test conditions are highly loaded and show evidence that stator hub sections stalled out in the distorted sector, perhaps as a result of exposure to excessively high tangential velocities when the rotor attempted to compensate for the distortion profile, and returned the local total pressure to a distortion level comparable to that at the inlet. Under other conditions the effects of stator choking have been to throttle off the regions of high total pressure, leaving discharge conditions much more uniform than the inlet conditions.

The results of the distortion transfer analysis suggest that a higher stator stagger, or perhaps a larger hub camber, would have given more favorable stage performance on and above the CTL line. It should be observed that the stage matching analysis really demands a fixed trailing edge angle for the stator of the first stage. Thus there is a potential application for a variable camber stator, such that the leading edge angle could be increased, relative to the design for undistorted flow, to satisfy either stage matching or distortion tolerance requirements.

5. COMPARISON OF INFLUENCES OF RADIAL AND CIRCUMFERENTIAL DISTORTIONS AND VARIABLE GEOMETRY BLADING ON STAGE PEAK EFFICIENCY AND STALL MARGIN

The efficiencies and stall margins at the CTL condition obtained at different speeds with the two vane schedules with radial and circumferential distortion were discussed in earlier sections. This section presents a direct comparison of the values of these parameters obtained with the two types of distortion patterns and the two vane schedules. The comparison is presented in Figure 75 in the form of differences in CTL efficiency and stall margin between undistorted inlet flow and the particular type of distortion. Significant results are seen in the figure. Compared to the undistorted inlet flow, there was a greater loss in CTL efficiency and stall margin at all speeds and vane schedules with radial distortion than with circumferential distortion. Although the CTL efficiencies and stall margins at both vane schedules were nearly equal at 70% speed with circumferential distortion (as seen from Figures 81 and 84), Figure 75 shows that the losses in CTL efficiency and stall margin due to circumferential distortion were less at the 40°/8° vane schedule than at the nominal vane schedule. However, with radial distortion, the 40°/8° vane schedule, at 70% speed contributed to a nearly 90% recovery of the loss in stall margin that occurred at 0°/0° vane schedule though the loss in CTL efficiency was higher. The CTL efficiencies obtained with circumferential inlet distortion at the 40°/8° vane schedule were nearly equal to those obtained with undistorted inlet flow. In general, this figure shows that the use of variable camber inlet guide vanes contributes to reducing the losses in

efficiency and stall margin that result from distorted inlet flows. It should be emphasized, however, that considerable weight flow reductions occur when the variable geometry features are used. This is seen from Table XI which summarizes the values of peak efficiency and efficiencies, weight flows and pressure ratios at the CTL condition and at stall for the three types of inlet flow conditions and the two vane schedules at 70, 90 and 100% design speeds. Comparable data with the IGV's removed, taken from Reference 9, also have been included in Table XI.

V. CONCLUDING DISCUSSION

Task II of this contract was carried out to investigate the efficiency and stall margin potential of a 1500 ft/sec tip speed stage, to develop design methods and criteria for stages of this type, to evaluate the effectiveness of variable-geometry inlet guide vanes and stators in improving part-speed efficiency and weight flow range and to determine the effect of inlet flow distortions on stage performance including the effect of the variable-geometry blading on distortion tolerance. In addition, the Task II Stage was designed to operate at and above 1500 ft/sec tip speed with efficiency levels higher than could be achieved by the 1400 ft/sec design tip speed Task I Stage. Major results and conclusions are summarized below.

(i) The Task II rotor, which was designed with higher tip solidity, lower camber and with smaller throat areas than the Task I rotor, achieved higher efficiencies than the Task I rotor at speeds of 1500 ft/sec and above. The peak efficiencies attained by the Task II and Task I rotors at 1500 ft/sec tip speed were 0.868 and 0.859 respectively. At 1540 ft/sec, which is 110% design speed of the Task I rotor, the peak efficiencies of Task II and Task I rotors were 0.864 and 0.845 respectively. Although the Task I rotor had a slightly greater stall margin at high speeds, both rotors reached essentially equal levels of tip static pressure rise coefficient at stall. The Task I rotor had superior performance at part speed conditions.

(ii) The design techniques used for the Task II stage gave reasonably satisfactory results. The geometric angle of the flow induction surface of the rotor blade was slightly too large in the tip region, leading to a 1% deficiency in the flow below design intent. The tip throat area, at 95% of capture area, deliberately small by the current standards was large enough for establishment of the desired oblique shock pattern at the design point. The test data give no direct indication on how much smaller the throat area could have been without sacrificing the oblique structure. Data analysis identified hub and tip regions as areas for potential improvement of performance by reduction of losses, but without suggesting any specific design changes to accomplish the result.

(iii) The deviation angles at the outer half of the rotor were less than predicted by the design. It appears that the design method, which consisted of application of Carter's Rule for circular-arc meanline blades to equivalent constant-radius, constant-axial-velocity cascade sections underestimated the ability of this type of blading to deflect the air stream. Although it is likely that the lower-than-predicted deviation angles were the result of deflections produced by trailing edge shocks, the data obtained in this investigation were not sufficient to confirm this. Deviation angles for the inner half of the rotor were close to the design prediction.

(iv) Rotor tip static pressure survey data indicated that at 90% design speed, it was not possible for the leading edge normal shock to become oblique even at open throttle, low back pressure conditions. At 100% speed, for

high back pressure near-stall operation, the leading edge shock was normal to the flow but was located at the passage inlet. The oblique leading edge shock structure was established at lower back pressures at design speed. The leading edge shock was oblique at all back pressures at 110% design speed.

(v) A comparison of stator loading, deviation angle and loss levels with design intent showed that the stator design rules were adequate and that design intent had generally been met.

(vi) The objective off-design cruise condition of 54% design weight flow at 70% design speed could not be achieved at zero IGV turning before the onset of stall. However, an IGV turning of 40° and a corresponding stator setting of 8° enabled this condition to be realized with 83.7% efficiency and 18.5% stall margin with undistorted inlet flow. The use of the variable camber IGV at non-zero settings did not alter the stalling pressure ratio-flow relationship. However, it did alter the flow-speed and pressure ratio-speed characteristics of the compressor and thus provided flexibility of operation at off-design flow and speed conditions. The IGV losses were slightly higher than would be expected from a fixed camber, variable stagger vane row over moderately wide ranges of setting angle and inlet Mach number, but remain tolerable for greater closures.

(vii) An analysis performed to match a hypothetical second stage at 70% design speed to the Task II stage with undistorted inlet flow showed that the operating weight flow range (corrected to IGV inlet conditions) of the hypothetical two-stage fan increased 44% and 54% with IGV/Stator schedules of 20°/4° and 40°/8° respectively compared to that at the 0°/0° nominal schedule.

(viii) Radial inlet flow distortion caused considerable losses at all speeds in stage peak efficiency, stall pressure ratio and stall margin. At design speed and nominal vane schedule, the radially distorted flow caused a drop of 5.3 percentage points in peak efficiency and a drop in stall margin at the CTL condition from 0.135 with clean inlet flow to 0.034 with distorted inlet flow. Removal of the IGV caused an additional 0.02 drop in stall margin. Rotor tip aerodynamic loading at stall with radial distortion was approximately the same as that reached at stall with undistorted inlet flow. Low pressure ratios in the inner half of the rotor span caused low average rotor total pressure ratio at stall with radially distorted flow. Tip radial distortion caused high hub axial velocities and low tip axial velocities compared to design intent. The consequent departure of incidence angles from design value caused high losses in efficiency over the entire speed line.

(ix) The attenuation of the radial distortion at nominal vane schedule at maximum flow at 100% speed was small. However, the radial distortion was strongly attenuated at the near-stall condition at the same speed and vane schedule.

(x) The 90° one-per-rev circumferential distortion caused less loss in peak efficiency and stall margin than did radial distortion. At 100% speed, nominal vane schedule, the peak efficiency loss due to circumferential

distortion (relative to the undistorted inlet flow case) was 3.9%. At any given weight flow, the total pressure ratio in the case of flow with circumferential distortion was less than that achieved with undistorted inlet flow.

(xi) At nominal vane schedule, the circumferential inlet distortion was attentuated between 40 and 60 percent at stage exit at the tip and pitch sections. At the hub, however, there was little attenuation: the ratio of distortion parameter, defined as $(P_{max.} - P_{min.})/P_{max.}$, at the exit to that at inlet was between 82 and 99%. This poor attentuation at the hub resulted from flow separation in the stator hub region.

(xii) The variable camber IGV with inlet distortion present enabled operation of the stage with apparently adequate stall margin at the cruise condition of 54% flow and 70% speed. With tip radial distortion, the 40° IGV setting provided improved stall margin from the reference constant throttle line condition, with a small sacrifice in peak efficiency.

(xiii) The radial distortion at the 40° IGV setting, near-stall condition at 70% speed was over-attentuated between the stage inlet and the rotor exit resulting in higher-than-average total pressures at the tip region at rotor exit. This was due to the normally steep pressure-vs.-flow characteristic of the rotor tip region, which overshadowed the relatively mild tip distortion in determining the near-stall discharge pressure profile.

(xiv) Operation of the stage at the 40° IGV setting with inlet circumferential distortion, at 90% and 100% design speeds, provided slightly higher peak efficiency and stall margin than operation at the 0° IGV setting. At 70% design speed with inlet circumferential distortion, the peak efficiencies and stall margins at the 0° and 40° IGV settings were nearly equal. The cruise condition of 54% weight flow at 70% speed was achieved with 21% stall margin at 40° IGV setting with circumferential distortion. The stall line for both 0°/0° and 40°/8° vane schedules maintained the same pressure ratio-weight flow relationship. The speed-weight flow relationships, however, were different along the stall lines enabling operation at lower weight flows with added stall margin at the same speed with the 40°/8° vane schedule than with the nominal vane schedule.

(xv) Use of variable geometry blading had little influence on the ability to attenuate circumferential inlet flow distortion.

APPENDIX A

SYMBOLS

Symbol	Description	Units
A	Annulus or streamtube area	$in.^2$
C	Chord length of cylindrical section	in.
C_h	Enthalpy - equivalent static pressure rise coefficient	

$$C_h = \frac{2gJ\, c_p t_1 \left[\left(\frac{p_2}{p_1} \right)^{\frac{\gamma-1}{\gamma}} - 1 \right] - (U_2^2 - U_1^2)}{V_1'^2}$$

C_p	Static pressure rise coefficient,	----

$$C_p = \frac{P_2 - P_1}{P_1' - P_1}$$

c_p	Specific heat at constant pressure	Btu/lb-° R
D	Diffusion factor:	---

$$D_{rotor} = 1 - \frac{V_2'}{V_1'} + \frac{r_2 V_{\theta 2} - r_1 V_{\theta 1}}{2\bar{r}\ \sigma\ V_1'}$$

$$D_{stator} = 1 - \frac{V_2}{V_1} + \frac{r_1 V_{\theta 1} - r_2 V_{\theta 2}}{2\bar{r}\ \sigma\ V_1}$$

DP	Distortion Parameter = $\frac{P_{max.} - P_{min.}}{P_{max.}}$	
g	Acceleration due to gravity	32.174 ft/sec^2
i	Incidence angle, difference between flow angle and camber line angle at leading edge in cascade projection	Degrees
IDC	Index of Distortion, Circumferential = $\frac{P_{avg,\ immersion} - P_{min.,\ immersion}}{P_{avg,\ face}}$	

Symbol	Description	Units
J	Mechanical equivalent of heat	778.161 ft-lb/Btu
M	Mach number	---
N	Rotational speed	RPM
P	Total or stagnation pressure	PSIA
p	Static pressure	PSIA
r	Radius	in.
$\bar{r}$	Mean radius, average of streamline leading-trailing edge radii	in.
S	Spacing between blades	in.
SM	Stall Margin: for Rotor, $SM = \left[\left(\frac{\left(\frac{P_{1.51}}{P_{0.95}}\right)}{\frac{W\sqrt{\theta}}{\delta}}\right)_{Stall} \Big/ \left(\frac{\left(\frac{P_{1.51}}{P_{0.95}}\right)}{\frac{W\sqrt{\theta}}{\delta}}\right)_{CTL}\right] - 1$ for Stage, $SM = \left[\left(\frac{\left(\frac{P_{2.2}}{P_{0.40}}\right)}{\frac{W\sqrt{\theta}}{\delta}}\right)_{Stall} \Big/ \left(\frac{\left(\frac{P_{2.2}}{P_{0.40}}\right)}{\frac{W\sqrt{\theta}}{\delta}}\right)_{CTL}\right] - 1$	
T	Total or stagnation temperature	° R
t	Airfoil thickness	in.
t_m	Airfoil maximum thickness	in.
U	Rotor speed	ft/sec
V	Air velocity	ft/sec
W	Weight flow	lbs/sec
Z	Displacement along compressor axis	in.
β	Flow angle, angle whose tangent is the ratio of tangential to axial velocity	Degrees
$\Delta\beta$	Air turning angle, $\Delta\beta = \beta_1 - \beta_2$	Degrees
$\gamma°$	Blade-chord angle (stagger), angle in cascade projection between blade chord and axial direction	Degrees
γ	Ratio of specific heats	---
$\alpha°$	Angle of flow deflection across oblique shock	Degrees

Symbol	Description	Units
$\delta°$	Deviation angle, difference between flow angle and camber line angle at trailing edge in cascade projection	Degrees
δ	Pressure correction, $\frac{P_{actual}}{14.696 \text{ psia}}$	---
$\Delta r\theta$	Circumferential displacement about compressor axis, Figure 1(c)	in.
$\varepsilon°$	Slope of meridional streamline	Degrees
θ	Temperature correction, $\frac{T_{actual}}{518.7 \text{ °R}}$	---
η	Efficiency	---
$\kappa°$	Angle between tangent to blade meanline and the axial direction	Degrees
σ	Solidity, ratio of chord to spacing	---
$\phi°$	Camber angle, difference between angles in cascade projection of tangents to camberline at extremes of camberline arc	Degrees
ϕ	Flow coefficient	
ψ	Work coefficient, $gJc_p \Delta T/U^2_1$	
$\bar{\omega}$	Total pressure loss coefficient Rotor, $\bar{\omega}' = \frac{P'_{2id} - P'_2}{P'_1 - P_1}$, Stator and IGV $\bar{\omega} = \frac{P_1 - P_2}{P_1 - P_1}$	---
$\frac{\bar{\omega} \cos \beta_2}{2\sigma}$	Total Pressure Loss Parameter	---
$\sigma°_{cal}$	Calculated shock wave angle measured from upstream flow direction	Degrees

Subscripts	Description
a	ahead of shock (Table VI)
ad	Adiabatic
an	Annulus
b	behind shock (Table VI)
cor	Corrected to unity axial velocity ratio
CTL —	on a Constant Throttle Line through design stage pressure ratio at design speed, nominal vane schedule with undistorted inlet flow.
e	Edge of blade
F	Flap portion of Inlet Guide Vane
id	Ideal
j	Immersion
m	Meridional direction
N	Nose portion of Inlet Guide Vane
t	Tip at Station 1.0
z	Axial direction
θ	Tangential direction
0	Corrected to zero inlet swirl
1	Leading edge
2	Trailing edge
0.01, 0.18 0.95, 1.0, 1.51, 1.6, 2.20	Measurement station designations (Figures 6, 7)

Superscripts	
'	Relative to rotor
*	Corrected to standard atmospheric or indicated condition.

REFERENCES

1. Seyler, D.R. and Smith, L.H., Jr.: "Single Stage Experimental Evaluation of High Mach Number Compressor Rotor Blading, Part 1 - Design of Rotor Blading," NASA CR-54581, April 1, 1967.

2. Seyler, D.R. and Gostelow, J.P.: "Single Stage Experimental Evaluation of High Mach Number Compressor Rotor Blading, Part 2 - Performance of Rotor 1B," NASA CR-54582, September 22, 1967.

3. Gostelow, J.P., Krabacher, K.W., and Smith, L.H., Jr.: "Performance Comparisons of High Mach Number Compressor Rotor Blading," NASA CR-1256, December, 1968.

4. Koch, C.C., Bilwakesh, K.R., and Doyle, V.L.: "Evaluation of Range and Distortion Tolerance for High Mach Number Transonic Fan Stages, Task I Stage Final Report," Volume I, NASA CR-72806, August, 1971.

5. Koch, C.C., Bilwakesh, K.R., and Doyle, V.L.: "Evaluation of Range and Distortion Tolerance for High Mach Number Transonic Fan Stages, Task I Stage Final Report," Volume II, NASA CR-72064, August, 1971.

6. Doyle, V.L. and Koch, C.C.: "Evaluation of Range and Distortion Tolerance for High Mach Number Transonic Fan Stages, Design Report," NASA CR-72720, July 23, 1970.

7. Bilwakesh, K.R.: "Evaluation of Range and Distortion Tolerance for High Mach Number Transonic Fan Stages, Task II Stage Data and Performance Report for Undistorted Inlet Flow Testing," NASA CR-72787, January, 1971.

8. Tesch, W.A. and Doyle, V.L.: "Evaluation of Range and Distortion Tolerance for High Mach Number Transonic Fan Stages, Task II Stage Data and Performance Report for Inlet Flow Distortion Testing," NASA CR-72786, January 1971.

9. Tesch, W.A.: "Evaluation of Range and Distortion Tolerance for High Mach Number Transonic Fan Stages, Task IV Stage Data and Performance Report for Casing Treatment Investigations," Volume I, NASA CR-72872, March, 1971.

10. Dunavant, C.J.: "Cascade Investigation of a Related Series of 6-Percent-Thick Guide-Vane Profiles and Design Charts," US NACA TN 3959, May, 1957.

11. NASA: "Aerodynamic Design of Axial Flow Compressors," NASA SP-36, Revised 1965.

Table I. Summary of NASA Task II Stage Design Specifications.

Rotor inlet corrected tip speed, ft/sec	1500
Stage inlet corrected weight flow, lbs/sec	226.0
Stage total-pressure ratio	1.659
Stage adiabatic efficiency	0.854
Number of inlet guide vanes	24
Inlet guide vane total-pressure loss, percent inlet total pressure	0.37
Inlet guide vane exit flow angle, degrees	0
Rotor inlet tip diameter, inches	36.5
Rotor inlet hub/tip radius ratio	0.5
Rotor inlet corrected weight flow per unit annulus area, lbs/sec-sq ft	41.62
Rotor inlet tip relative Mach number	1.526
Rotor tip diffusion factor	0.368
Rotor total-pressure ratio	1.686
Rotor adiabatic efficiency	0.883
Rotor tip solidity	1.4
Rotor aspect ratio	2.36
Number of rotor blades	44
Stator inlet hub absolute Mach number	0.766
Stator exit flow angle, degrees	0
Stator hub diffusion factor	0.435
Stator total-pressure loss, percent stator inlet total pressure	1.22
Stator hub solidity	2.155
Stator aspect ratio	2.065
Number of stator vanes	46

Table II. Inlet Guide Vane Design Parameters.

Number of Vanes = 24

Design Parameters	Manufacturing Section									Units
	1	2	3	4	5	6	7	8	9	
r	18.389	17.885	17.435	15.485	13.465	11.375	8.940	8.100	7.390	Inches
r/r_t	1.0076	0.9800	0.9553	0.8485	0.7378	0.6233	0.4899	0.4438	0.4049	---
C_N	1.280	1.254	1.230	1.129	1.024	0.915	0.788	0.745	0.708	Inches
C_F	4.975	4.873	4.782	4.388	3.979	3.557	3.064	2.894	2.751	Inches
$C_N + C_F$	6.255	6.127	6.012	5.517	5.003	4.472	3.852	3.639	3.459	Inches
σ	1.299	1.309	1.317	1.361	1.419	1.502	1.646	1.716	1.788	---
Z_N	2.706	2.658	2.613	2.425	2.228	2.028	1.793	1.711	1.642	Inches
Z_F	1.279	1.253	1.230	1.128	1.023	0.914	0.788	0.744	0.707	Inches
$\Delta r\theta°/\sin\phi°$	1.1800	1.1477	1.1188	0.9936	0.8640	0.7299	0.5737	0.5198	0.4742	Inches
$\Delta r\theta°/X$ *	0.922	0.916	0.909	0.881	0.844	0.798	0.728	0.699	0.671	---

*Ref: Figure 1(c)

Table III. Aerodynamic and Geometric Design Parameters on Design Streamlines.

(a) Rotor

Number of Blades = 44

Design Parameter	Tip Streamline SL 1	SL 2	SL 3	SL 4	SL 5	SL 6	SL 7	SL 8	Hub SL 9	Units
$\bar{r}$	18.03	17.60	17.22	15.57	13.93	12.28	10.54	10.06	9.63	Inches
r_1	18.173	17.706	17.308	15.581	13.860	12.097	10.171	9.620	9.128	Inches
r_2	17.891	17.493	17.139	15.567	14.008	12.466	10.904	10.493	10.141	Inches
V_1'	1652	1610	1591	1452	1345	1208	1042	996	945	Ft/sec
V_2'	1200	1164	1132	998	868	746	643	622	610	Ft/sec
M_1'	1.526	1.510	1.490	1.374	1.258	1.130	0.983	0.941	0.907	---
M_2'	1.023	0.992	0.966	0.856	0.747	0.648	0.571	0.557	0.551	---
$\bar{\omega}$	0.1634	0.1486	0.1355	0.1004	0.0803	0.0668	0.0707	0.0766	0.0821	---
C	3.601	3.599	3.596	3.587	3.527	3.446	3.388	3.374	3.361	Inches
σ	1.400	1.431	1.462	1.610	1.777	1.967	2.251	2.331	2.443	---
tm/C	0.0227	0.0259	0.0287	0.0437	0.0562	0.0660	0.0747	0.0768	0.0785	---
D	0.368	0.371	0.381	0.409	0.456	0.495	0.514	0.515	0.501	---
β_1'	66.3	64.4	63.5	60.9	58.2	55.7	53.4	52.7	51.7	Degrees
β_2'	59.3	59.5	59.3	56.1	50.6	42.0	27.9	22.9	18.4	Degrees
$\Delta\beta'$	7.0	4.9	4.2	4.8	7.6	13.7	25.5	29.8	33.3	Degrees
$\kappa°_1$	63.30	61.28	60.22	57.01	53.75	50.70	48.50	48.00	47.50	Degrees
$\kappa°_2$	57.27	57.52	57.18	52.85	46.10	35.05	16.84	10.35	4.56	Degrees
i	3.00	3.12	3.28	3.89	4.45	5.00	4.90	4.70	4.20	Degrees
$\delta°$	2.03	1.98	2.12	3.25	4.50	6.95	11.06	12.55	13.84	Degrees
$\gamma°$	61.94	60.79	59.85	55.32	49.56	41.59	31.46	28.65	25.95	Degrees
$\phi°$	6.03	3.76	3.04	4.16	7.65	15.65	31.66	37.65	42.94	Degrees

Table III. Aerodynamic and Geometric Design Parameters on Design Streamlines (Concluded).

(b) Stator

Number of Blades = 46

Design Parameter	Tip Streamline SL 1	SL 2	SL 3	SL 4	SL 5	SL 6	SL 7	SL 8	Hub SL 9	Units
$\bar{r}$	17.836	17.443	17.103	15.642	14.228	12.855	11.489	11.134	10.831	Inches
$r_{1.6}$	17.836	17.432	17.083	15.586	14.132	12.706	11.263	10.882	10.553	Inches
$r_{2.0}$	17.836	17.454	17.123	15.697	14.325	13.005	11.715	11.386	11.109	Inches
$V_{1.6}$	725	729	732	744	764	796	844	860	874	Ft/Sec
$V_{2.0}$	597	596	595	595	598	605	621	627	634	Ft/Sec
$M_{1.6}$	0.615	0.620	0.624	0.639	0.659	0.690	0.737	0.753	0.766	---
$M_{2.0}$	0.500	0.500	0.501	0.503	0.507	0.515	0.529	0.535	0.541	---
$\bar{\omega}$	0.0404	0.0393	0.0383	0.0396	0.0451	0.0520	0.0650	0.0707	0.0754	---
C	3.650	3.633	3.606	3.493	3.396	3.299	3.222	3.199	3.184	Inches
σ	1.4983	1.5197	1.5438	1.6288	1.7386	1.8794	2.0536	2.1045	2.1557	---
tm/C	0.0650	0.0640	0.0629	0.0588	0.0548	0.0507	0.0468	0.0458	0.0450	---
D	0.3784	0.3790	0.3787	0.3847	0.3954	0.4100	0.4273	0.4317	0.4346	---
β_1	37.12	36.73	36.48	37.00	38.57	40.52	43.43	44.45	45.43	Degrees
β_2	0	0	0	0	0	0	0	0	0	Degrees
κ°_1	40.09	39.48	39.06	39.10	40.15	41.24	42.85	43.55	44.00	Degrees
κ°_2	-13.11	-.10.99	-10.21	-8.94	-8.80	-9.17	-10.41	-11.31	-12.54	Degrees
i	-2.97	-2.75	-2.58	-2.10	-1.58	-0.72	0.58	0.90	1.43	Degrees
δ°	13.11	10.99	10.21	8.44	8.80	9.17	10.41	11.31	12.54	Degrees
γ°	13.46	14.21	14.24	14.58	15.76	16.99	18.89	19.43	19.62	Degrees
ϕ°	53.20	50.57	49.27	48.04	48.95	50.41	53.26	54.86	56.54	Degrees

Table IV. Geometric Parameters on Rotor and Stator Blade Element Sections.

Blade Row	Percent Immersion	r_j		κ°_j		$\bar{r}$	Φ°	σ_j	t_m/C	C	γ°
		Edge 1	Edge 2	Edge 1	Edge 2						
ROTOR	5	17.706	17.525	61.28	57.52	17.616	3.76	1.431	0.0256	3.6	60.9
	10	17.350	17.138	60.25	57.18	17.244	3.07	1.461	0.0285	3.596	60.0
	30	15.610	15.567	57.07	52.85	15.589	4.22	1.612	0.044	3.587	55.40
	50	13.900	14.008	53.90	46.10	13.954	7.80	1.733	0.0562	3.530	49.6
	70	12.150	12.425	50.80	34.70	12.288	16.10	1.964	0.066	3.446	41.59
	90	10.212	10.904	48.58	16.84	10.558	31.74	2.248	0.0747	3.388	31.50
	95	9.625	10.500	48.02	10.70	10.063	37.32	2.347	0.0768	3.374	28.65
STATOR	5	17.450	17.463	39.47	-11.13	17.457	50.60	1.523	0.064	3.633	14.21
	10	17.075	17.125	39.11	-10.10	17.100	49.21	1.544	0.0629	3.606	14.24
	30	15.610	15.700	39.01	-8.87	15.655	47.88	1.631	0.0590	3.492	14.57
	50	14.175	14.363	39.80	-8.75	14.269	48.55	1.742	0.0550	3.392	15.72
	70	12.725	12.980	40.86	-9.10	12.853	49.96	1.880	0.0507	3.299	18.87
	90	11.300	11.720	42.22	-10.58	11.510	52.80	2.051	0.0470	3.225	18.87
	95	10.950	11.388	42.76	-12.36	11.169	55.12	2.098	0.0460	3.202	19.41

Table V. Major Instrumentation List for Task II S age Testing.

(a). Undistorted Inlet Flow Tests

Location	Shakedown Stall Test	Shakedown Performance Test	Undistorted Inlet Flow Tests
0.01 Vehicle Inlet	6 7-element P, p rakes 24 T t/c's	→	→
0.95 Rotor Inlet		7 14-element P wake rakes	
		1 p, β wedge probe with C.T.*	# →
		1 P, T, p, β combination probe with C.T. *	
1.51 Stator Inlet		1 P, T, β Cobra Probe	# →
	3 hot wire probes	1 p wedge probe # →	# →
2.20 Stage Exit	7 14-element P, T wake rakes	→	→
		1 p, β wedge probe	# →

* C.T. = Circumferential Traverse capability

Radial Traverse probes

Table V. Major Instrumentation List for Task II Stage Testing (Concluded).

(b). Distortion Tests

Location	Instrumentation
0.01 Vehicle Inlet	6 7-element pitot-static rakes 24 total-temperature thermocouples
0.18 Stage Inlet	2 7-element total pressure distortion rakes 1 4-parameter combination probe (total temperature and pressure, static pressure, flow angle)
0.95 Rotor Inlet	1 4-parameter combination probe with circumferential traverse capability
1.51 Stator Inlet	1 4-parameter combination probe 3 hot-wire probes
2.20 Stage Exit	7 14-element wake rakes (total temperature and pressure) 1 4-parameter combination probe

Table VI. Rotor Tip Leading Edge Shock Studies.

Reading	137	139	141			132		134		144	169
Figure	19(a)	19(b)	19(c)			19(d)		19(e)		19(f)	19(g)
Type	A	A	B	C	-	B	C	B	C	A	A
Pressure Surface P_a	11.0	10.8	11.2	11.2	---	11.0	11.0	10.0	10.0	10.6	11.6
Pressure Surface P_b	18.0	20.0	28.3	23.0	---	23.8	19.2	23.9	28.6	18.4	23.8
Pressure Surface P_b/P_a	1.636	1.85	2.53	2.05	---	2.16	1.75	2.39	2.86	1.74	2.05
Pressure Surface P'_a	42.77	42.98	42.43	34.65	---	35.65	29.7	35.73	48.2	51.42	51.44
Pressure Surface M'_a	1.54	1.55	1.52	1.38	---	1.41	1.28	1.48	1.61	1.69	1.63
Pressure Surface $\sigma°_{cal}$	53.5	58.0	---	---	---	---	---	---	---	49.0	49.0
Pressure Surface M'_b	1.18	1.08	0.69	0.75	---	0.735	0.8	0.71	0.67	1.295	1.07
Pressure Surface P'_b	42.5	41.6	39.1	33.4	---	34.0	29.2	33.5	38.5	50.52	49.48
Pressure Surface $\alpha°$	9.5	12.0	---	---	---	---	---	---	---	12.0	14.0
Pressure Surface $\sigma°_{fig}$	58.0	59.4	---	---	---	---	---	---	---	---	---
Type	A	A	B	C	A	B	C	B	C	A	A
Mid-Passage P_a	11.0	11.6	10.6	10.6	10.6		11.0		10.0	11.0	10.0
Mid-Passage P_b	17.0	18.0	28.3	20.0	20.0		20.0		19.0	16.4	18.0
Mid-Passage P_b/P_a	1.545	1.55	2.67	1.89	1.89		1.82		1.9	1.49	1.8
Mid-Passage P'_a	42.77	42.98	42.43	30.6	42.43		30.7		28.8	51.42	51.44
Mid-Passage M'_a	1.54	1.50	1.56	1.33	1.56		1.30		1.33	1.66	1.73
Mid-Passage $\sigma°_{cal}$	51.7	53.5	---	---	58.5		---		---	45.6	48.8
Mid-Passage M'_b	1.225	1.175	0.68	0.77	1.06		0.78		0.77	1.385	1.31
Mid-Passage P'_b	42.6	42.7	38.6	29.8	40.6		30.0		28.1	51.11	50.41
Mid-Passage $\alpha°$	8.6	8.5	---	---	12.3		---		---	8.0	11.75
Type	A	A	A	C	D		C	B	C	A	A
Suction Surface P_a	9	8.6	8.0	8.0	8.0		11.0	11.8	11.8	9.0	7.2
Suction Surface P_b	13	15.0	21.0	21.0	21.0		22.2	23.7	19.0	14.0	18.5
Suction Surface P_b/P_a	1.44	1.75	2.63	2.63	2.63		2.02	2.01	1.61	1.555	2.57
Suction Surface P'_a	42.77	42.98	42.43	31.6	42.43		33.6	35.73	29.8	51.42	51.44
Suction Surface M'_a	1.675	1.71	1.75	1.55	1.75		1.37	1.37	1.23	1.8	1.94
Suction Surface $\sigma°_{cal}$	44	48.5	61.7	---	---		---	---	---	42.6	45.2
Suction Surface M'_b	1.42	1.31	1.0	0.684	1.04		0.75	0.76	0.82	1.485	1.265
Suction Surface P'_b	42.6	42.1	39.8	28.8	41.6		32.4	34.5	29.45	50.96	49.51
Suction Surface $\alpha°$	7.35	11.0	17.8	---	0		---	---	---	8.7	13.9

Same as on pressure surface. (Mid-Passage)

Same as on pressure surface. (Suction Surface)

Type A: Oblique shock on meridional stream surface. Relative total pressure upstream from blade element data. Static pressure downstream from isobar plot.

Type B: Normal shock on meridional stream surface. Relative total pressure upstream from blade element data. Static pressure downstream from shock calculated.

Type C: Normal shock on meridional stream surface. Static pressure downstream from isobar plot. Relative total pressure upstream calculated.

Type D: Incident and reflected oblique shocks on meridional stream surface. Relative total pressure upstream from blade element data. Static pressure downstream of reflected shock from isobar plot. Equal shock deflections.

Table VII. Stage Distortion Transfer Parameters in Flow with Circumferential Inlet Distortion.

% Speed	Vane Schedule	$W\sqrt{\theta}/\delta$ lbs/sec	Condition	Percent Immersion From Tip	(DP)* at Plane 0.18	Distortion Transfer $(DP)/(DP)_{0.18}$		IDC** at Plane 0.18	Distortion Transfer $(IDC)/(IDC)_{0.18}$	
						After Rotor	After Stator		After Rotor	After Stator
100	0°/0°	221.5	Max. Flow	10	0.171	0.692	0.598	0.121	0.489	0.562
				50	0.177	0.724	0.55	0.129	0.726	0.358
				90	0.181	1.209	0.819	0.185	1.385	0.765
100		221.8	Near Stall	10	0.153	1.035	0.61	0.104	0.733	0.240
				50	0.16	0.599	0.516	0.116	0.422	0.375
				90	0.159	0.339	0.951	0.117	0.208	0.909
70		153.8	Intermed-iate Flow	10	0.067	0.695	0.396	0.048	0.547	0.374
				50	0.072	0.429	0.518	0.051	0.393	0.484
				90	0.074	0.984	0.817	0.054	0.752	0.967
100	40°/8°	164.9	Intermed-iate Flow	10	0.078	1.270	0.827	0.054	0.657	0.479
				50	0.078	0.854	0.369	0.057	0.462	0.249
				90	0.075	0.675	1.209	0.055	0.711	1.115
70		128.2	Max. Flow	10	0.045	0.327	0.463	0.032	0.131	0.336
				50	0.044	0.633	0.34	0.029	0.692	0.426
				90	0.042	0.788	0.615	0.031	0.62	0.646
70		109.5	Near Stall	10	0.031	0.605	0.54	0.021	0.276	0.355
				50	0.032	0.489	0.57	0.023	0.270	0.429
				90	0.030	0.376	1.201	0.022	0.297	1.119

*DP - Distortion Parameter $= \dfrac{(P_{Max.} - P_{Min.})}{(P_{Max.})}$

**IDC = Index of Distortion, Circumferential $= \left(\dfrac{P_{Avg,\ Immersion} - P_{Min.,\ Immersion}}{P_{Avg,\ Face}} \right)$

Table VIII. Stage Response to Circumferentially Distorted Inlet Flow - Qualitative Description.

Element	Immersion From Tip	Response	0°/0° IGV/Stator Schedule			40°/8° IGV/Stator Schedule		
			100% N Maximum Flow	100% N Near Stall	70% N Intermediate Flow	100% N Intermediate Flow	70% N Maximum Flow	70% N Near Stall
Rotor Total Pressure Depression	10%	Remains	Yes	---	---	---	---	---
		Filled In	---	---	Yes	---	Yes	---
		Inverted	---	Yes	---	Yes	---	Yes
	50%	Remains	---	---	---	---	---	---
		Filled In	Partially	---	Yes	---	Partially	---
		Inverted	---	Yes	---	Yes	---	Yes
	90%	Remains	Yes	---	Yes	Yes	---	---
		Filled In	---	Yes	---	---	Partially	Yes
		Inverted	---	---	---	---	---	---
Stator Loss in Undistorted Sector	10%	Choke	---	---	---	---	---	---
		Low Loss	Yes	Yes	Yes	Yes	Yes	---
		Stall	---	---	---	---	---	Yes
	50%	Choke	Yes	---	---	---	---	---
		Low Loss	---	Yes	Yes	Yes	Yes	Yes
		Stall	---	---	---	---	---	---
	90%	Choke	Yes	---	---	---	Yes	---
		Low Loss	---	Yes	Yes	---	---	---
		Stall	---	---	---	Yes	---	Yes
Stator Loss in Screen Shadow	10%	Choke	Yes	---	---	---	---	---
		Low Loss	---	---	Yes	---	Yes	---
		Stall	---	Yes	---	Yes	---	Yes
	50%	Choke	---	---	---	---	---	---
		Low Loss	Yes	---	Yes	Yes	Yes	Yes
		Stall	---	Yes	---	---	---	---
	90%	Choke	---	---	---	---	?	---
		Low Loss	Yes	---	Yes	---	---	---
		Stall	---	Yes	---	Yes	?	Yes

Table IX. Stage Response to Circumferentially Distorted Inlet Flow - Local Pressure Ratio.

Pressure Ratio to Plane	Sector	Immersion	0°/0° IGV/Stator Schedule			40°/8° IGV/Stator Schedule		
			100% N Maximum Flow	100% N Near Stall	70% N Intermediate Flow	70% N Intermediate Flow	100% N Maximum Flow	100% N Near Stall
$P_{1.51}/P_{0.19}$	Undistorted	10	1.38	1.62	1.26	1.37	1.12	1.26
		50	1.45	1.63	1.26	1.29	1.1[illegible]	1.21
		90	1.61	1.62	1.31	1.37	1.16	1.21
	Entering Screen Shadow	10	1.38	1.70	1.28	1.38	1.17	1.28
		50	1.45	1.75	1.28	1.30	1.13	1.21
		90	1.59	1.77	1.33	1.37	1.17	1.21
	Leaving Screen Shadow	10	1.72	2.09	1.37	1.60	1.15	1.32
		50	1.76	2.02	1.35	1.45	1.14	1.25
		90	1.81	1.97	1.36	1.48	1.19	1.24
$P_{2.20}/P_{0.18}$	Undistorted	10	1.34	1.59	1.25	1.35	1.12	1.23
		50	1.37	1.61	1.25	1.27	1.10	1.19
		90	1.43	1.60	1.28	1.25	1.12	1.16
	Entering Screen Shadow	10	1.24	1.67	1.28	1.36	1.16	1.24
		50	1.31	1.73	1.27	1.28	1.12	1.18
		90	1.31	1.68	1.32	1.19	1.14	1.15
	Leaving Screen Shadow	10	1.31	1.98	1.33	1.51	1.16	1.26
		50	1.34	1.94	1.35	1.39	1.14	1.23
		90	1.38	1.63	1.36	1.23	1.16	1.21

Table X. Operational Pressure Ratio Limits in Undistorted Flow.

Pressure Ratio to Plane	Immersions	0°/0° IGV/Stator Schedule				40°/8° IGV/Stator Schedule			
		100% N		70% N		100% N		70% N	
		Maximum Flow	Near Stall	Maximum Flow	Near Stall	Maximum Flow	Near Stall	Maximum Flow	Near Stall
$\frac{P_{1.51}}{P_{0.18}}$	10	1.485	1.847	1.163	1.338	1.219	1.517	1.116	1.298
	50	1.519	1.780	1.202	1.313	1.187	1.370	1.108	1.218
	90	1.605	1.713	1.265	1.331	1.252	1.355	1.148	1.201
Overall Average		1.519	1.804	1.204	1.330	1.226	1.373	1.119	1.244
$\frac{P_{2.20}}{P_{0.18}}$	10	1.465	1.812	1.155	1.323	1.202	1.469	1.110	1.260
	50	1.490	1.751	1.180	1.303	1.178	1.342	1.102	1.205
	90	1.561	1.637	1.240	1.322	1.171	1.307	1.120	1.177
Overall Average		1.488	1.770	1.180	1.317	1.195	1.341	1.107	1.222

Table XI. Summary of Key Stage Performance Parameters in Clean Inlet and Distorted Inlet Flows.

Percent Speed			70			90			100		
IGV/Stator Schedule			0/0	40/8	No IGV	0/0	40/8	No IGV	0/0	40/8	No IGV
	η_{peak}	U.I.	0.850	0.839	0.861	0.841	0.822	0.851	0.840	0.805	0.845
		R.D.	0.830	0.785	0.821	0.800	0.790	0.796	0.787	0.782	0.774
		C.D.	0.837	0.835	0.814	0.815	0.834	0.831	0.801	0.819	0.824
On CTL	η	U.I.	0.850	0.838	0.86	0.845	0.821	0.85	0.830	0.798	0.835
		R.D.	0.825	(0.785)*	0.82	0.800	0.787	0.795	0.772	0.760	0.77
		C.D.	0.835	0.835	0.811	0.813	0.820	0.830	0.800	0.800	0.822
	$W\sqrt{\theta}/\delta$, lb/sec	U.I.	155.0	123.0	157.0	201.6	153.2	201.7	223.8	165.4	223.8
		R.D.	155.0	122.0	156.8	195.3	152.0	196.5	214.8	163.0	214.7
		C.D.	153.5	122.2	154.5	196.0	151.8	197.3	215.8	165.0	215.9
	P/P	U.I.	1.279	1.159	1.284	1.535	1.268	1.535	1.659	1.321	1.658
		R.D.	1.278	1.156	1.282	1.493	1.263	1.502	1.613	1.311	1.61
		C.D.	1.271	1.156	1.274	1.498	1.261	1.489	1.618	1.320	1.618
At Stall	$W\sqrt{\theta}/\delta$, lb/sec	U.I.	127.5	107.7	127.0	184.2	136.4	182.5	210.8	159.0	205.5
		R.D.	148.2	107.7	151.0	193.5	139.0	198.0	212.0	157.2	213.5
		C.D.	128.3	105.5	133.0	187.0	136.0	183.5	205.5	157.2	204.5
	P/P	U.I.	1.318	1.221	1.32	1.594	1.390	1.605	1.779	1.425	1.8
		R.D.	1.295	1.205	1.291	1.505	1.335	1.498	1.646	1.371	1.628
		C.D.	1.312	1.210	1.311	1.530	1.350	1.547	1.660	1.389	1.656
Stall Margin	S.M.** at CTL	U.I.	0.253	0.203	0.271	0.137	0.231	0.156	0.135	0.122	0.182
		R.D.	0.059	0.181	0.046	0.017	0.156	-0.01	0.034	0.084	0.017
		C.D.	0.235	0.212	0.195	0.071	0.195	0.117	0.077	0.105	0.081

** S.M. = $\left[\left(\frac{P/P}{W\sqrt{\theta}/\delta}\right)_{stall} \Big/ \left(\frac{P/P}{W\sqrt{\theta}/\delta}\right)_{CTL}\right]$

U.I. = Undistorted Inlet
R.D. = Radial Distortion
C.D. = Circumferential Distortion

*See Page 25 for a discussion of this efficiency.

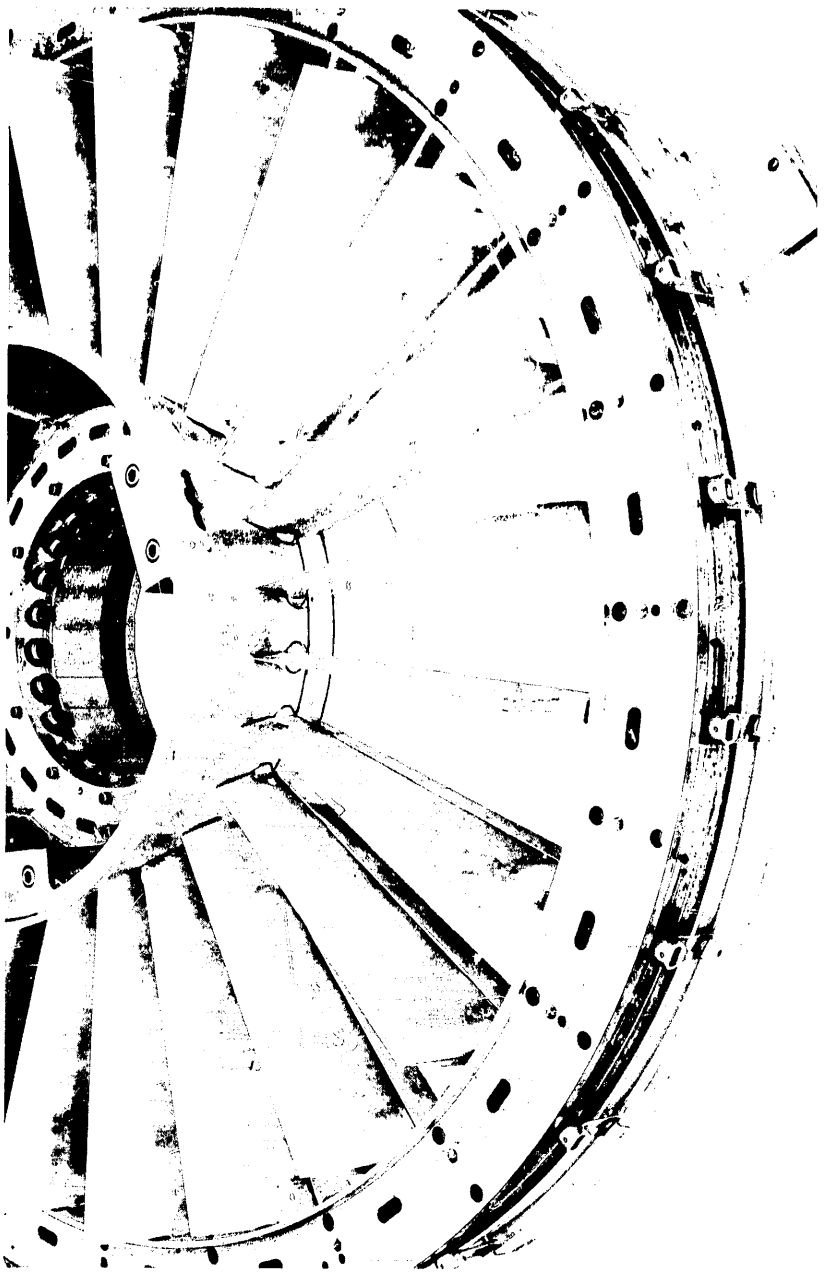

(a) Photograph at 0° (Nominal) Setting Angle

Figure 1. Views of Variable Camber Inlet Guide Vanes.

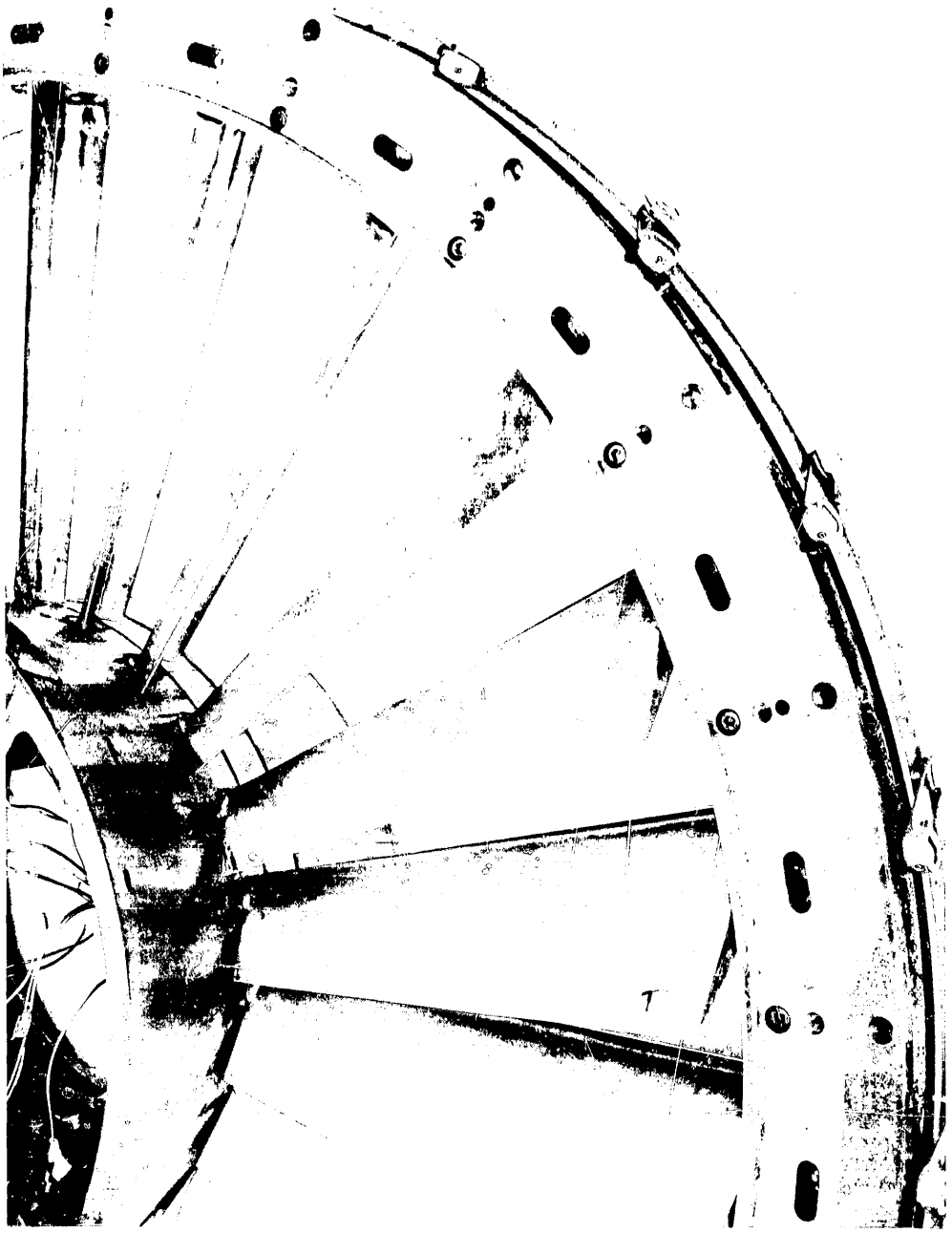

(b) Photograph at 40° Setting Angle

Figure 1. Views of Variable Camber Inlet Guide Vanes (Continued).

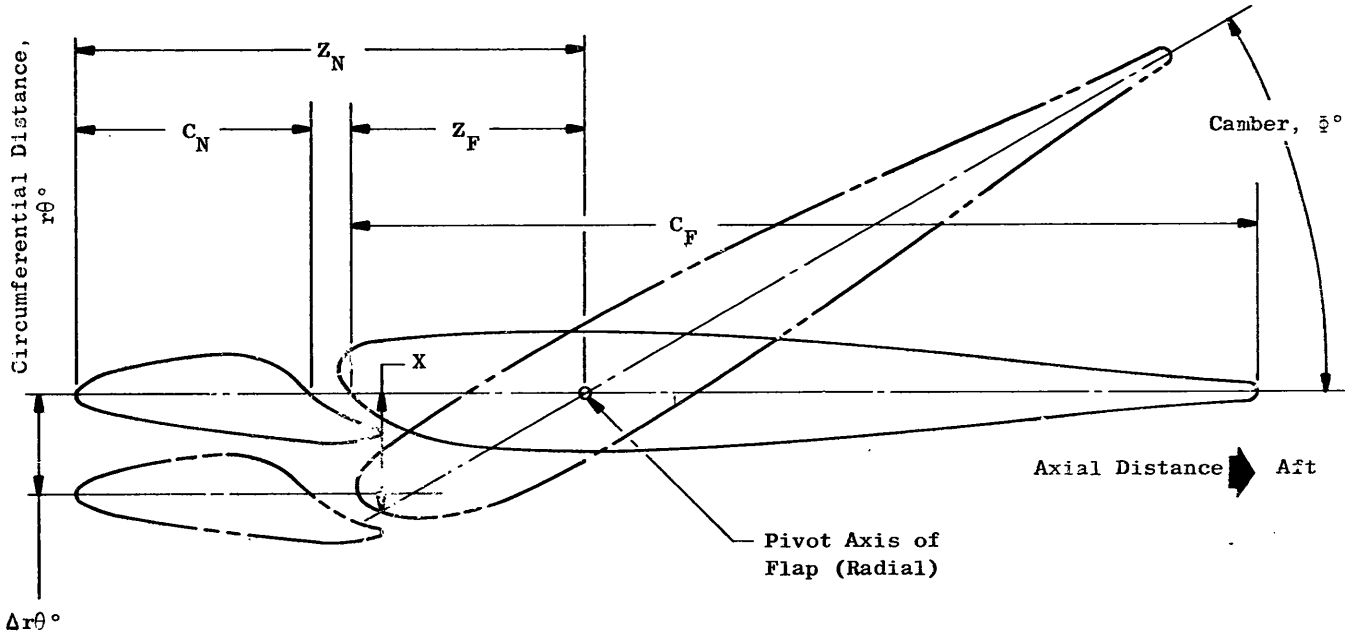

(c) Pitchline Section at 0° and 30° Turning

Figure 1. Views of Variable Camber Inlet Guide Vanes (Concluded).

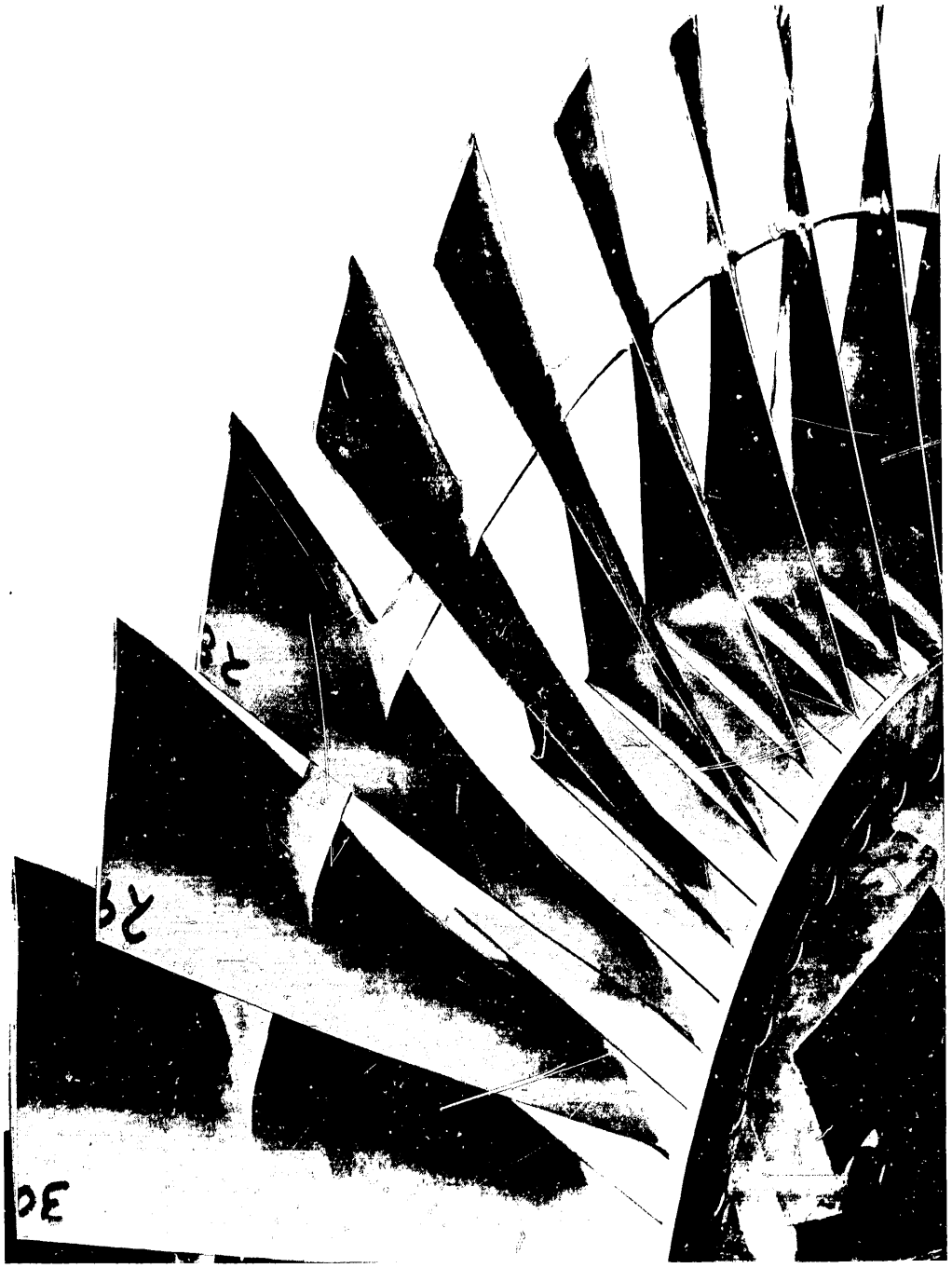

Figure 2. Photograph of Rotor.

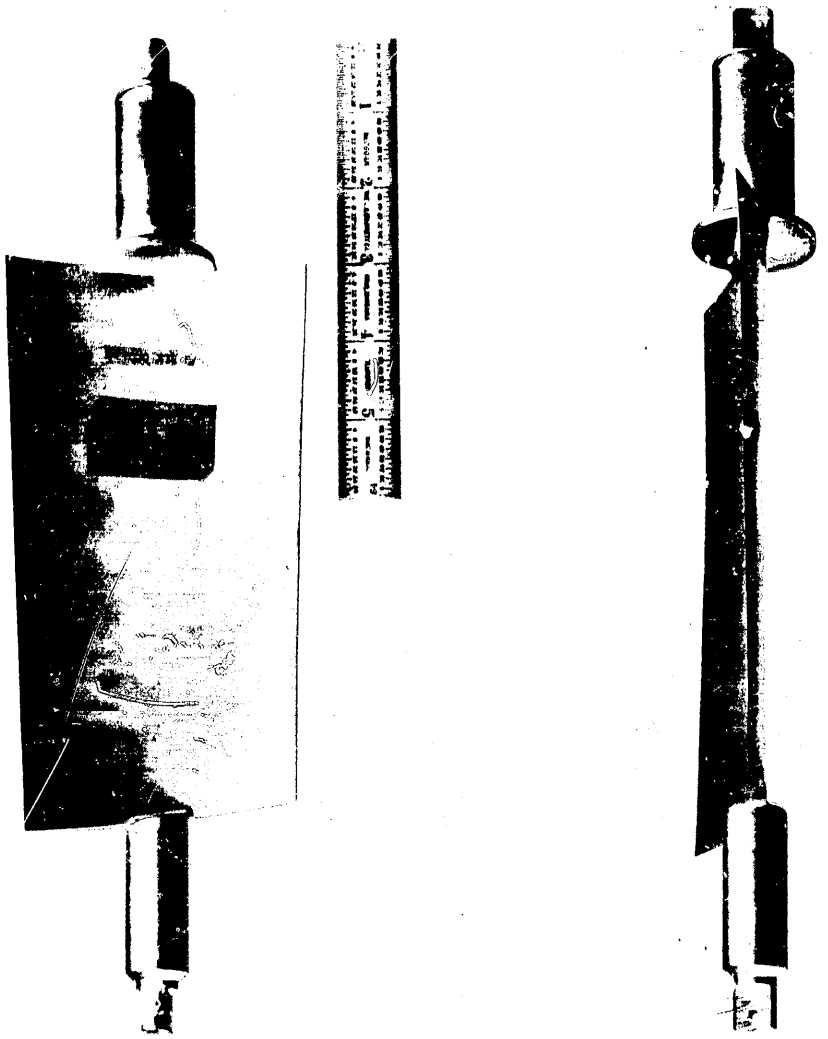

Figure 3. Photographs of a Variable-Stagger Stator Vane.

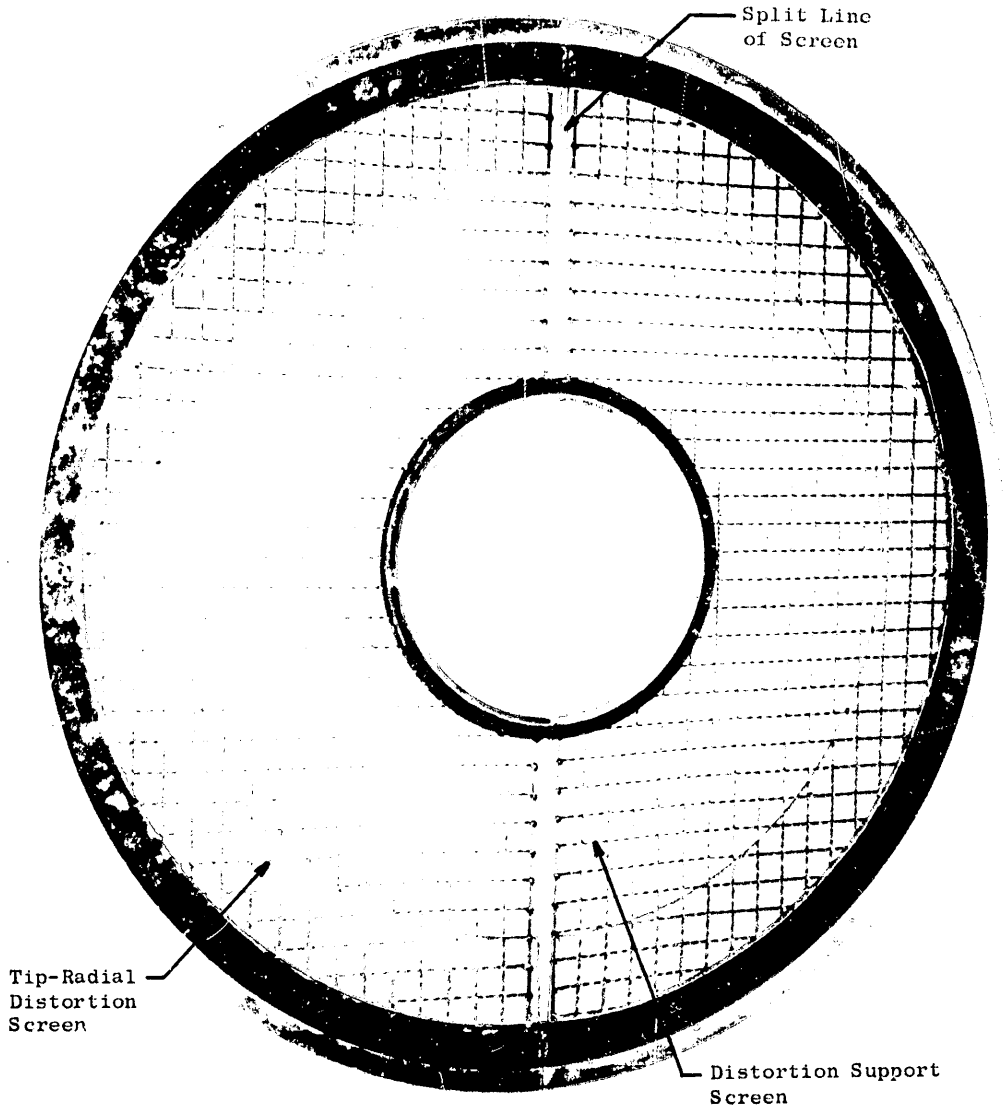

Figure 4. Tip-Radial Distortion Screen.

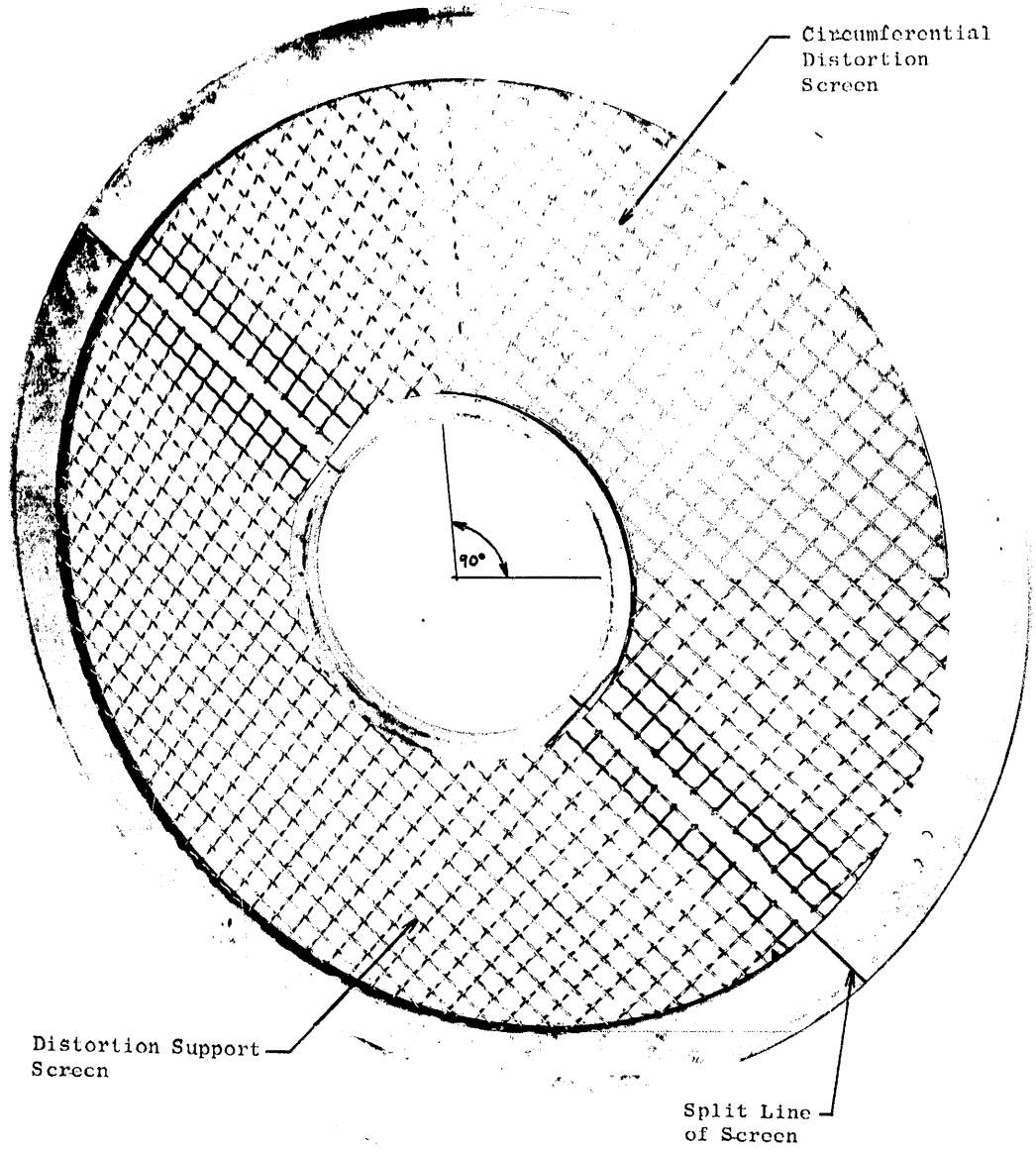

Figure 5. Circumferential Distortion Screen.

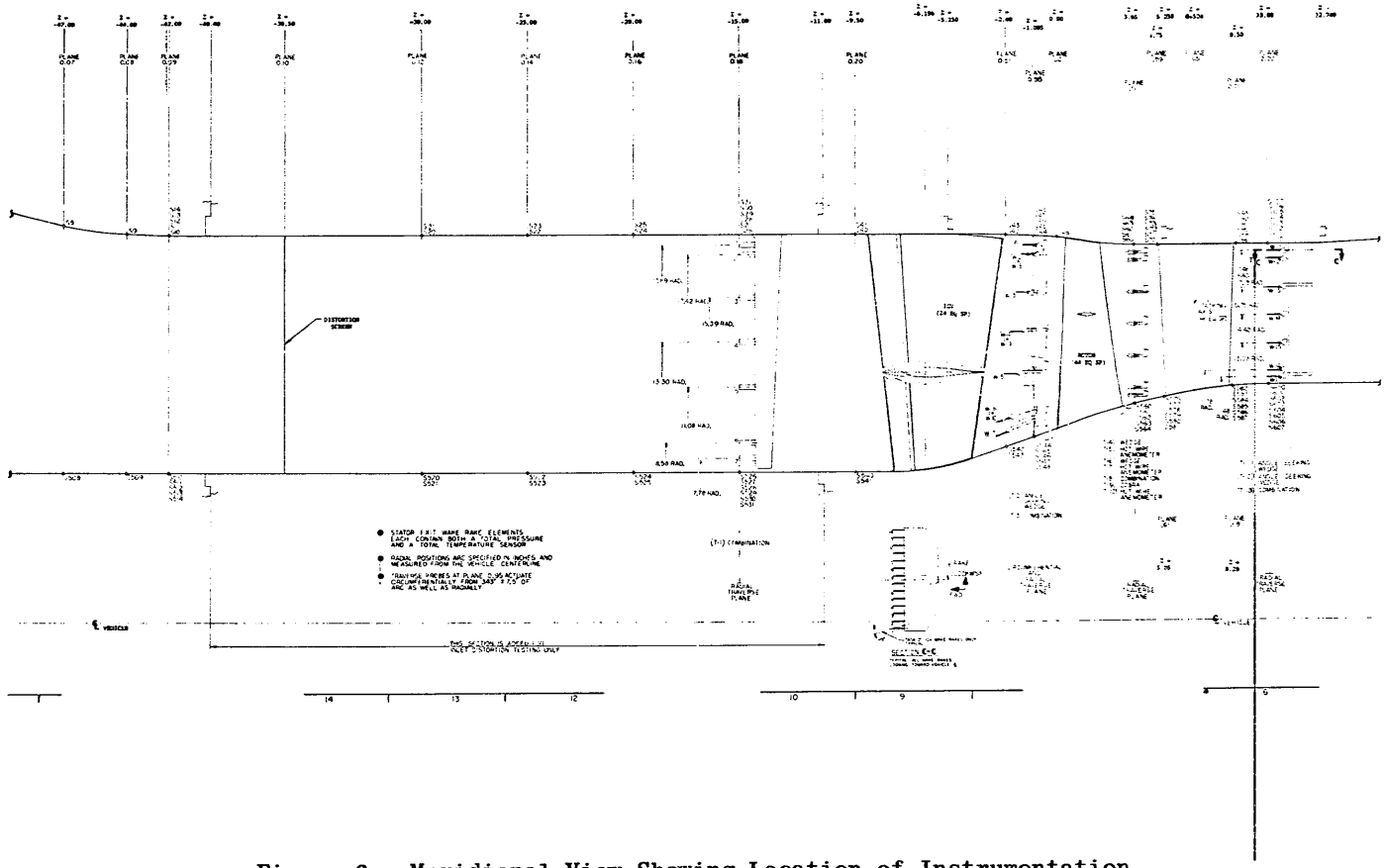

Figure 6. Meridional View Showing Location of Instrumentation.

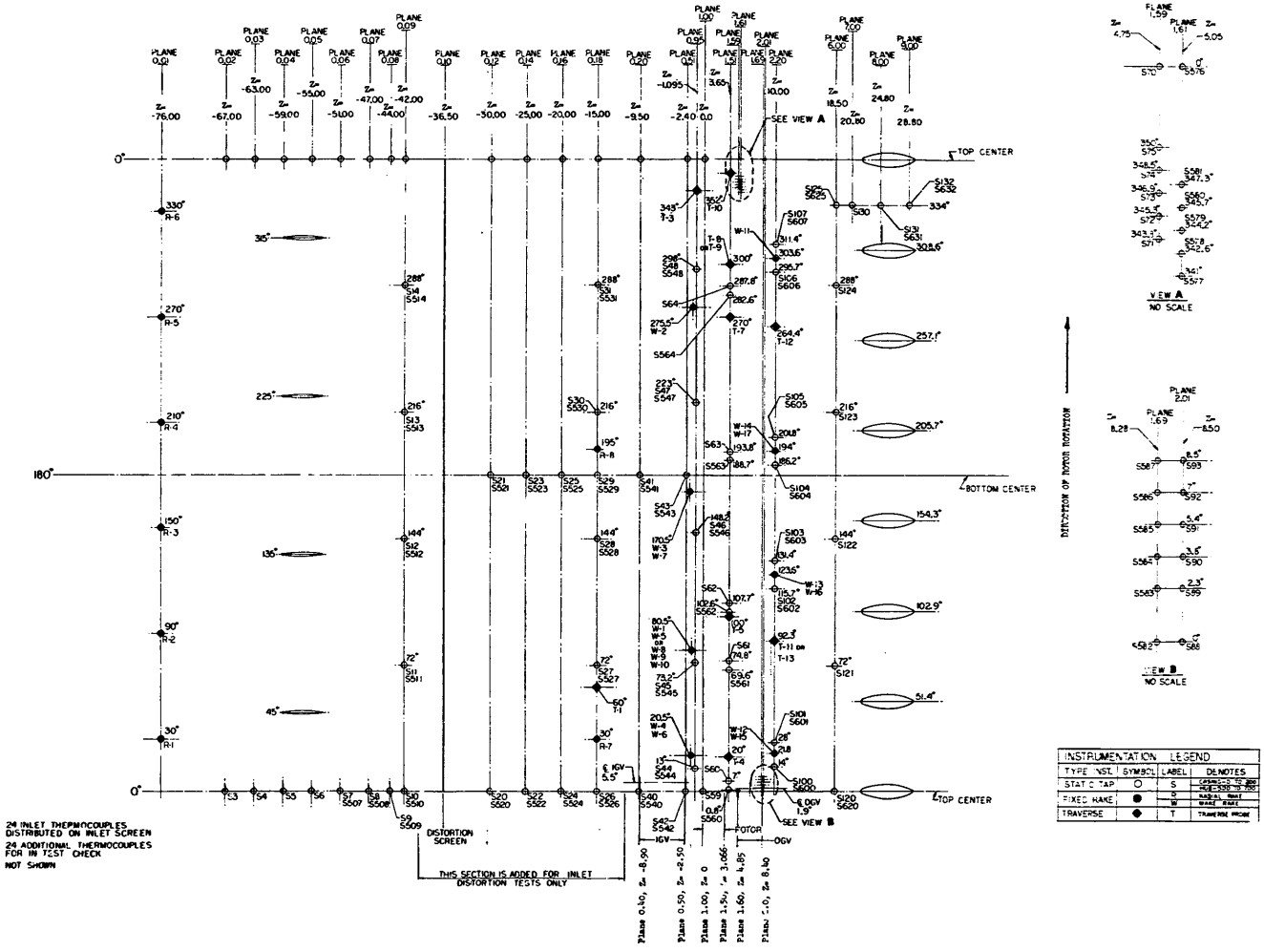

Figure 7. Development Showing Circumferential Location of Instrumentation.

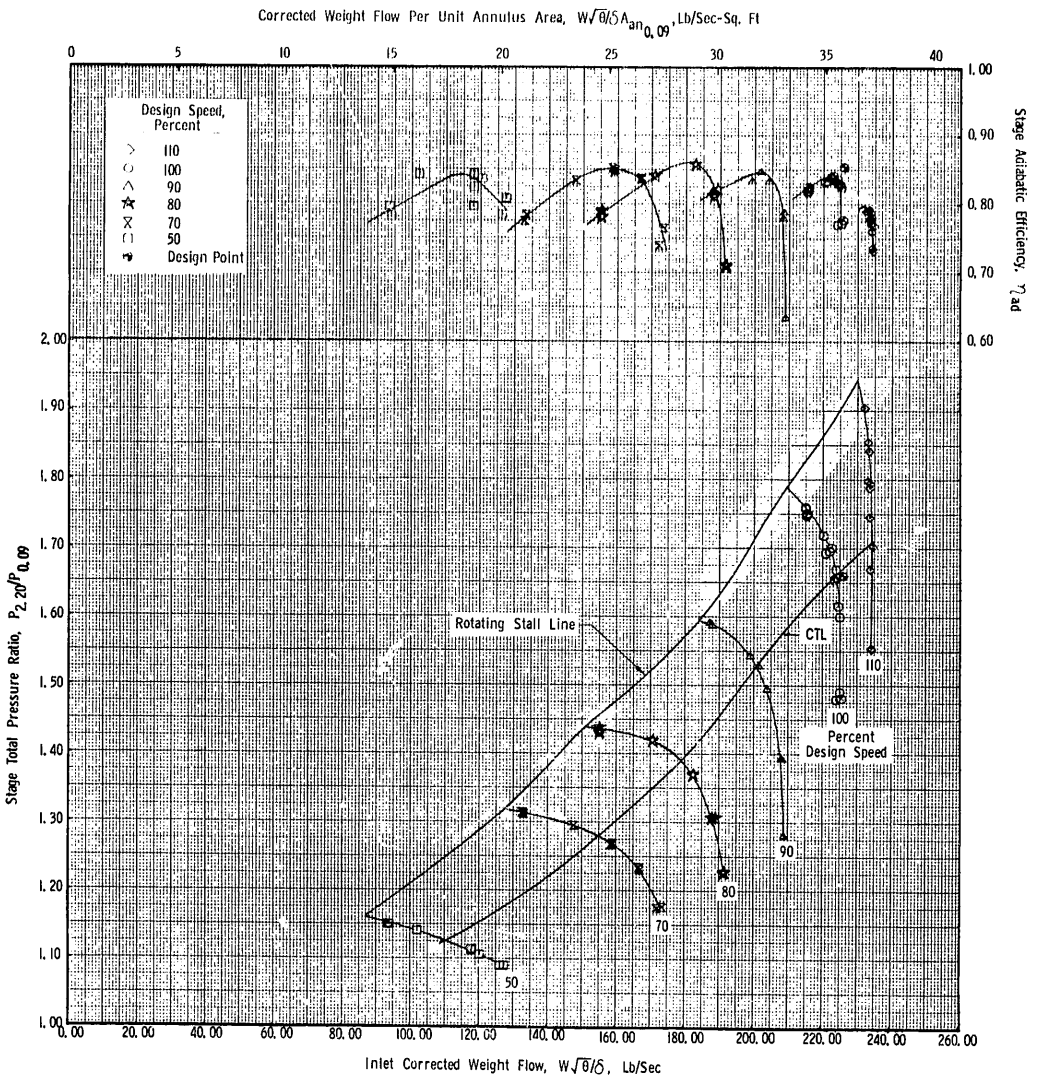

Figure 8. Stage Performance Map for IGV/Stator Schedule 0°/0°.

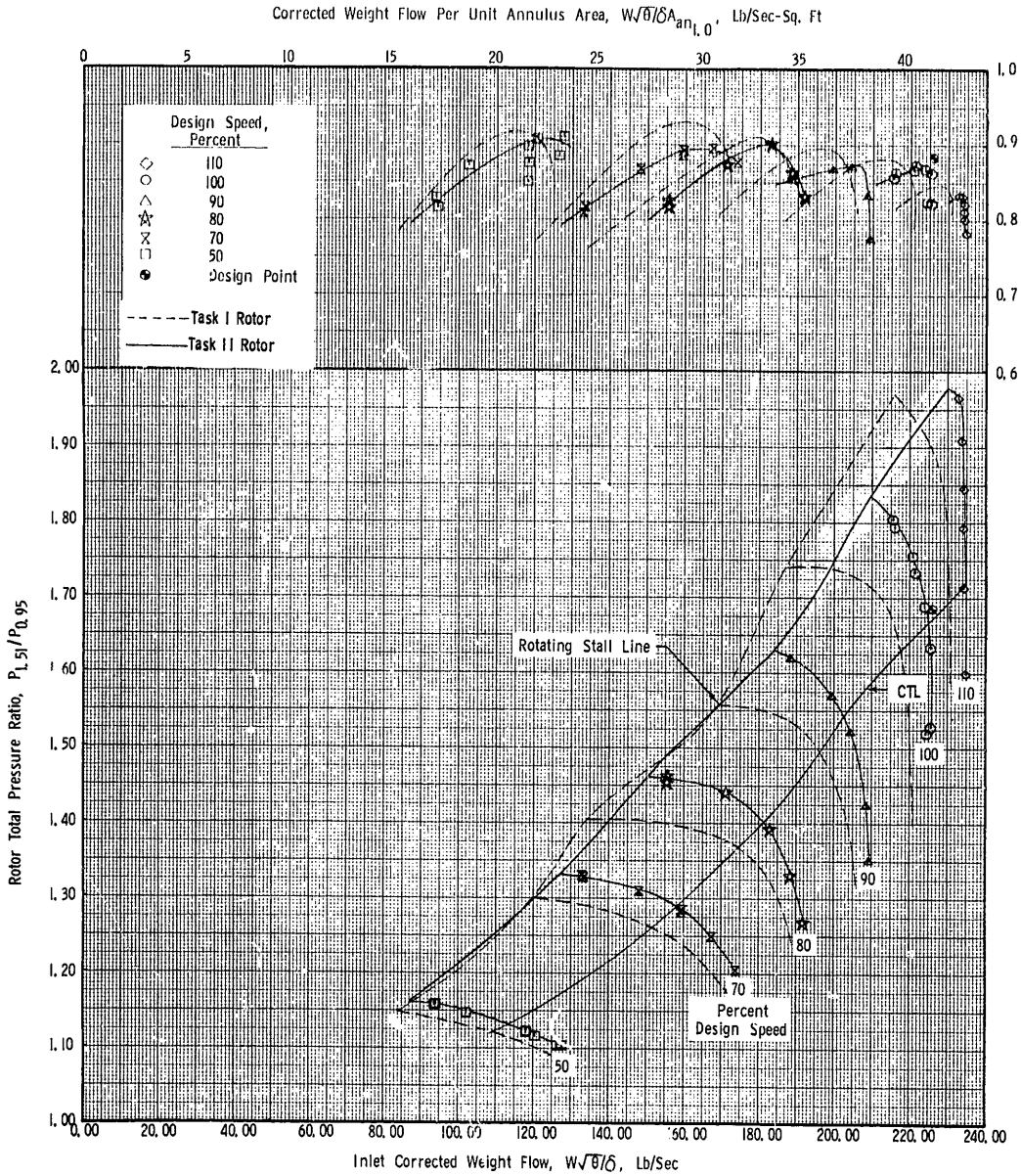

Figure 9. Rotor Performance Maps for Task II Rotor at 0°/0° Vane Schedule and Task I Rotor; Undistorted Inlet Flow.

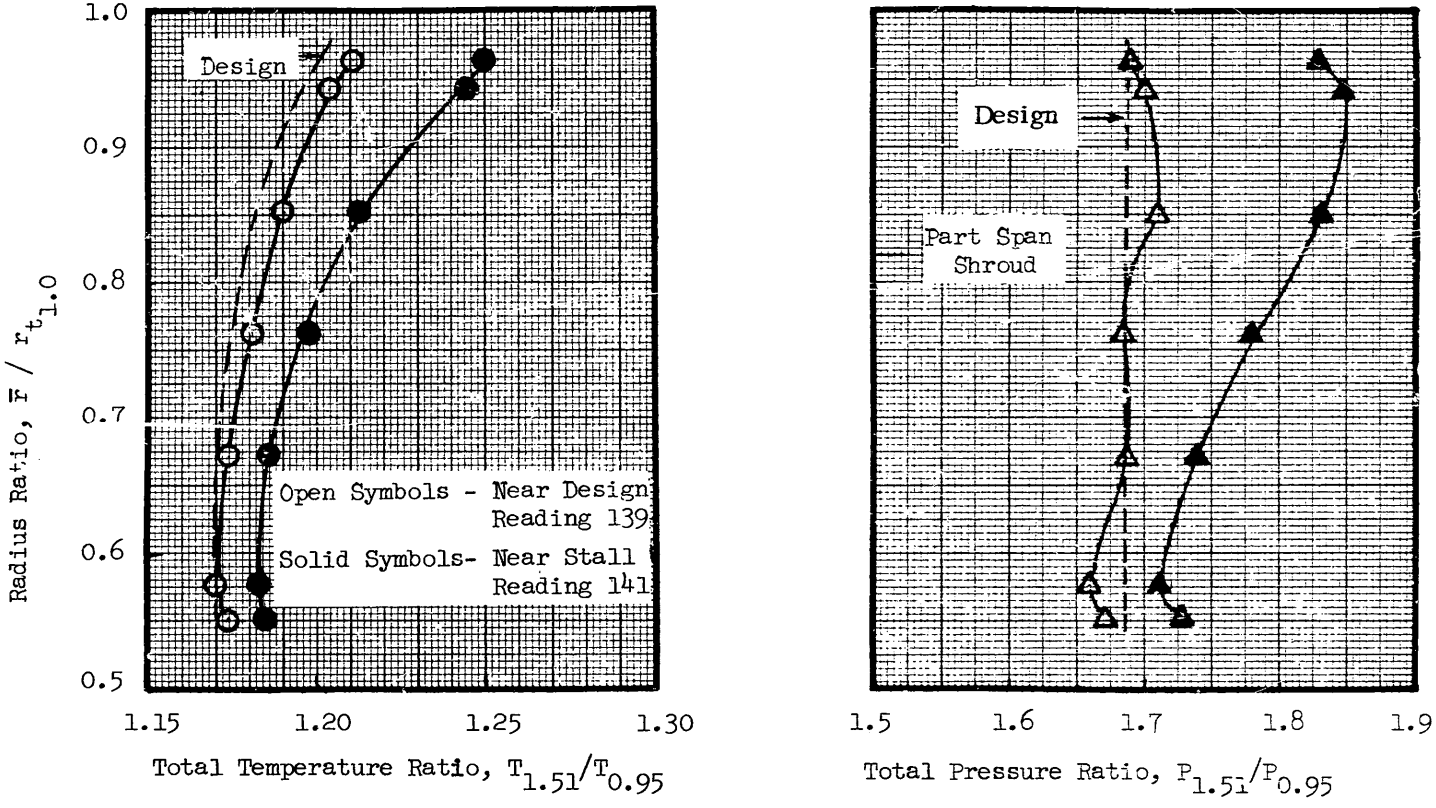

Figure 10. Radial Profiles of Rotor Total Temperature and Pressure Ratios; 100% Speed, IGV/Stator Schedule 0°/0°, Near Design and Near Stall Conditions, Undistorted Inlet.

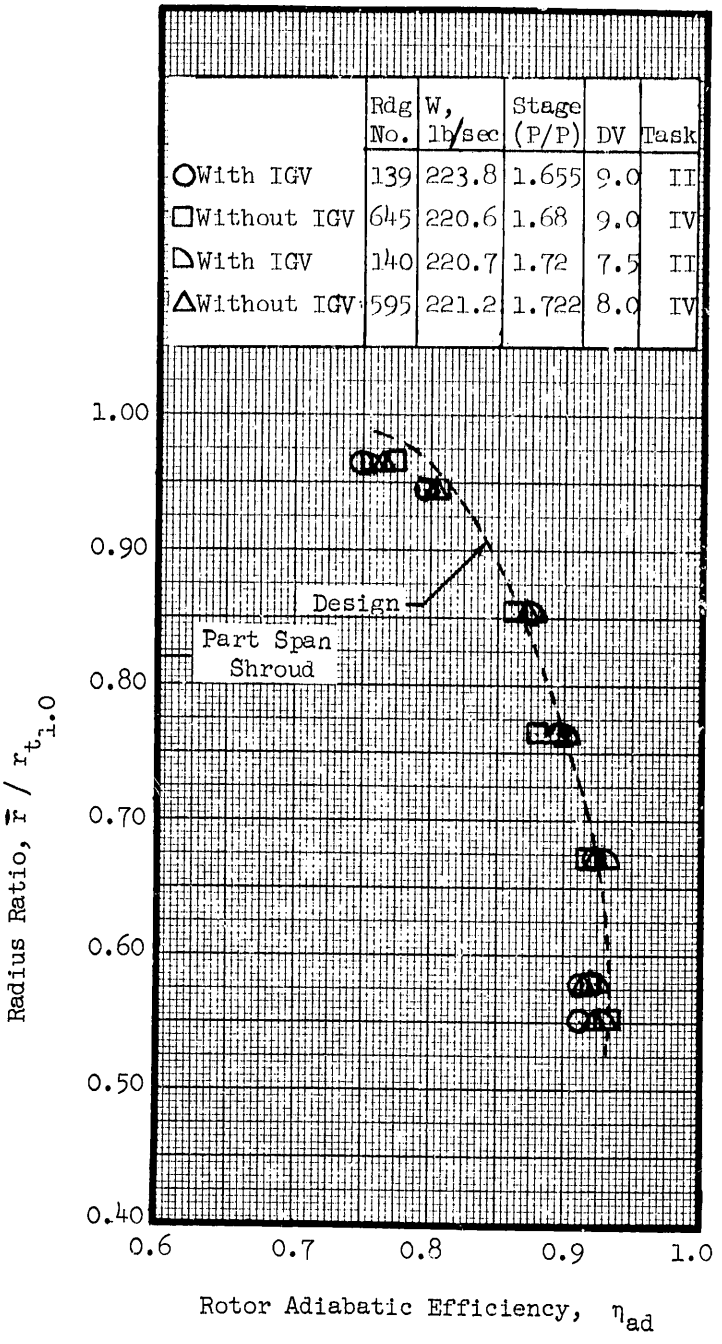

Figure 11. Radial Profile of Rotor Adiabatic Efficiency; 100% Speed, IGV/Stator Schedule 0°/0°, Near Design Condition (Reading 139), Undistorted Inlet.

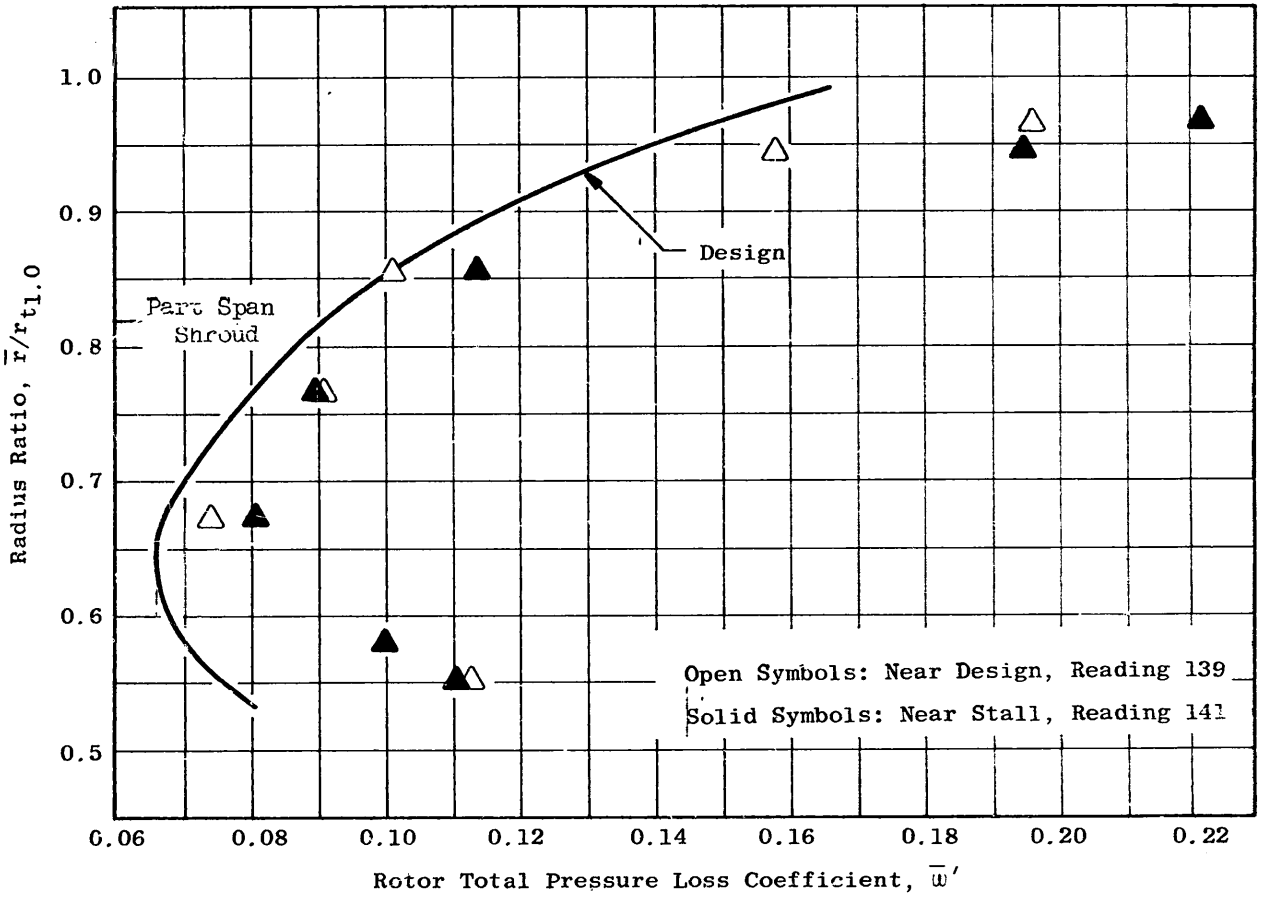

Figure 12. Radial Profiles of Rotor Total Pressure Loss Coefficient, 100% Speed, IGV/Stator Schedule 0°/0°, Near Design and Near Stall Conditions, Undistorted Inlet.

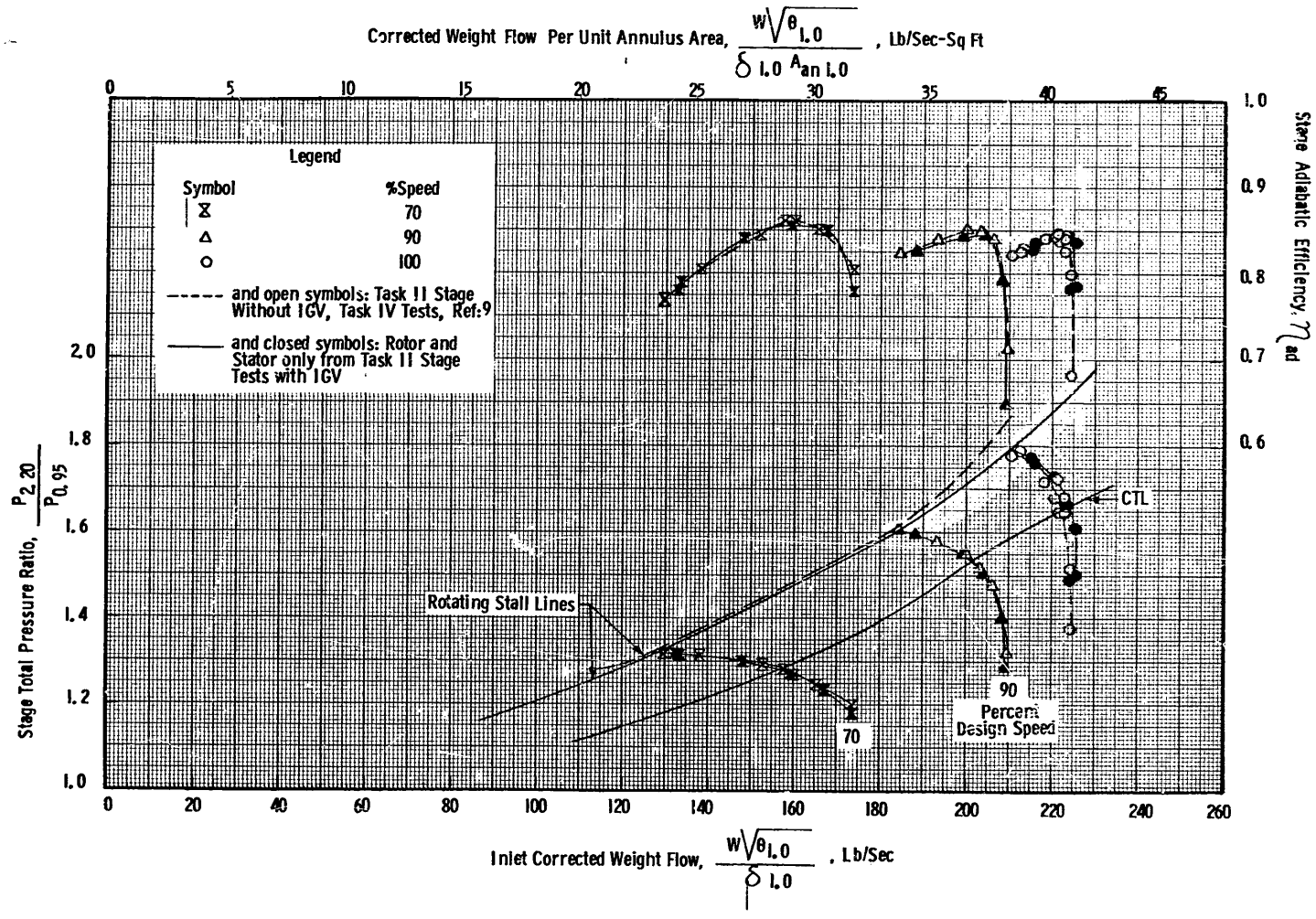

Figure 13. Task II Stage Performance Map with Inlet Guide Vanes at Nominal Setting and without Inlet Guide Vanes; Stator at Nominal Setting.

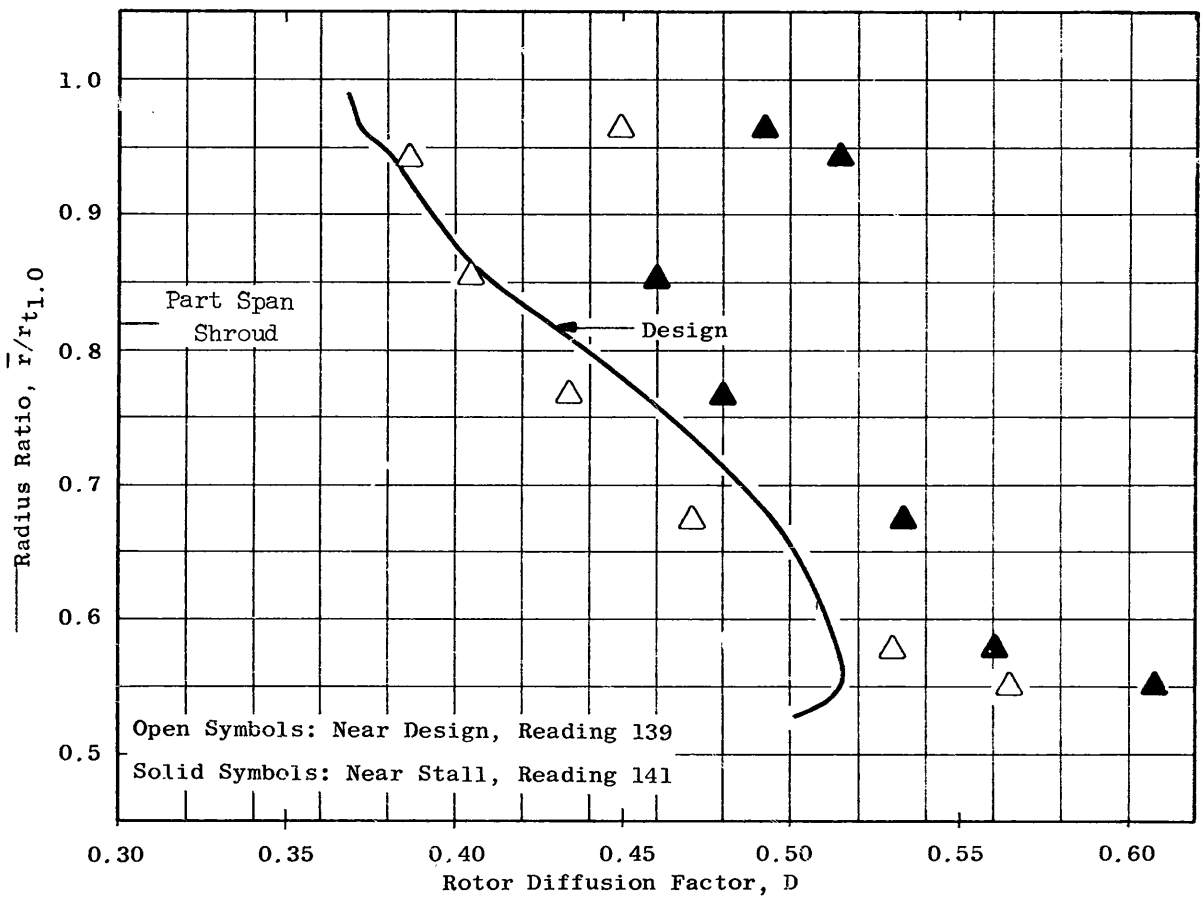

Figure 14. Radial Profiles Rotor Diffusion Factor; 100% Speed, IGV/Stator Schedule 0°/0°, Near Design and Near Stall Conditions, Undistorted Inlet.

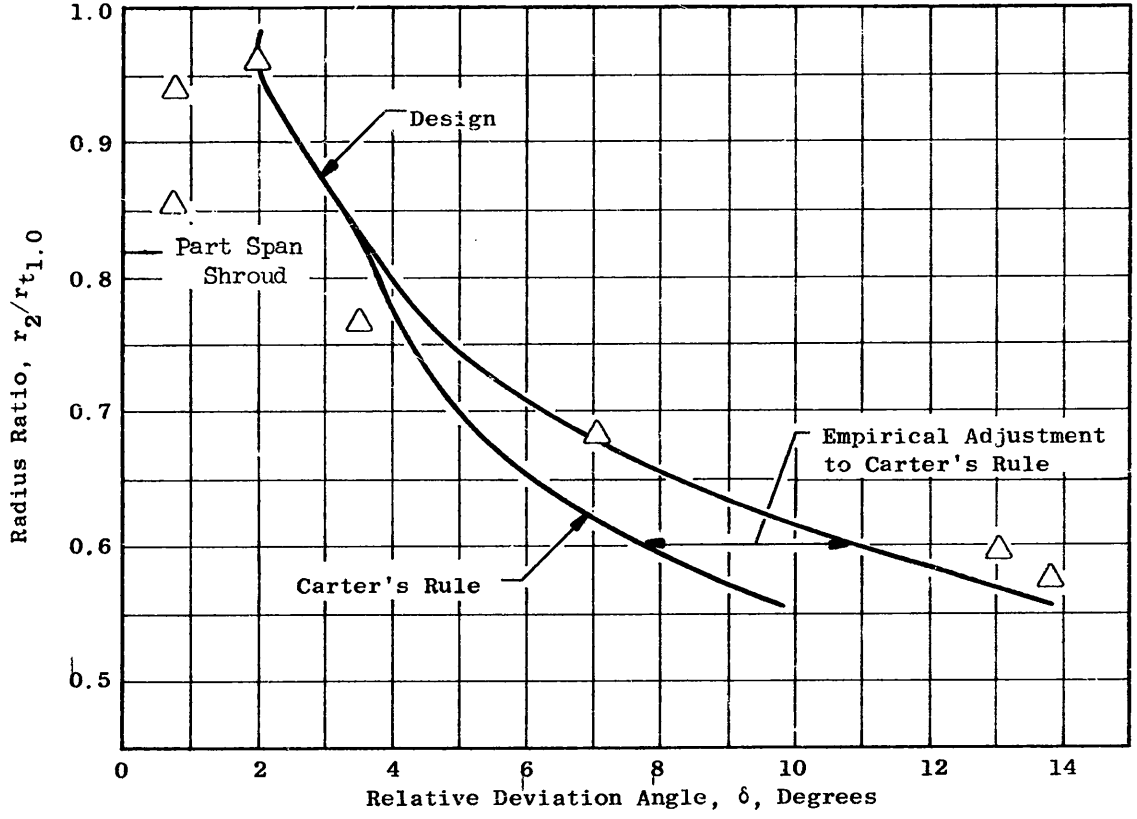

Figure 15. Radial Profile of Rotor Relative Deviation Angle; 100% Speed, IGV/Stator Schedule 0°/0°, Near Design Condition, Undistorted Inlet.

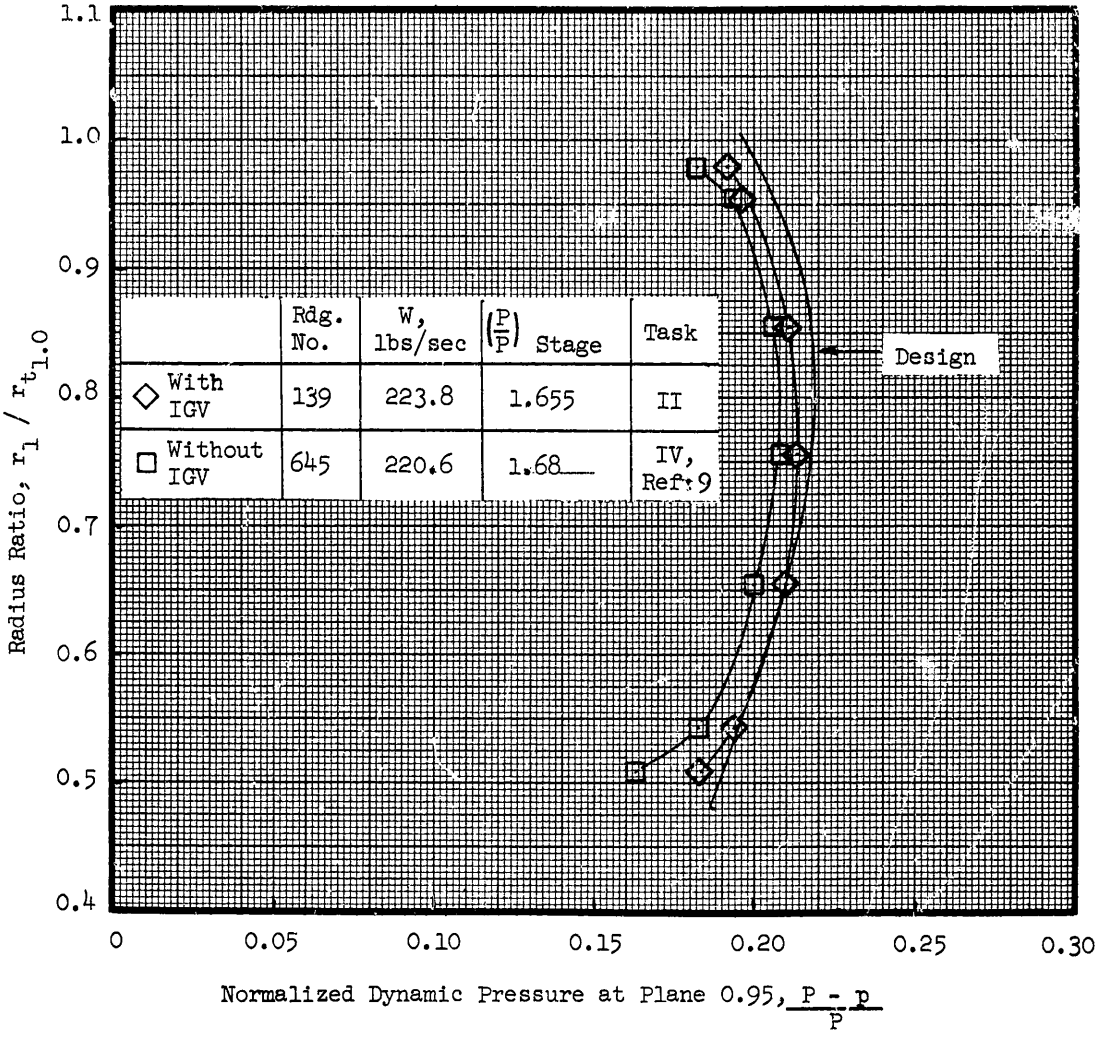

Figure 16. Radial Profile of Normalized Dynamic Pressure at Rotor Inlet Measurement Plane; 100% Speed, IGV/Stator Schedule 0°/0°, Near Design Condition, Undistorted Inlet.

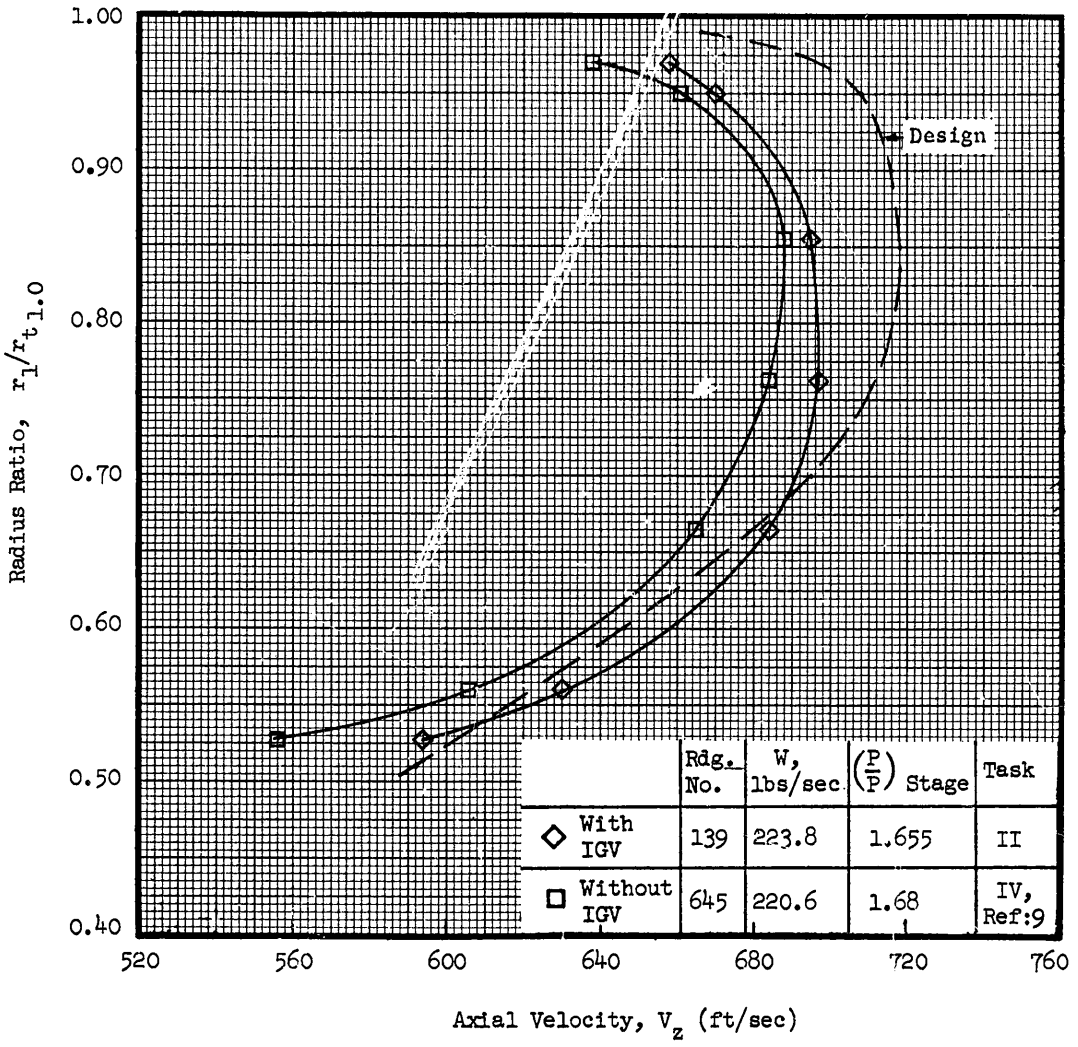

Figure 17. Radial Profile of Rotor Inlet Axial Velocity; 100% Speed, IGV/ Stator Schedule 0°/0°, Near Design Condition, Undistorted Inlet.

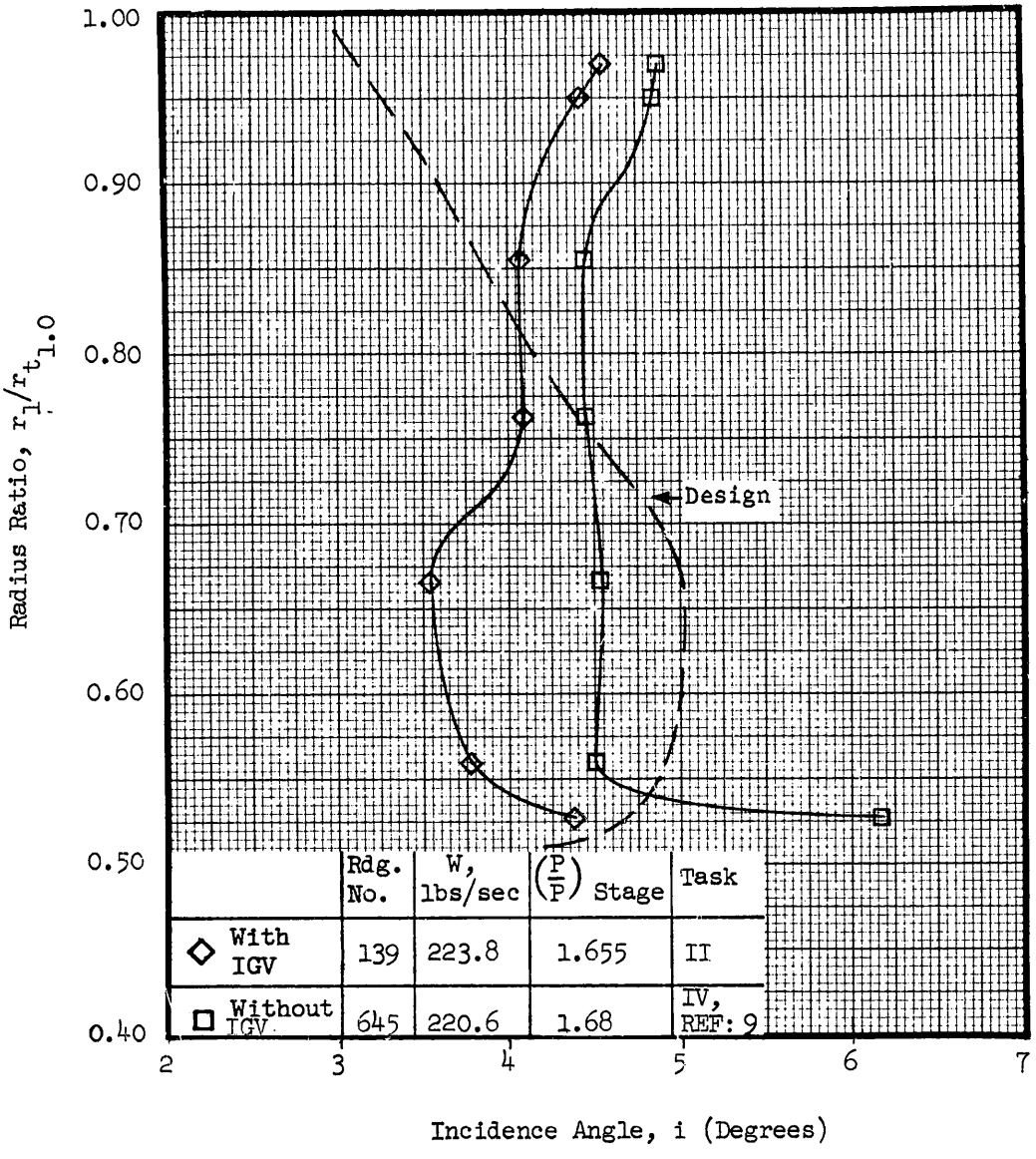

Figure 18. Radial Profile of Rotor Incidence Angle; 100% Speed, IGV/Stator Schedule 0°/0°, Near Design Condition, Undistorted Inlet.

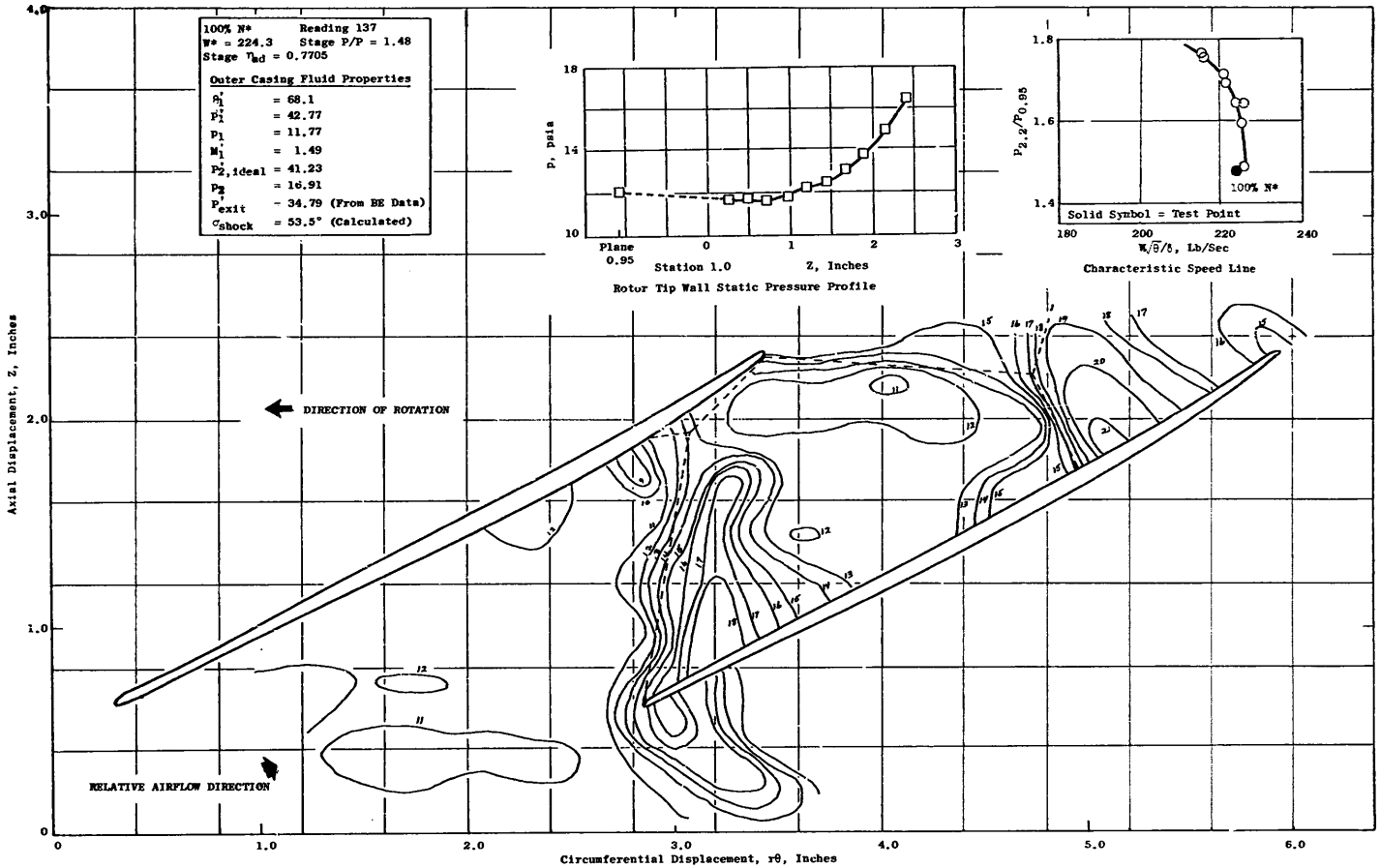

(a) 100% Speed, Open Throttle.

Figure 19. Rotor Blade Tip Static Pressure Contours at 0°/0° IGV/Stator Schedule with Undistorted Inlet Flow.

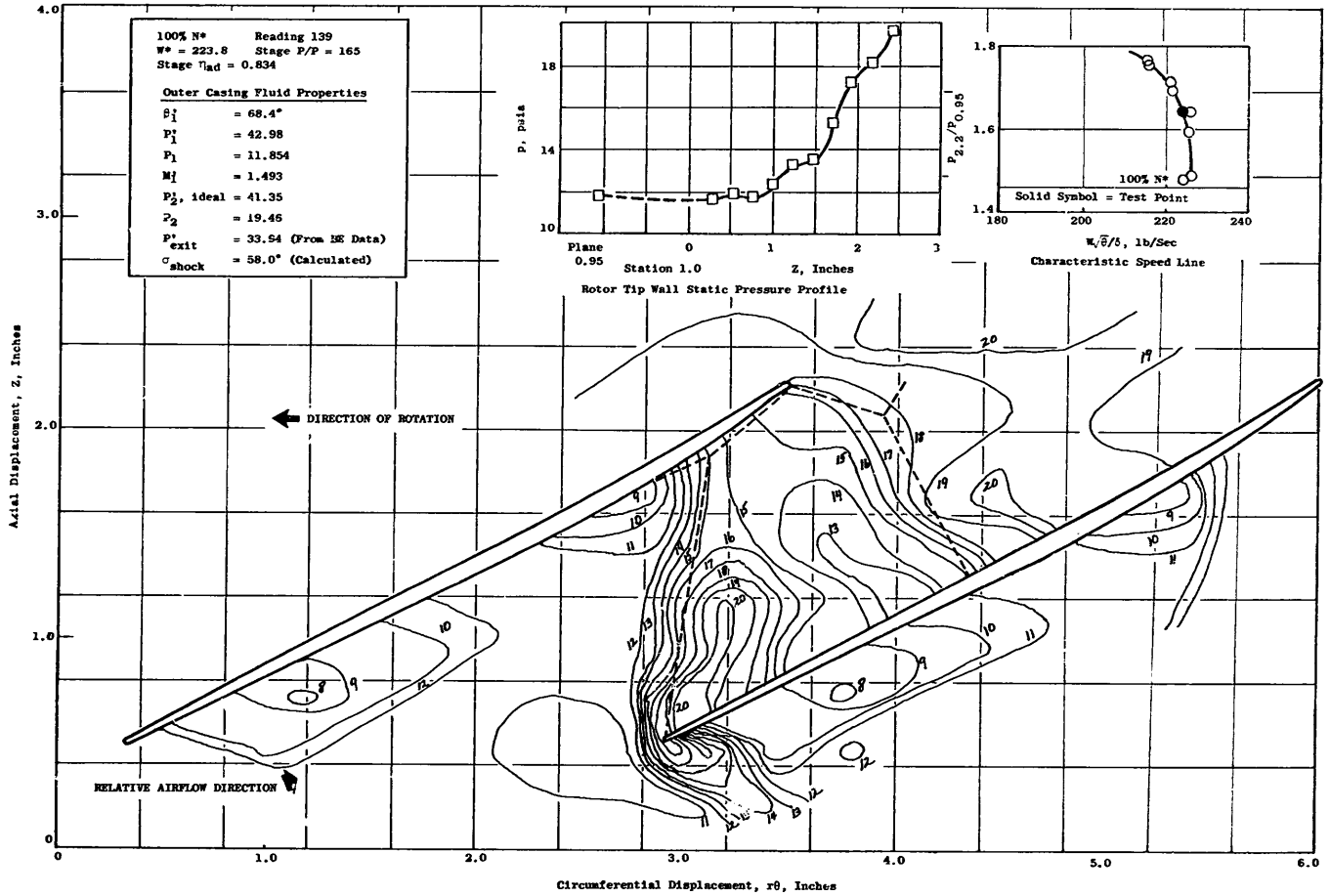

(b) 100% Speed, Near Design.

Figure 19. Rotor Blade Tip Static Pressure Contours at 0°/0° IGV/Stator Schedule with Undistorted Inlet Flow (Continued).

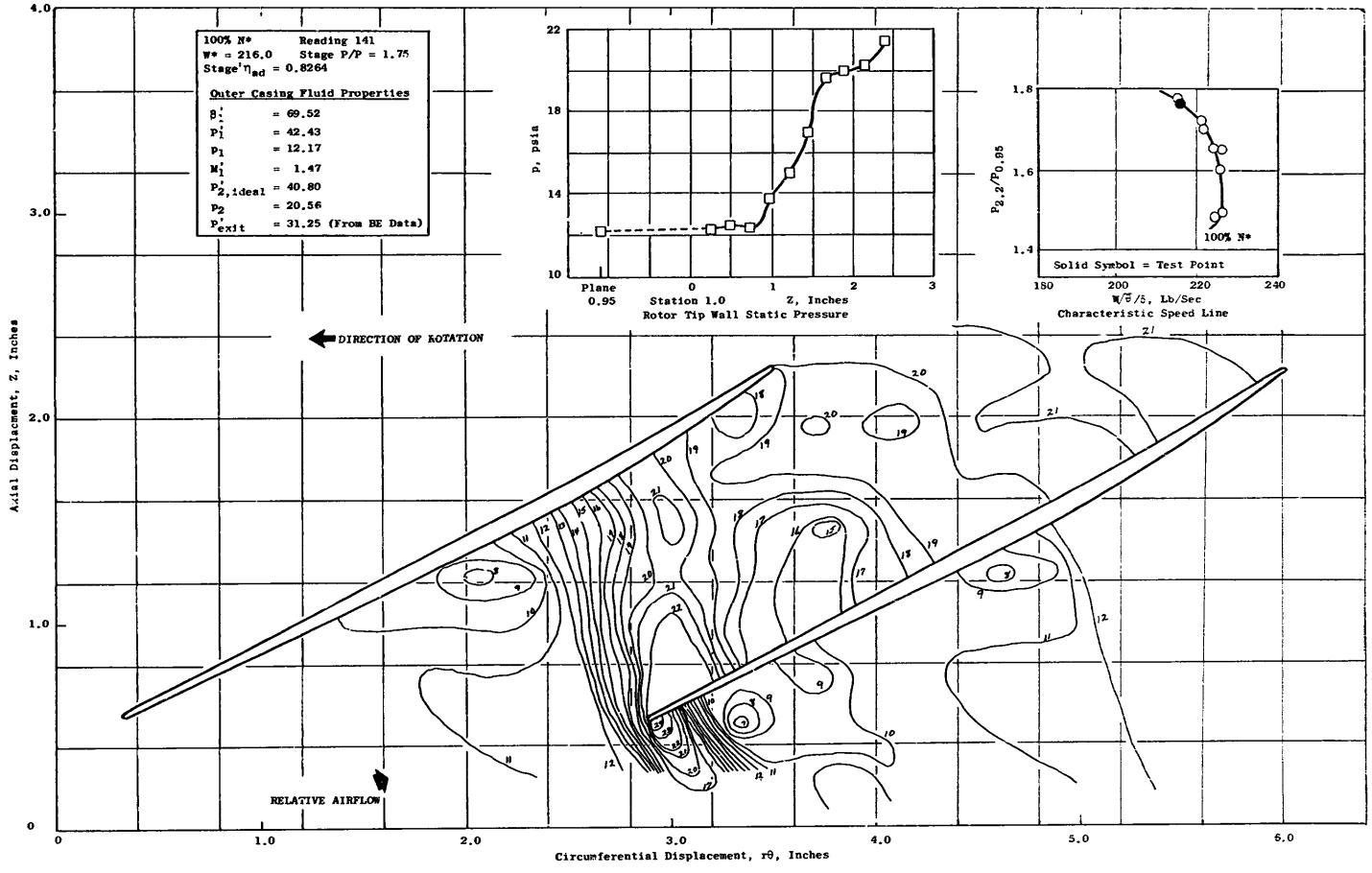

(c) 100% Speed, Near Stall.

Figure 19. Rotor Blade Tip Static Pressure Contours at 0°/0° IGV/Stator Schedule with Undistorted Inlet Flow (Continued).

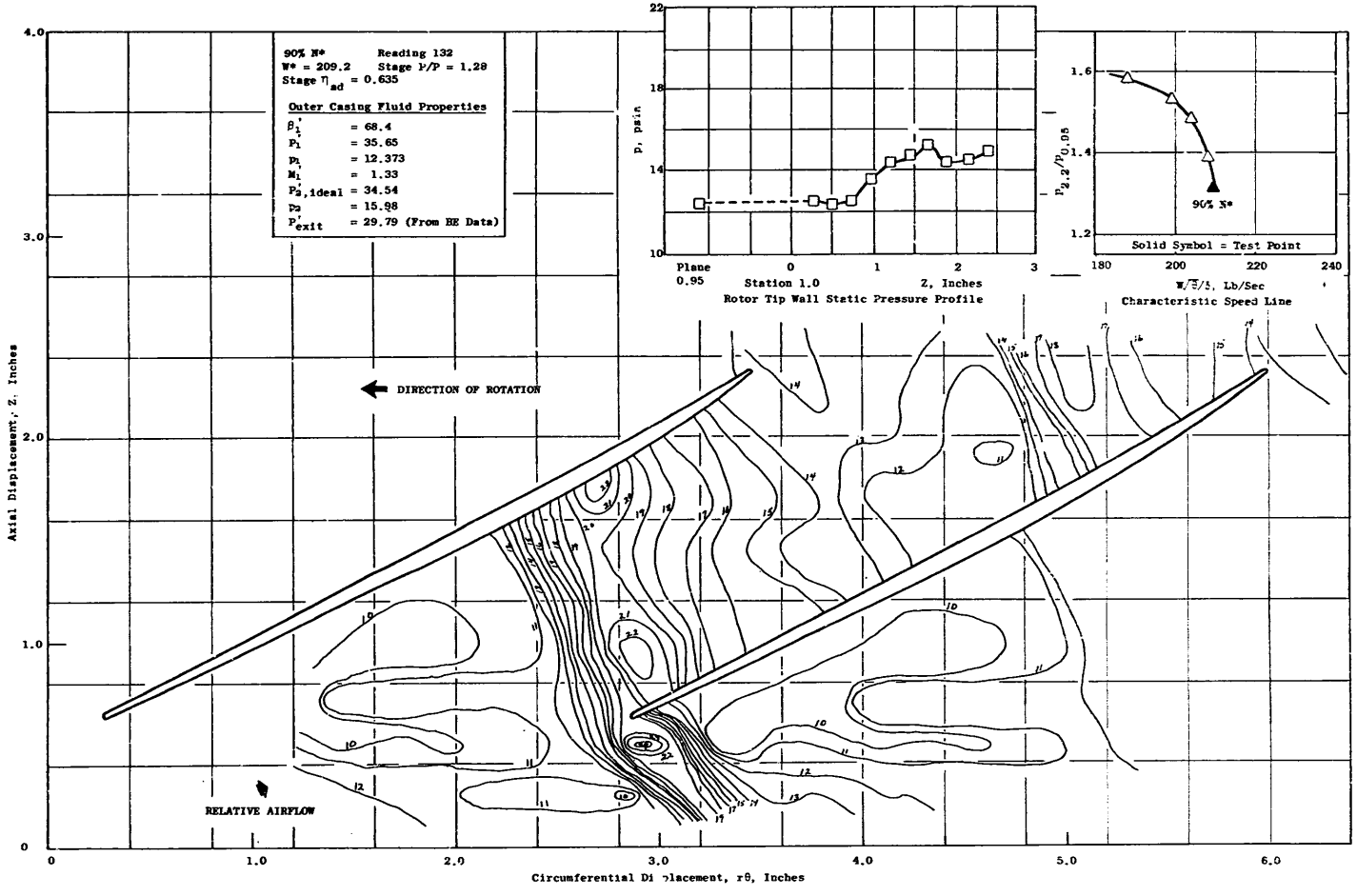

(d) 90% Speed, Open Throttle.

Figure 19. Rotor Blade Tip Static Pressure Contours at 0°/0° IGV/Stator Schedule with Undistorted Inlet Flow (Continued).

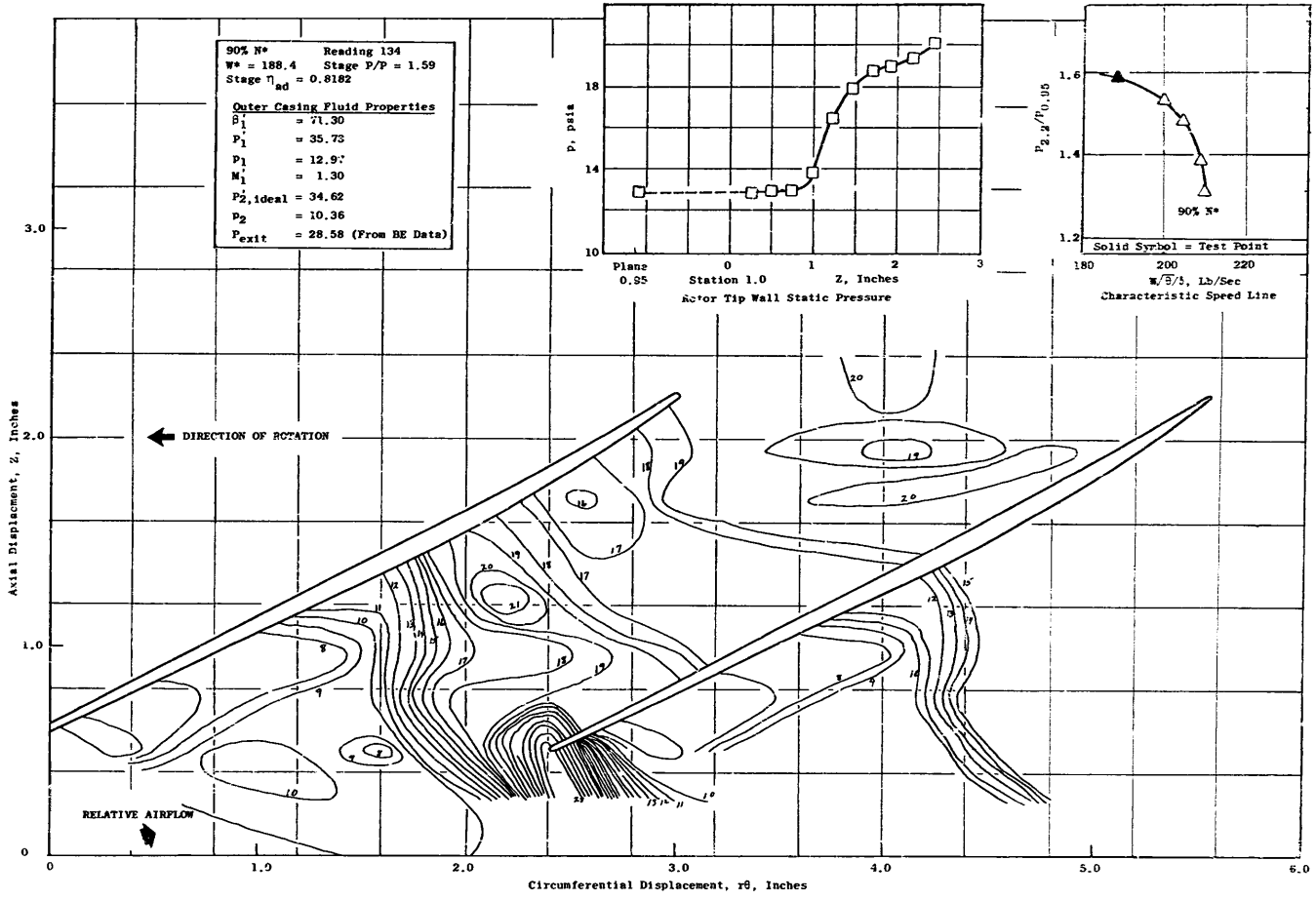

(e) 90% Speed, Near Stall.

Figure 19. Rotor Blade Tip Static Pressure Contours at 0°/0° IGV/Stator Schedule with Undistorted Inlet Flow (Continued).

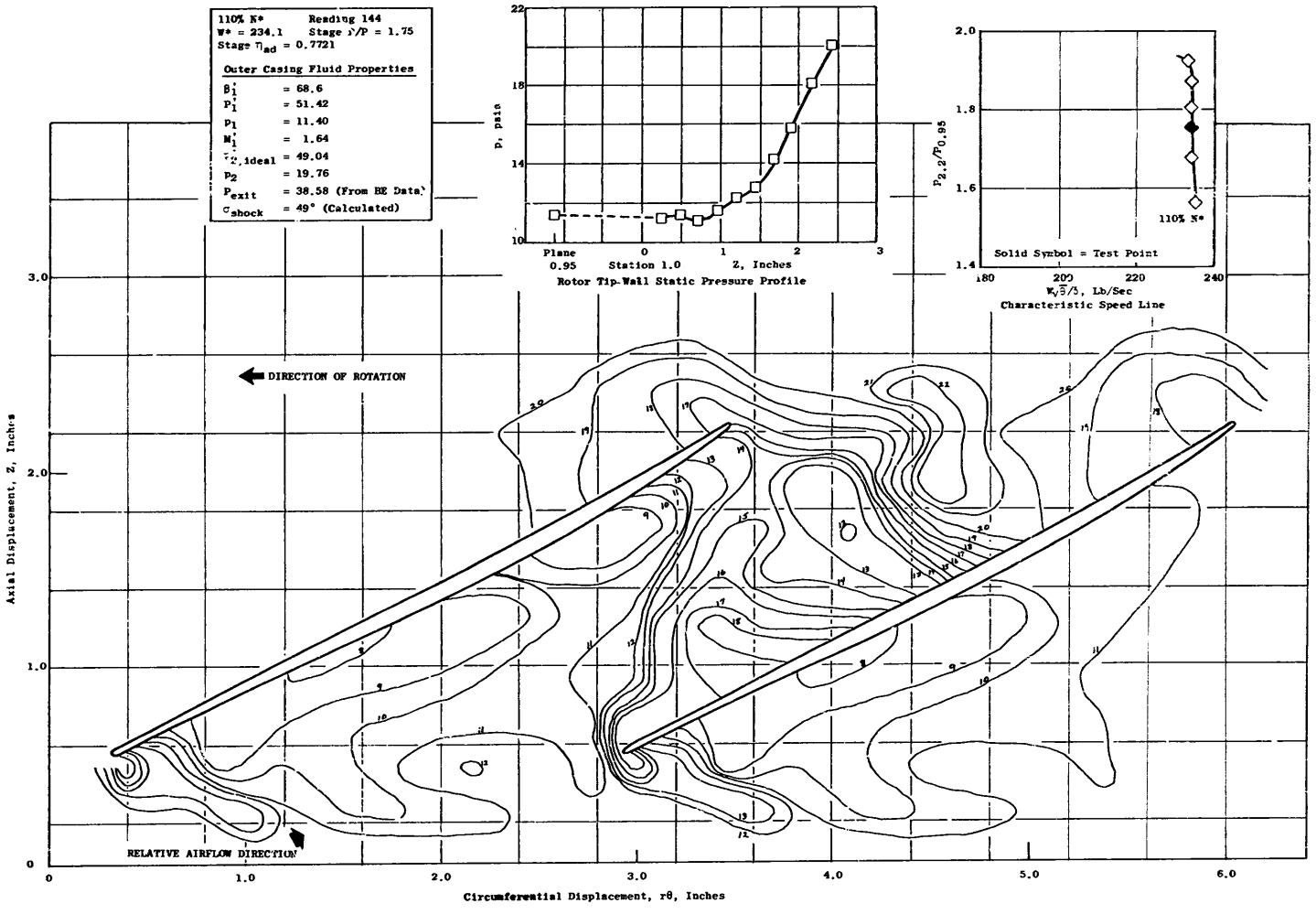

(f) 110% Speed, Intermediate Flow.

Figure 19. Rotor Blade Tip Static Pressure Contours at 0°/0° IGV/Stator Schedule with Undistorted Inlet Flow (Continued).

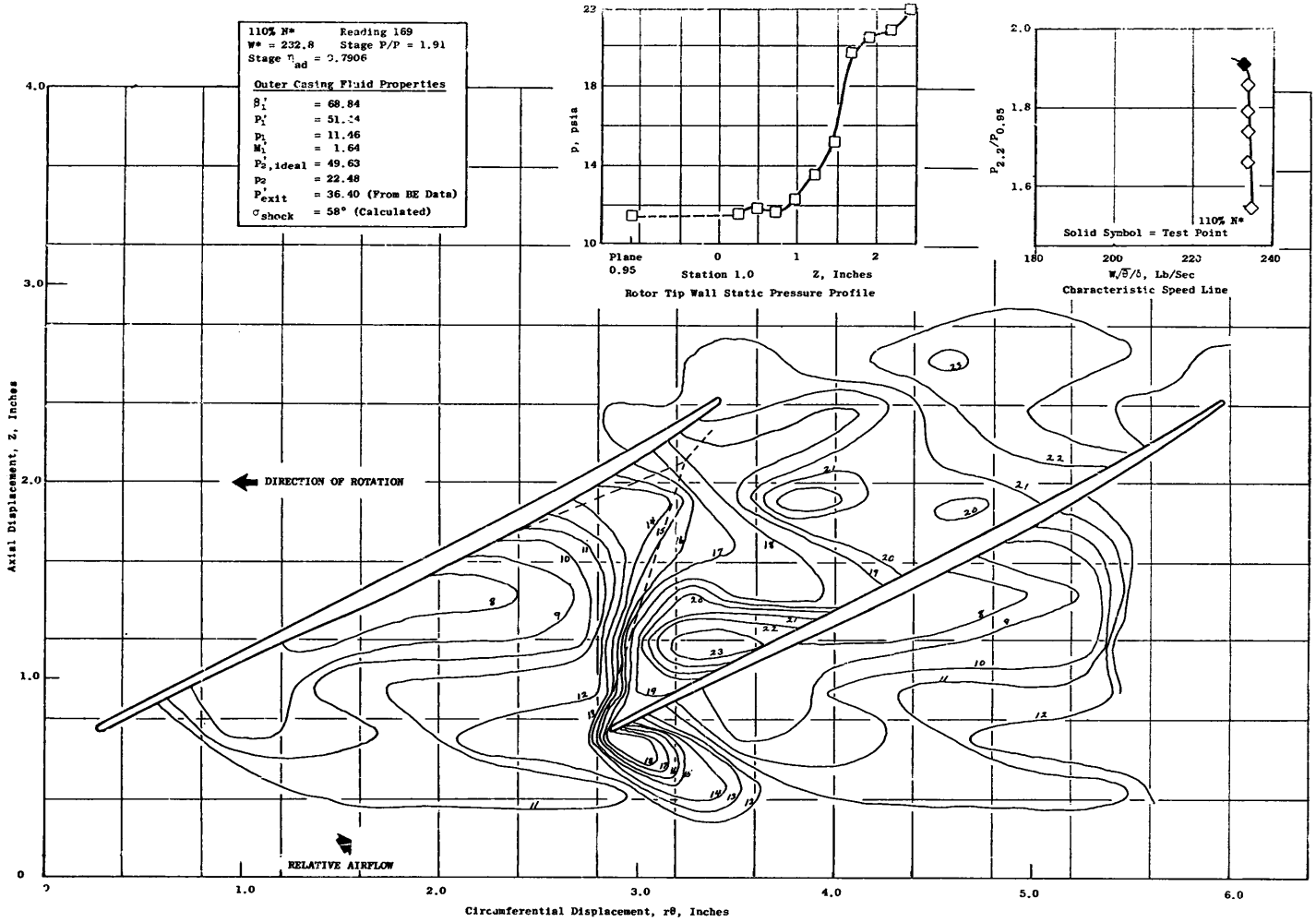

(g) 110% Speed, Near Stall.

Figure 19. Rotor Blade Tip Static Pressure Contours at 0°/0° IGV/Stator Schedule with Undistorted Inlet Flow (Concluded).

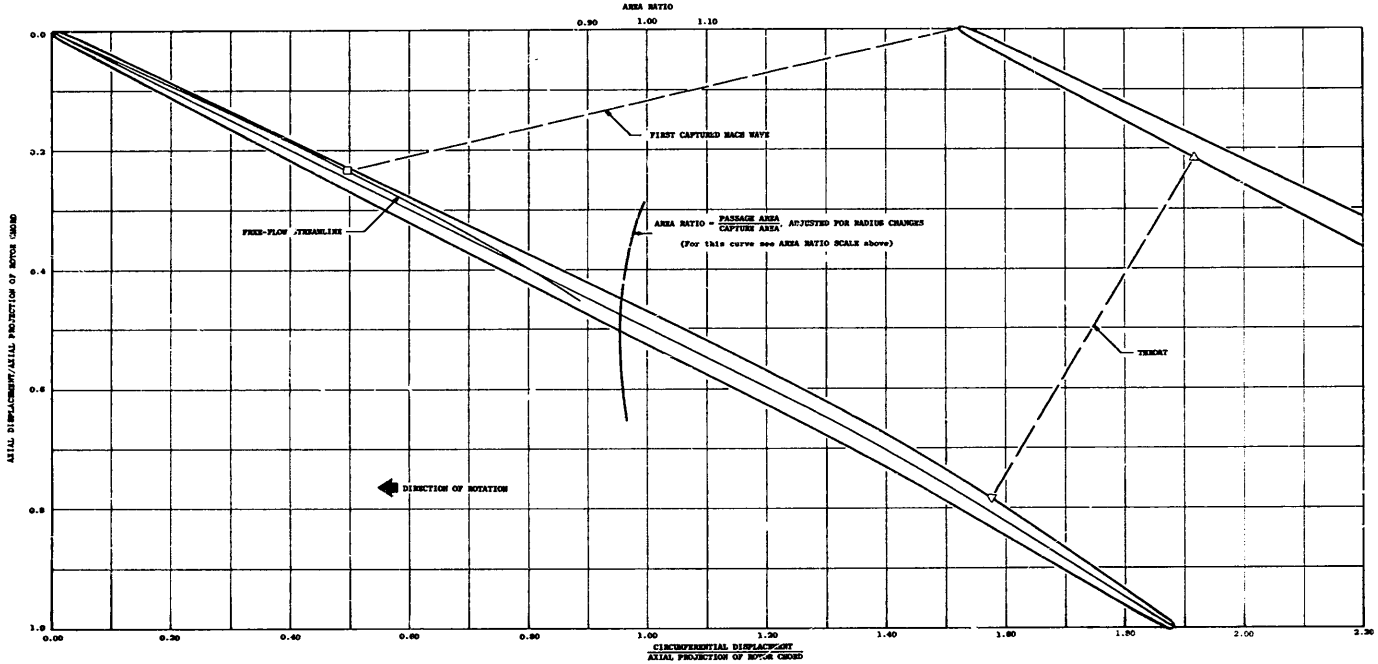

(a) 0% Immersion from Tip

Figure 20. Rotor Blade Shapes Showing Free Flow Streamlines and Throat Locations.

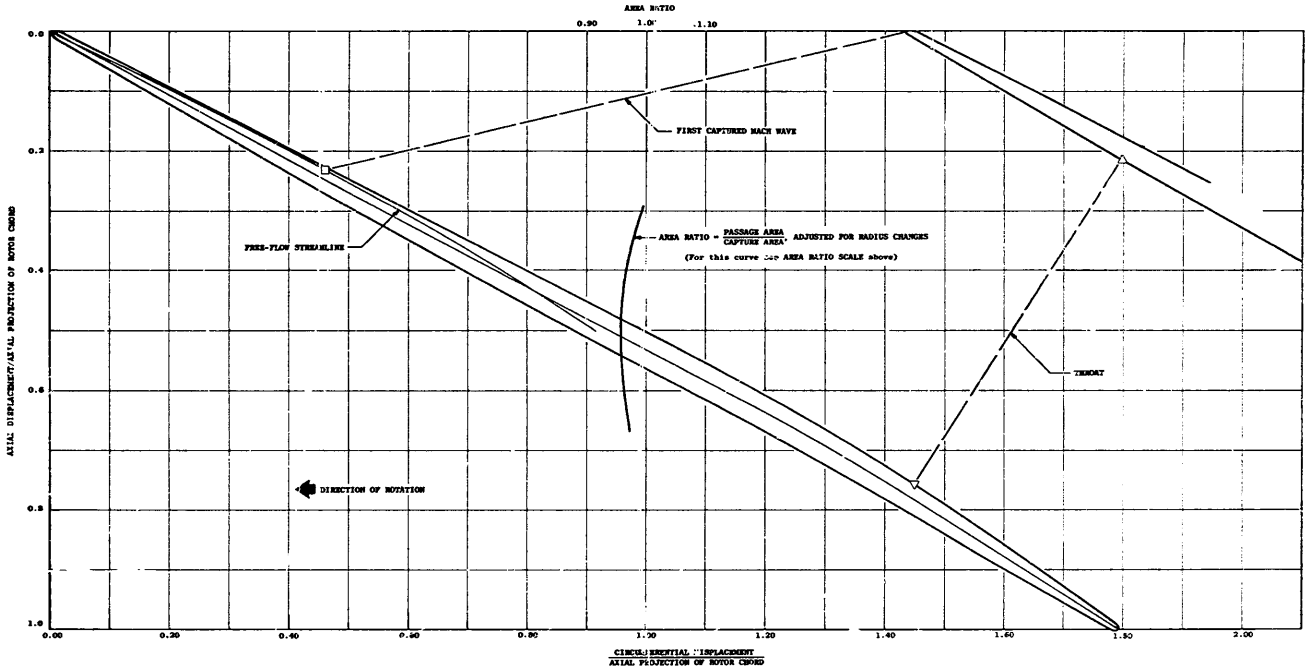

(b) 5% Immersion from Tip

Figure 20. Rotor Blade Shapes Showing Free Flow Streamlines and Throat Locations (Continued).

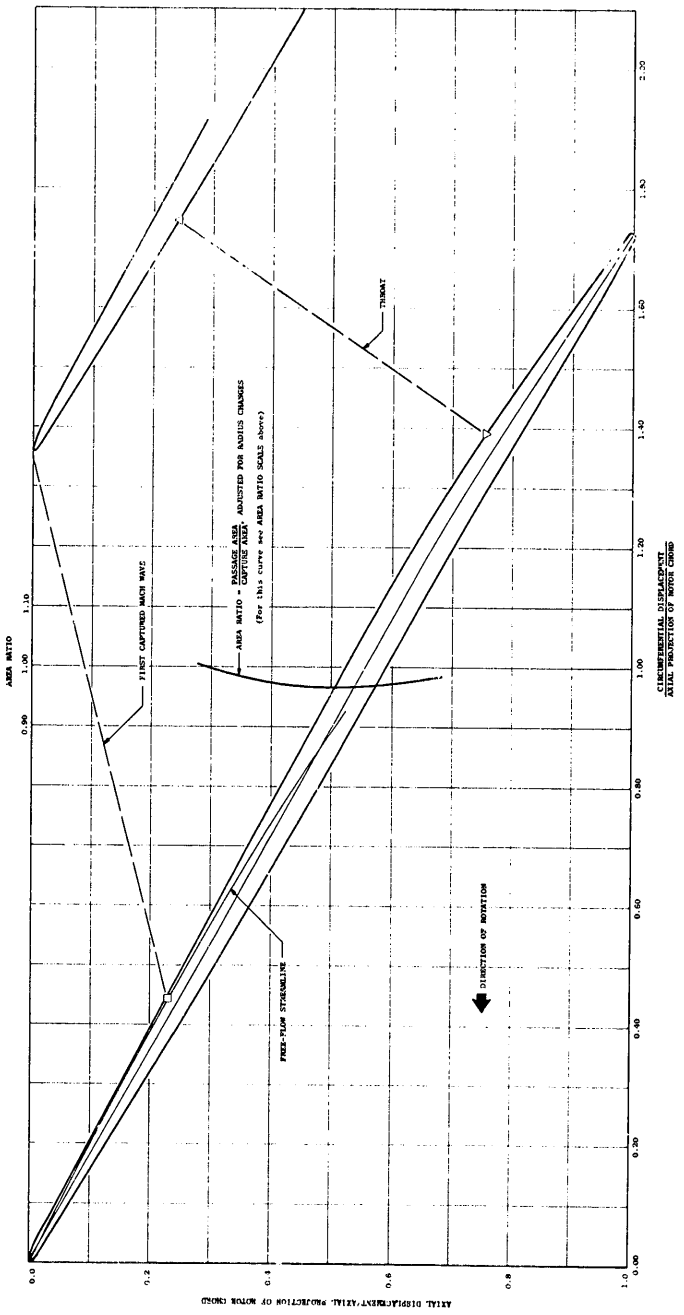

(c) 10% Immersion from Tip

Figure 20. Rotor Blade Shapes Showing Free Flow Streamlines and Throat Locations (Continued).

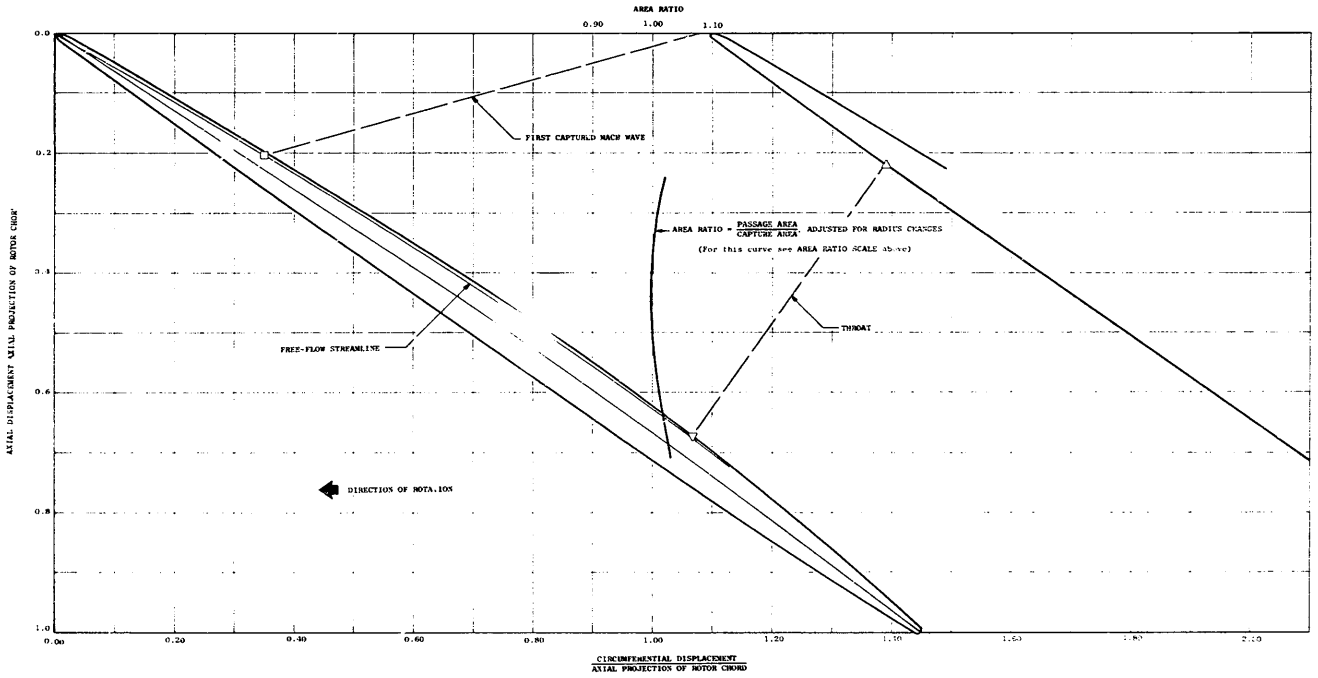

(d) 30% Immersion from Tip

Figure 20. Rotor Blade Shapes Showing Free Flow Streamlines and Throat Locations (Concluded).

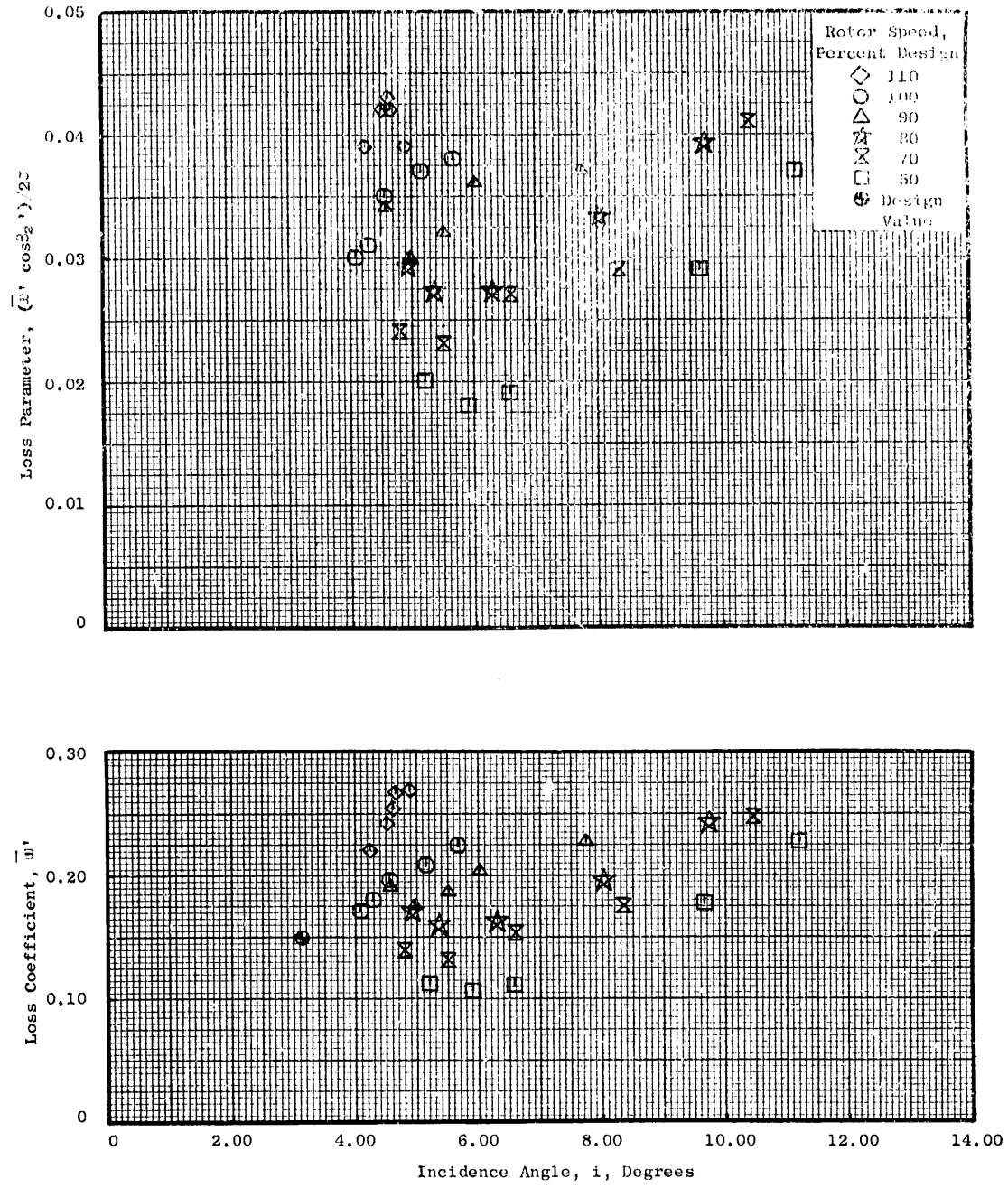

(a) 5% Immersion from Tip

Figure 21. Rotor Blade Element Data for IGV/Stator Schedule 0°/0°; Undistorted Inlet Flow.

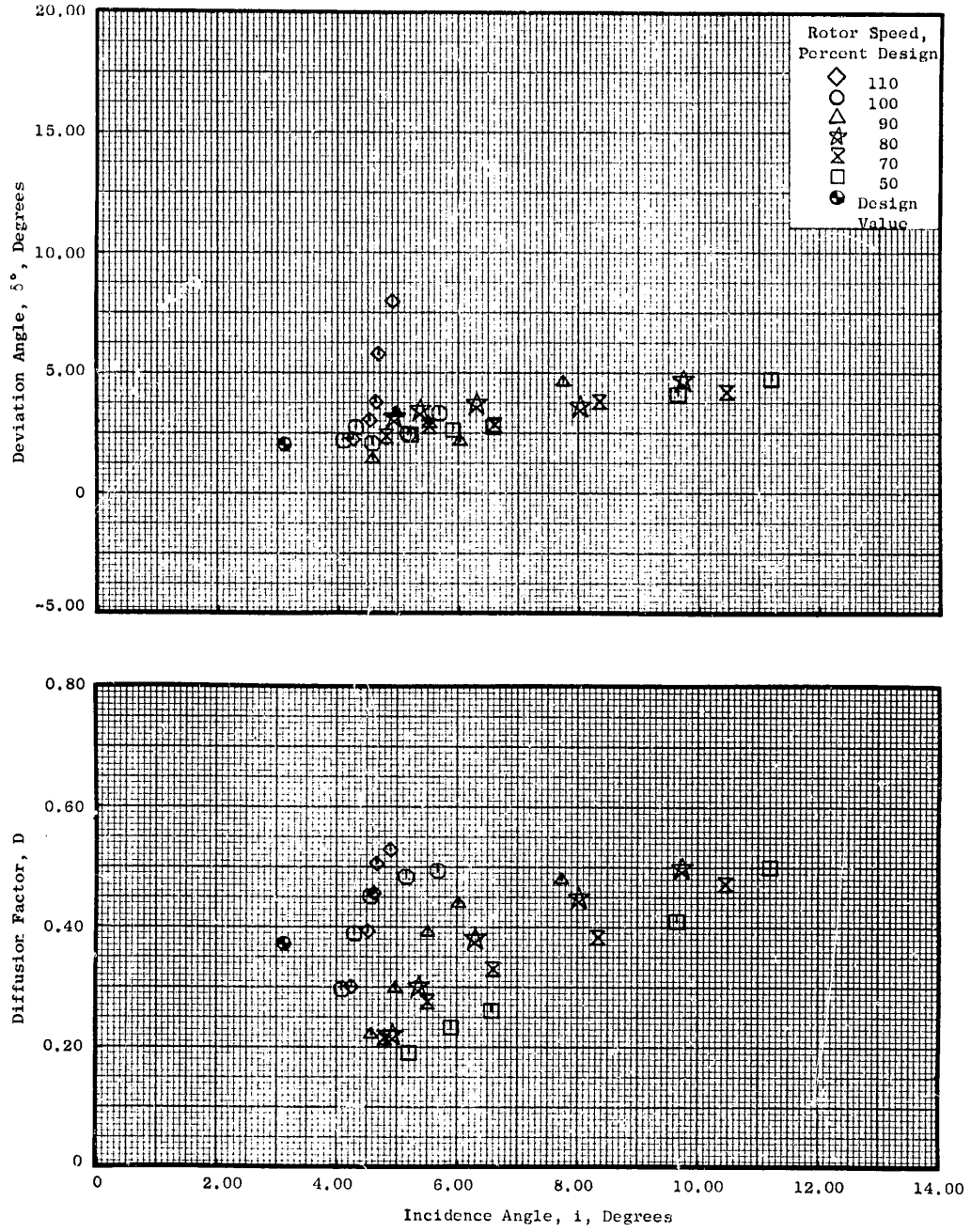

(a) 5% Immersion from Tip (Concluded)

Figure 21. Rotor Blade Element Data for IGV/Stator Schedule 0°/0°; Undistorted Inlet Flow (Continued).

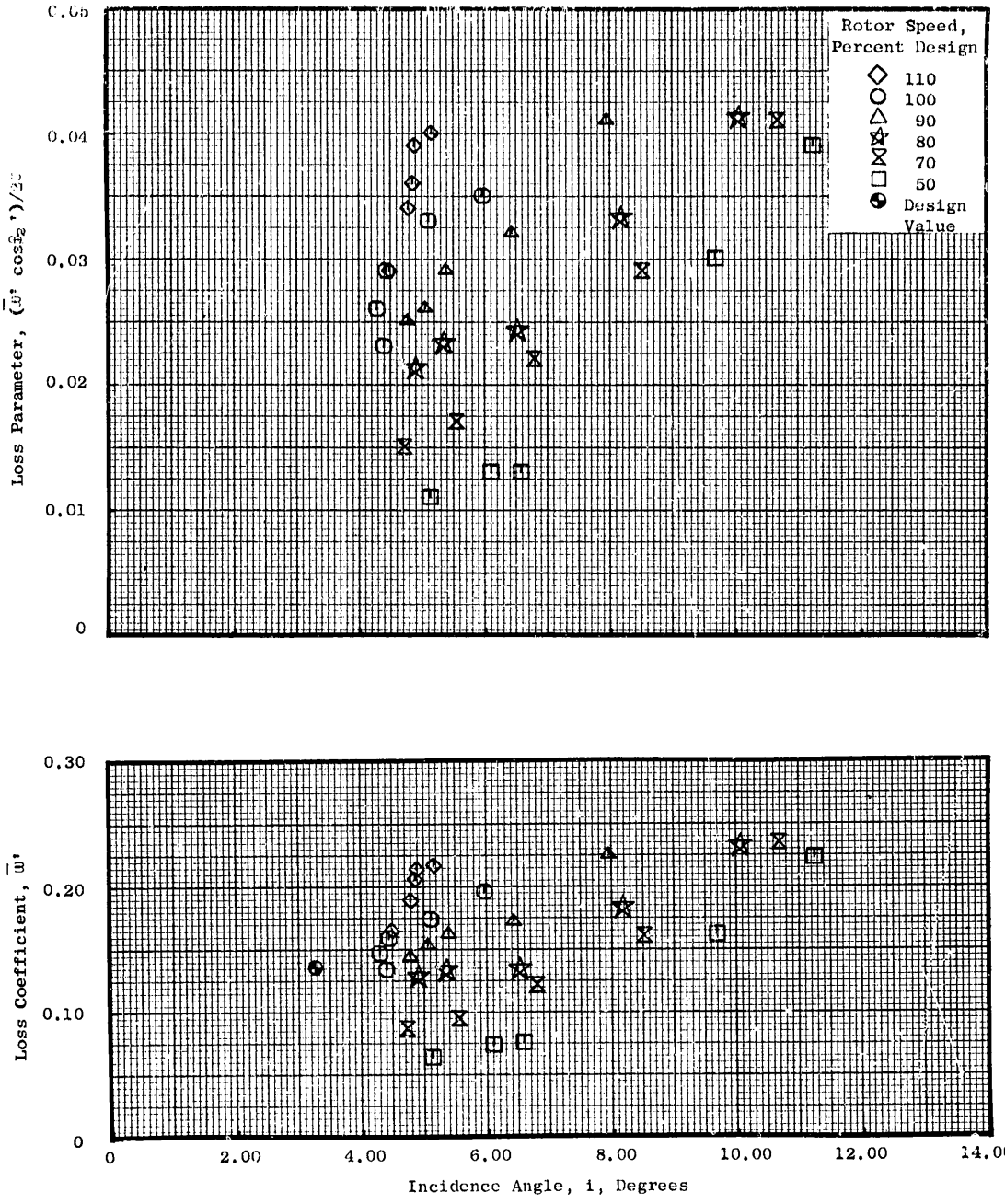

(b) 10% Immersion from Tip

Figure 21. Rotor Blade Element Data for IGV/Stator Schedule 0°/0°; Undistorted Inlet Flow (Continued).

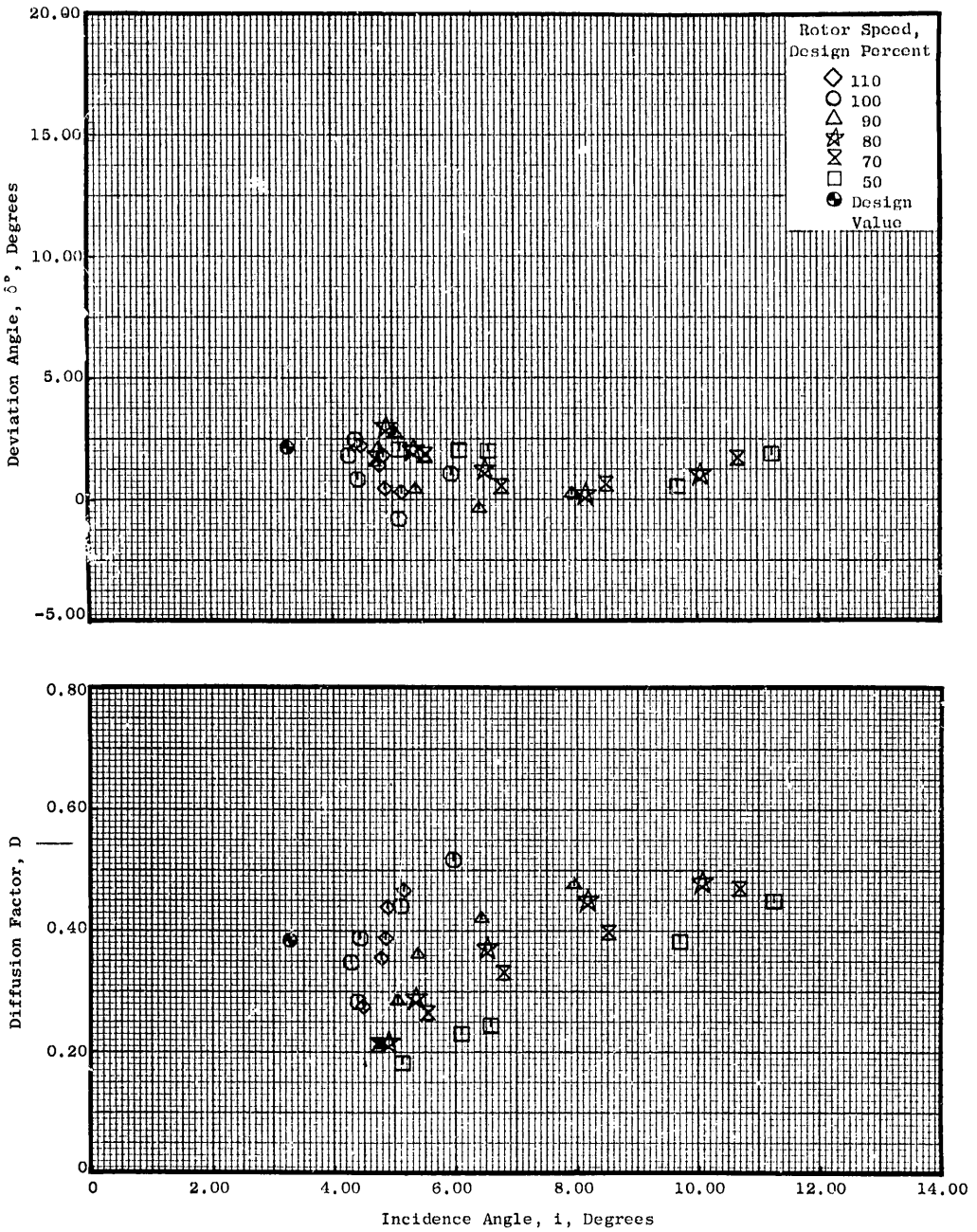

(b) 10% Immersion from Tip (Concluded)

Figure 21. Rotor Blade Element Data for IGV/Stator Schedule 0°/0°; Undistorted Inlet Flow (Continued).

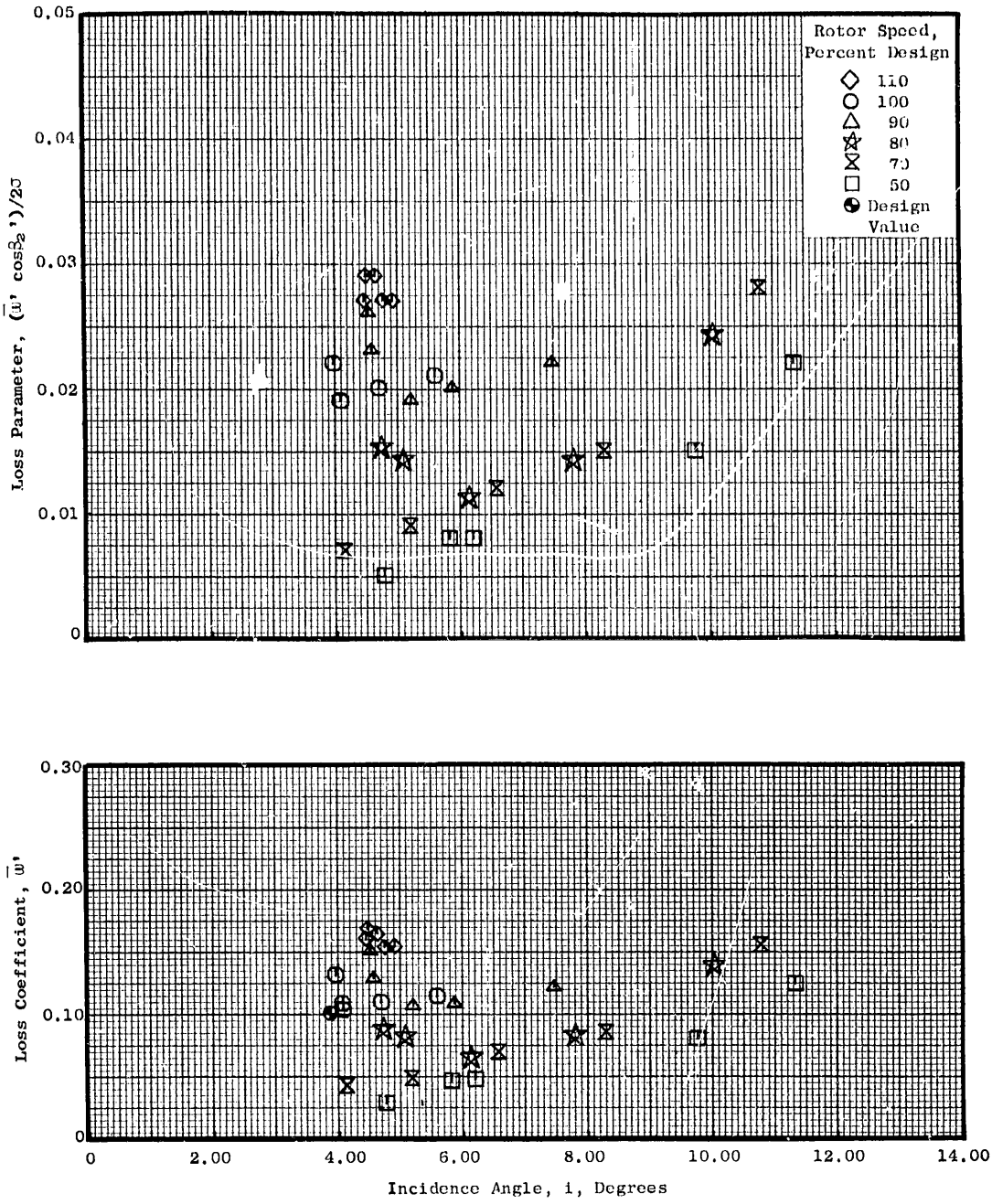

(c) 30% Immersion from Tip

Figure 21. Rotor Blade Element Data for IGV/Stator Schedule 0°/0°; Undistorted Inlet Flow (Continued).

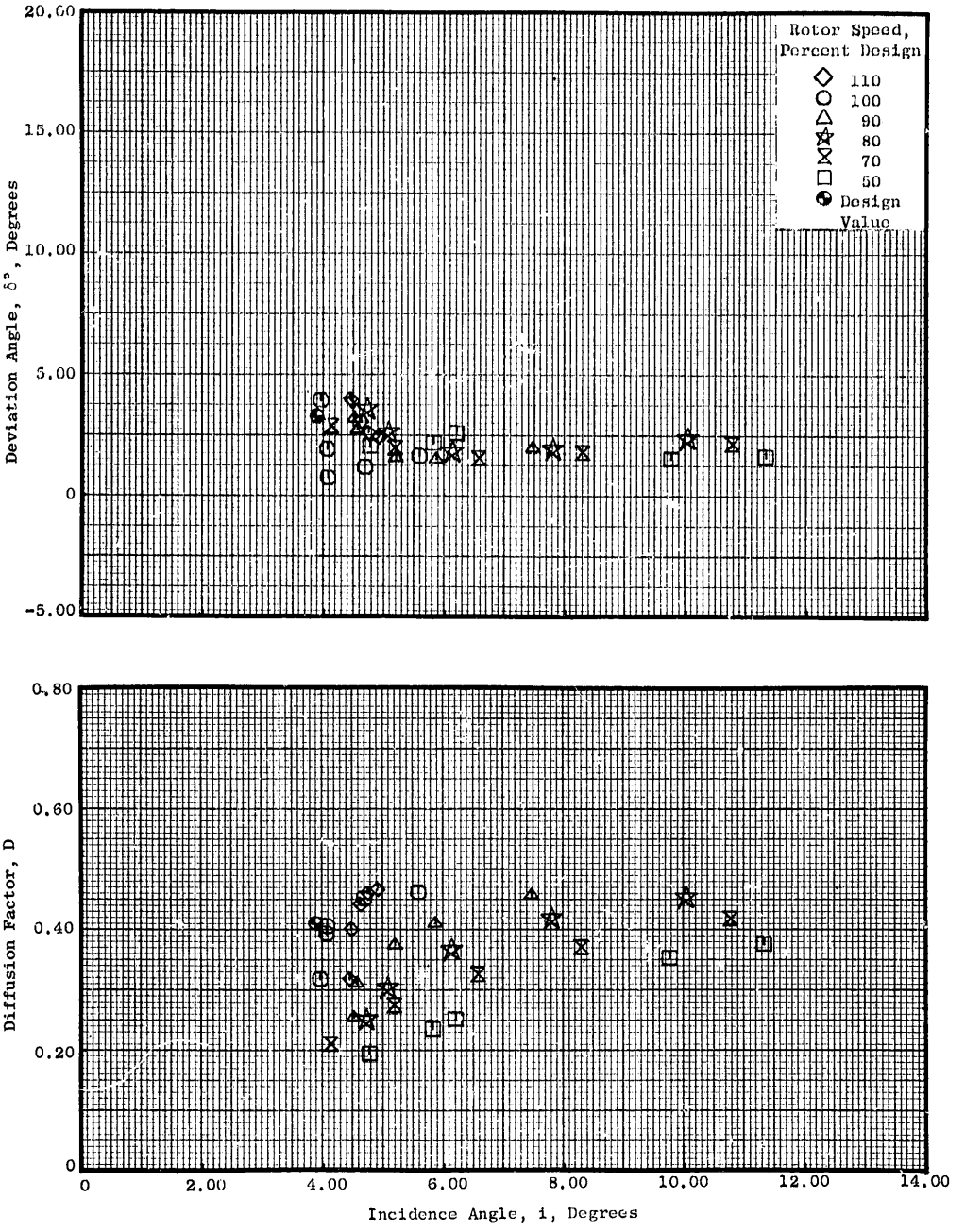

(c) 30% Immersion from Tip (Concluded)

Figure 21. Rotor Blade Element Data for IGV/Stator Schedule 0°/0°; Undistorted Inlet Flow (Continued).

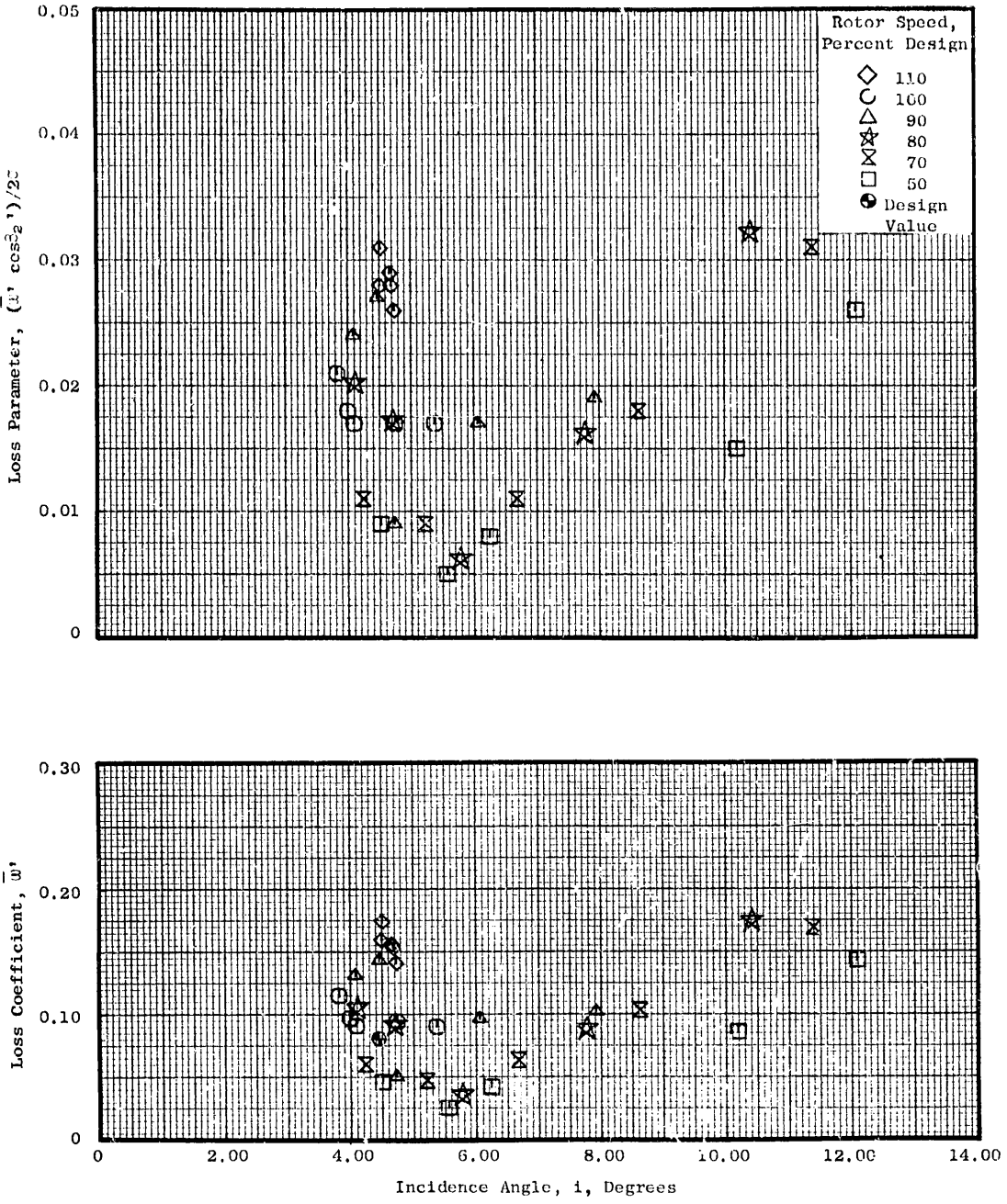

(d) 50% Immersion from Tip

Figure 21. Rotor Blade Element Data for IGV/Stator Schedule 0°/0°; Undistorted Inlet Flow (Continued).

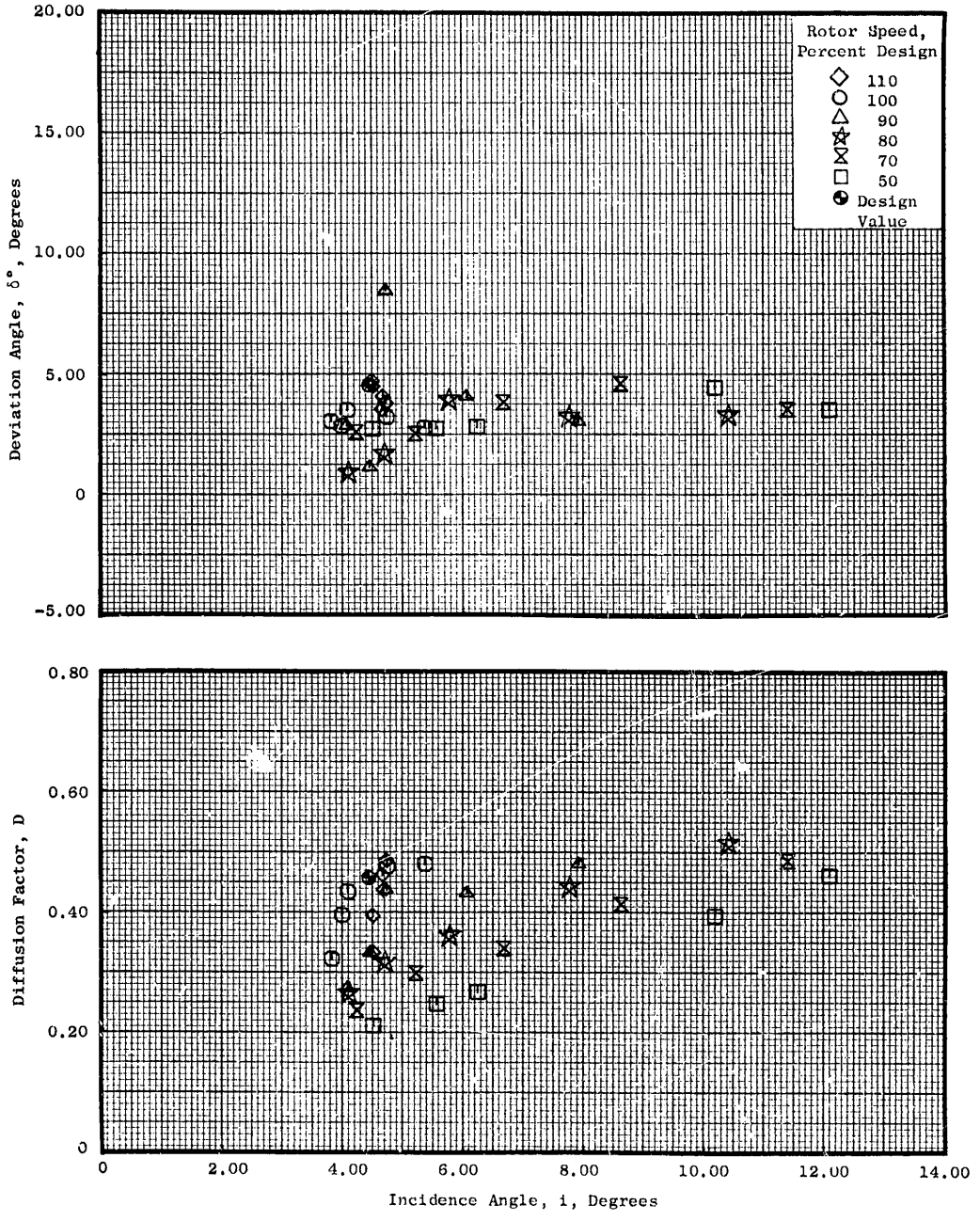

(d) 50% Immersion from Tip (Concluded)

Figure 21. Rotor Blade Element Data for IGV/Stator Schedule 0°/0°; Undistorted Inlet Flow (Continued).

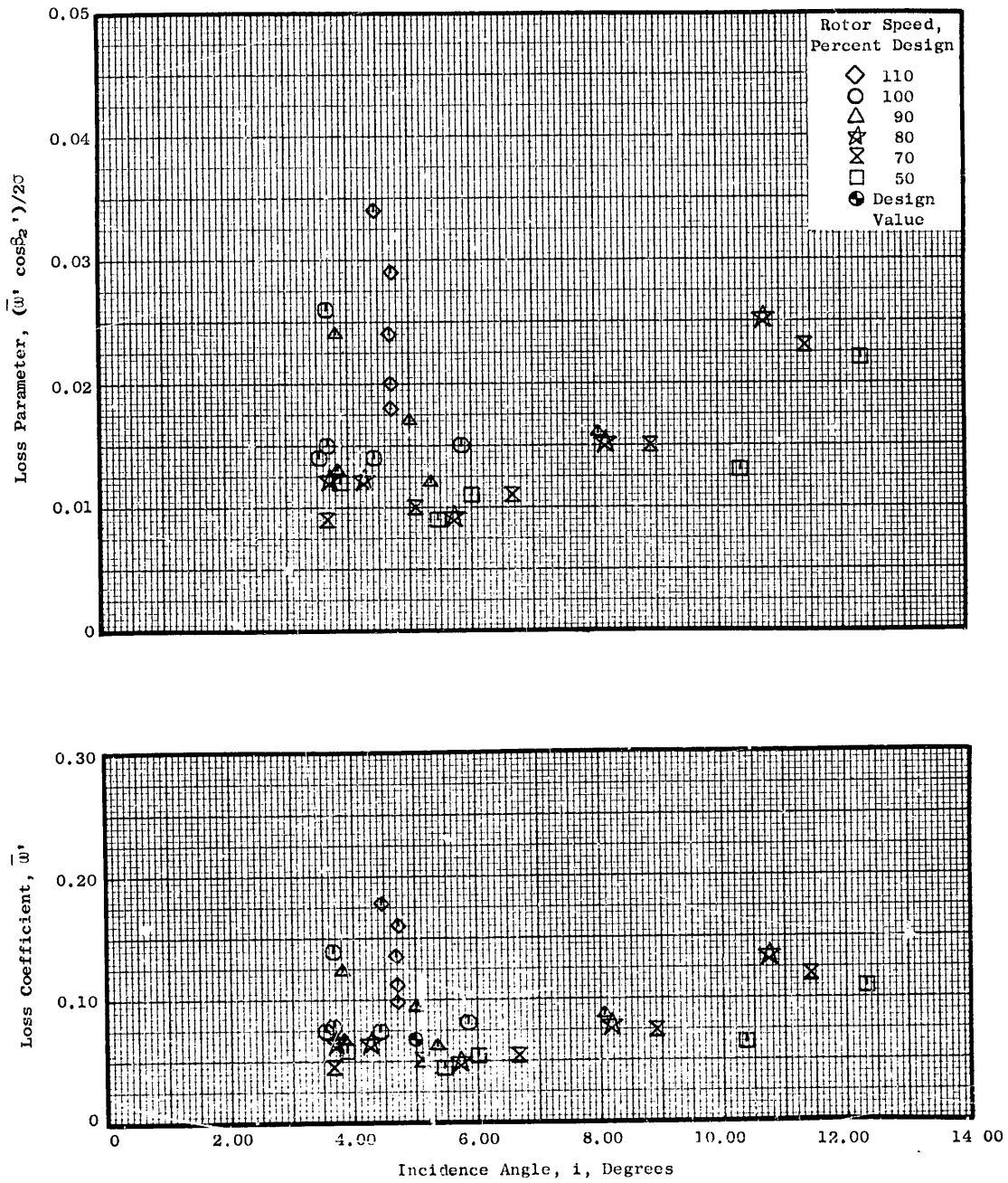

(e) 70% Immersion from Tip

Figure 21. Rotor Blade Element Data for IGV/Stator Schedule 0°/0°; Undistorted Inlet Flow (Continued).

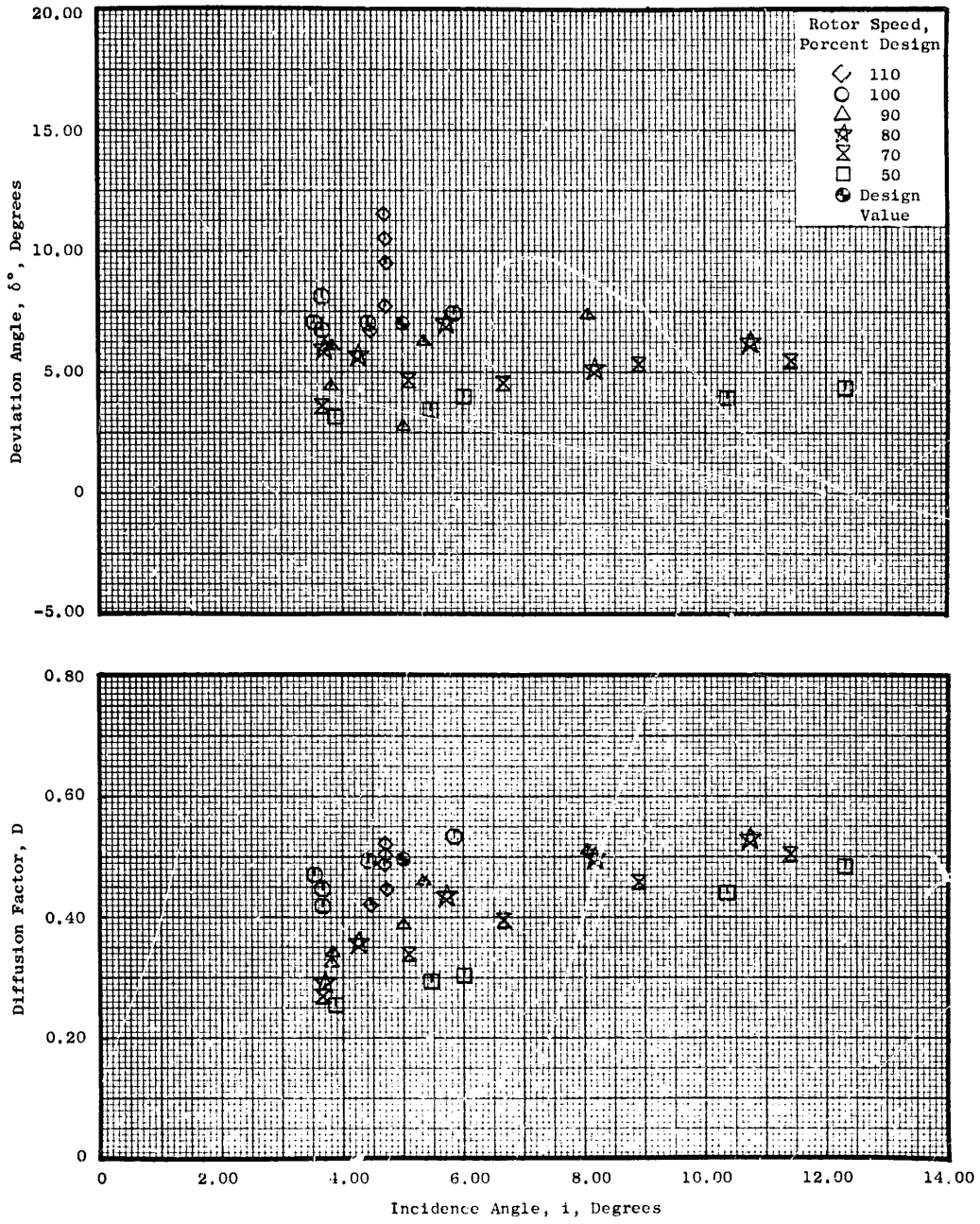

(e) 70% Immersion from Tip (Concluded)

Figure 21. Rotor Blade Element Data for IGV/Stator Schedule 0°/0°; Undistorted Inlet Flow (Continued).

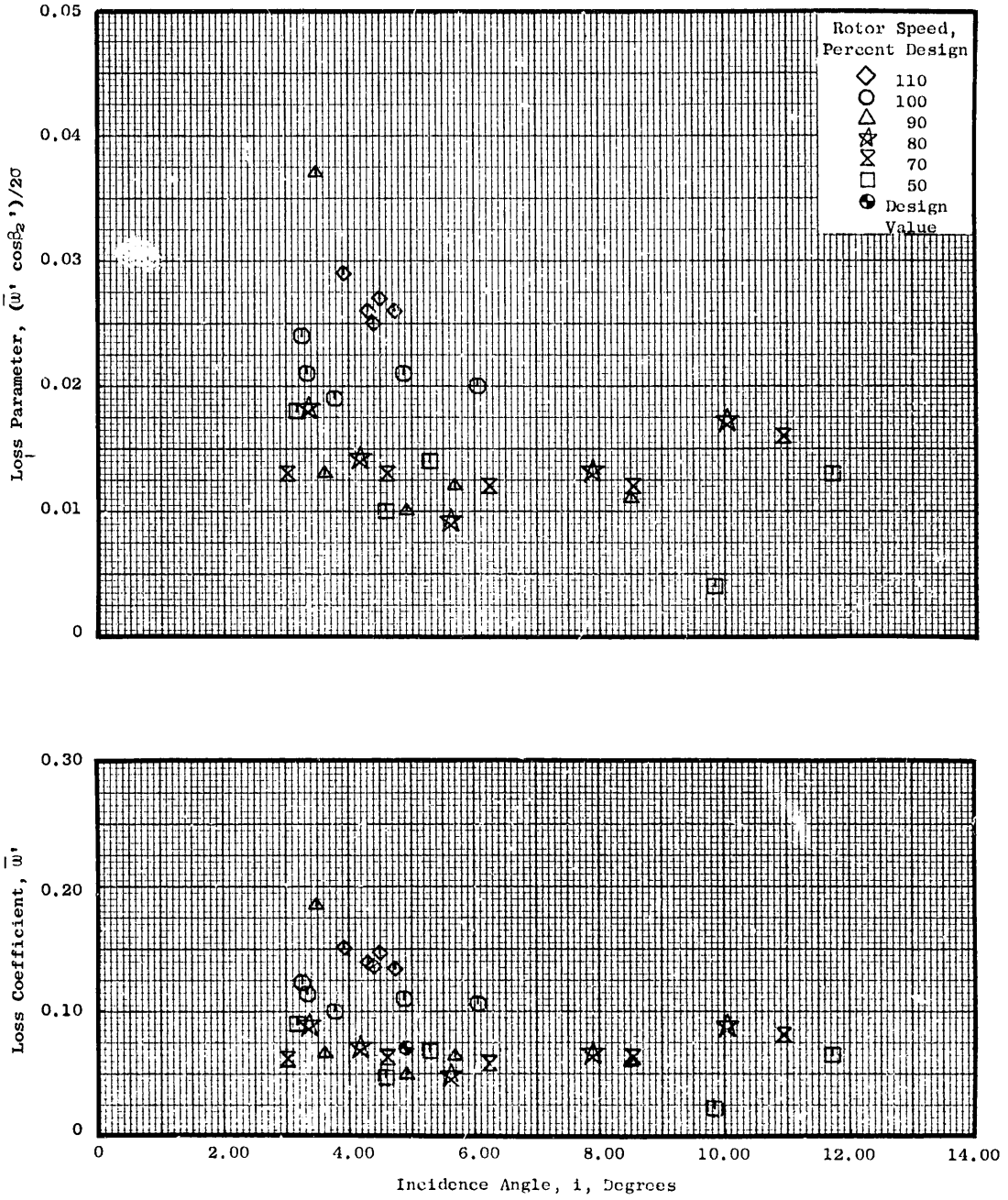

(f) 90% Immersion from Tip

Figure 21. Rotor Blade Element Data for IGV/Stator Schedule 0°/0°; Undistorted Inlet Flow (Continued).

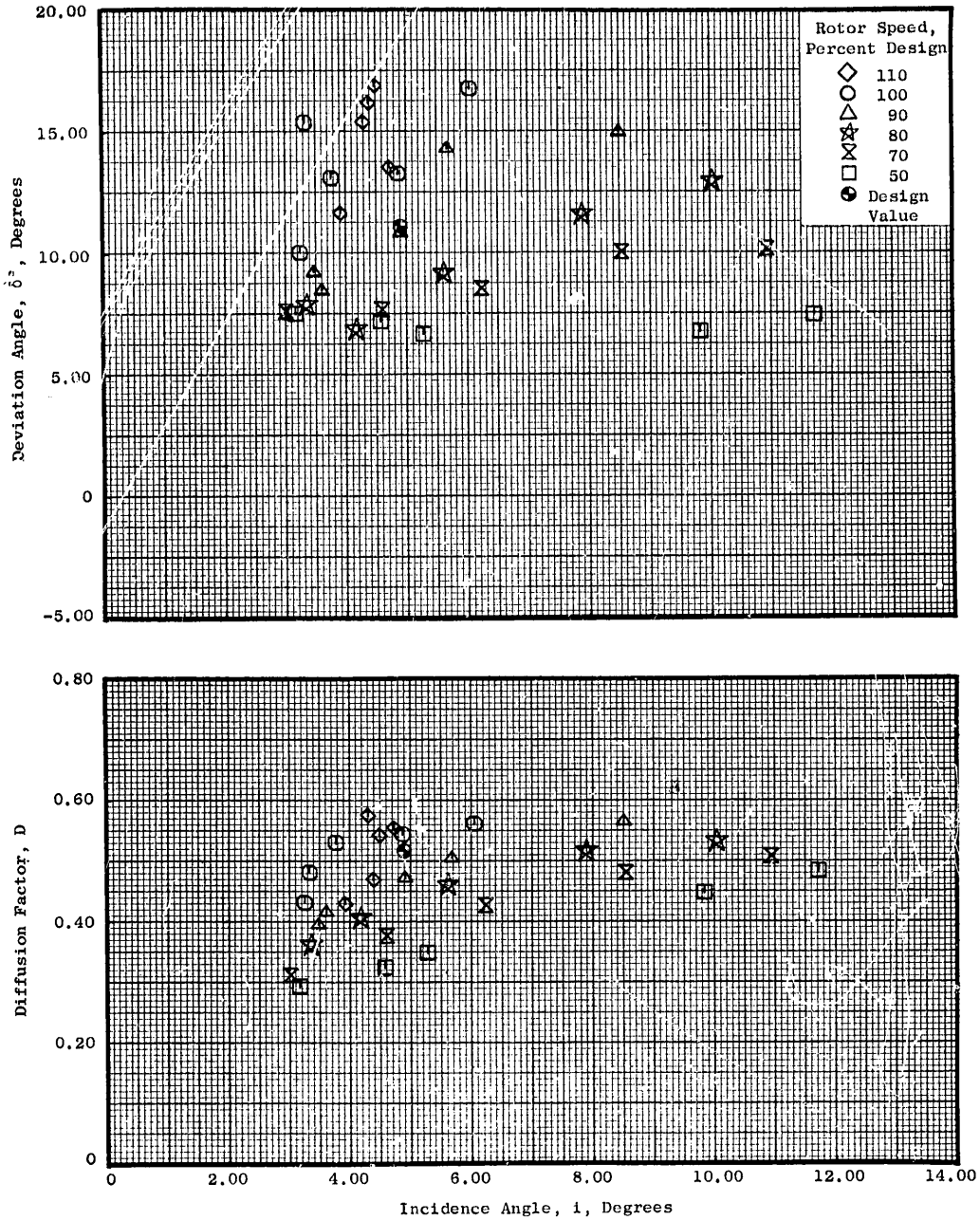

(f) 90% Immersion from Tip (Concluded)

Figure 21. Rotor Blade Element Data for IGV/Stator Schedule 0°/0°; Undistorted Inlet Flow (Continued).

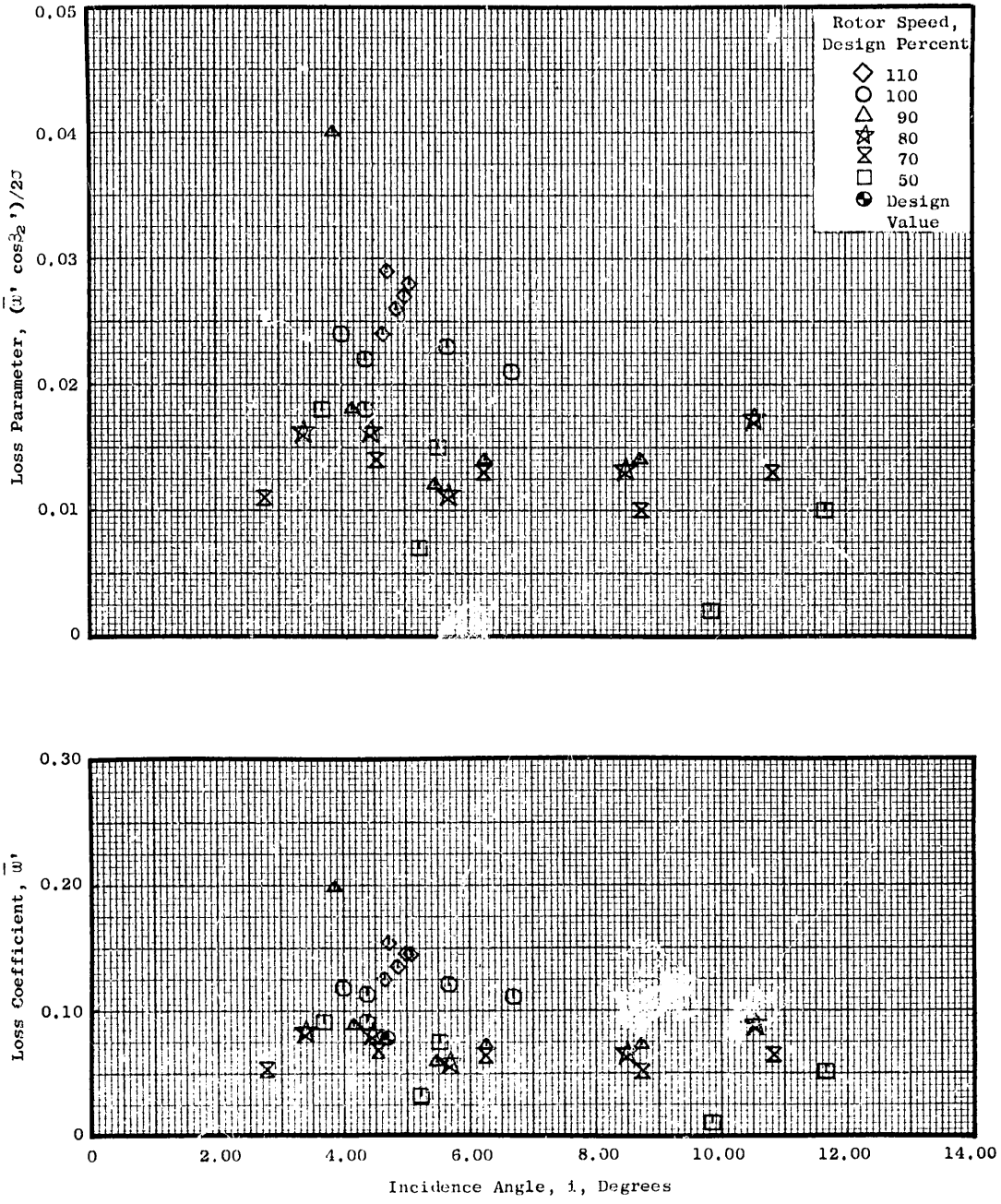

(g) 95% Immersion from Tip

Figure 21. Rotor Blade Element Data for IGV/Stator Schedule 0°/0°; Undistorted Inlet Flow (Continued).

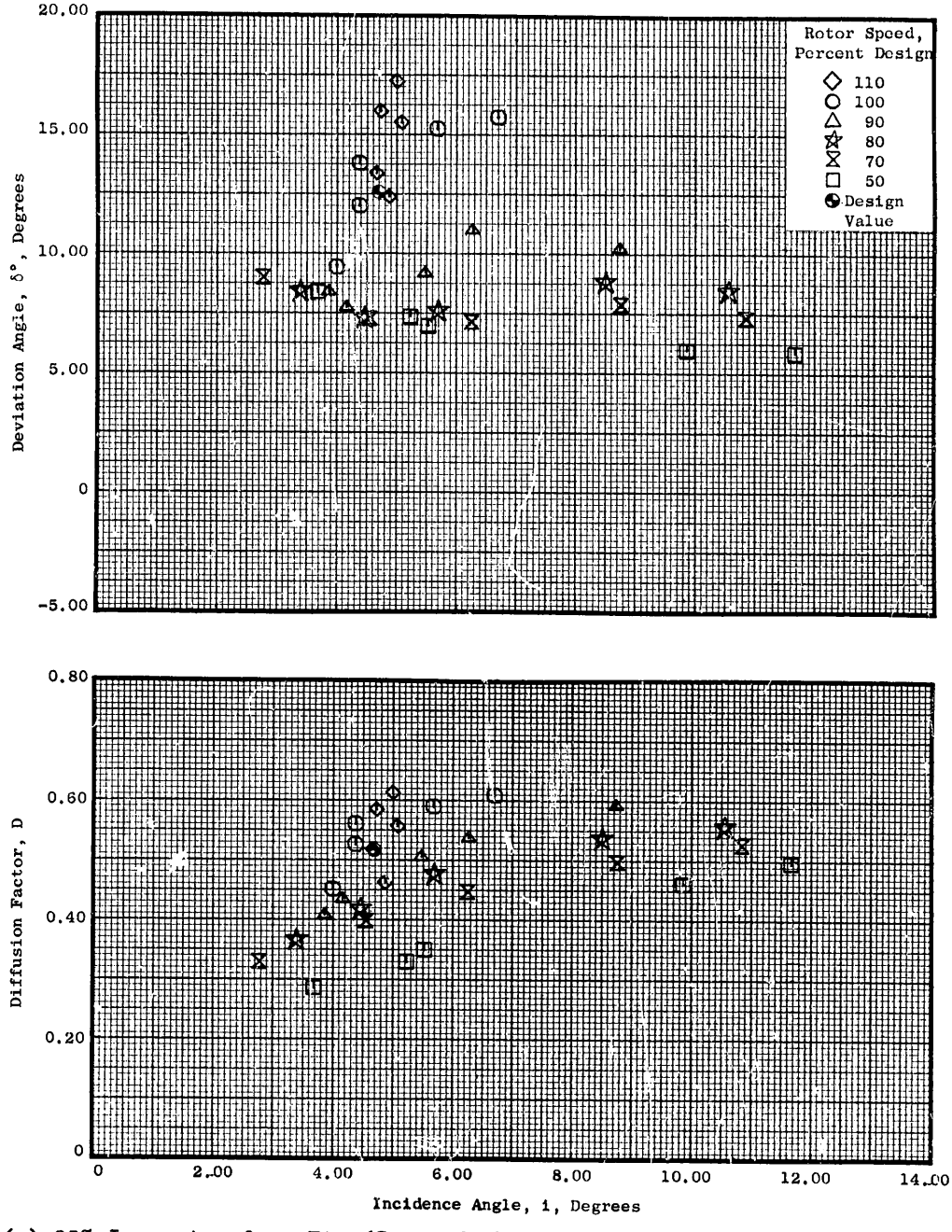

(g) 95% Immersion from Tip (Concluded)

Figure 21. Rotor Blade Element Data for IGV/Stator Schedule 0°/0°; Undistorted Inlet Flow (Concluded).

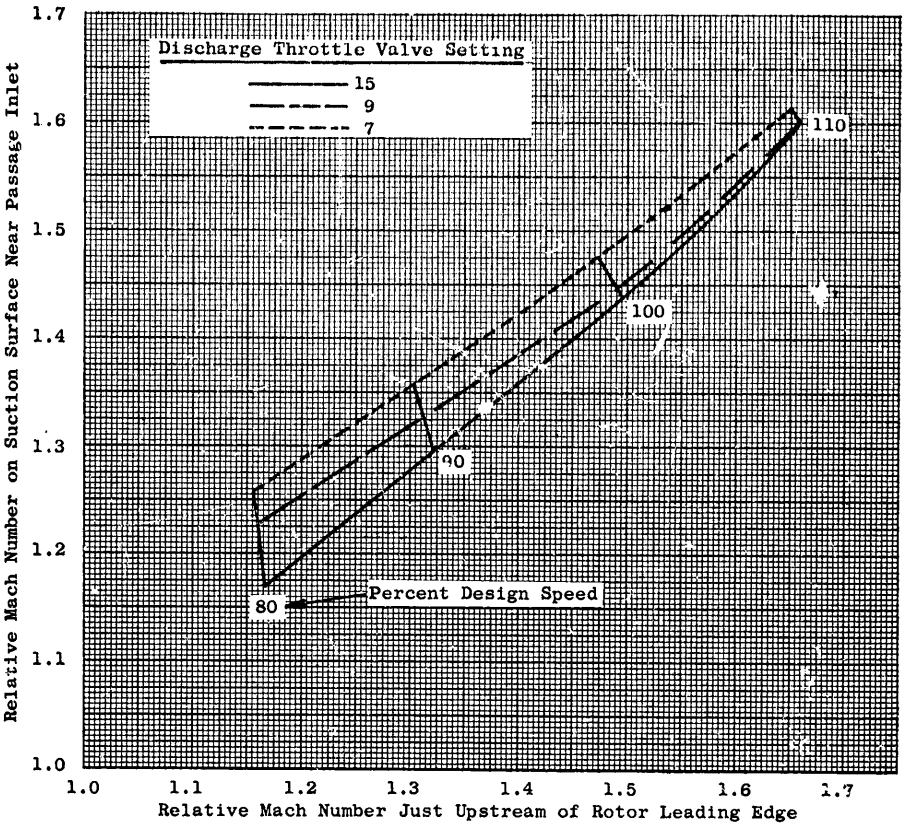

(a) Determination of Relative Mach Number on Suction Surface

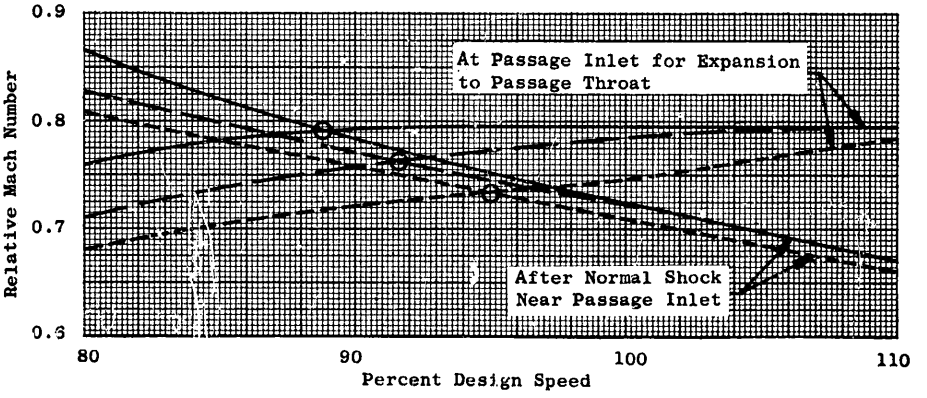

(b) Conditions for Establishment of Oblique Shock Structure at Leading Edge for Ratio of Passage Throat Area to Inlet Area of 0.96

Figure 22. Rotor Cascade Starting Analysis (Based on Streamline at 10% Immersion from Tip).

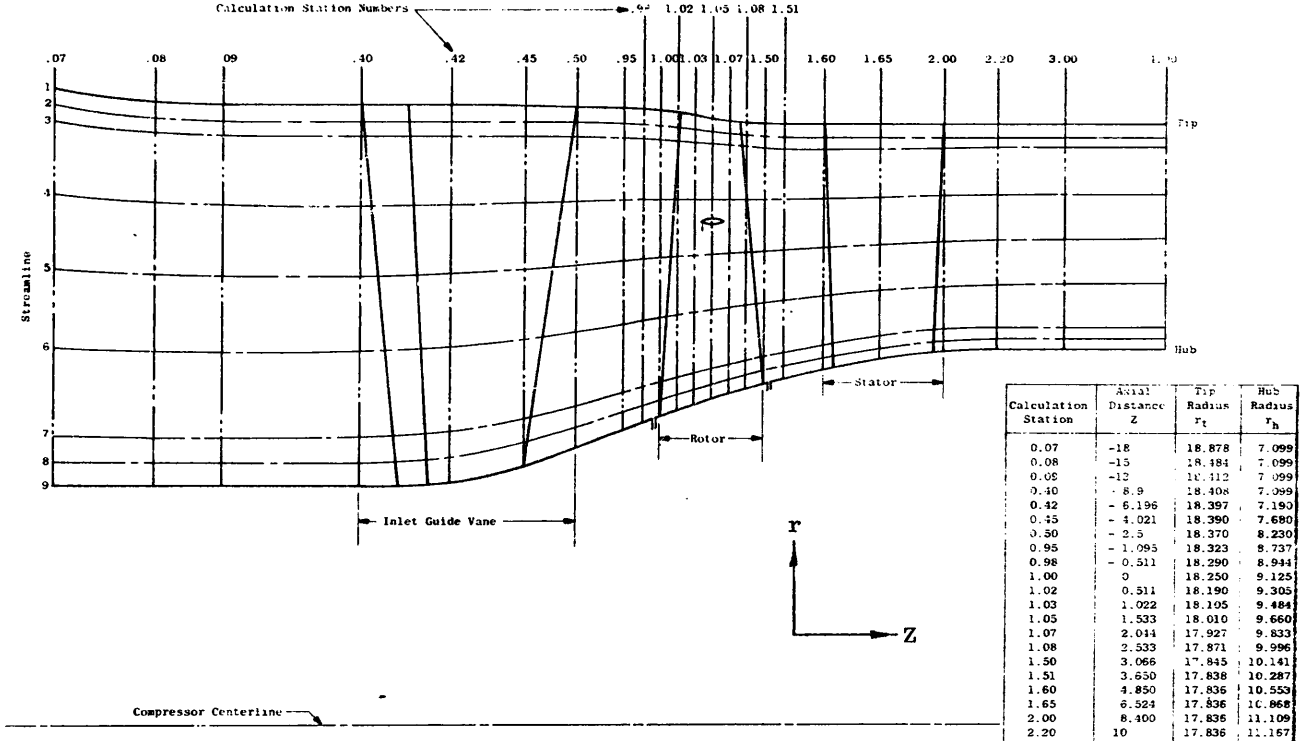

Calculation Station	Axial Distance Z	Tip Radius r_t	Hub Radius r_h
0.07	-18	18.878	7.099
0.08	-15	18.484	7.099
0.09	-12	18.112	7.099
0.40	- 8.9	18.408	7.099
0.42	- 6.196	18.397	7.190
0.45	- 4.021	18.390	7.680
0.50	- 2.5	18.370	8.230
0.95	- 1.095	18.323	8.737
0.98	- 0.511	18.290	8.944
1.00	0	18.250	9.125
1.02	0.511	18.190	9.305
1.03	1.022	18.105	9.484
1.05	1.533	18.010	9.660
1.07	2.044	17.927	9.833
1.08	2.533	17.871	9.996
1.50	3.066	17.845	10.141
1.51	3.650	17.838	10.287
1.60	4.850	17.836	10.553
1.65	6.524	17.836	10.868
2.00	8.400	17.836	11.109
2.20	10	17.836	11.167
3.00	12	17.836	11.170
4.00	15	17.836	11.170

Figure 23. Compressor Flowpath.

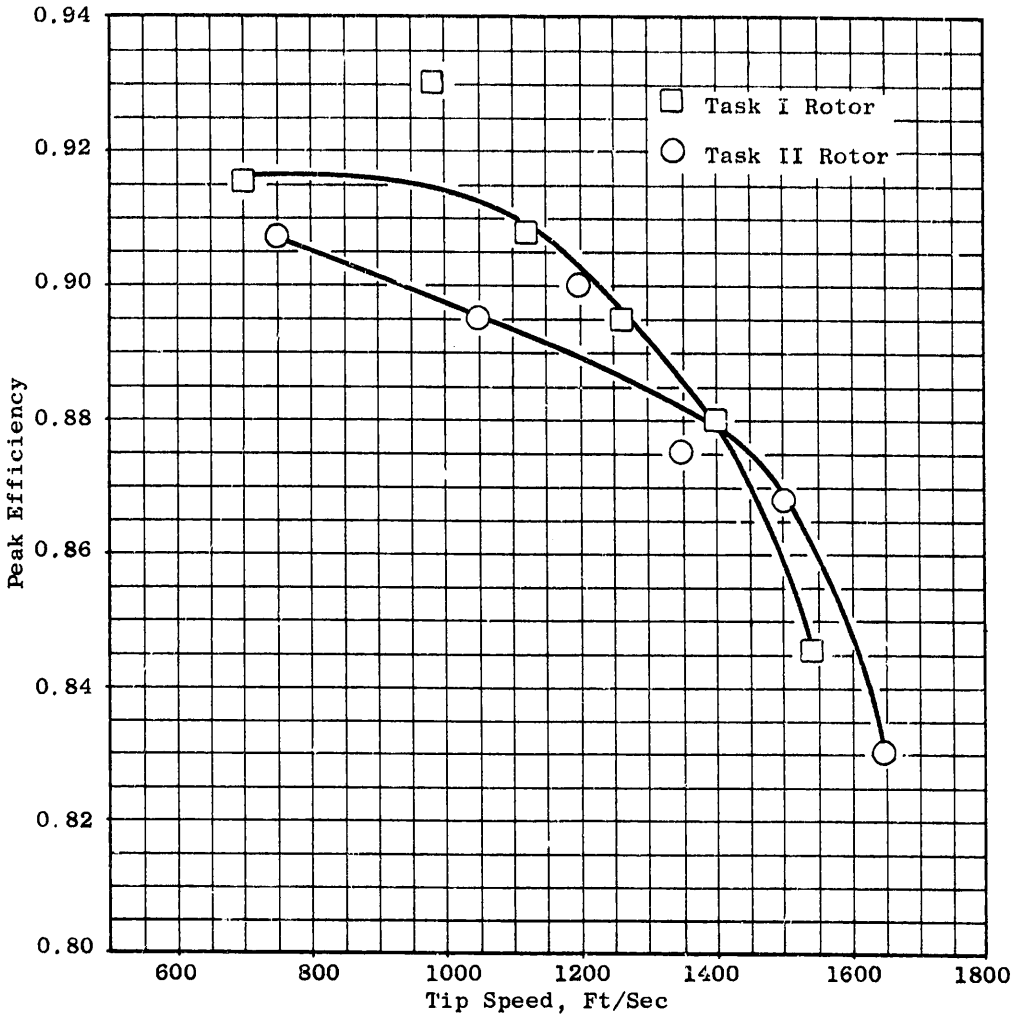

(a) Peak Efficiency Versus Tip Speed

Figure 24. Comparisons Between Task II Rotor at 0°/0° Vane Schedule and Task I Rotor; Undistorted Inlet Flow.

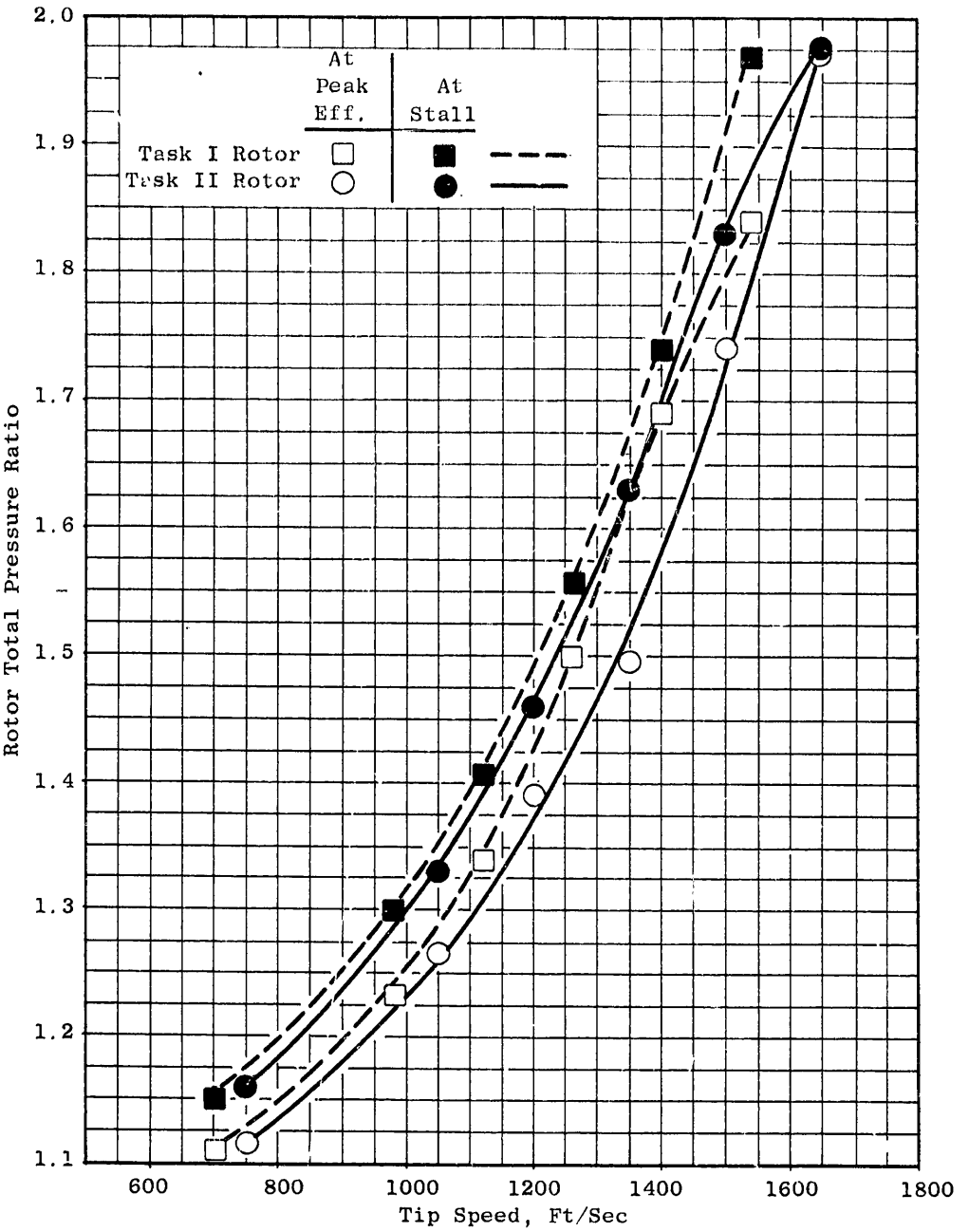

(b) Pressure Ratio at Stall and at Peak Efficiency Versus Tip Speed

Figure 24. Comparisons Between Task II Rotor at 0°/0° Vane Schedule and Task I Rotor; Undisorted Inlet Flow (Continued).

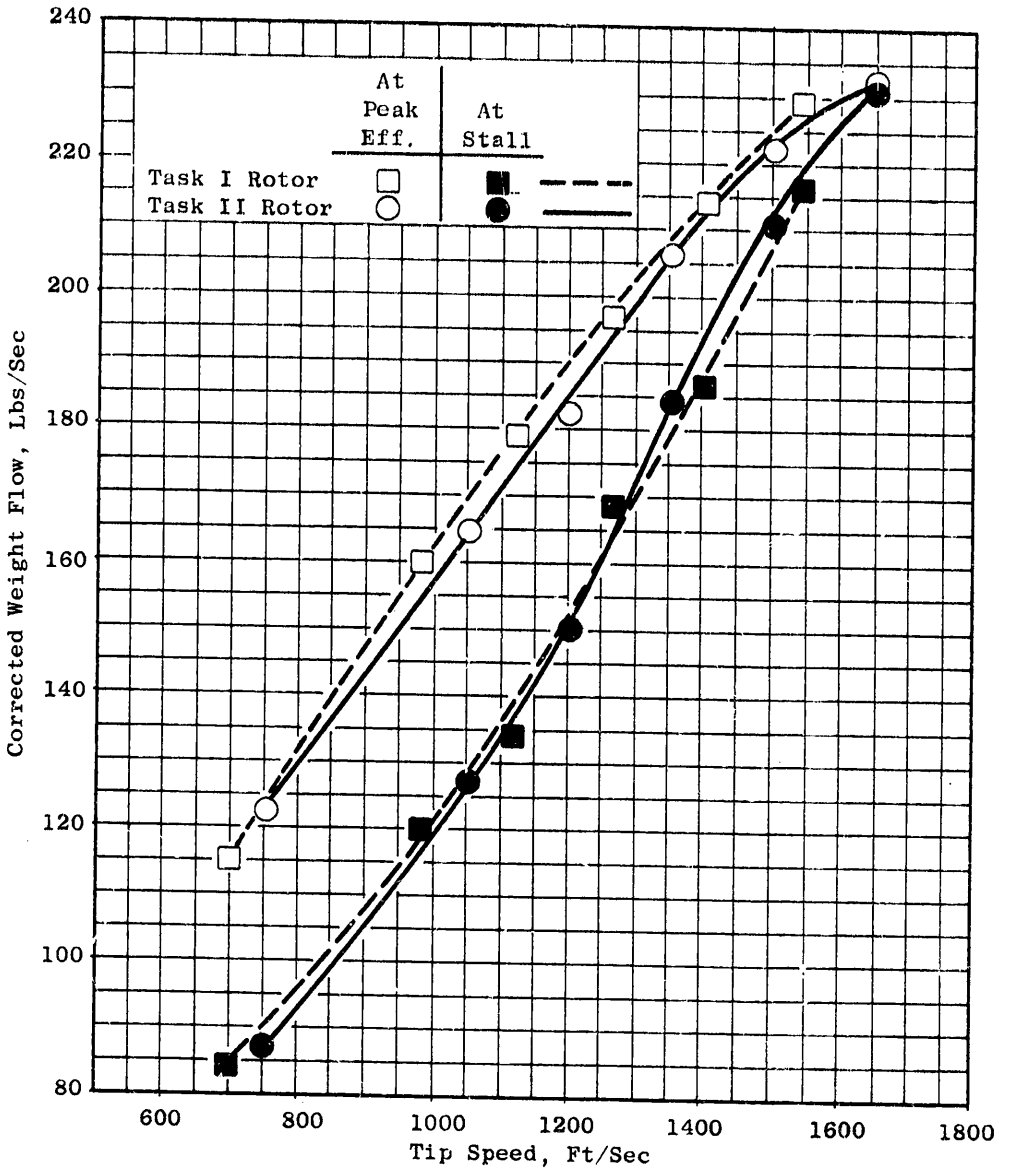

(c) Weight Flow at Stall and at Peak Efficiency Versus Tip Speed

Figure 24. Comparisons Between Task II Rotor at 0°/0° Vane Schedule and Task I Rotor; Undistorted Inlet Flow (Concluded).

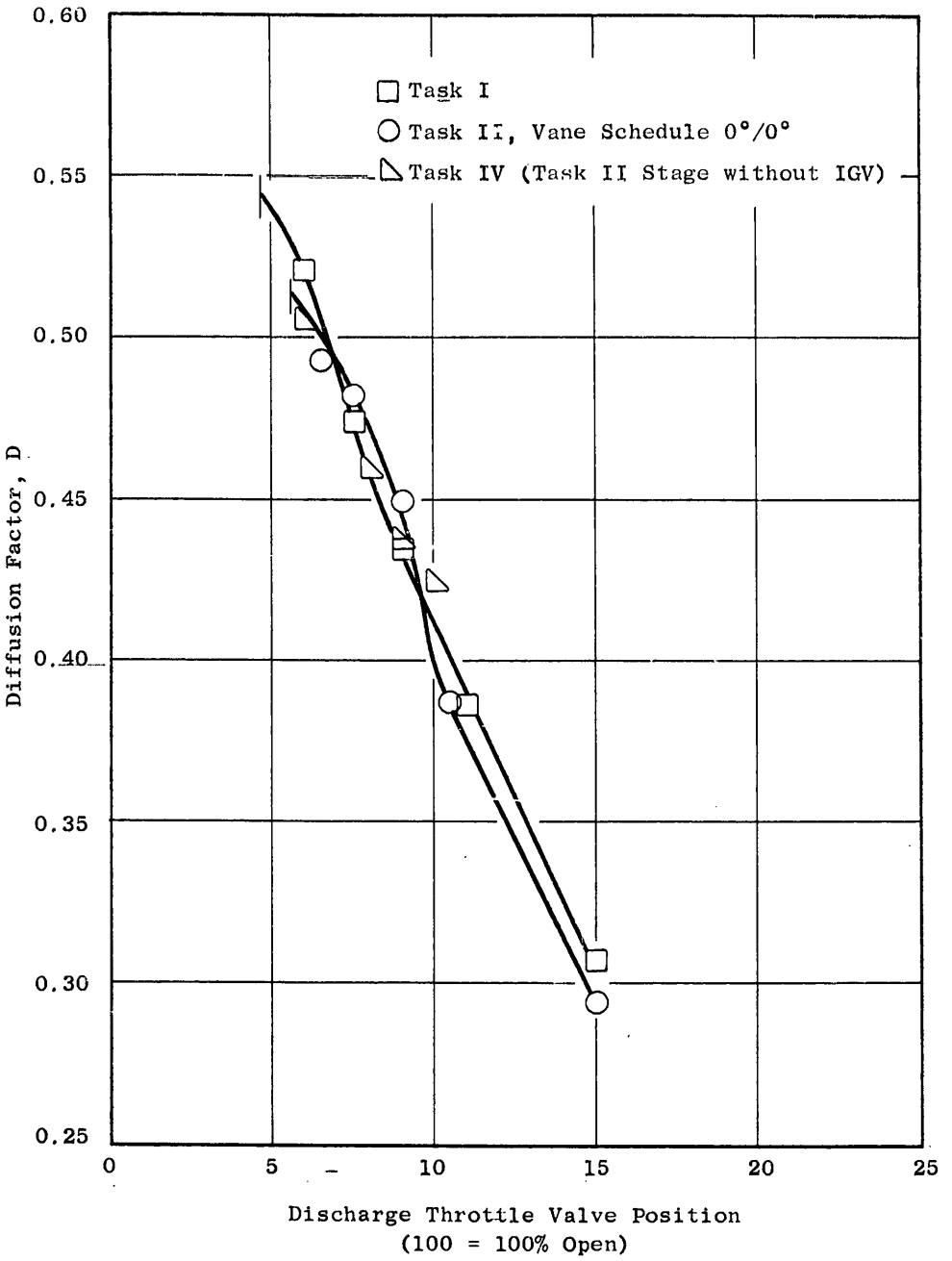

(a) 5% Immersion from Tip

Figure 25. Variation of Task I and Task II Rotor Diffusion Factors with Throttle Valve Setting; 100% Speed, Undistorted Inlet Flow

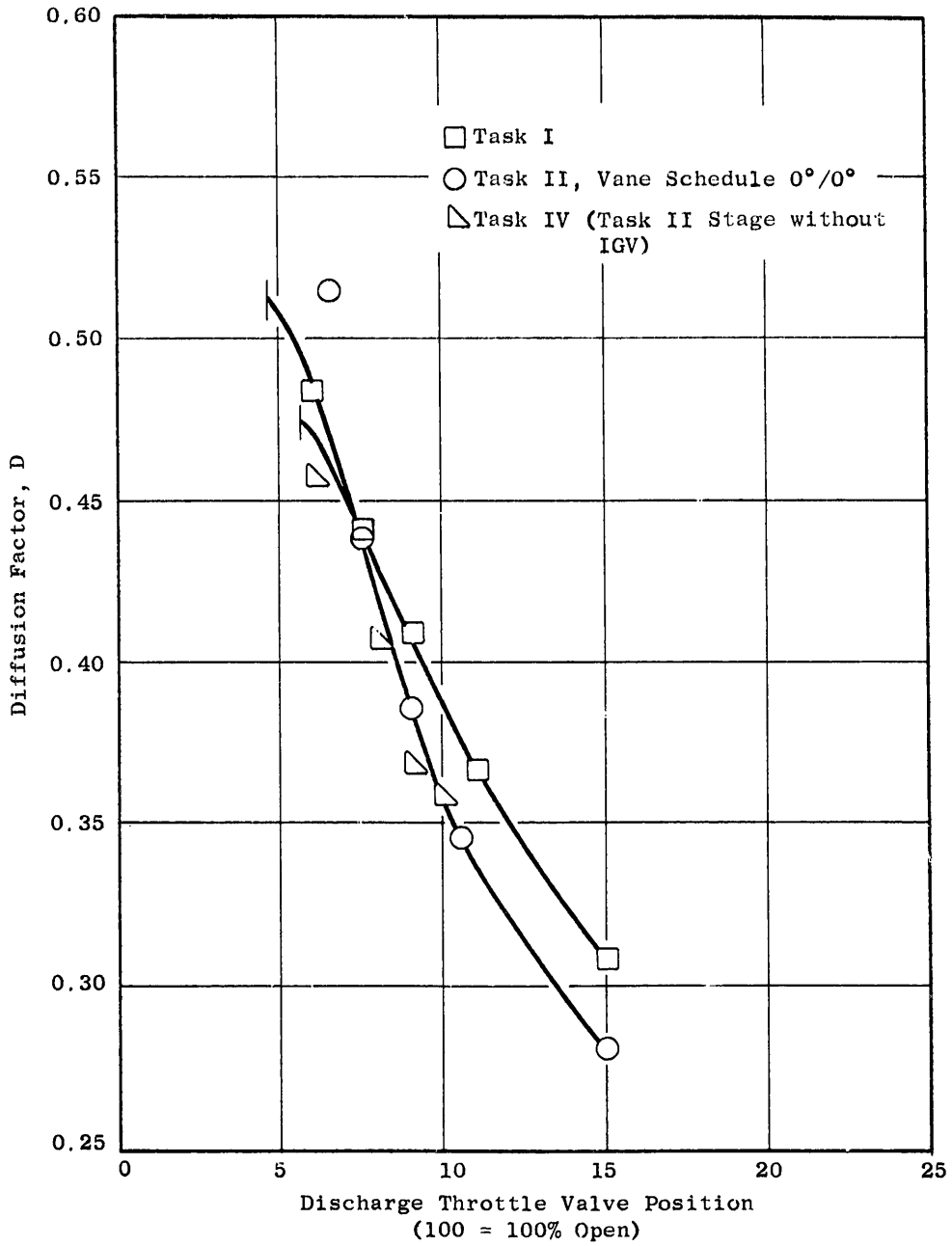

(b) 10% Immersion from Tip

Figure 25. Variation of Task I and Task II Rotor Diffusion Factors with Throttle Valve Setting; 100% Speed, Undistorted Inlet Flow (Continued).

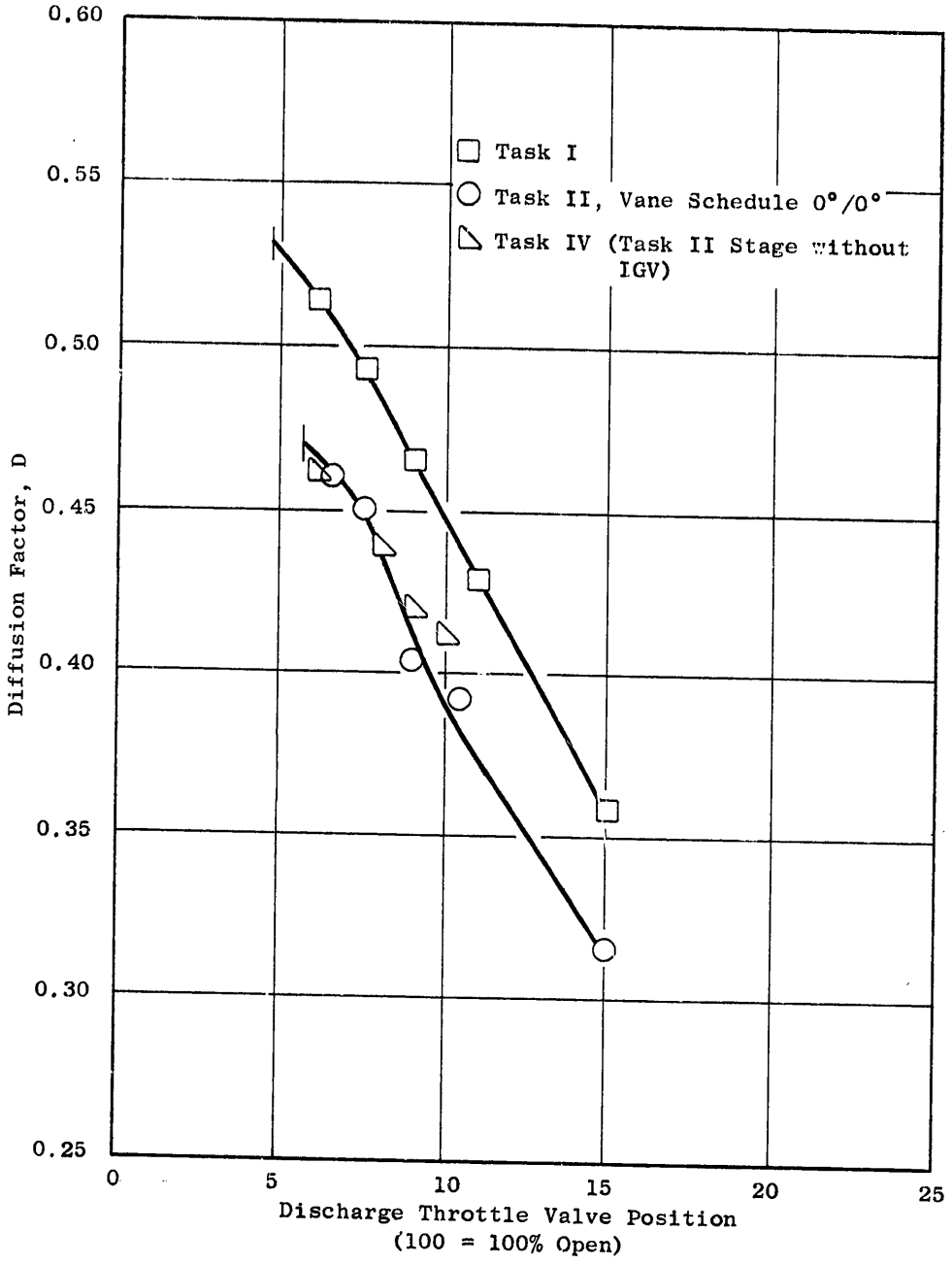

(c) 30% Immersion from Tip

Figure 25. Variation of Task I and Task II Rotor Diffusion Factors with Throttle Valve Setting; 100% Speed, Undistorted Inlet Flow (Continued).

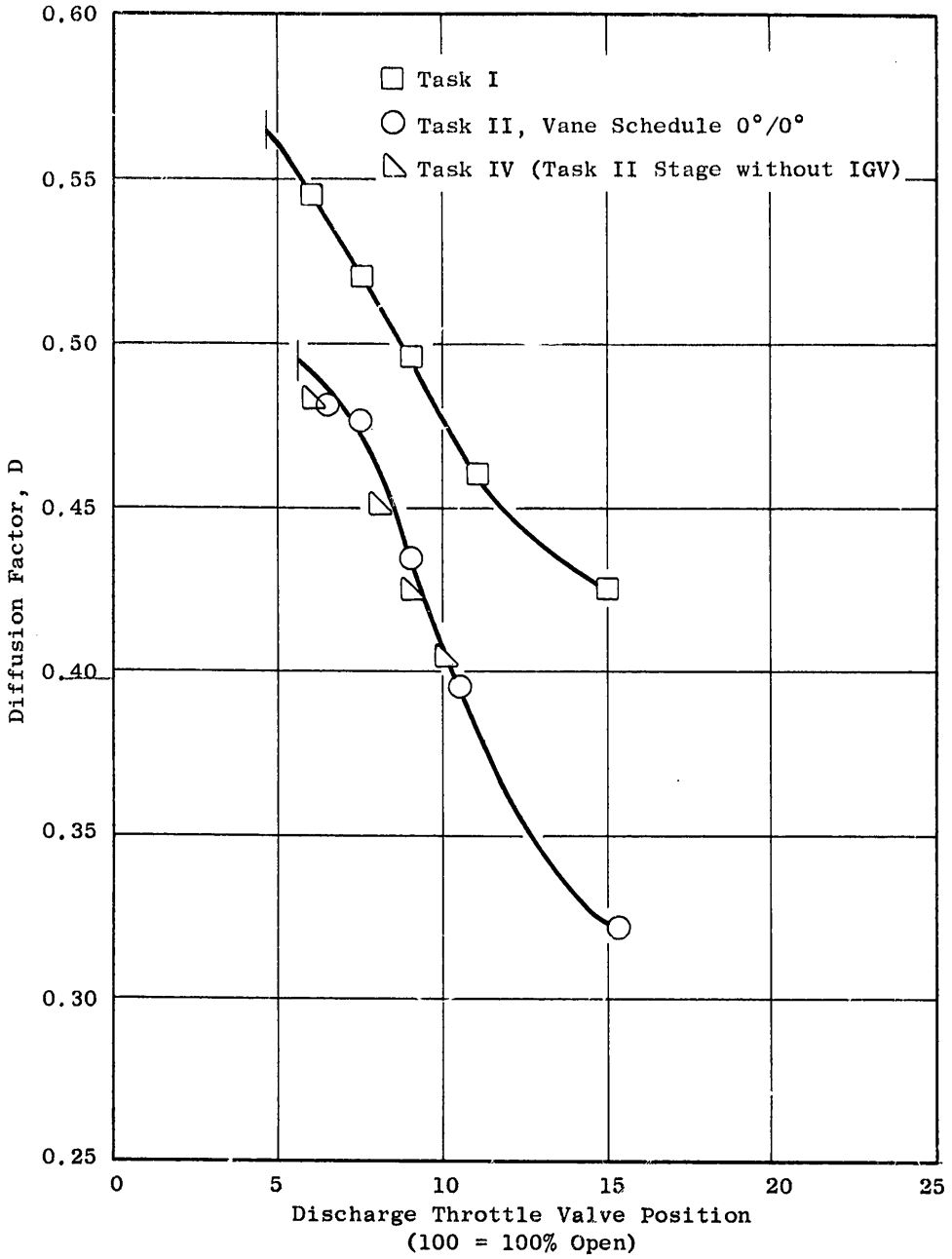

(d) 50% Immersion from Tip

Figure 25. Variation of Task I and Task II Rotor Diffusion Factors with Throttle Valve Setting; 100% Speed, Undistorted Inlet Flow (Continued).

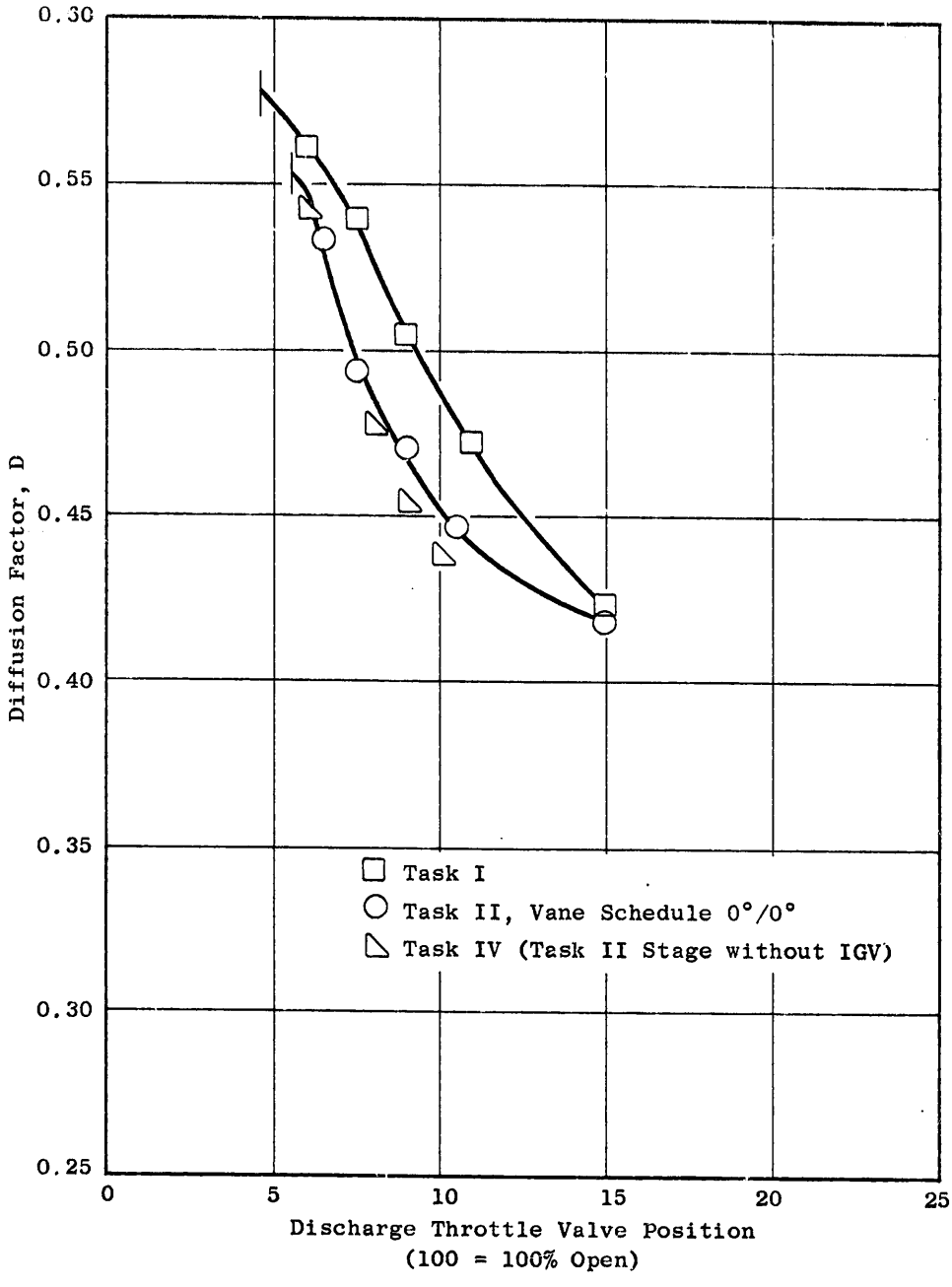

(e) 70% Immersion from Tip

Figure 25. Variation of Task I and Task II Rotor Diffusion Factors with Throttle Valve Setting; 100% Speed, Undistorted Inlet Flow (Continued).

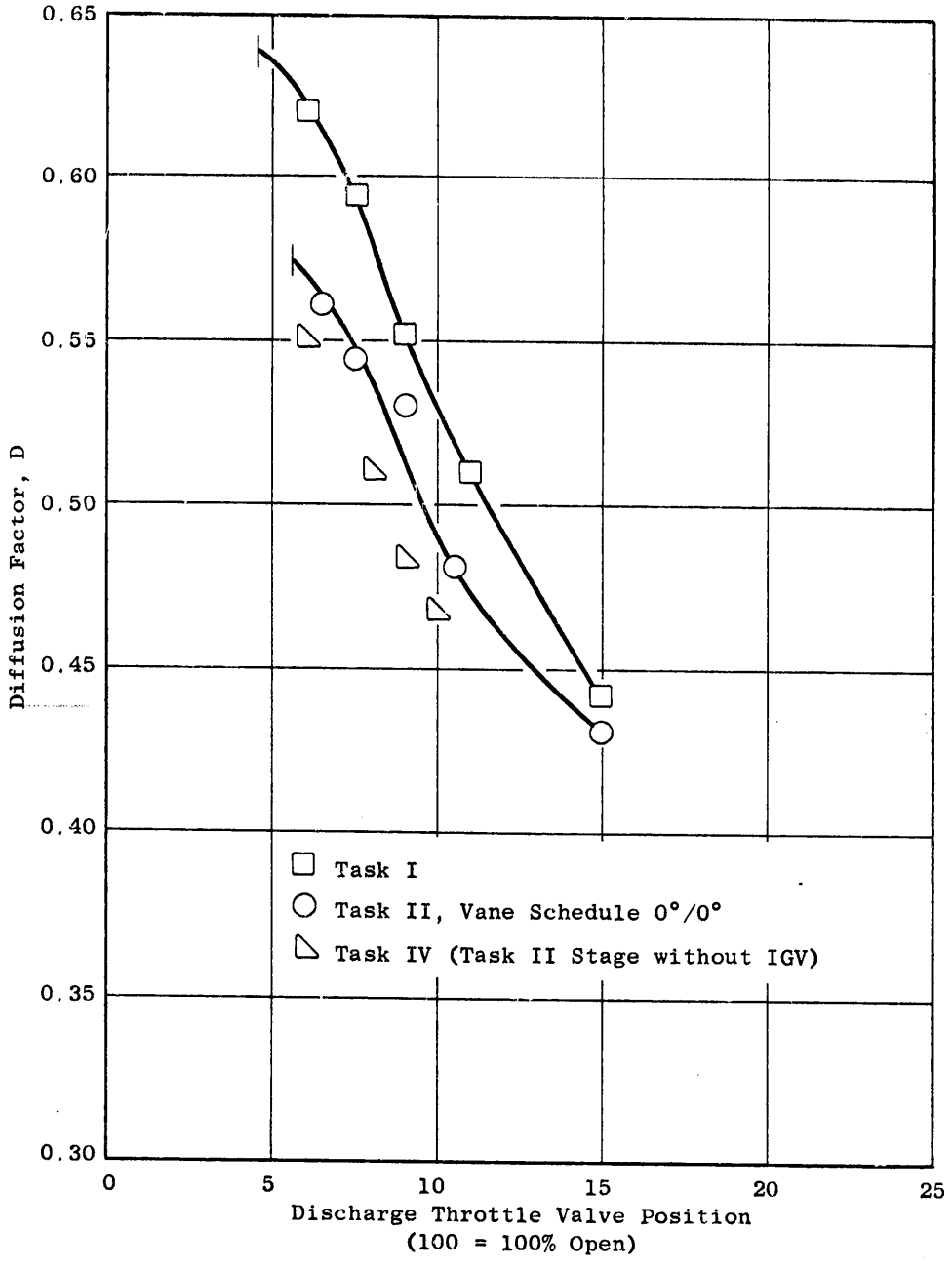

(f) 90% Immersion from Tip

Figure 25. Variation of Task I and Task II Rotor Diffusion Factors with Throttle Valve Setting; 100% Speed, Undistorted Inlet Flow (Continued).

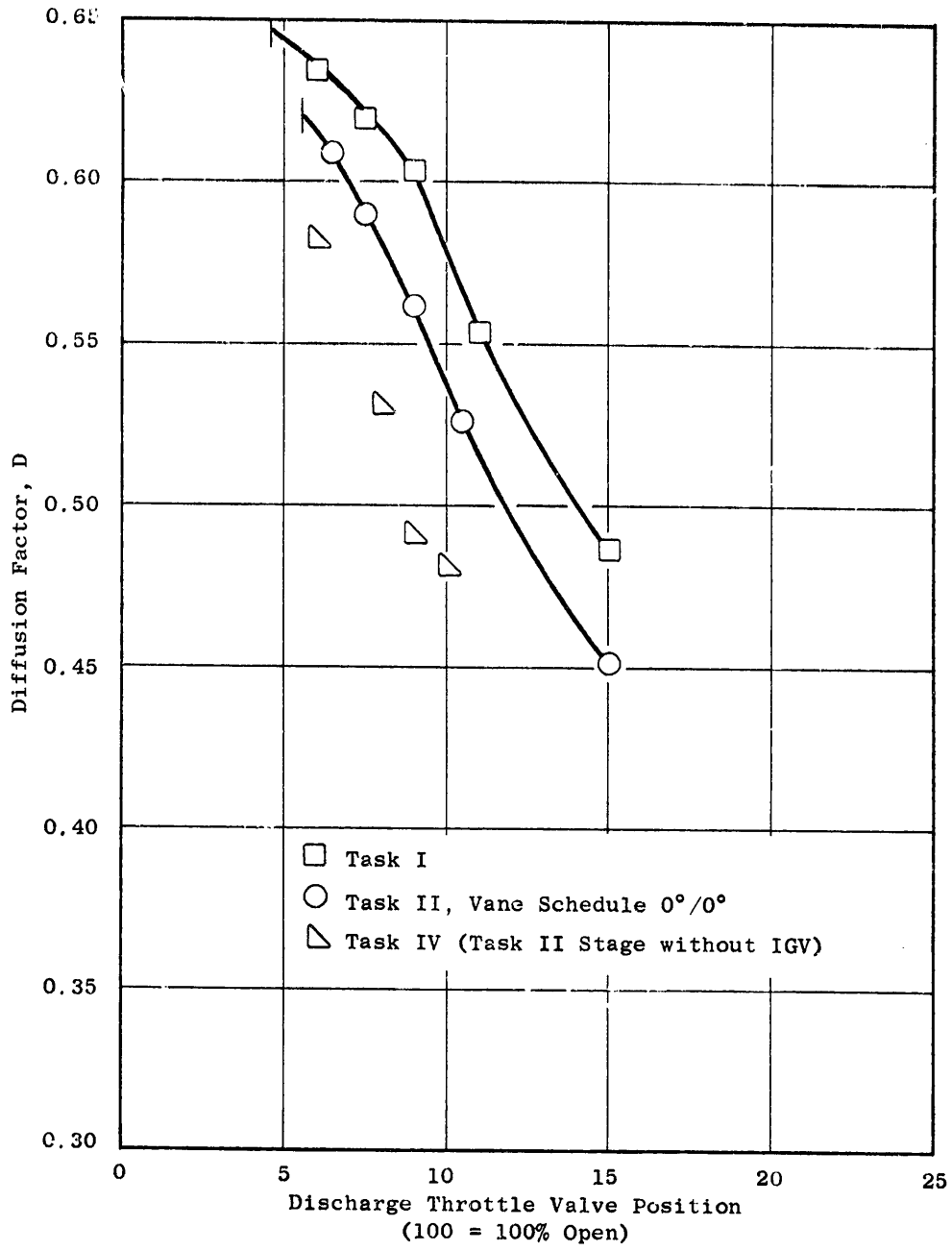

(g) 95% Immersion from Tip

Figure 25. Variation of Task I and Task II Rotor Diffusion Factors with Throttle Valve Setting; 100% Speed, Undistorted Inlet Flow (Concluded).

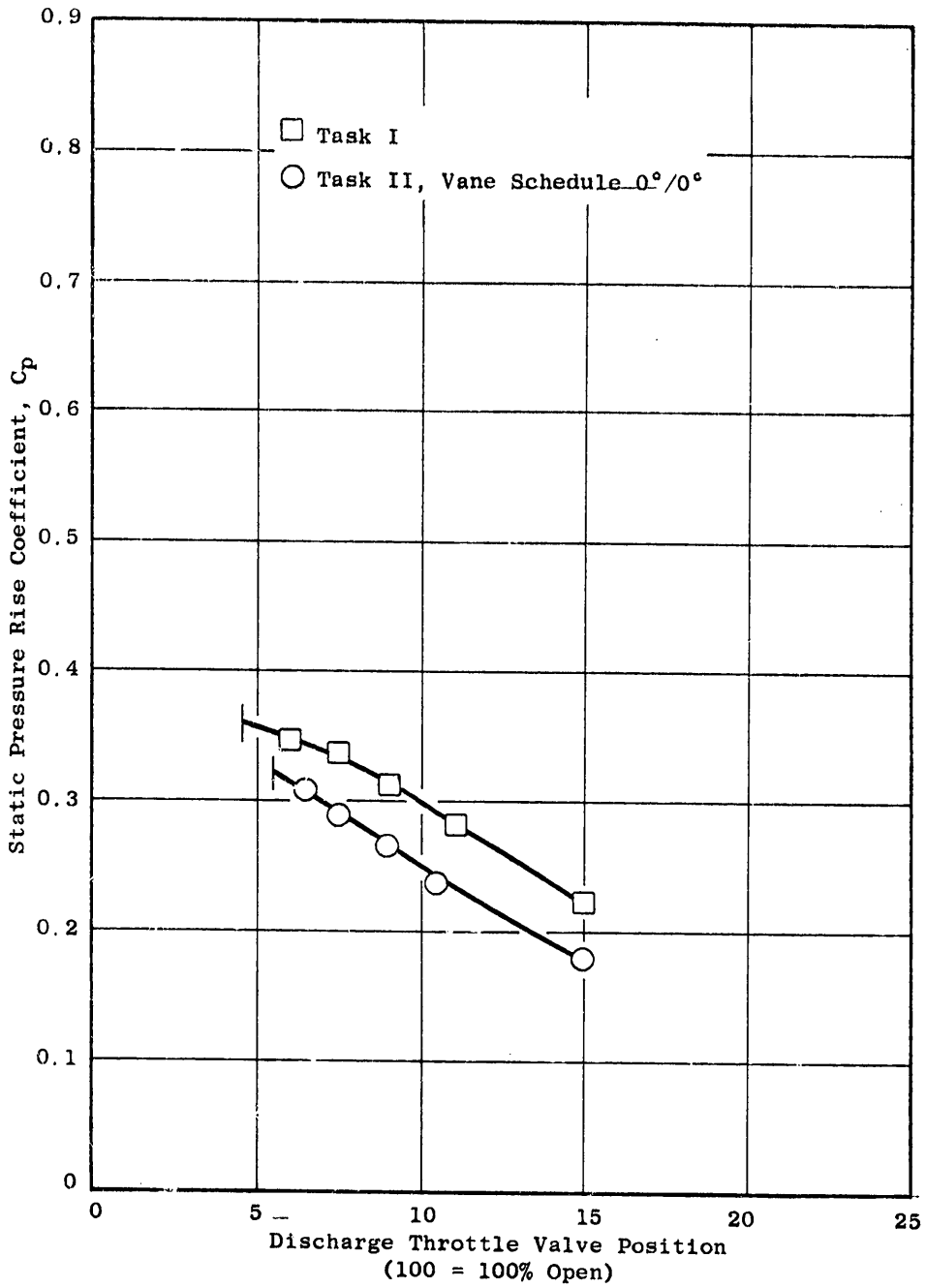

(a) 5% Immersion from Tip

Figure 26. Variation of Task I and Task II Rotor Static Pressure Rise Coefficient with Throttle Valve Setting, 100% Speed, Undistorted Inlet Flow.

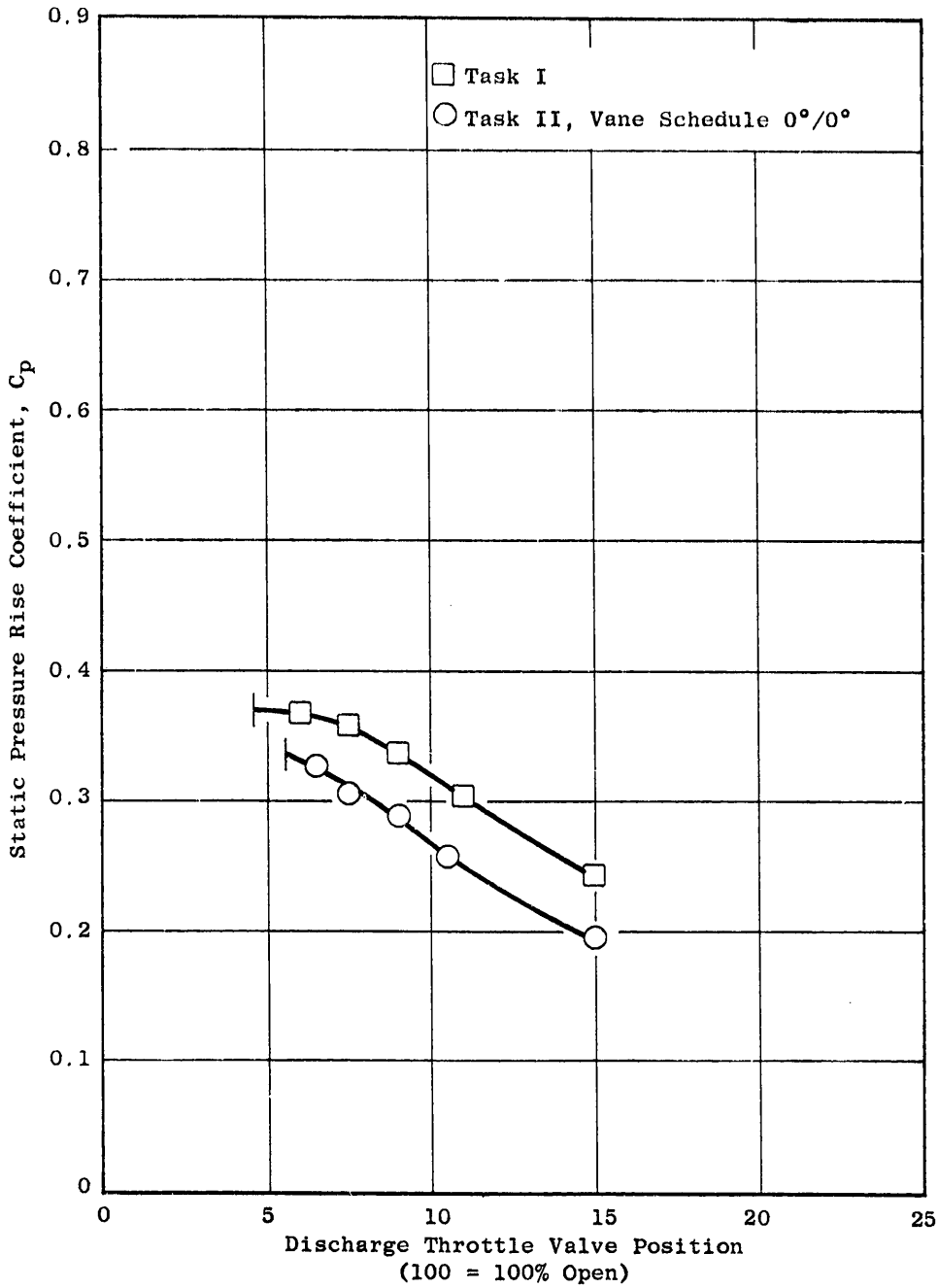

(b) 10% Immersion from Tip

Figure 26. Variation of Task I and Task II Rotor Static Pressure Rise Coefficient with Throttle Valve Setting, 100% Speed, Undistorted Inlet Flow (Continued).

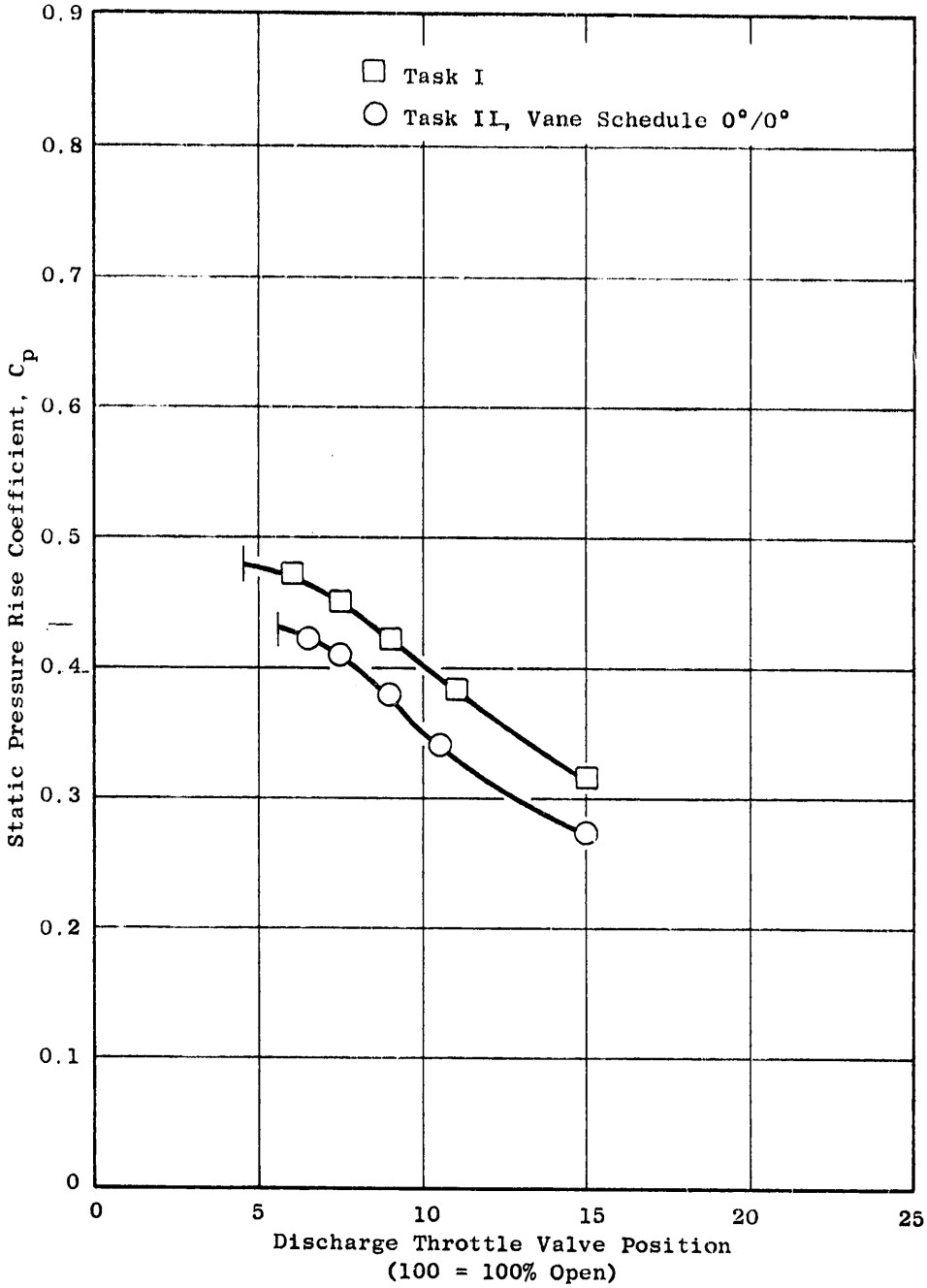

(c) 30% Immersion from Tip

Figure 26. Variation of Task I and Task II Rotor Static Pressure Rise Coefficient with Throttle Valve Setting, 100% Speed, Undistorted Inlet Flow (Continued).

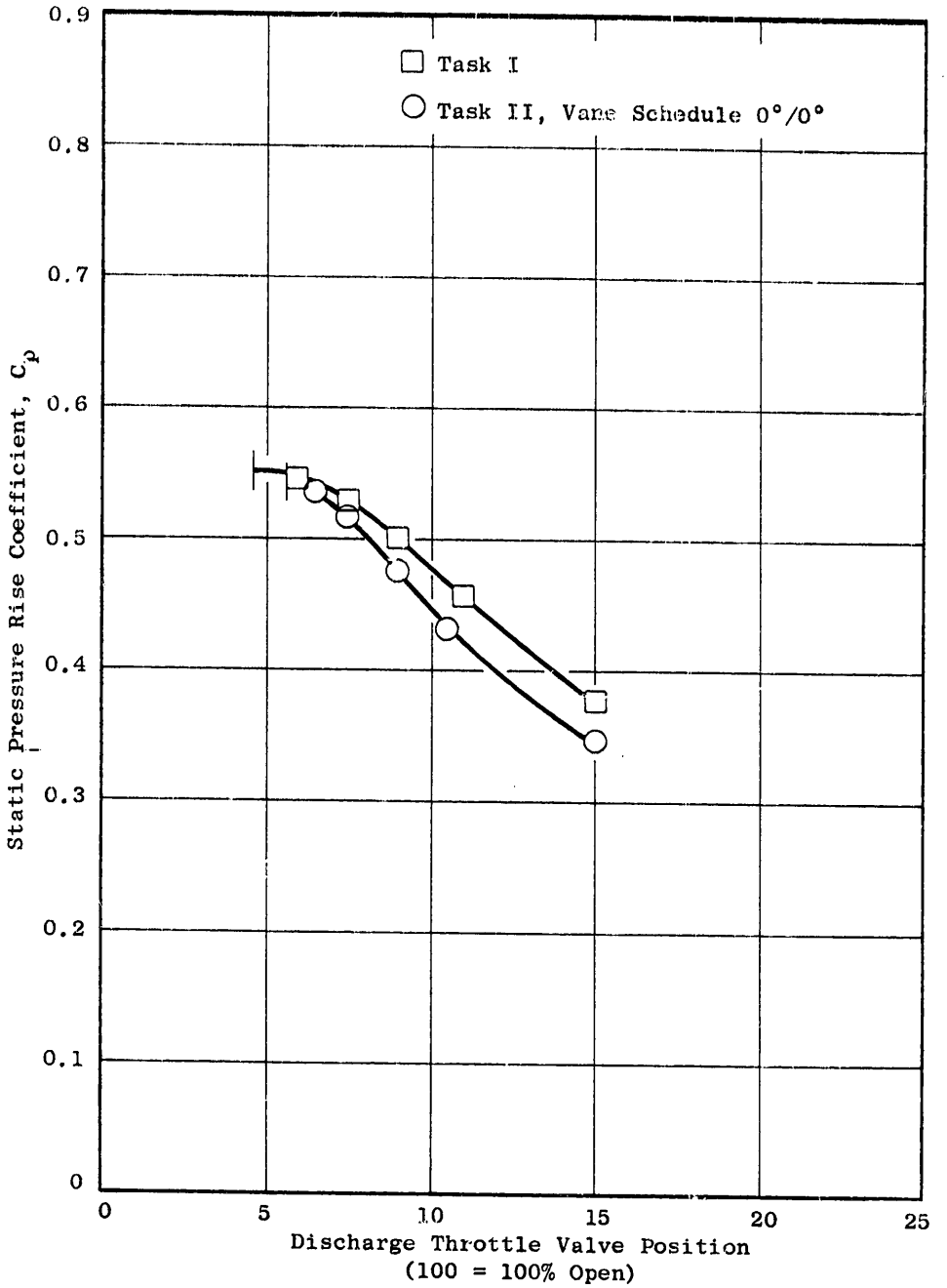

(d) 50% Immersion from Tip

Figure 26. Variation of Task I and Task II Rotor Static Pressure Rise Coefficient with Throttle Valve Setting, 100% Speed, Undistorted Inlet Flow (Continued).

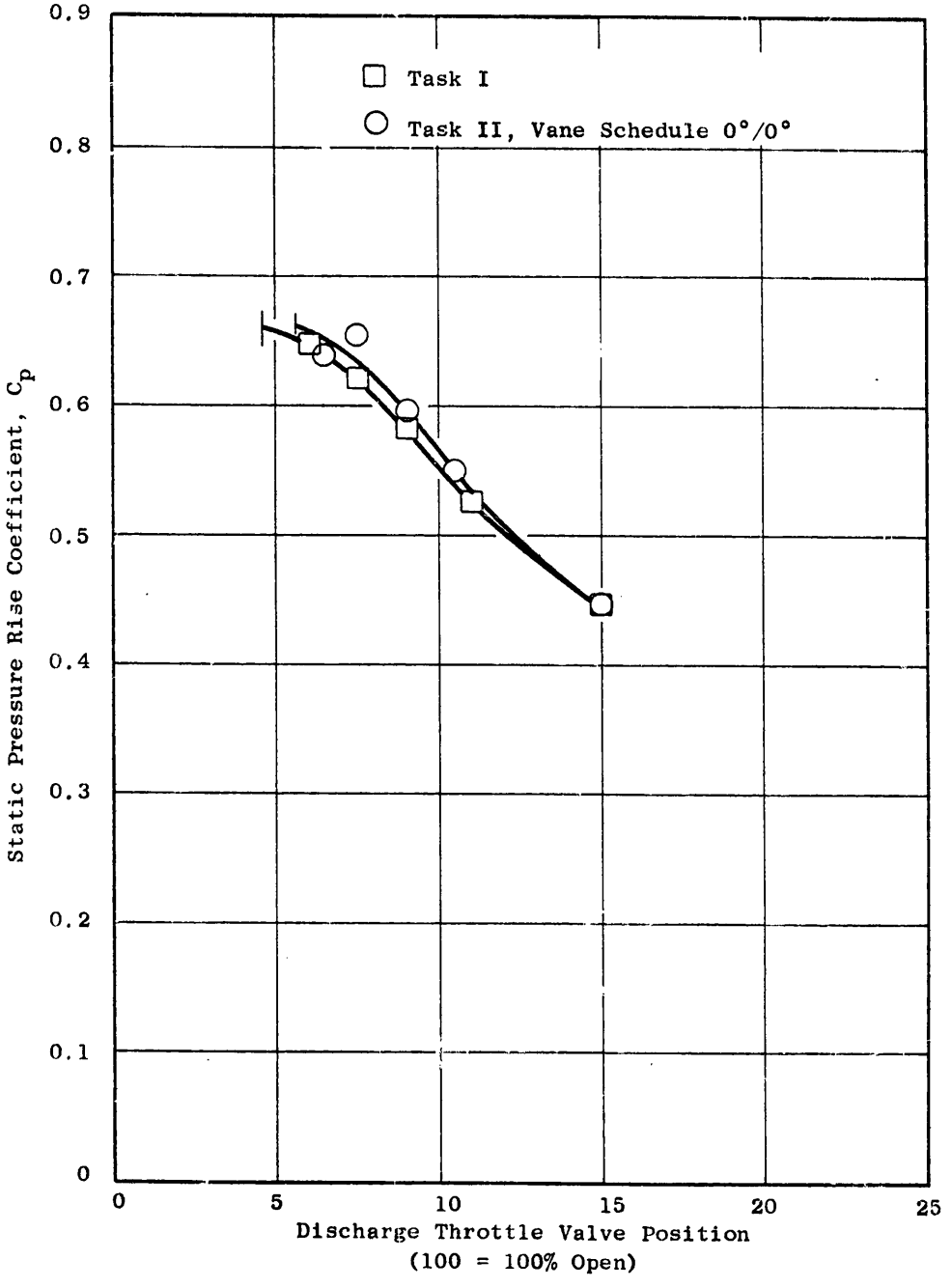

(e) 70% Immersion from Tip

Figure 26. Variation of Task I and Task II Rotor Static Pressure Rise Coefficient with Throttle Valve Setting, 100% Speed, Undistorted Inlet Flow (Continued).

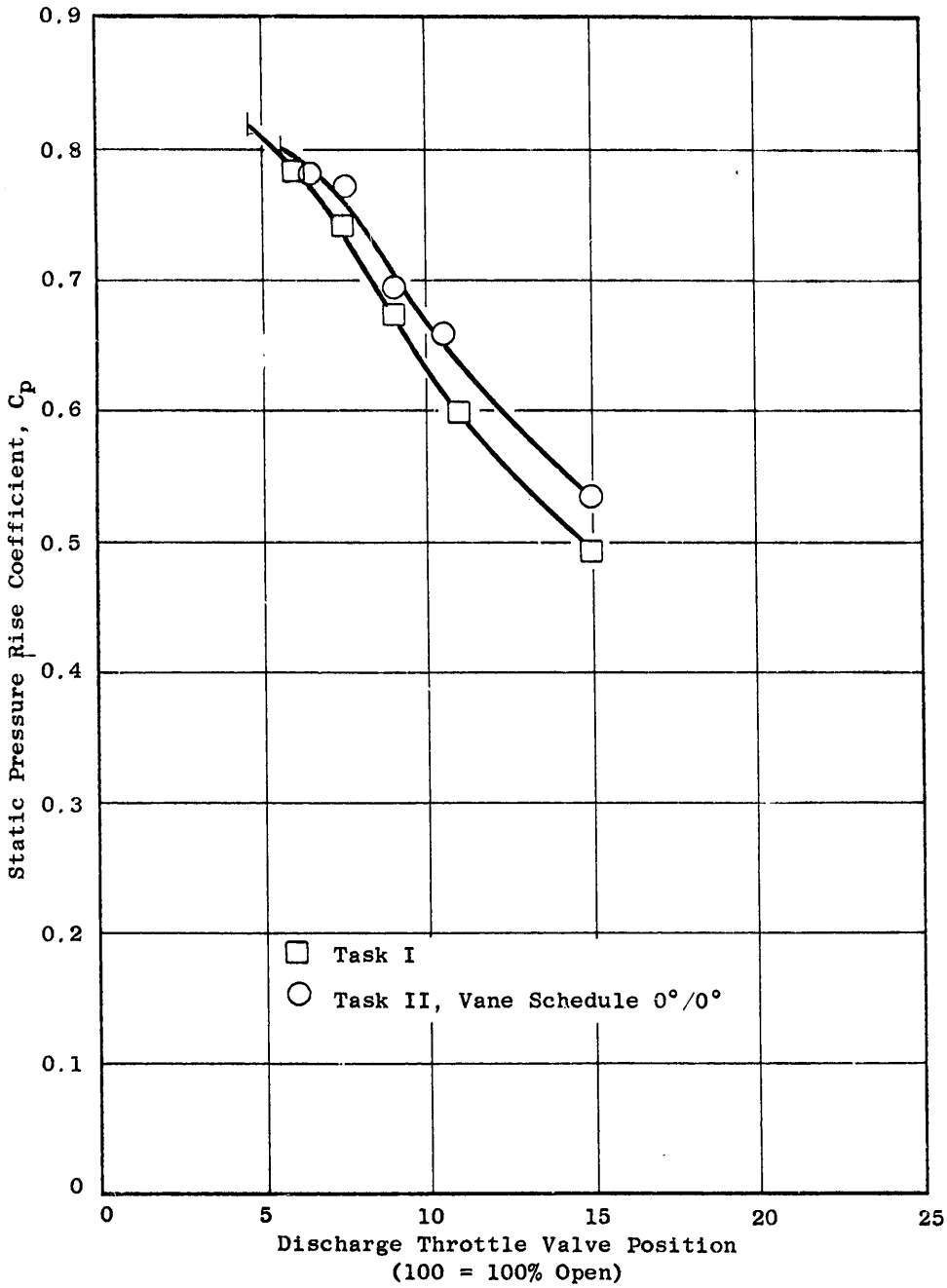

(f) 90% Immersion from Tip

Figure 26. Variation of Task I and Task II Rotor Static Pressure Rise Coefficient with Throttle Valve Setting, 100% Speed, Undistorted Inlet Flow (Continued).

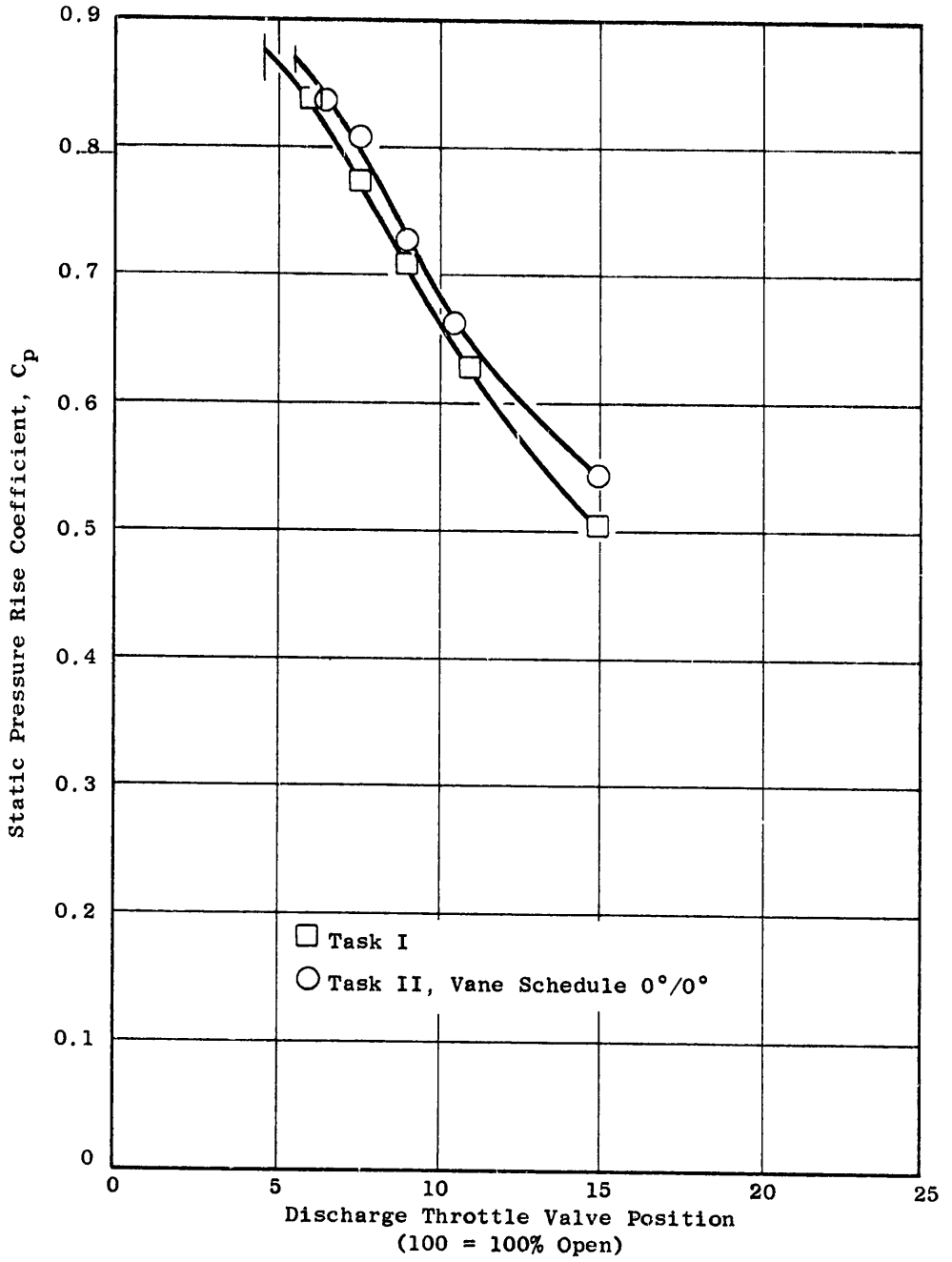

(g) 95% Immersion from Tip

Figure 26. Variation of Task I and Task II Rotor Static Pressure Rise Coefficient with Throttle Valve Setting, 100% Speed, Undistorted Inlet Flow (Concluded).

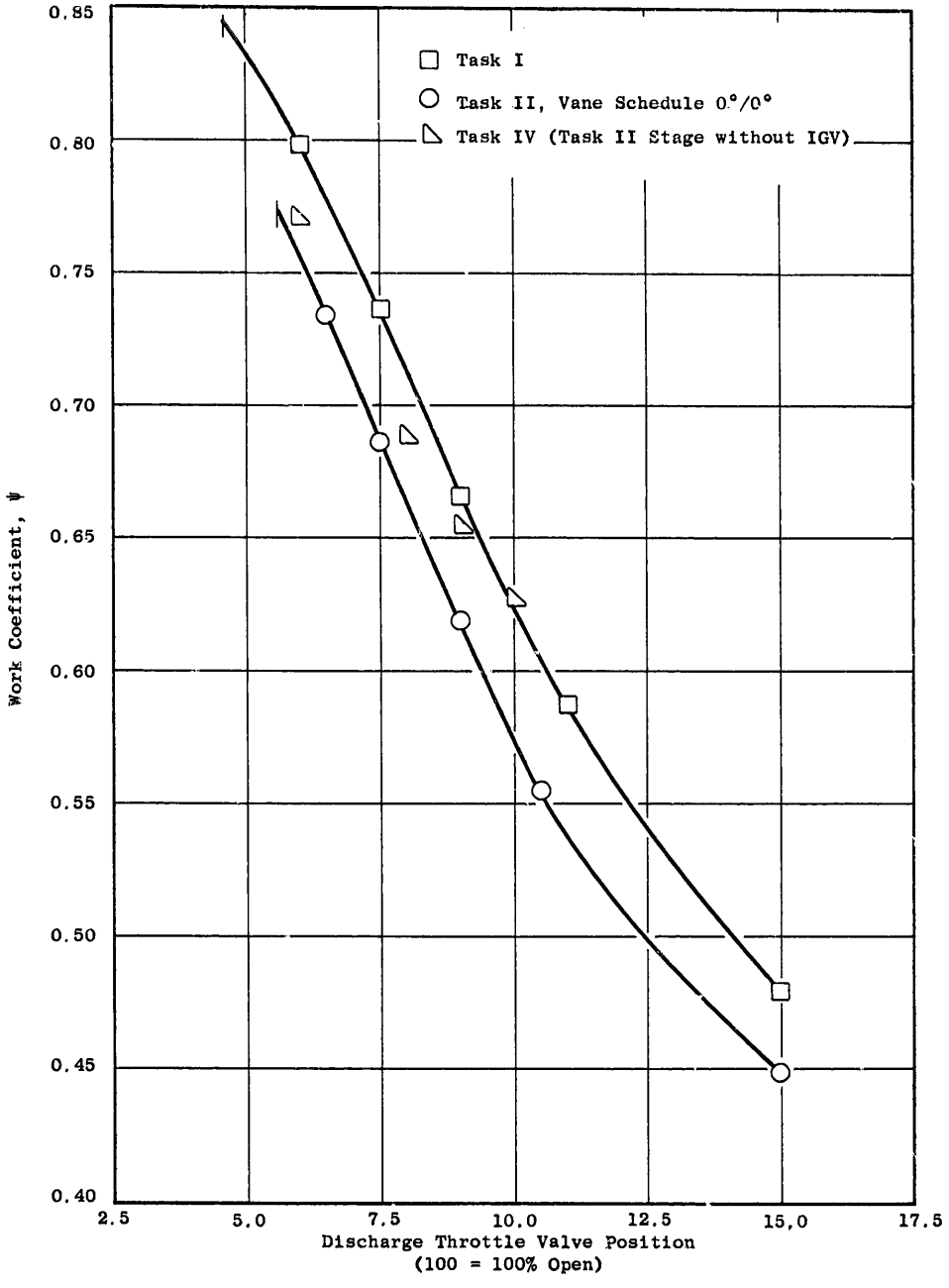

(a) 5% Immersion from Tip

Figure 27. Variation of Task I and II Work Coefficients with Throttle Valve Setting; 100% Speed, Undistorted Inlet Flow.

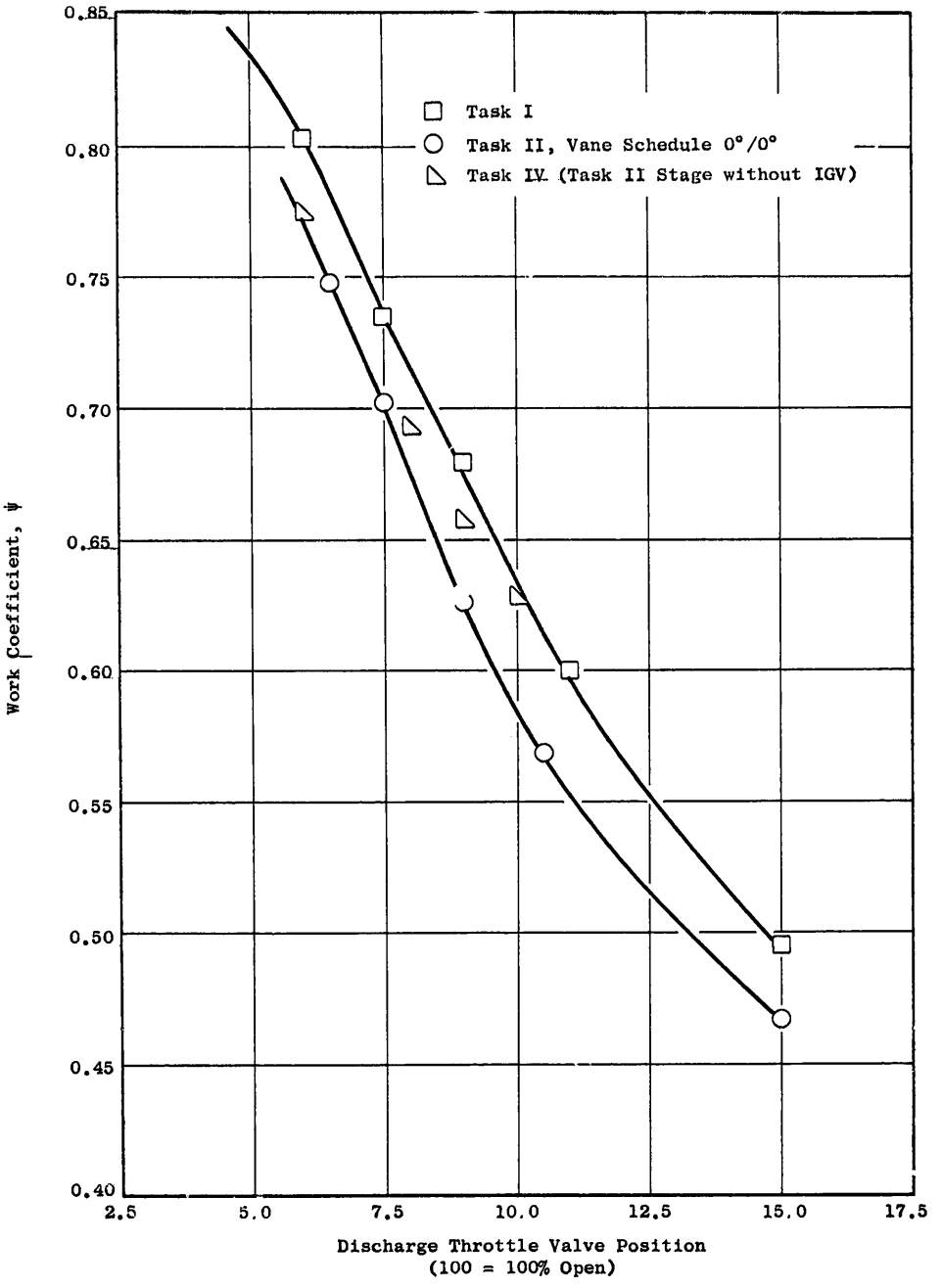

(b) 10% Immersion from Tip

Figure 27. Variation of Task I and II Work Coefficients with Throttle Valve Setting; 100% Speed, Undistorted Inlet Flow (Continued).

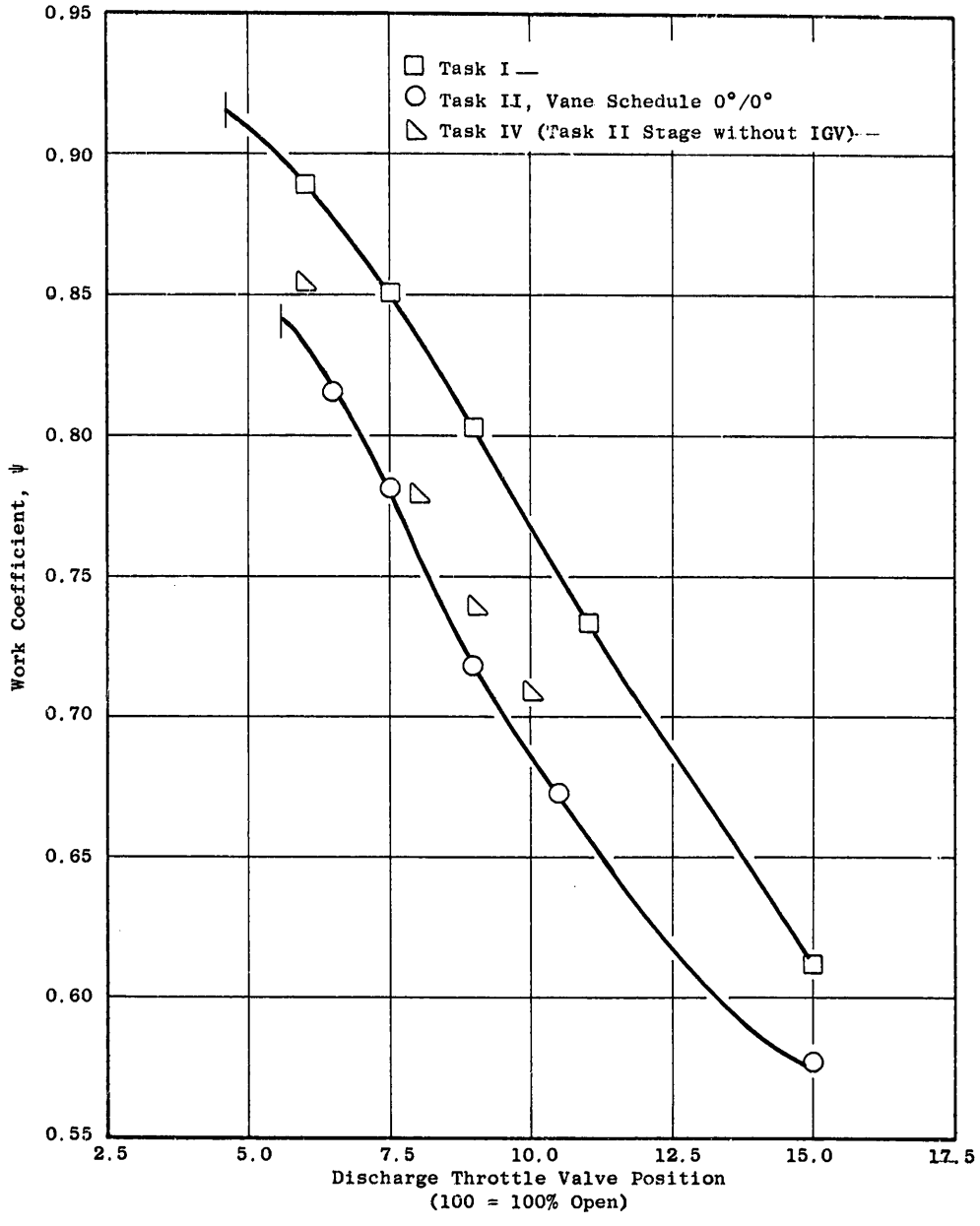

(c) 30% Immersion from Tip

Figure 27. Variation of Task I and II Work Coefficients with Throttle Valve Setting; 100% Speed, Undistorted Inlet Flow (Continued).

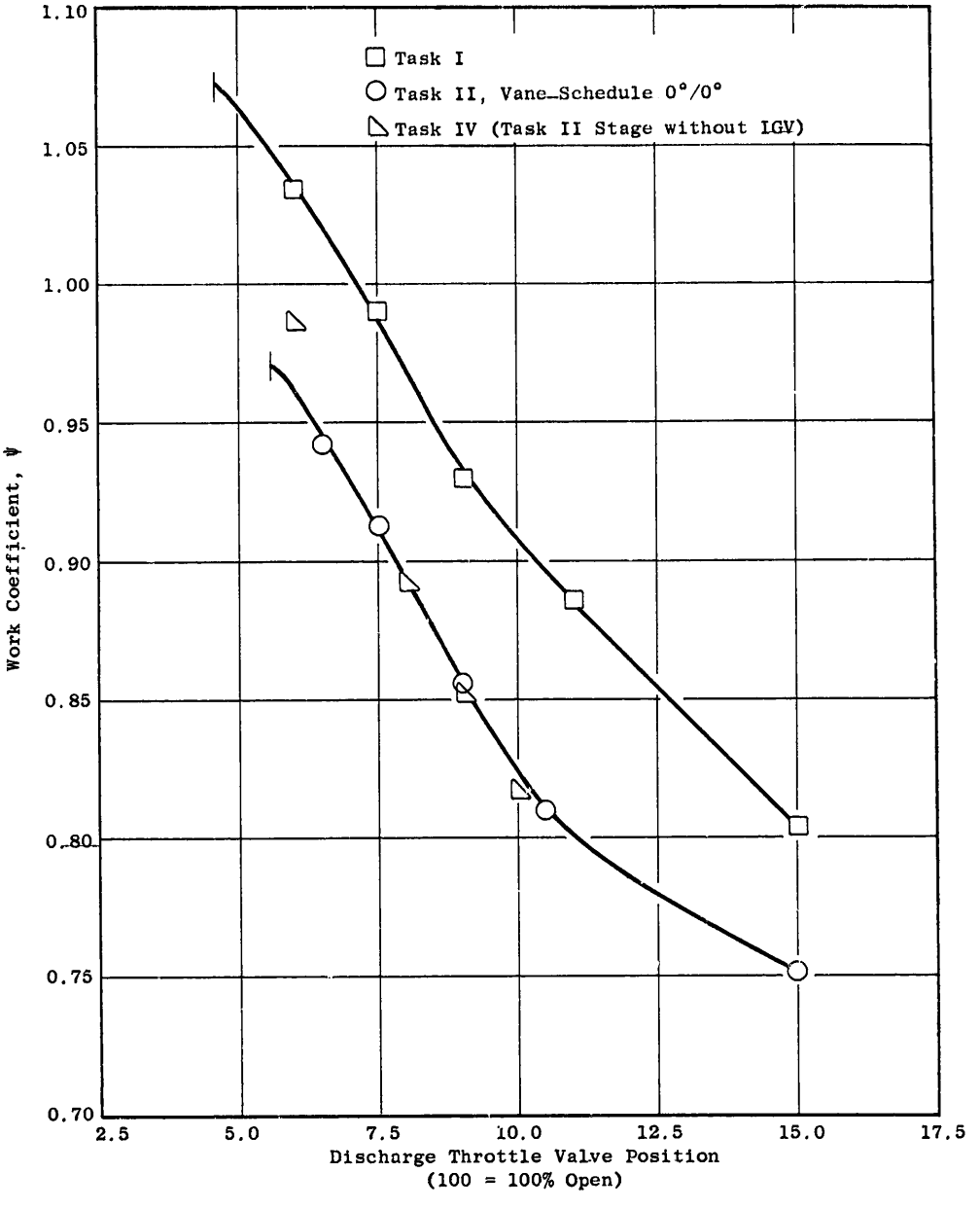

(d) 50% Immersion from Tip

Figure 27. Variation of Task I and II Work Coefficients with Throttle Valve Setting; 100% Speed, Undistorted Inlet Flow (Continued).

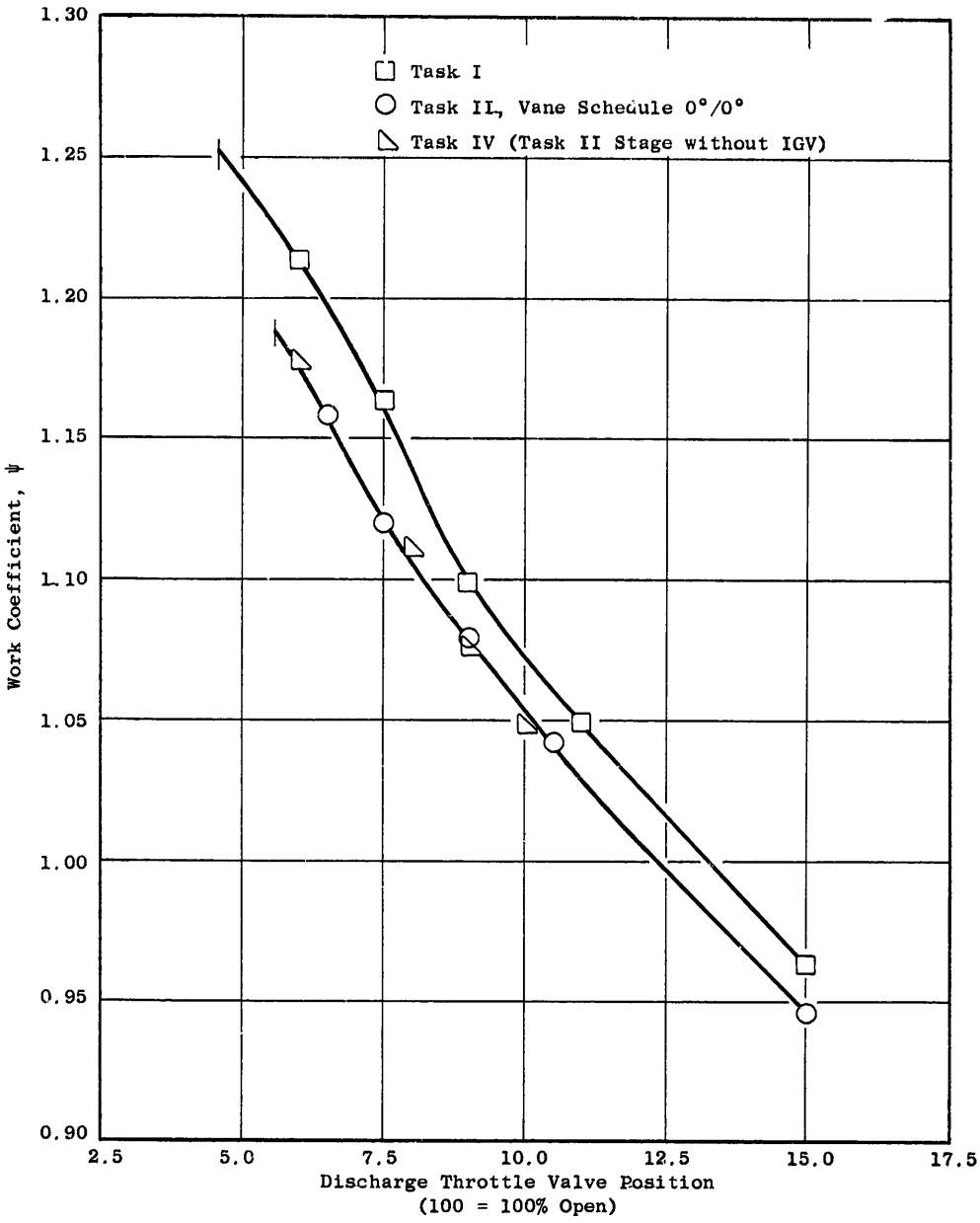

(e) 70% Immersion from Tip

Figure 27. Variation of Task I and II Work Coefficients with Throttle Valve Setting; 100% Speed, Distorted Inlet Flow (Continued).

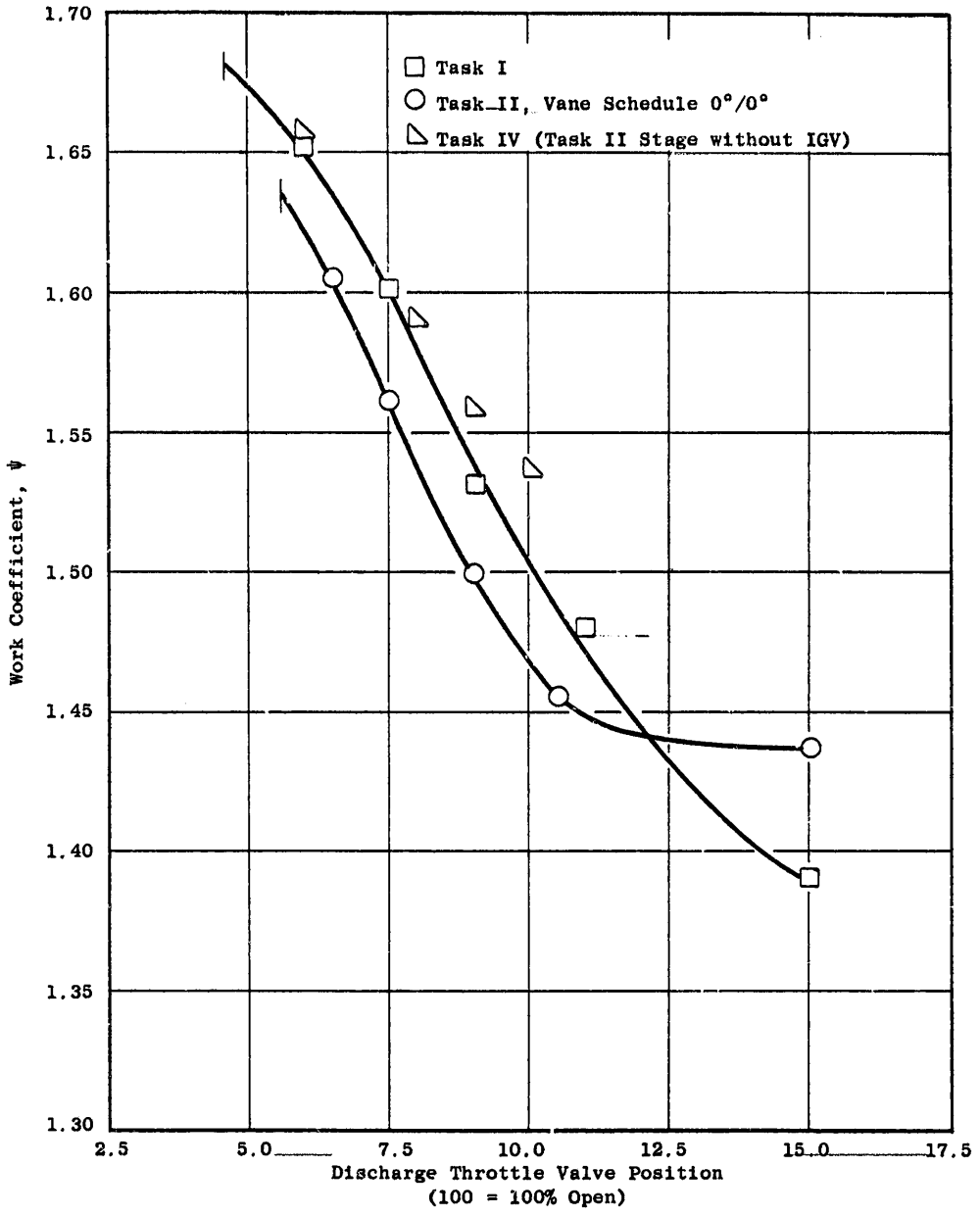

(f) 90% Immersion from Tip

Figure 27. Variation of Task I and II Work Coefficients with Throttle Valve Setting; 100% Speed, Undistorted Inlet Flow (Continued).

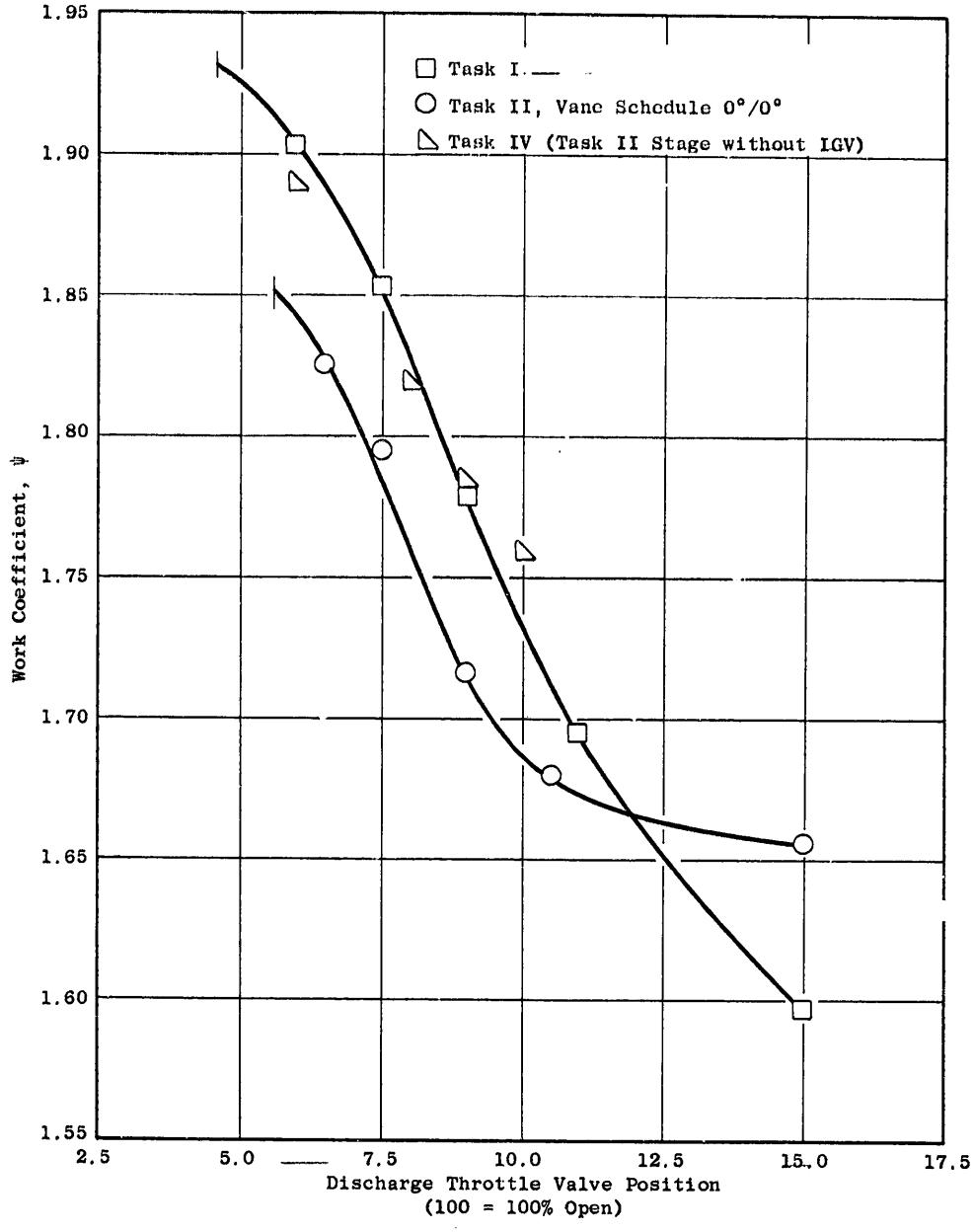

(g) 95% Immersion from Tip

Figure 27. Variation of Task I and II Work Coefficients with Throttle Valve Setting; 100% Speed, Undistorted Inlet Flow (Concluded).

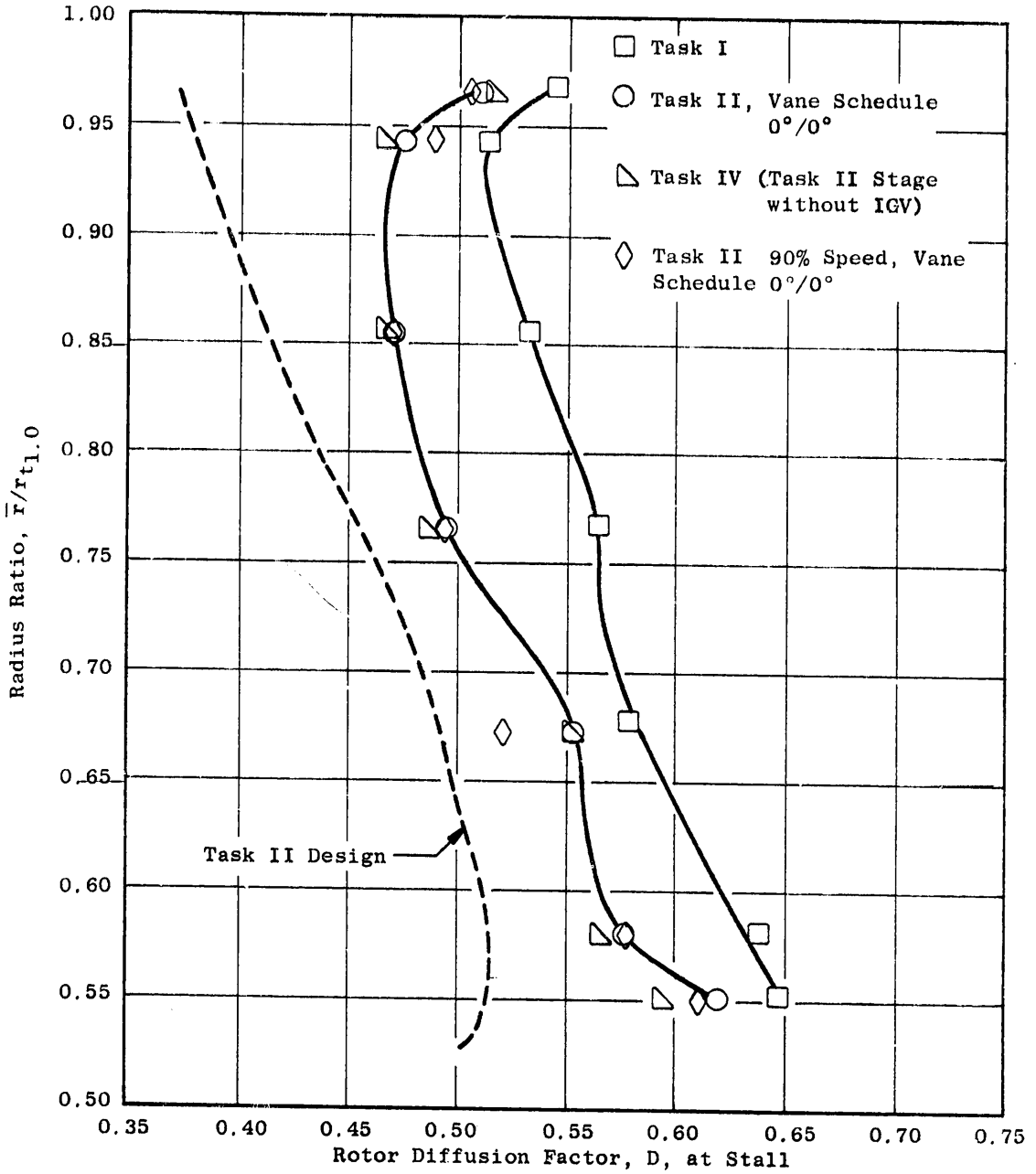

Figure 28. Comparison of Radial Profiles of Task I and Task II Rotor Diffusion Factors at Stall; 100% Speed, Undistorted Inlet Flow.

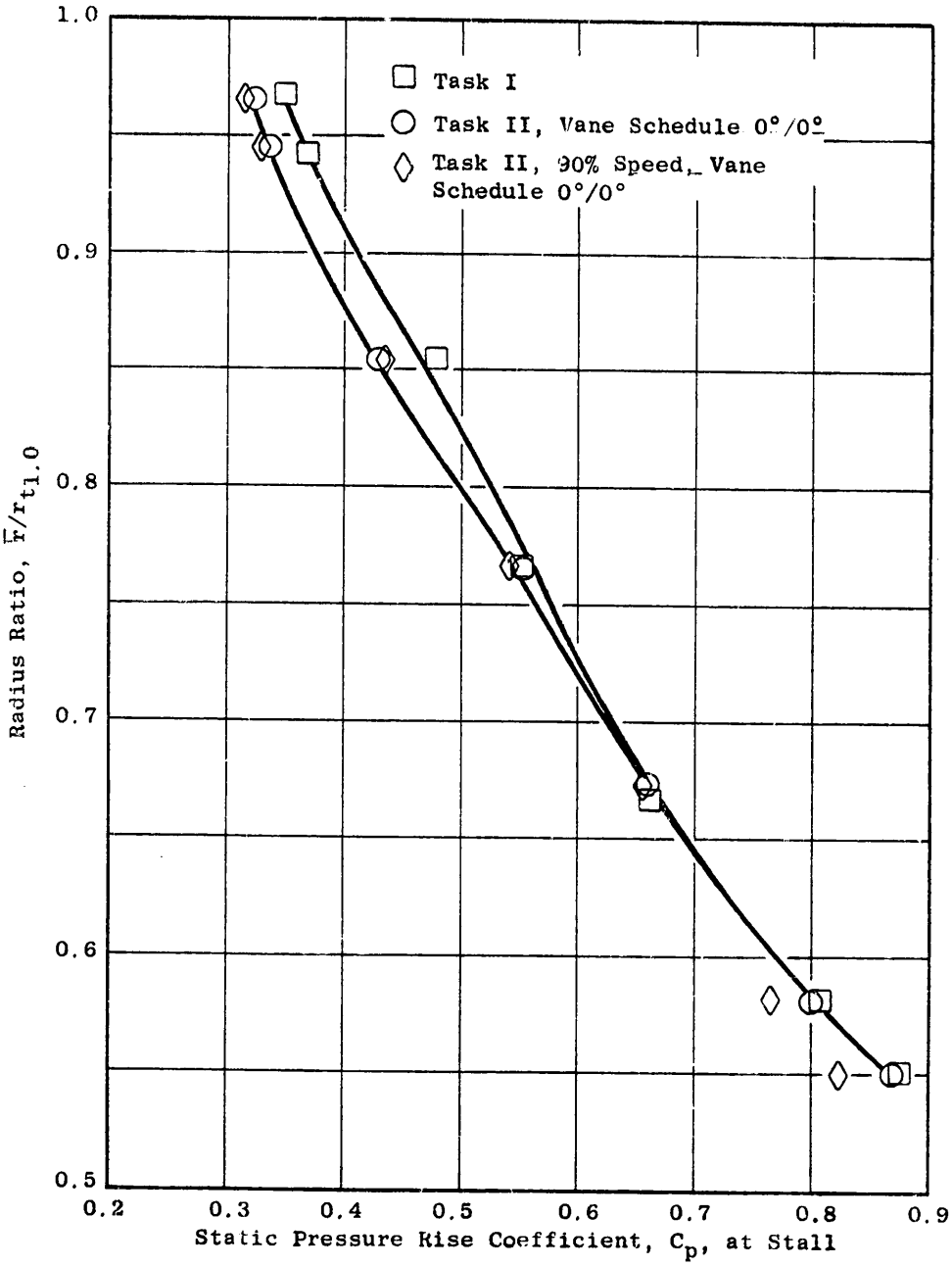

Figure 29. Comparison of Radial Profiles of Task I and Task II Rotor Static Pressure Rise Coefficient at Stall; 100% Speed, Undistorted Inlet Flow.

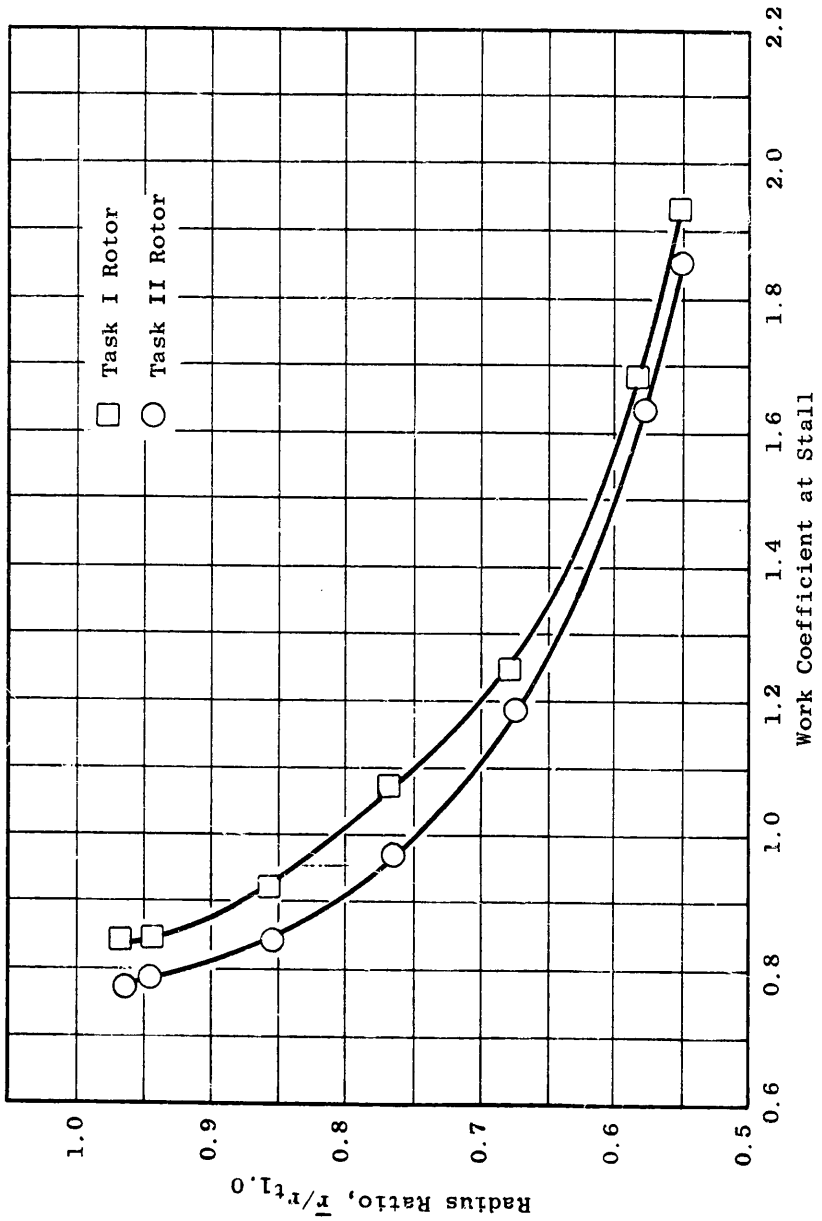

Figure 30. Comparison of Radial Profiles of Task I and Task II Rotor Work Coefficients at Stall; 100% Speed, Undistorted Inlet Flow.

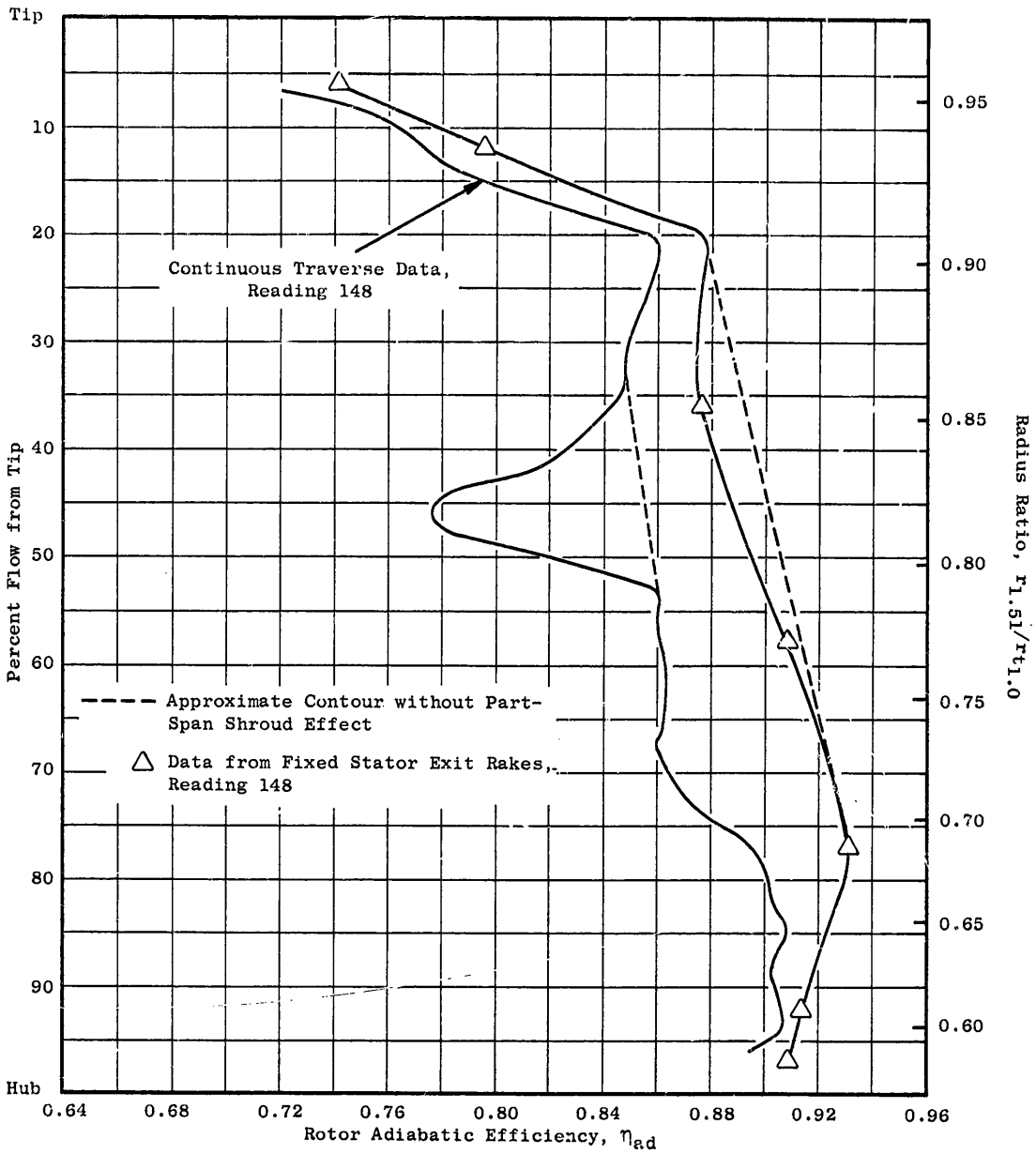

(a) 100% Speed, Near Design Flow

Figure 31. Comparison of Radial Profiles of Rotor Adiabatic Efficiency Obtained from Rotor Exit Detailed Traverses and Stator Exit Fixed Instrumentation at IGV/Stator Schedule 0°/0°, Undistorted Inlet Flow.

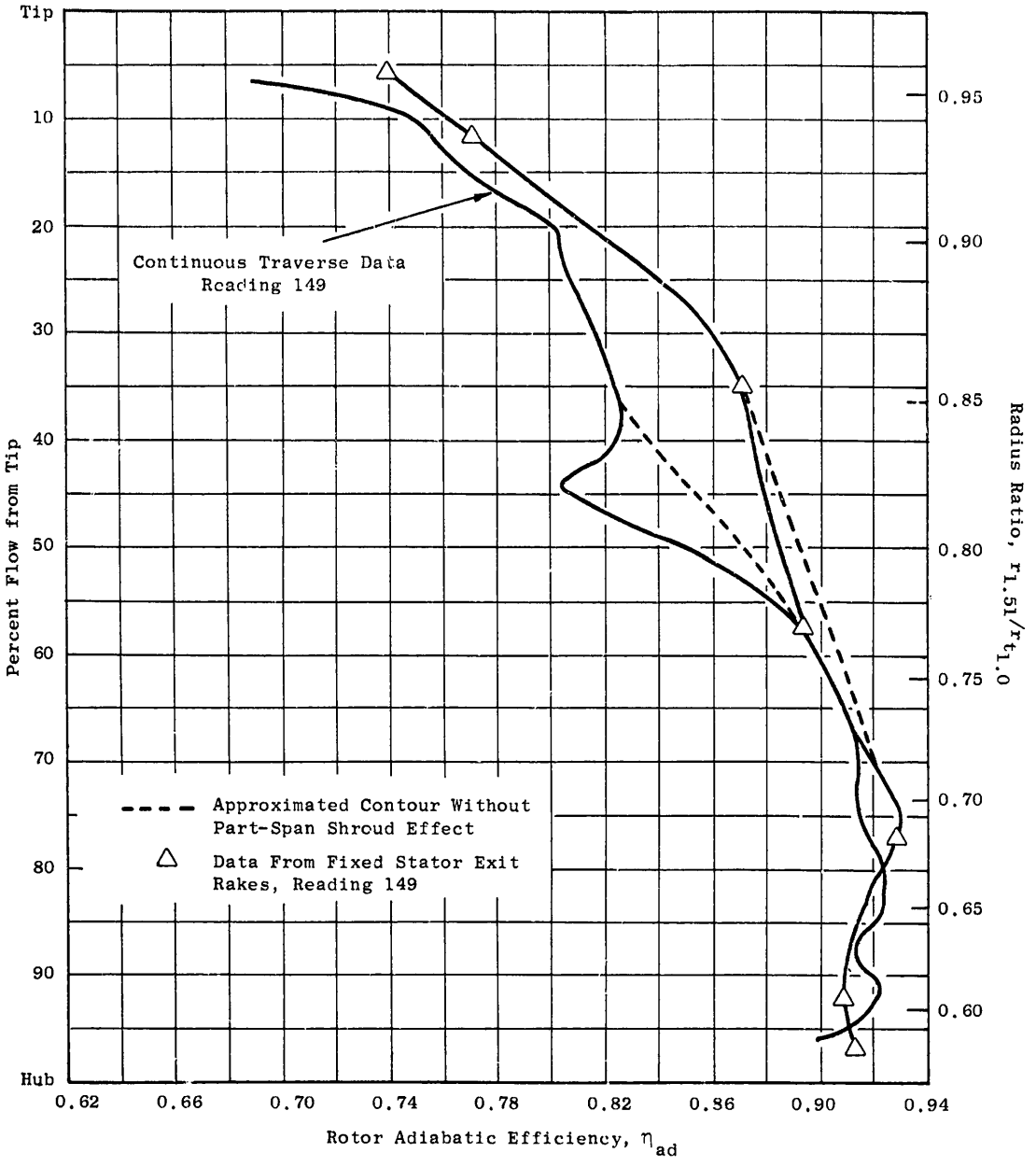

(b) 100% Speed Near Stall

Figure 31. Comparison of Radial Profiles of Rotor Adiabatic Efficiency Obtained from Rotor Exit Detailed Traverses and Stator Exit Fixed Instrumentation at IGV/Stator Schedule 0°/0°, Undistorted Inlet Flow (Continued).

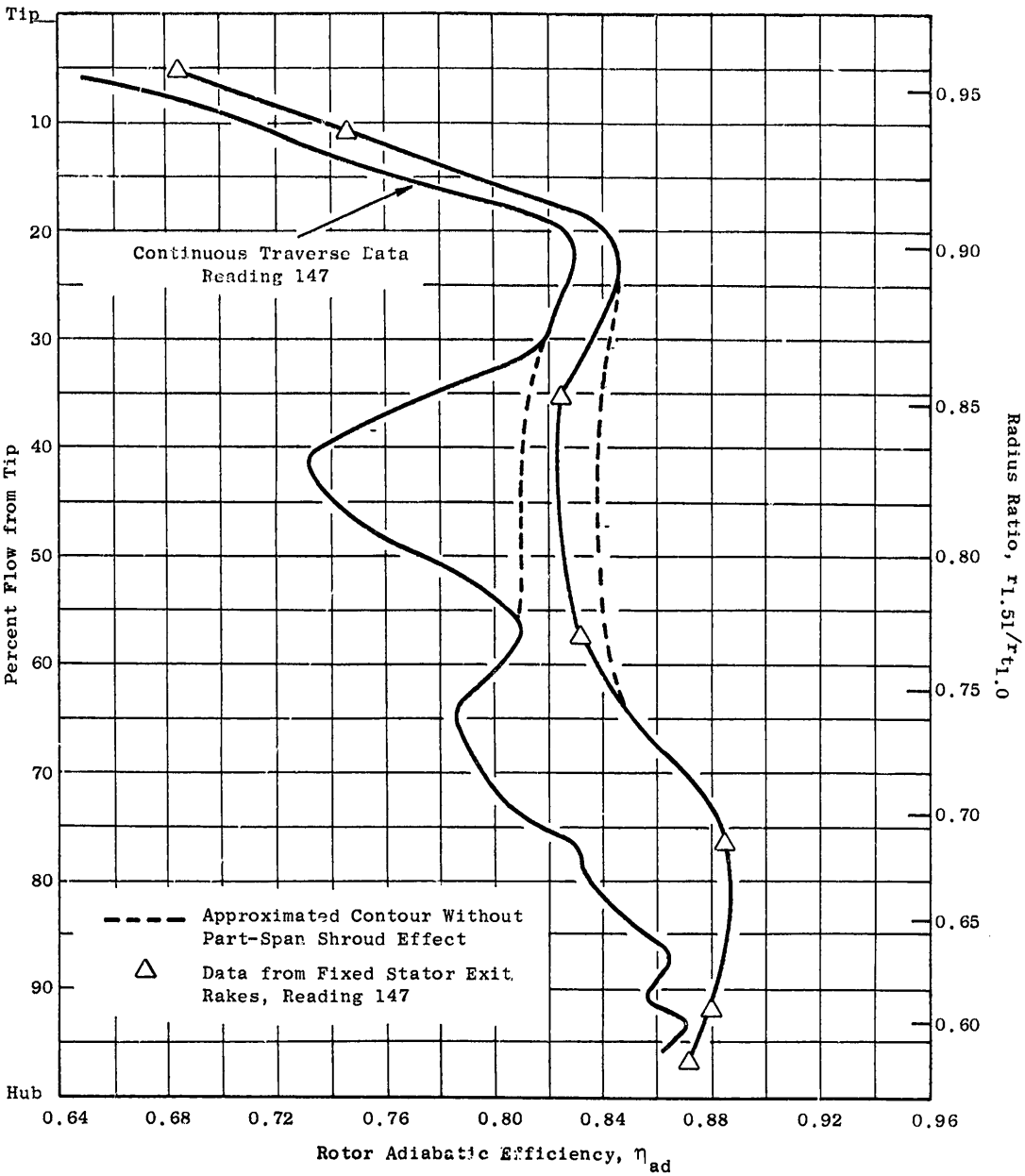

(c) 110% Speed, Approximately on a Constant Throttle Line Through Design Point

Figure 31. Comparison of Radial Profiles of Rotor Adiabatic Efficiency Obtained from Rotor Exit Detailed Traverses and Stator Exit Fixed Instrumentation at IGV/Stator Schedule 0°/0°, Undistorted Inlet Flow (Concluded).

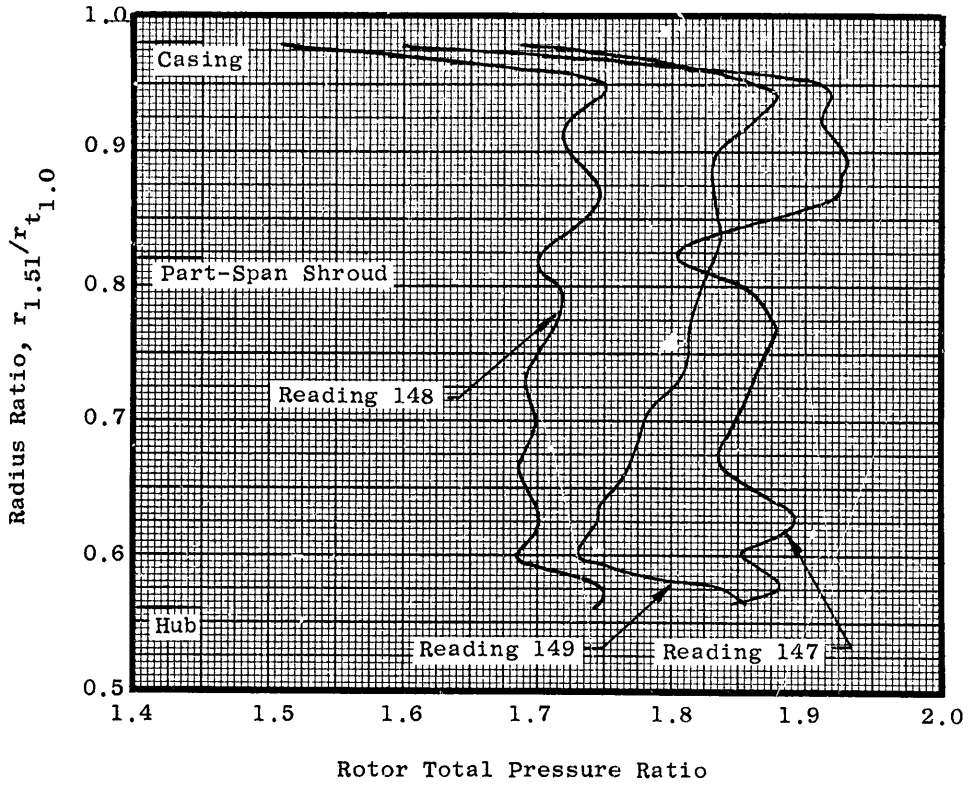

(a) Radial Variation of Rotor Total Pressure Ratio

Figure 32. Continuous Traverse Data at Rotor Exit Plane 1.51 for Readings 147 (110% Design Speed, Approximately on a Constant, Throttle Line Through Design Point), 148 (100% Design Speed, Near Design Point), and 149 (100% Design Speed, Near Stall).

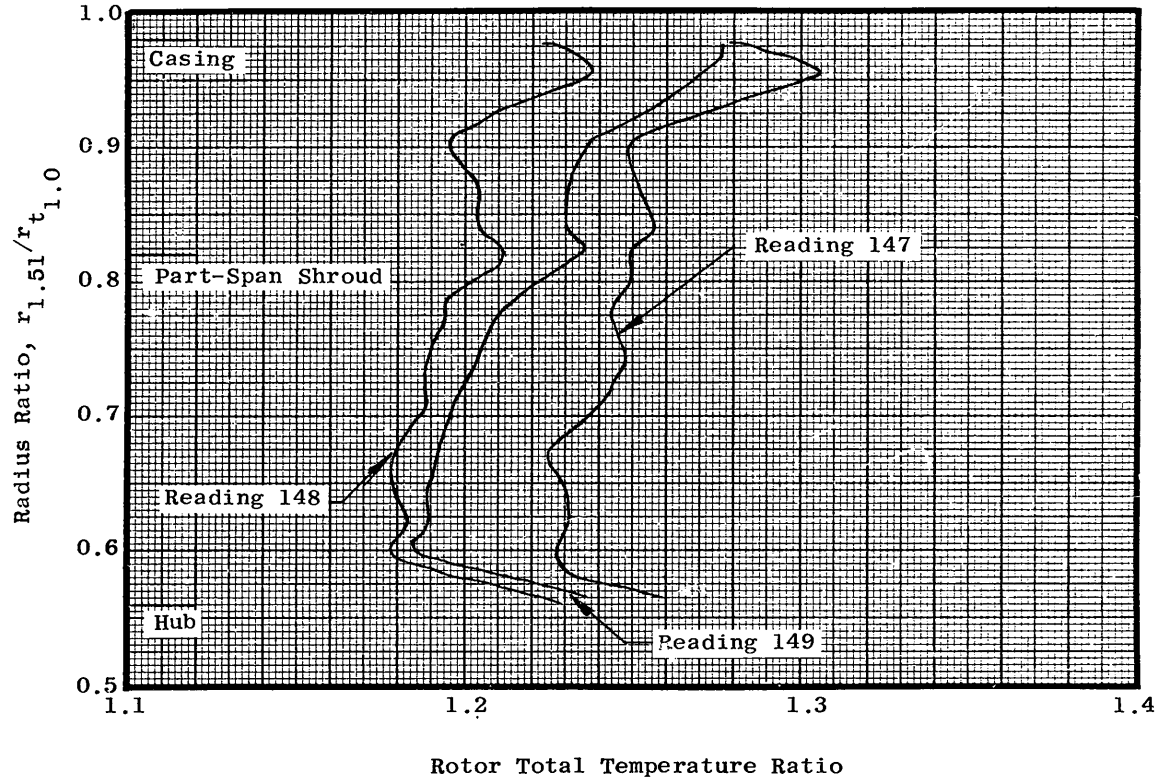

(b) Radial Variation of Rotor Total Temperature Ratio

Figure 32. Continuous Traverse Data at Rotor Exit Plane 1.51 for Readings 147 (110% Design Speed, Approximately om a Constant Throttle Line Through Design Point), 148 (100% Design Speed, Near Design Point), and 149 (100% Design Speed, Near Stall) (Continued).

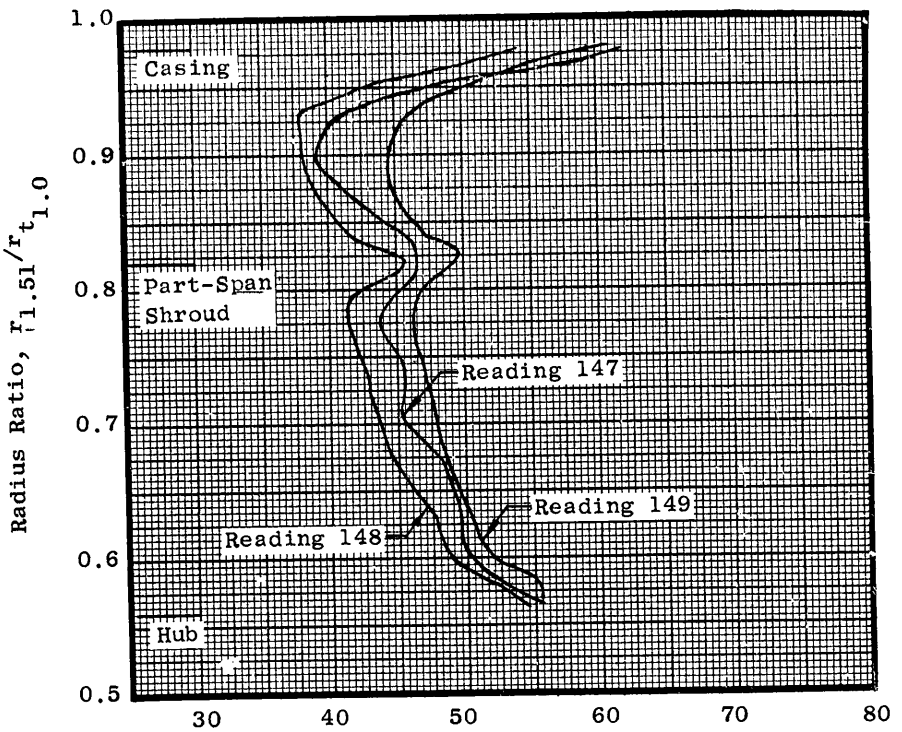

(c) Radial Variation of Absolute Air Angle at Rotor Exit

Figure 32. Continuous Traverse Data at Rotor Exit Plane 1.51 for Readings 147 (110% Design Speed, Approximately on a Constant, Throttle Line Through Design Point), 148 (100% Design Speed, Near Design Point), and 149 (100% Design Speed, Near Stall) (Concluded).

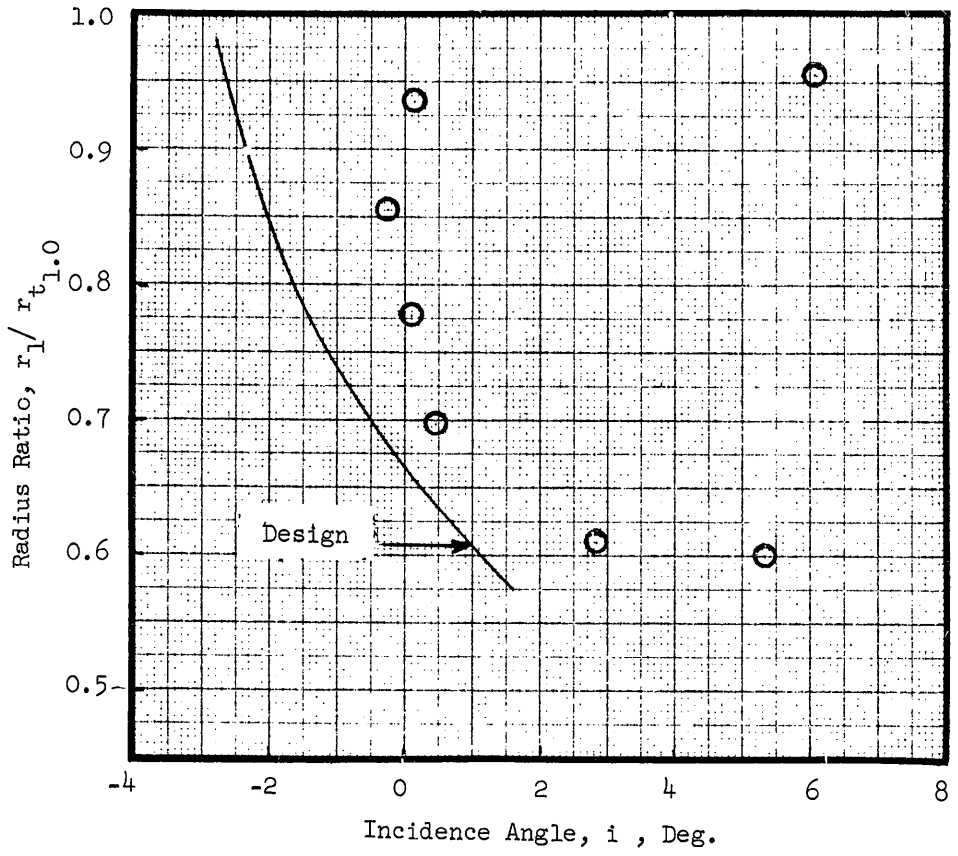

Figure 33. Radial Profile of Stator Incidence Angles at 0°/0° IGV/Stator Schedule; 100% Speed, Near Design Condition, Undistorted Inlet Flow.

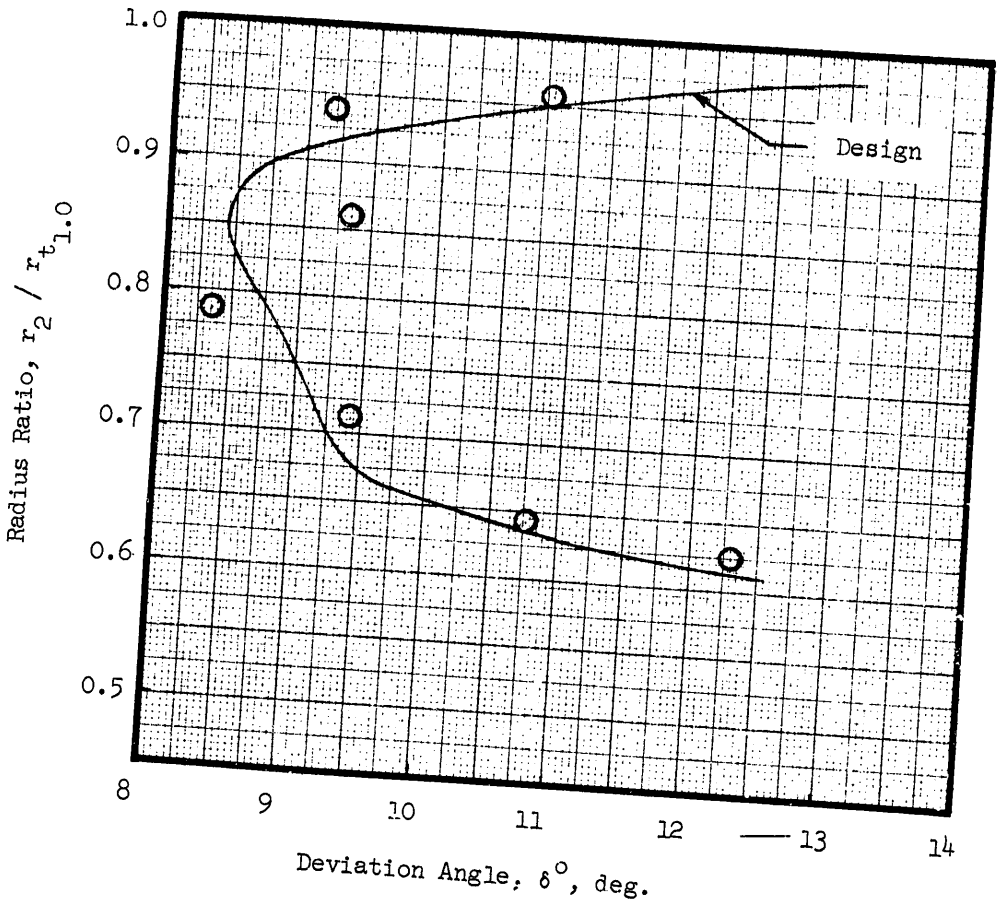

Figure 34. Radial Profile of Stator Deviation Angle at 0°/0° IGV/ Stator Schedule; 100% Speed, Near Design Condition, Undistorted Inlet Flow.

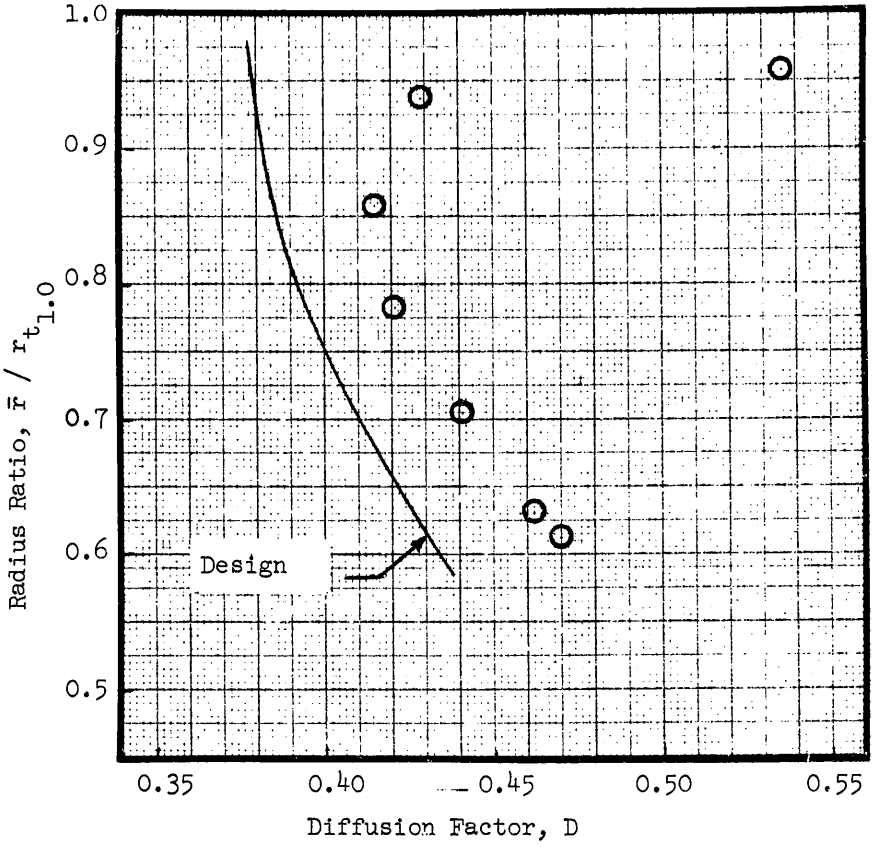

Figure 35. Radial Profile of Stator Diffusion Factor at 0°/0° IGV/Stator Schedule; 100% Speed, Near Design Condition, Undistorted Inlet Flow.

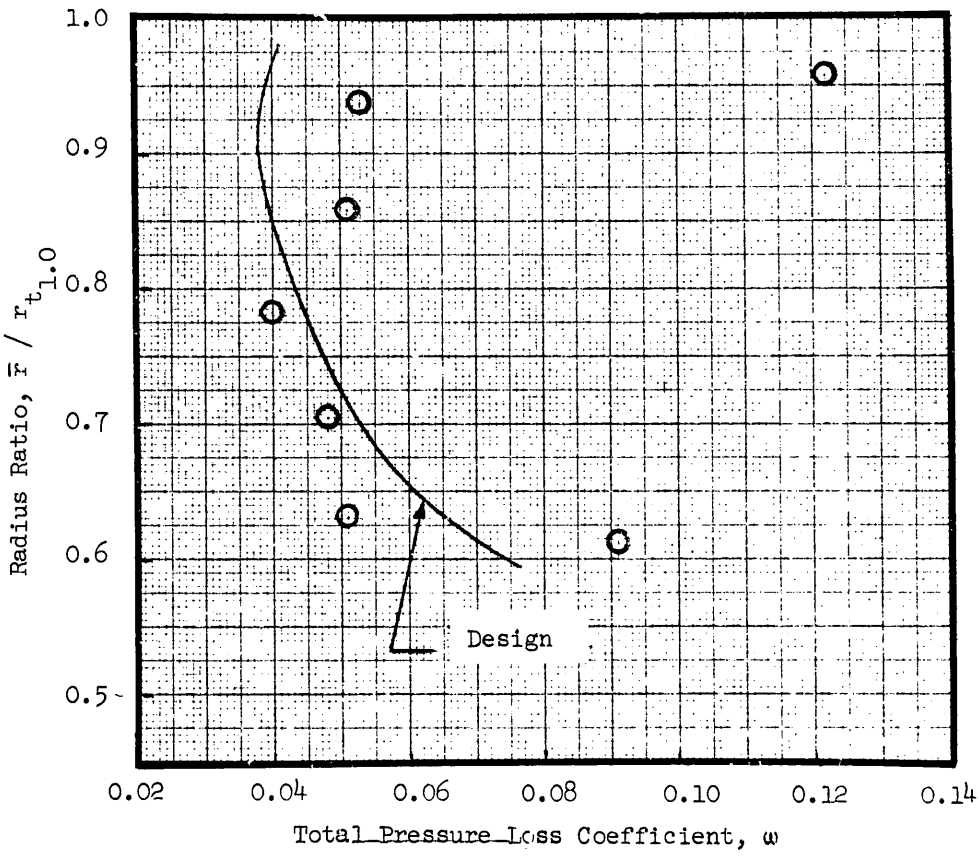

Figure 36. Radial Profile of Stator Total Pressure Loss Coefficient at 0°/0° IGV/Stator Schedule; 100% Speed, Near Design Condition, Undistorted Inlet Flow.

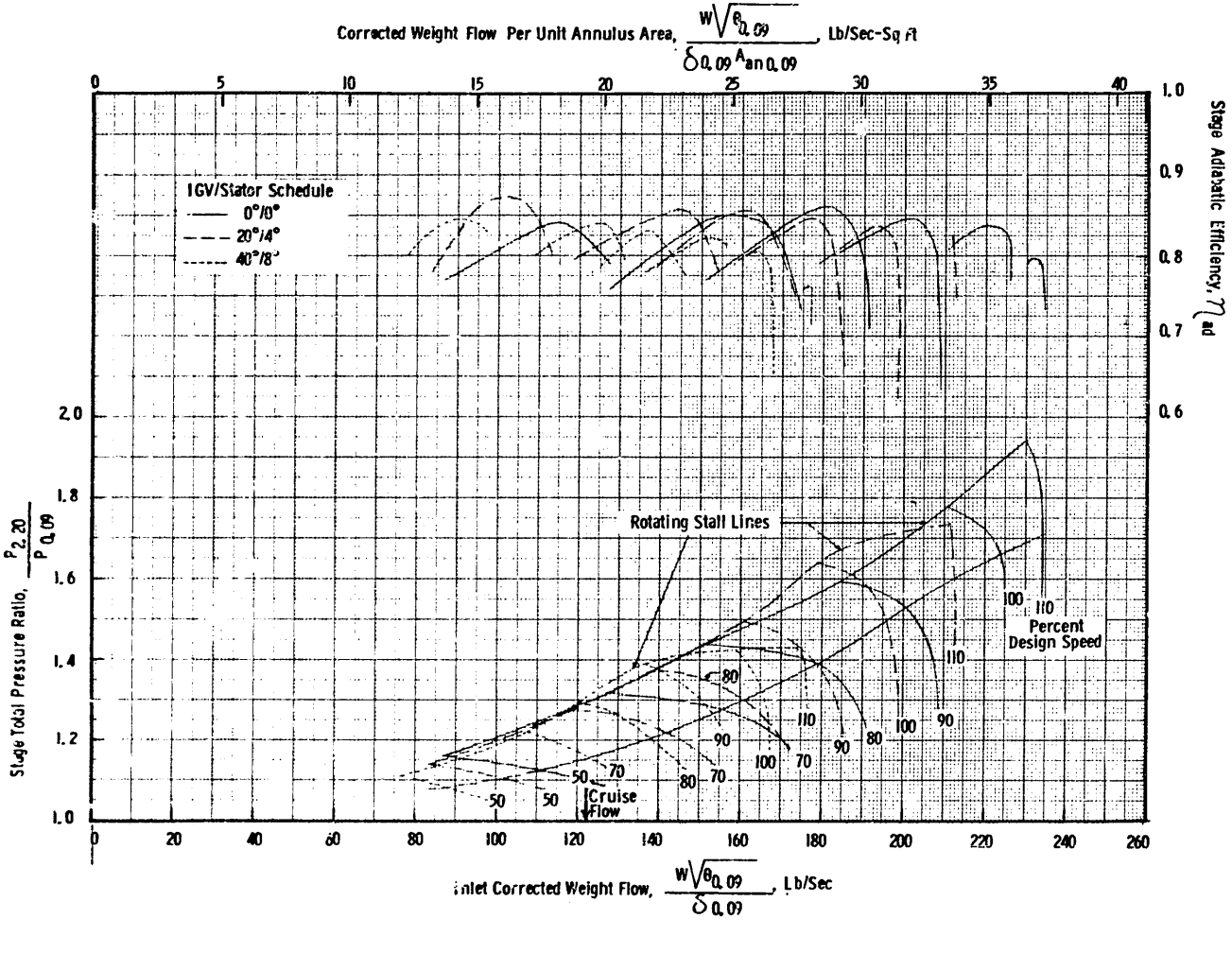

Figure 37. Consolidated Task II Stage Performance Map for All Three IGV/Stator Schedules; Undistorted Inlet Flow.

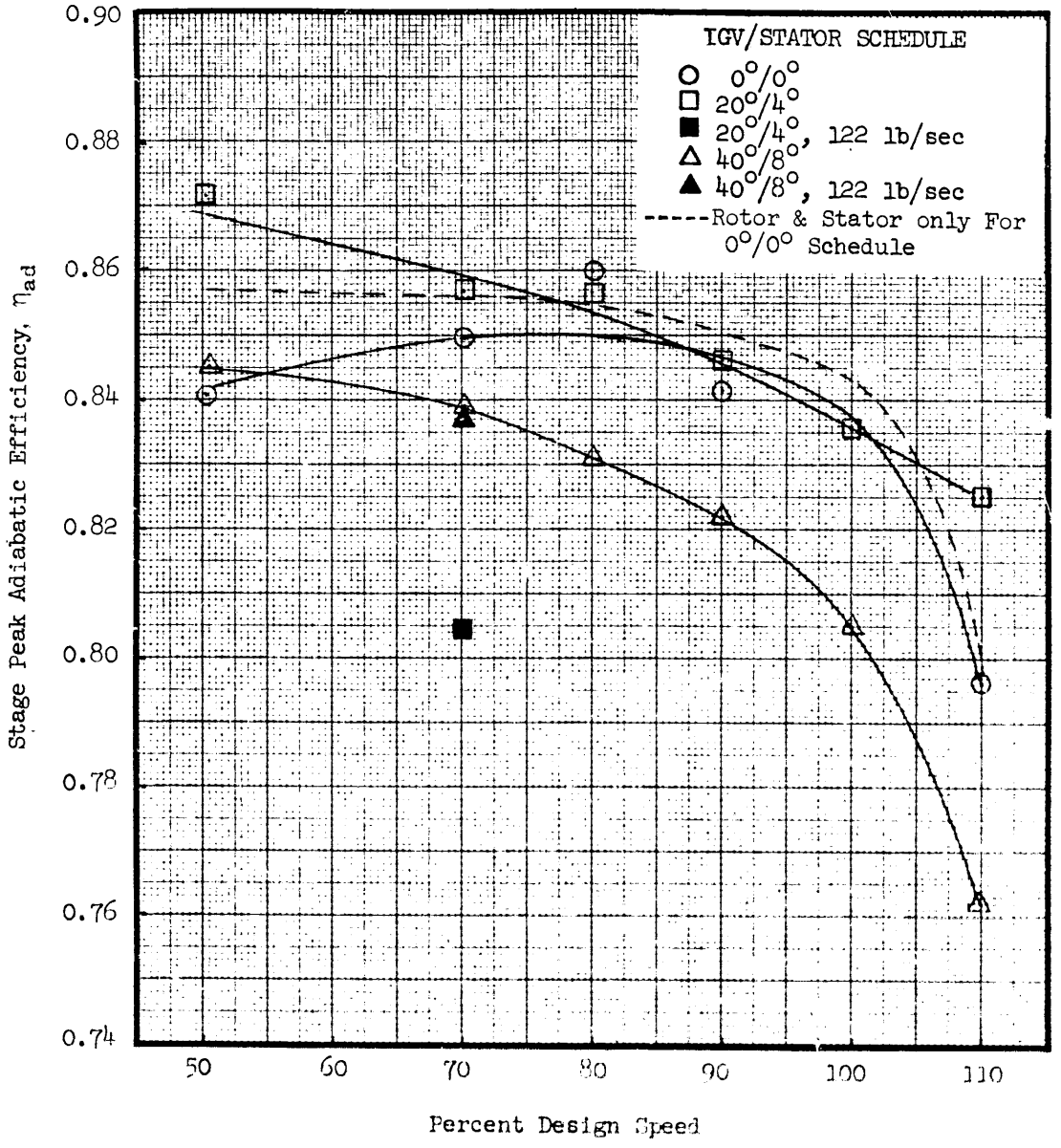

Figure 38(a). Variation of Task II Stage Peak Adiabatic Efficiency with Rotor Speed and Vane Schedule; Undistorted Inlet Flow.

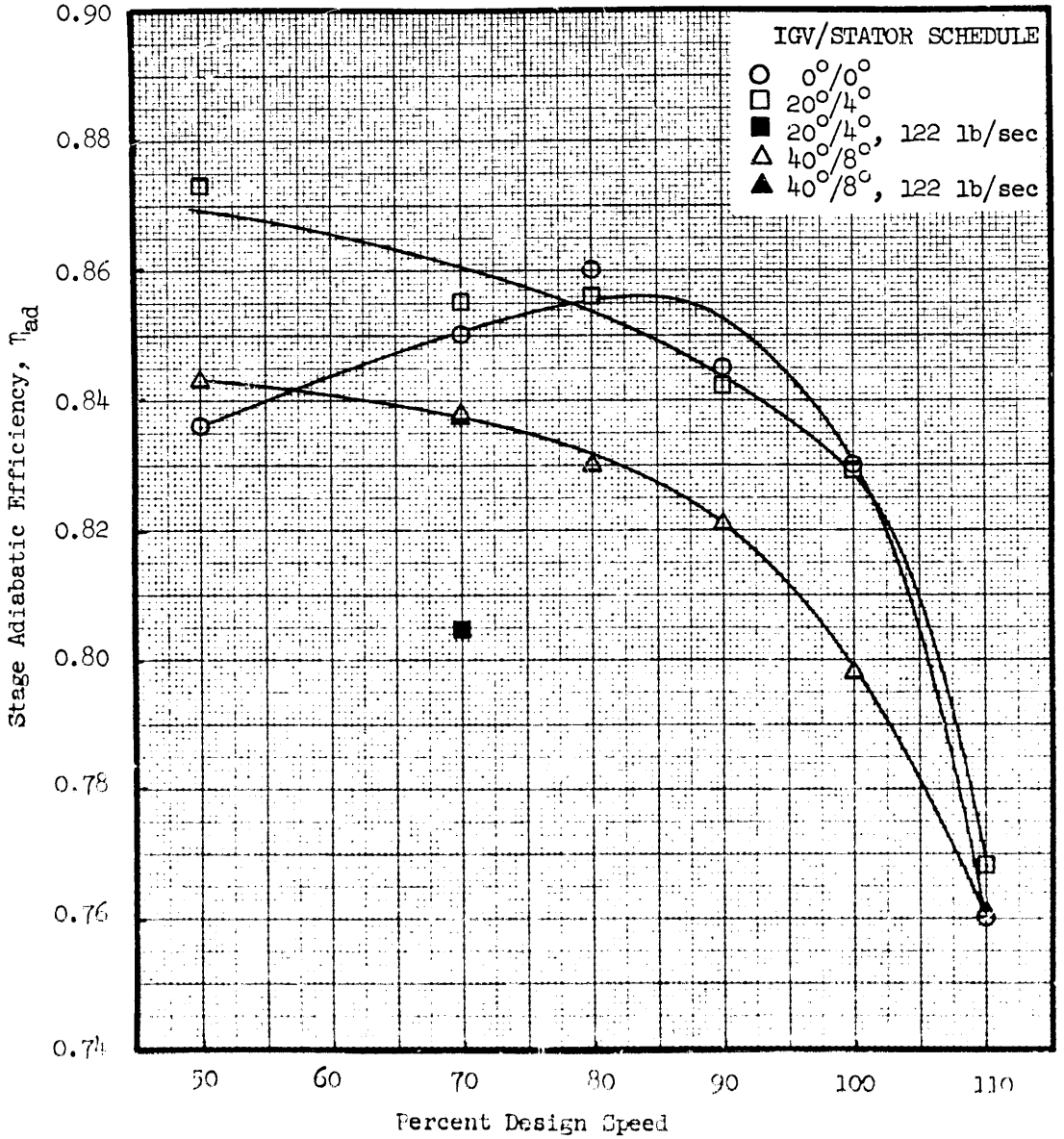

Figure 38(b). Variation of Stage Adiabatic Efficiency with Rotor Speed and Vane Schedule at the CTL Condition, Undistorted Inlet Flow.

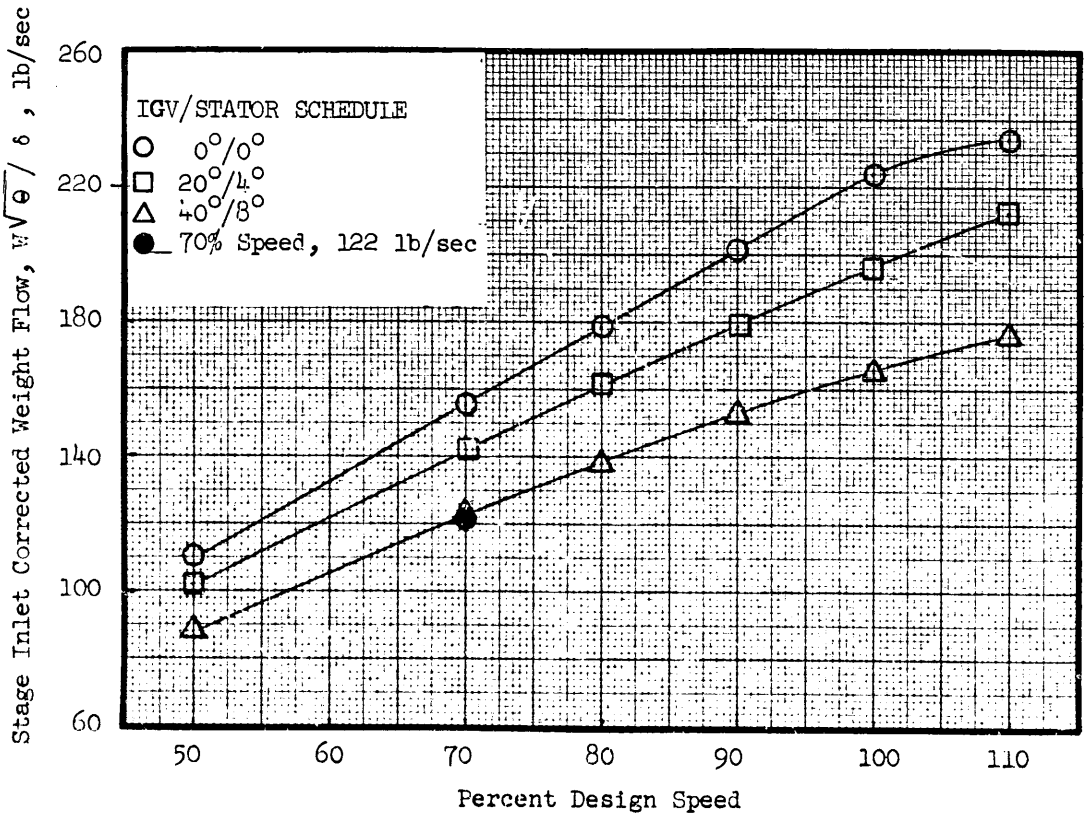

Figure 39. Variation of Stage Inlet Corrected Weight Flow with Rotor Speed and Vane Schedule at the CTL Condition, Undistorted Inlet Flow.

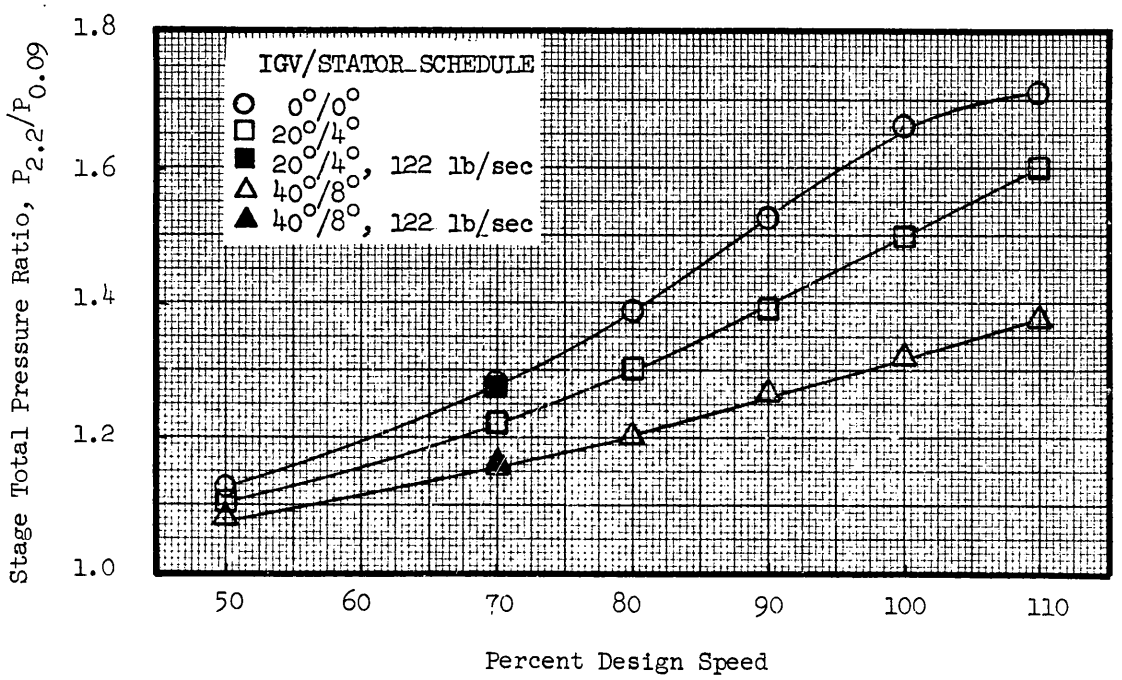

Figure 40. Variation of Stage Pressure Ratio with Rotor Speed and Vane Schedule at the CTL Condition; Undistorted Inlet Flow.

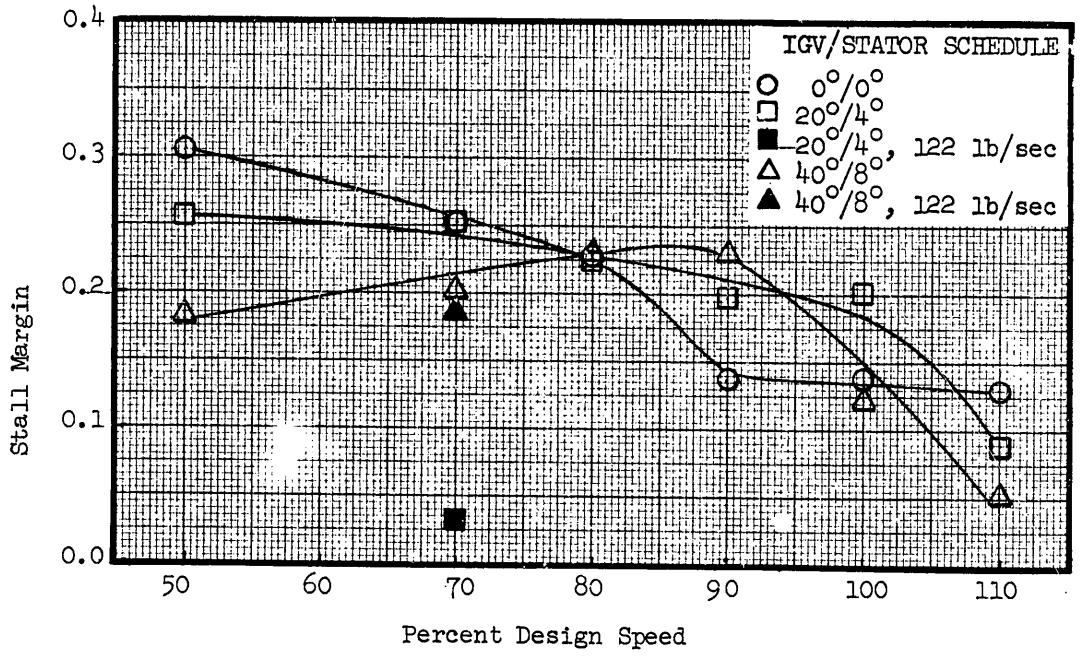

Figure 41. Variation of Stage Stall Margin with Rotor Speed and Vane Schedule at the CTL Condition, Undistorted Inlet Flow.

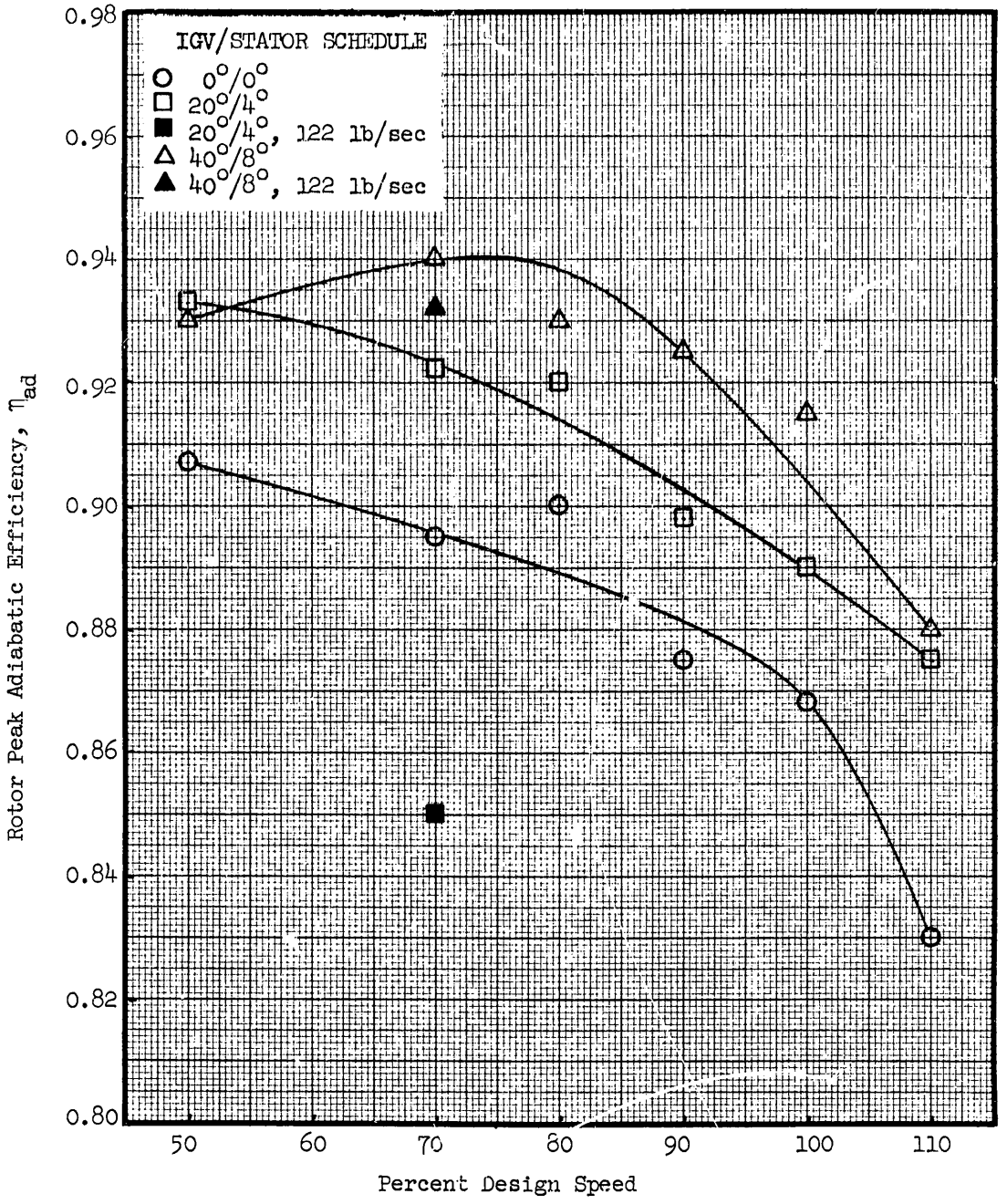

Figure 42(a). Variation of Rotor Peak Adiabatic Efficiency with Rotor Speed and Vane Schedule; Undistorted Inlet Flow.

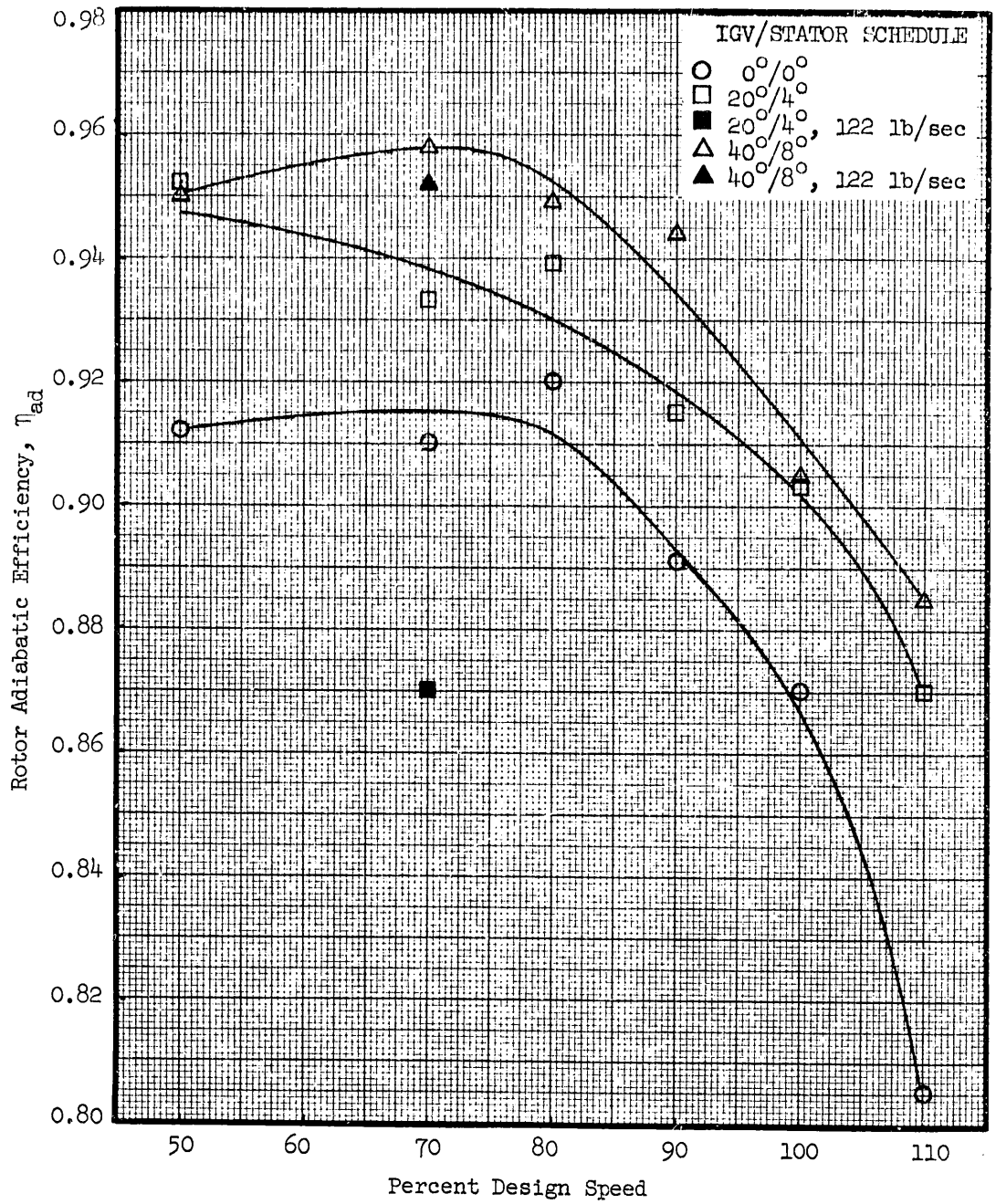

Figure 42(b). Variation of Rotor Adiabatic Efficiency with Rotor Speed and Vane Schedule at the CTL Condition; Undistorted Inlet Flow.

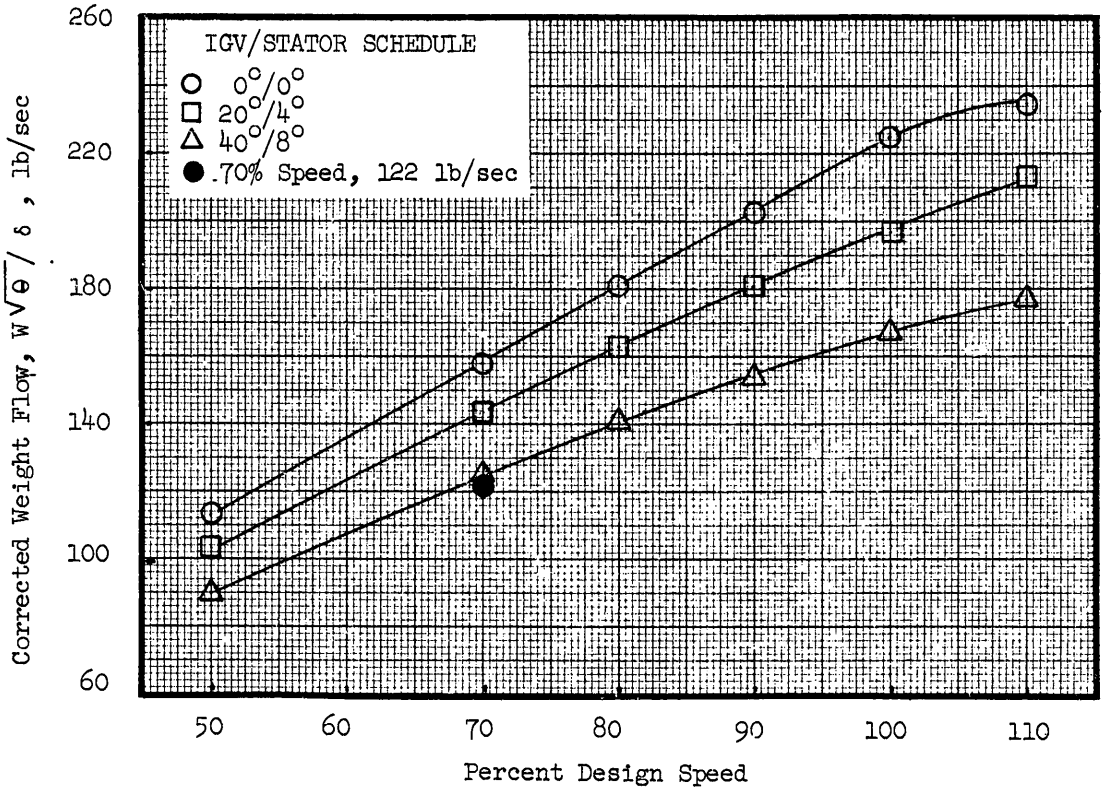

Figure 43. Variation of Stage Inlet Corrected Weight Flow with Rotor Speed and Vane Schedule at the CTL Condition, Undistorted Inlet Flow.

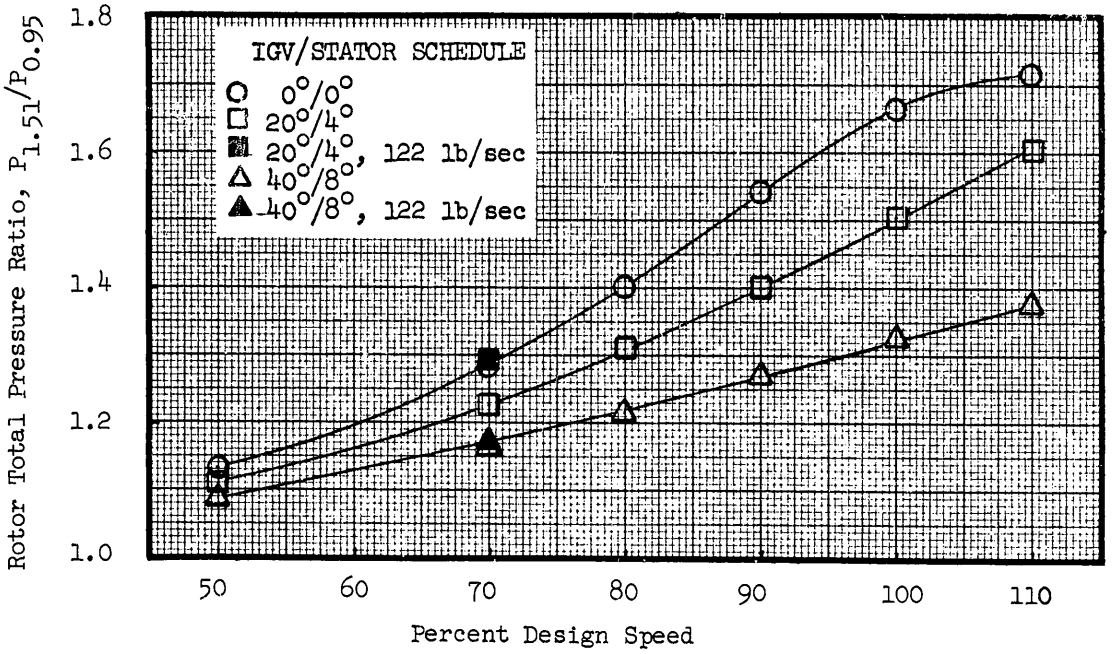

Figure 44. Variation of Rotor Total Pressure Ratio with Rotor Speed and Vane Schedule at the CTL Condition, Undistorted Inlet Flow.

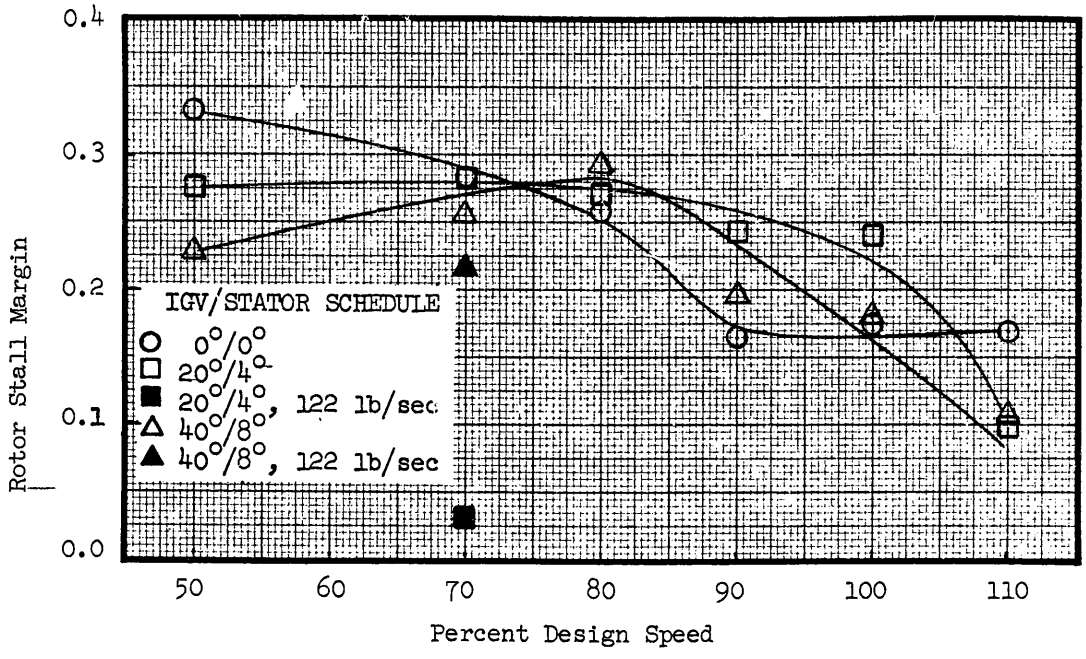

Figure 45. Variation of Rotor Stall Margin with Rotor Speed and Vane Schedule at the CTL Condition, Undistorted Inlet Flow.

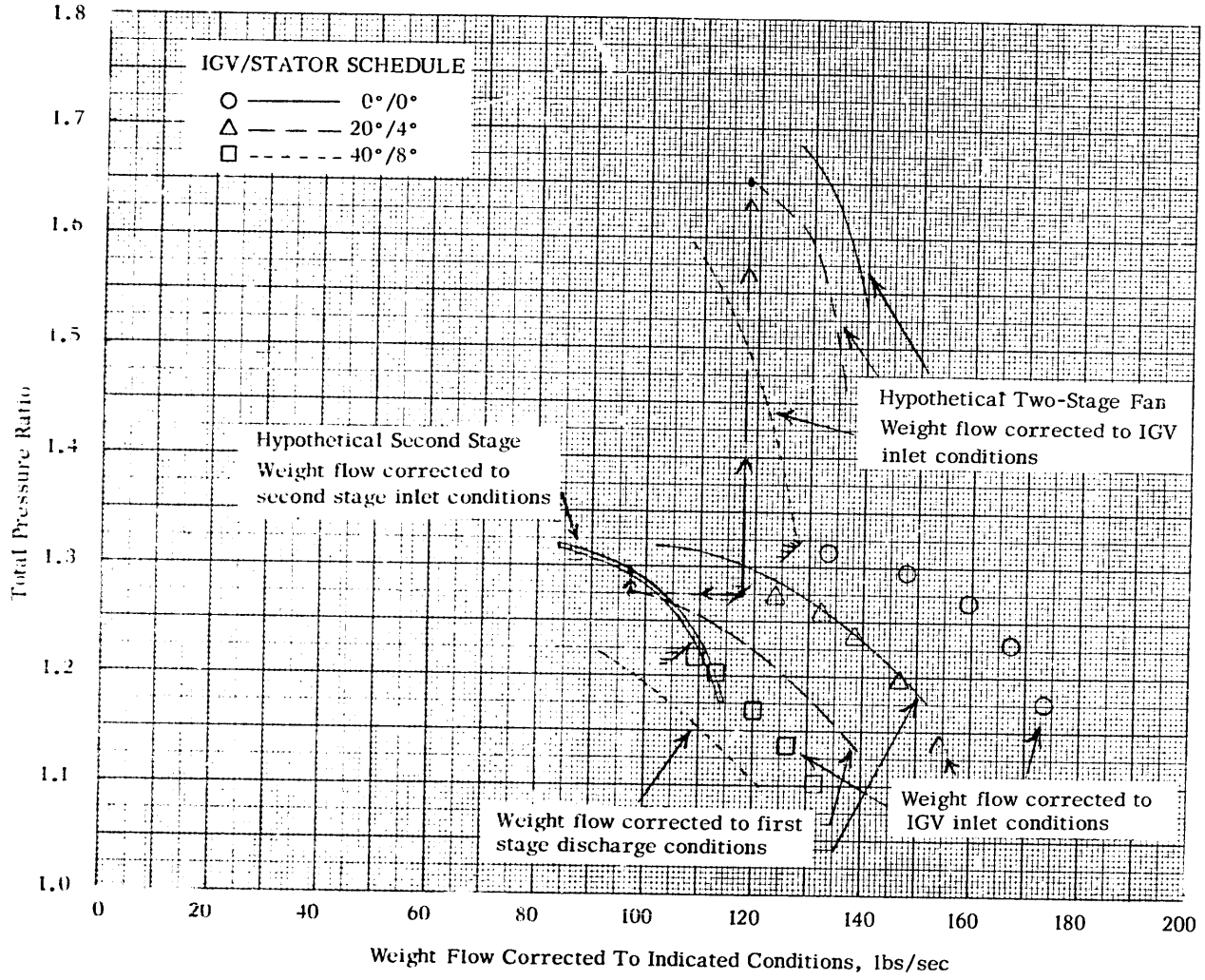

Figure 46. Stage-Matching Analysis Using Variable-Geometry Inlet Guide Vanes.

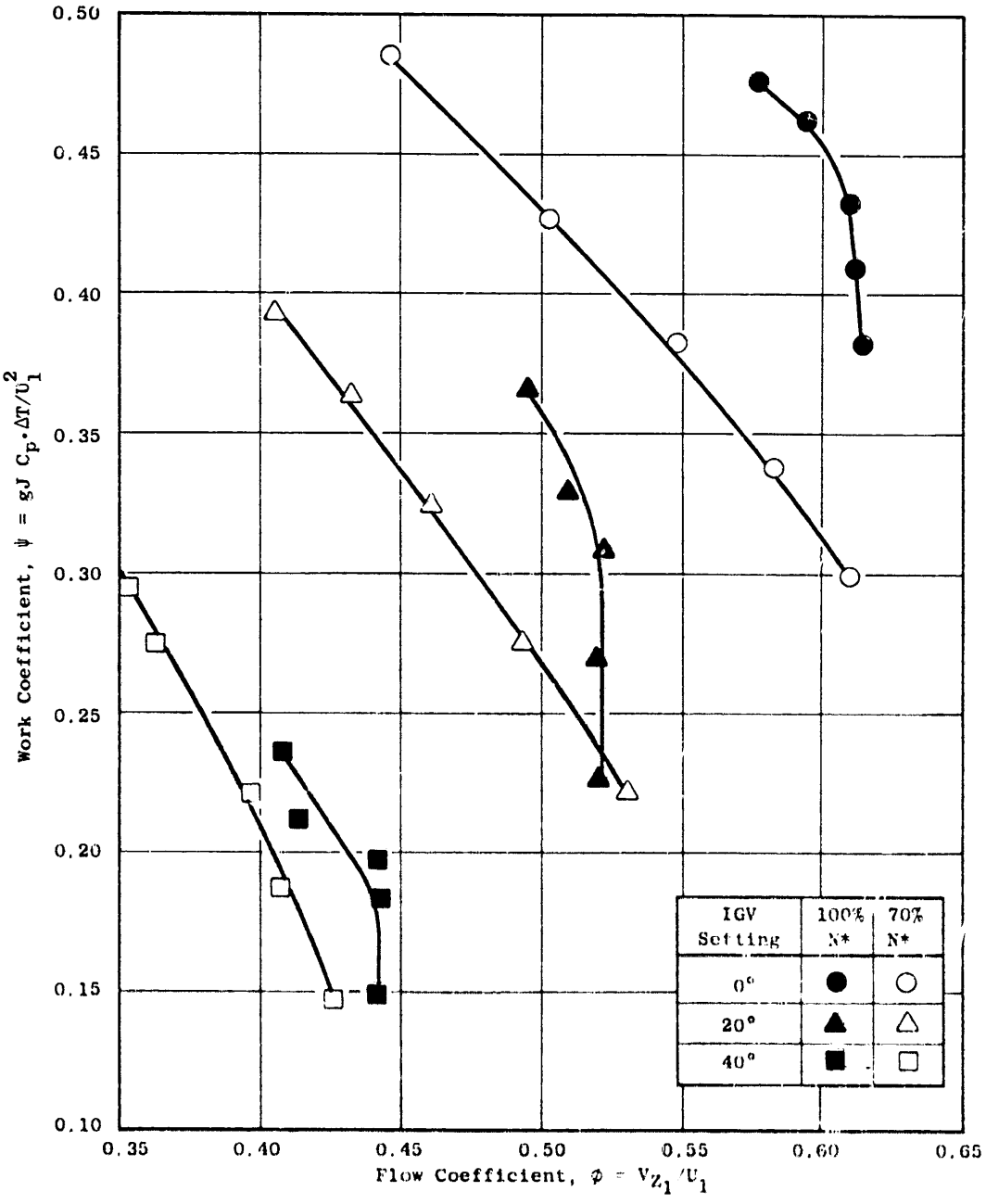

Figure 47. Rotor Blade Element Work Coefficient-Flow Coefficient Characteristics at Pitchline, Uncorrected for Inlet Swirl and Axial Velocity Change: Undistorted Inlet Flow.

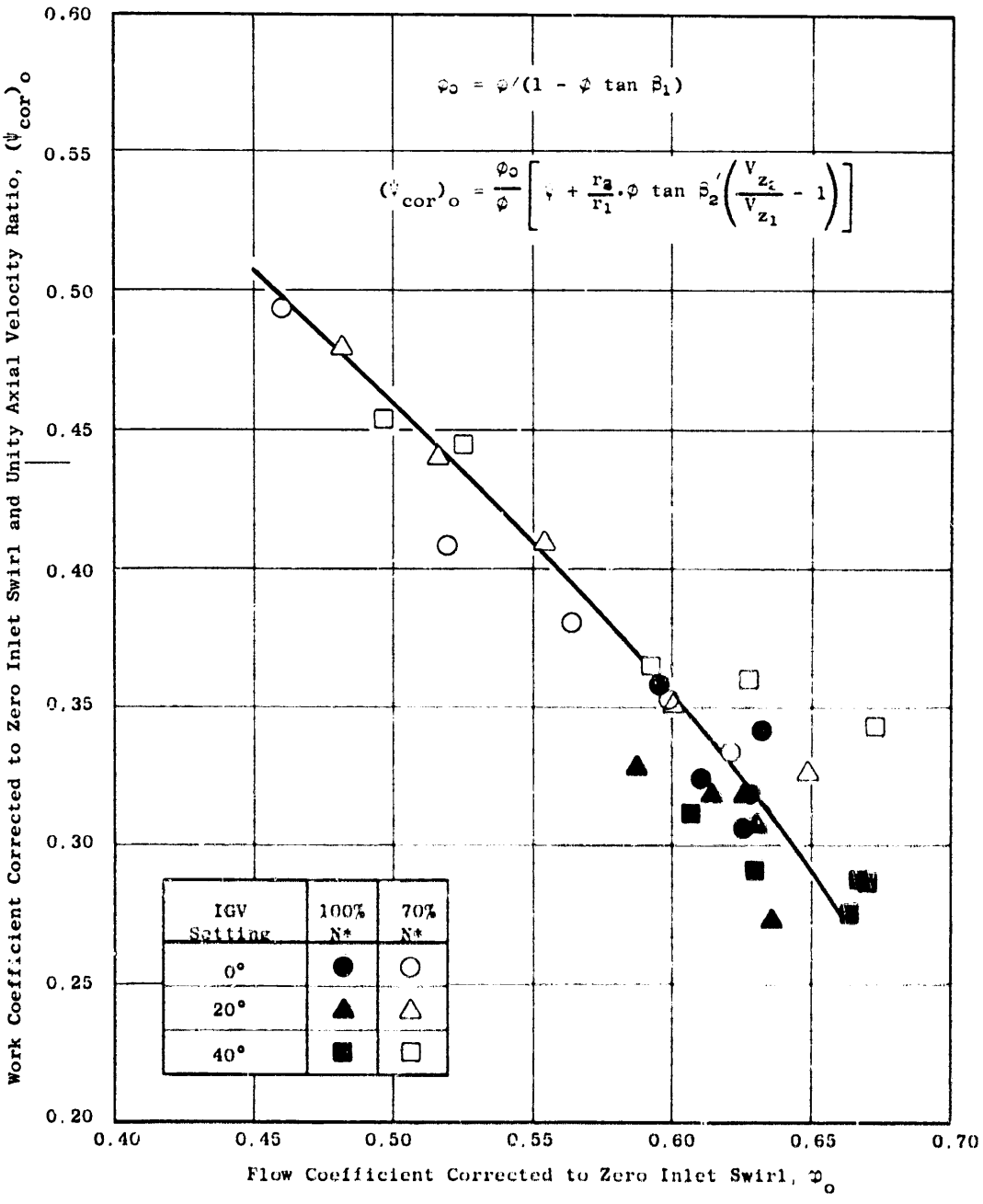

Figure 48. Rotor Blade Element Work Coefficient-Flow Coefficient Characteristics at Pitchline, Corrected for Inlet Swirl and Axial Velocity Change; Undistorted Inlet Flow.

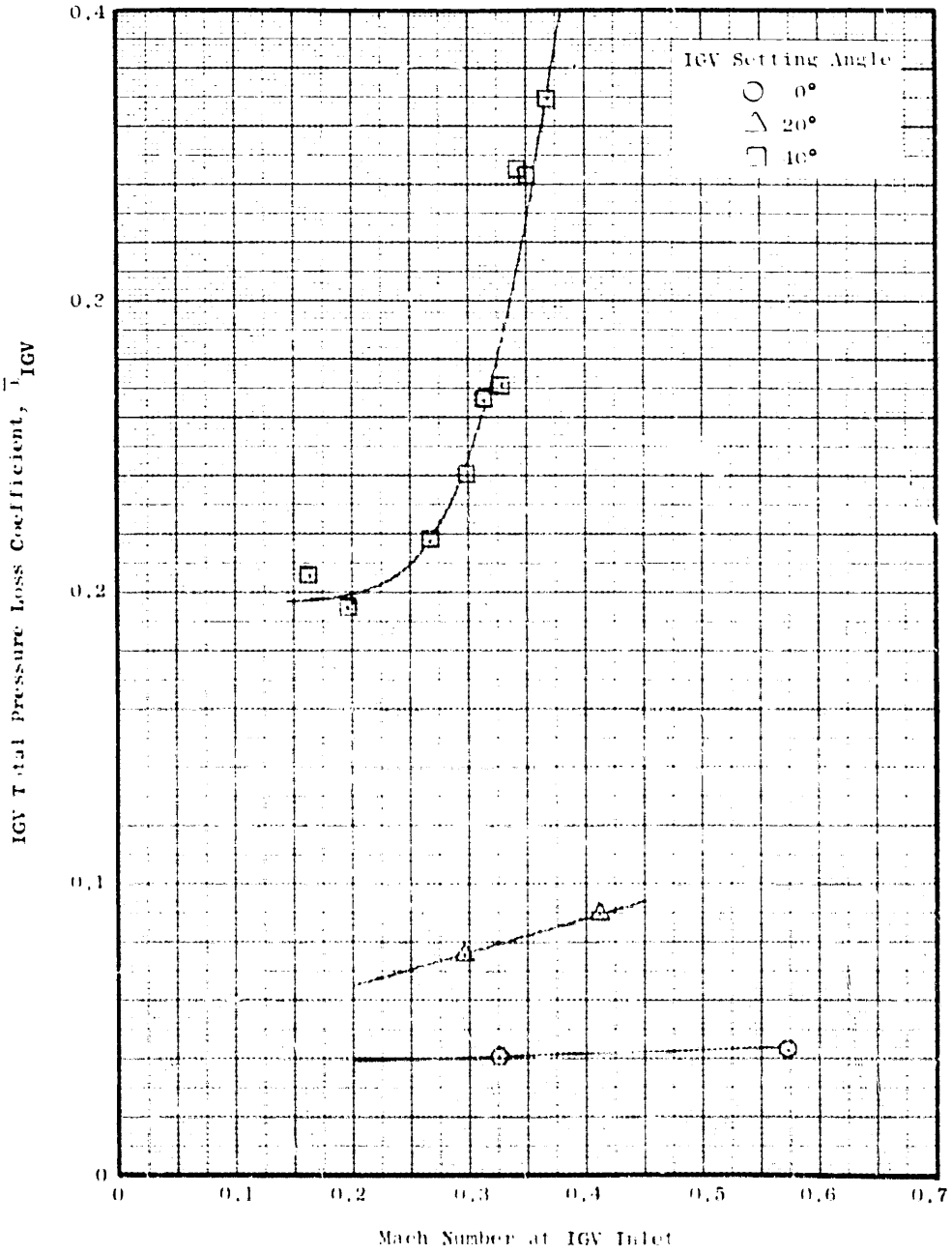

(a) 5% Immersion From Tip

Figure 49. Variation of IGV Total Pressure Loss Coefficient with Mach Number; Undistorted Inlet Flow.

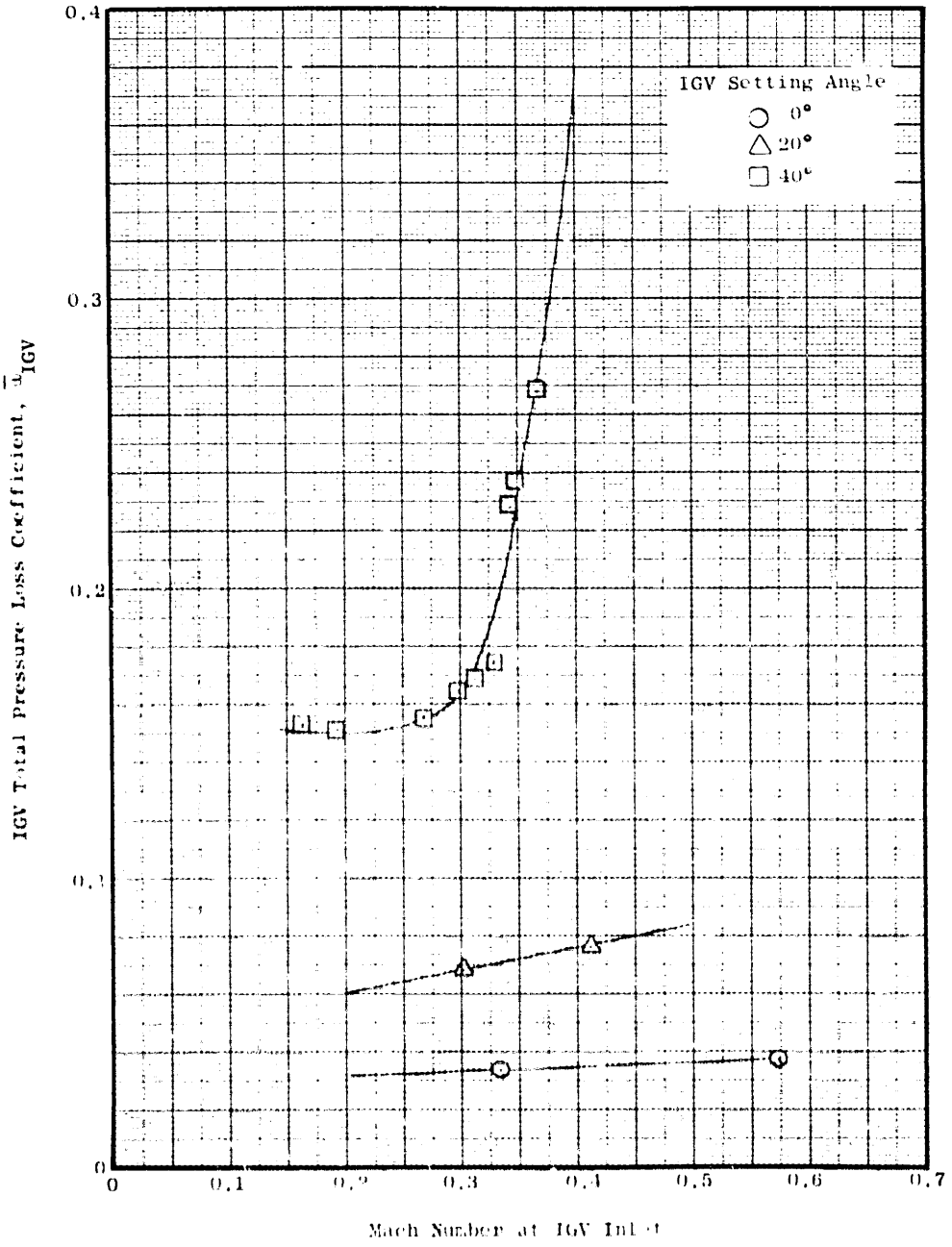

(b) 10% Immersion From Tip

Figure 49. Variation of IGV Total Pressure Loss Coefficient with Mach Number; Undistorted Inlet Flow (Continued).

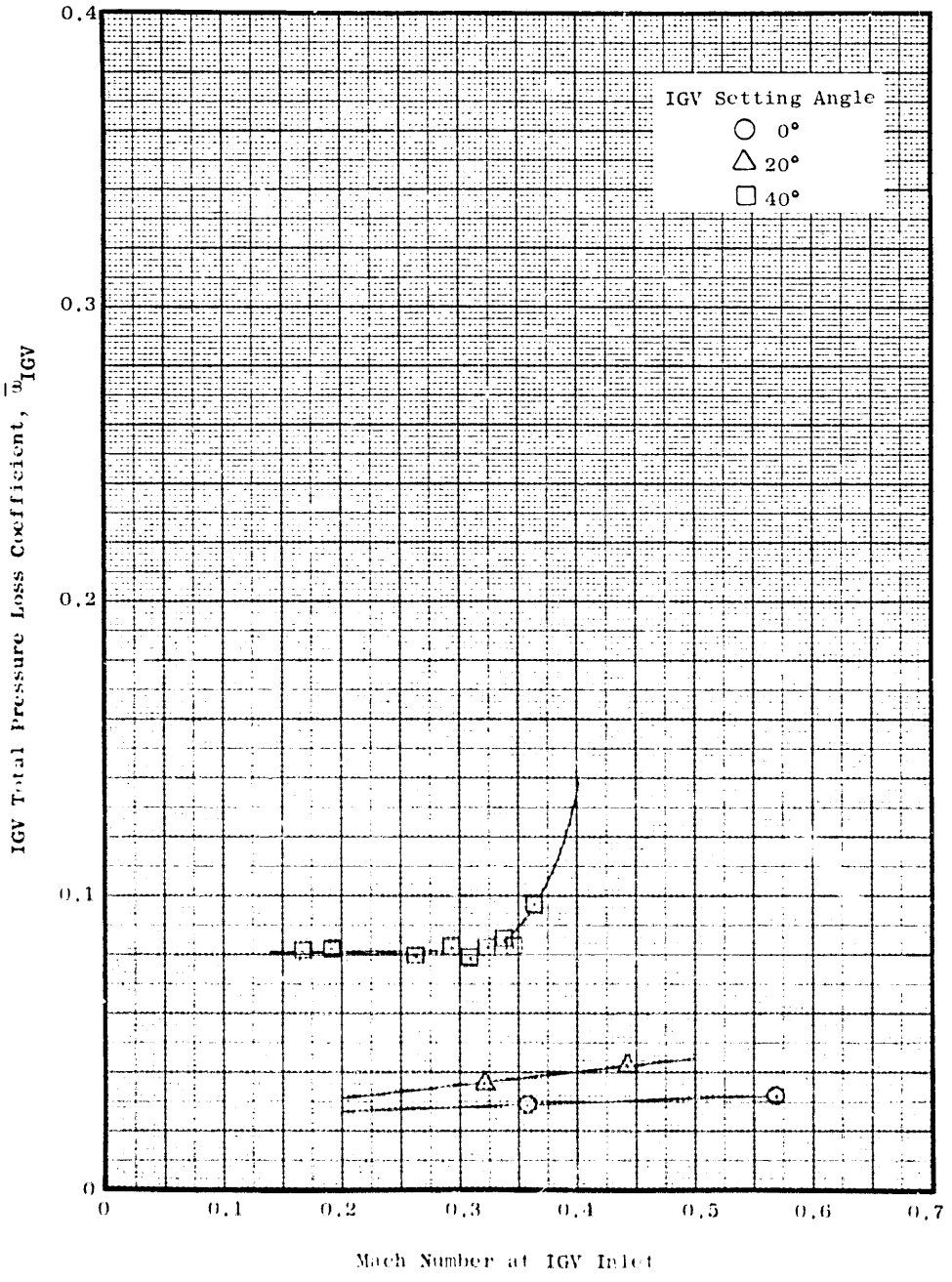

(c) 30% Immersion From Tip

Figure 49. Variation of IGV Total Pressure Loss Coefficient with Mach Number; Undistorted Inlet Flow (Continued).

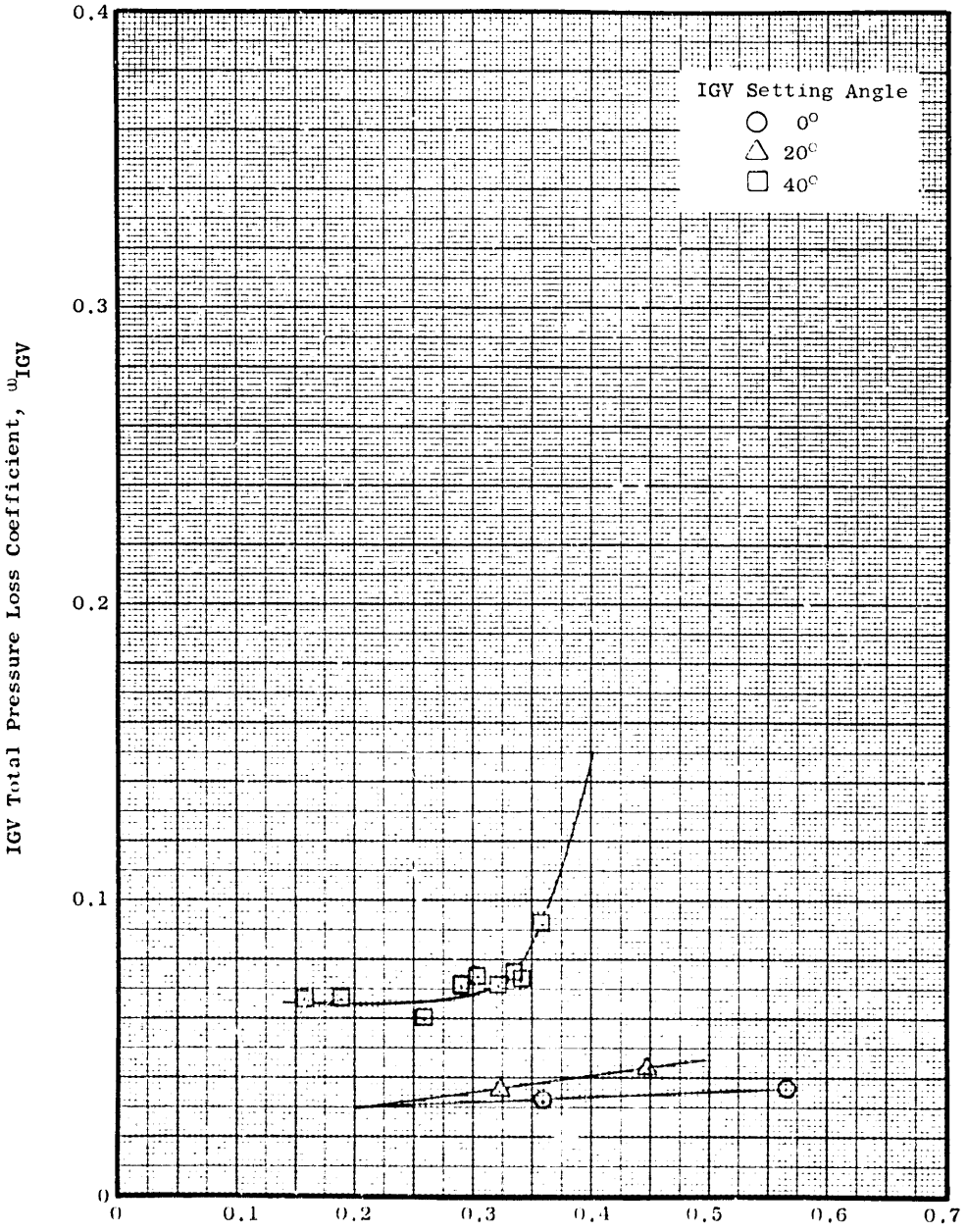

(d) 50% Immersion From Tip

Figure 49. Variation of IGV Total Pressure Loss Coefficient with Mach Number; Undistorted Inlet Flow (Continued).

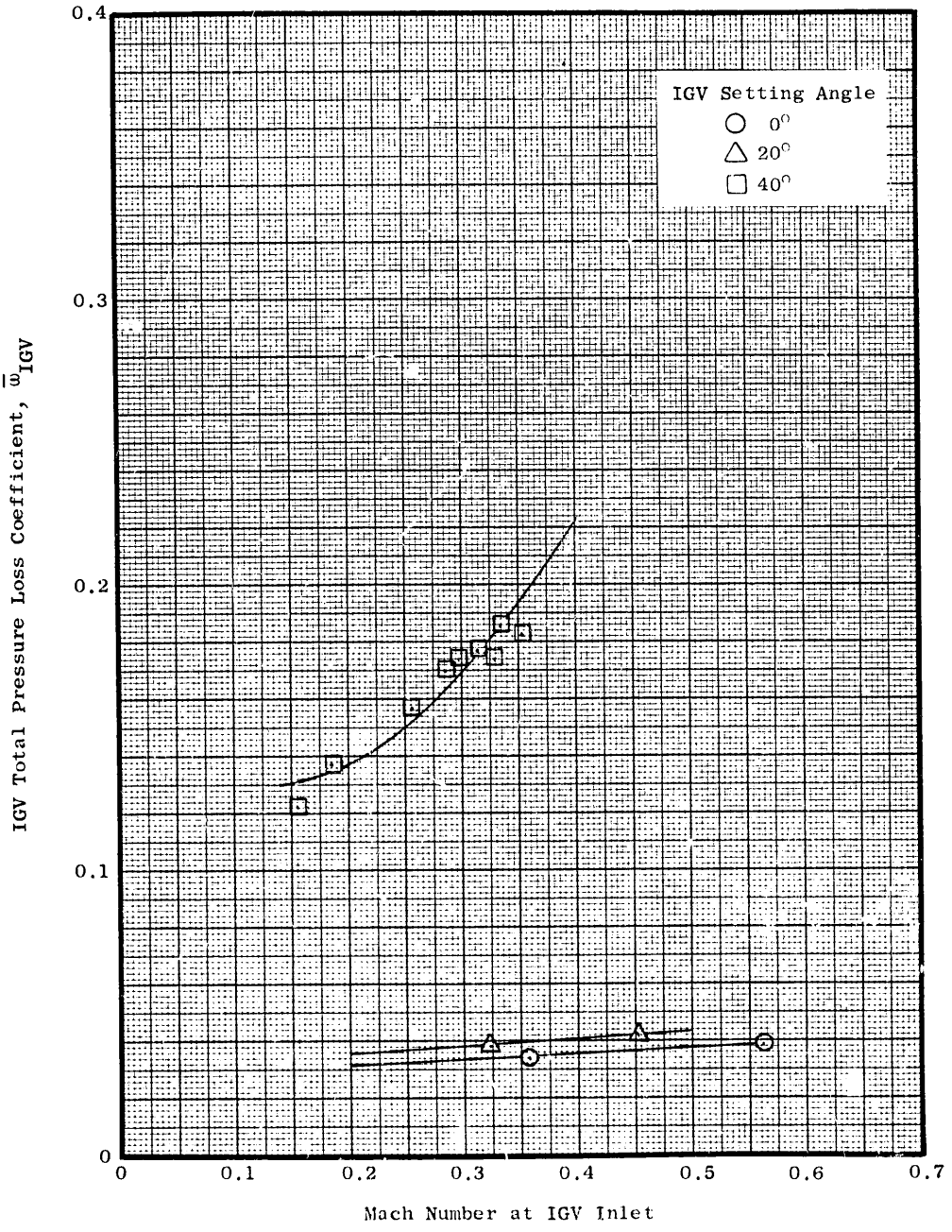

(e) 70% Immersion From Tip

Figure 49. Variation of IGV Total Pressure Loss Coefficient with Mach Number; Undistorted Inlet Flow (Continued).

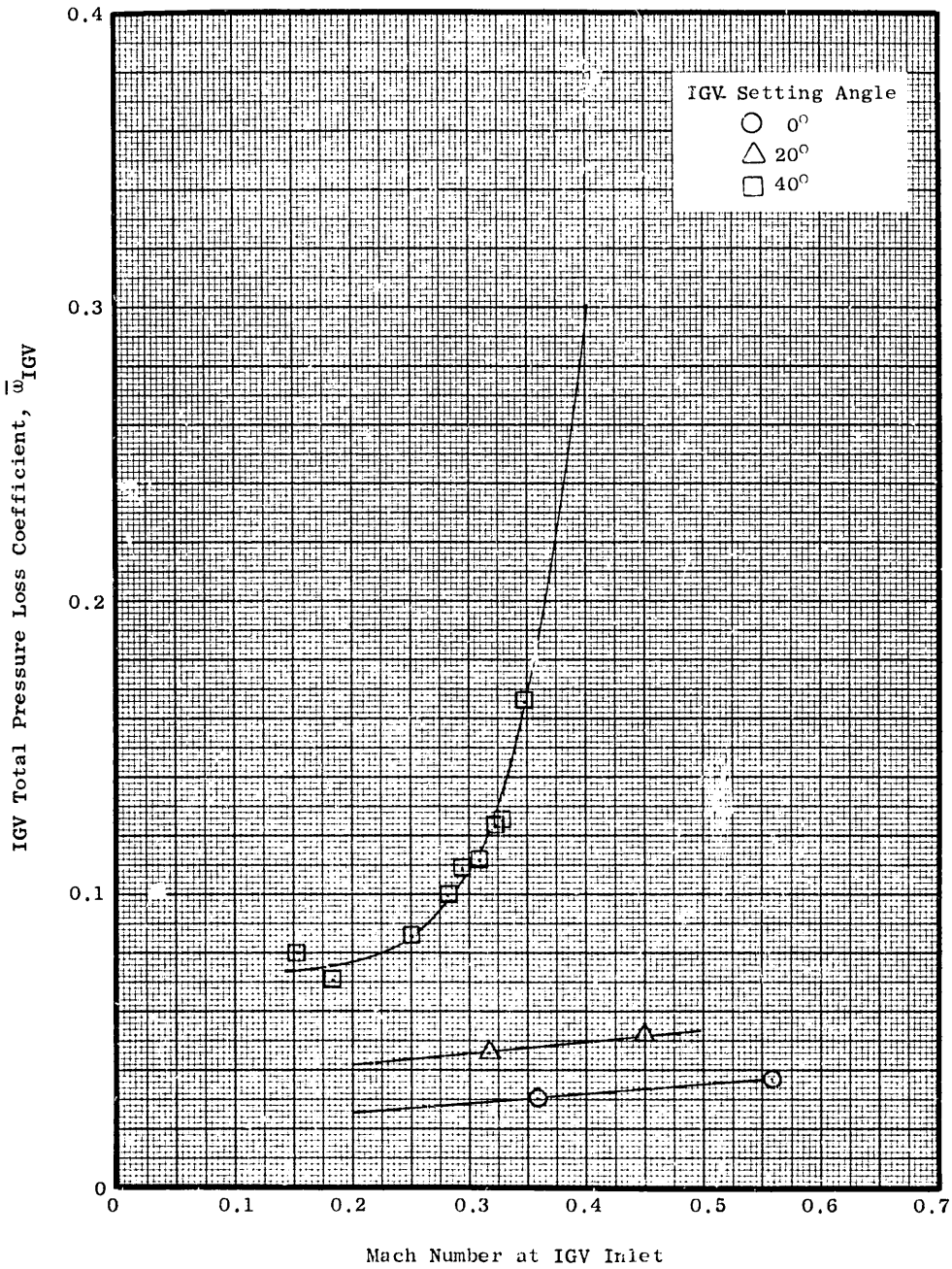

(f) 90% Immersion From Tip

Figure 49. Variation of IGV Total Pressure Loss Coefficient with Mach Number; Undistorted Inlet Flow (Continued).

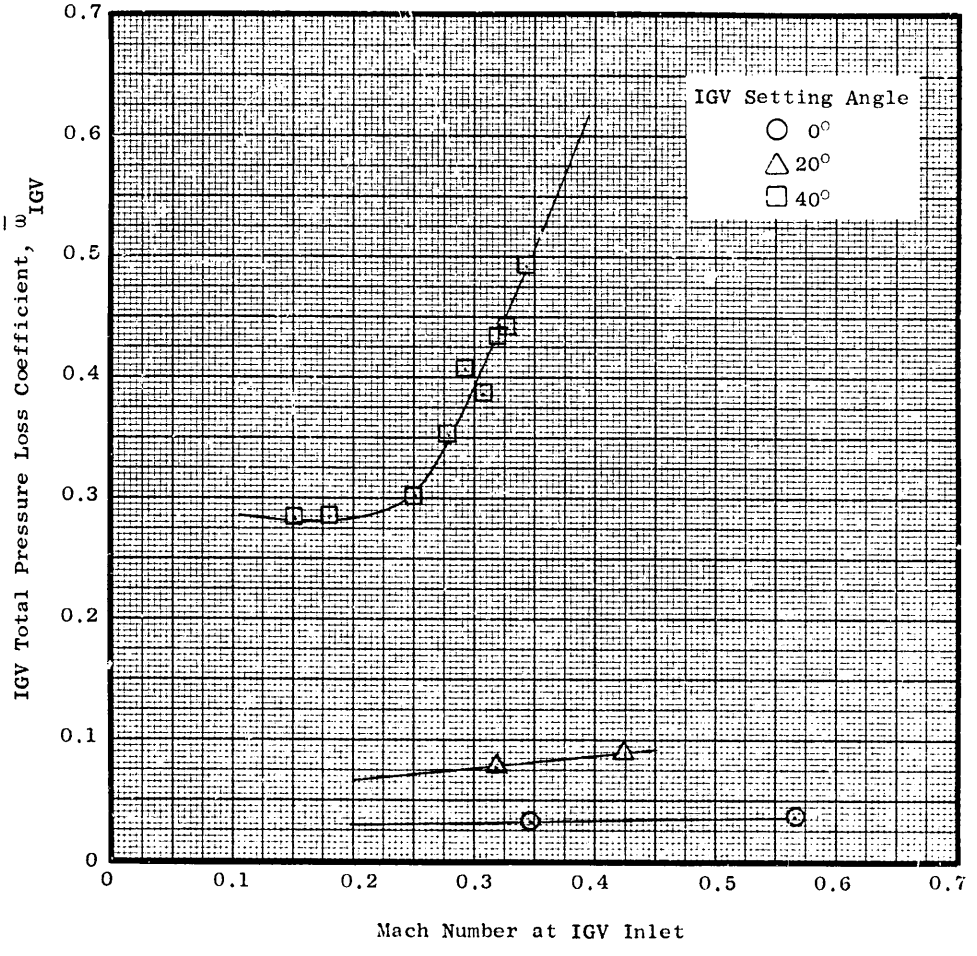

(g) 95% Immersion From Tip

Figure 49. Variation of IGV Total Pressure Loss Coefficient with Mach Number; Undistorted Inlet Flow (Concluded).

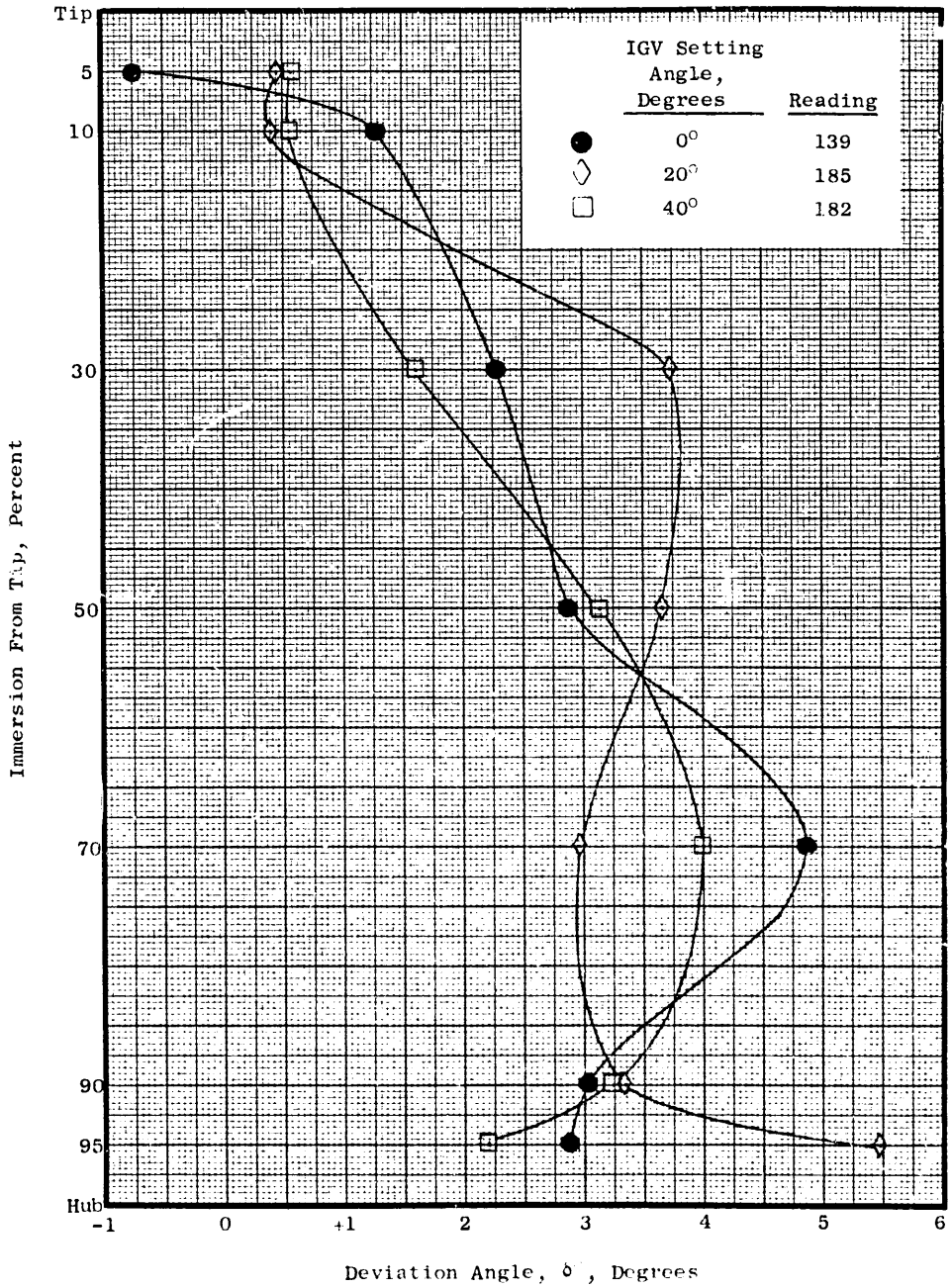

Figure 50. Radial Variation of IGV Deviation Angle at IGV Setting Angles of 0°, 20°, and 40°; Undistorted Inlet Flow.

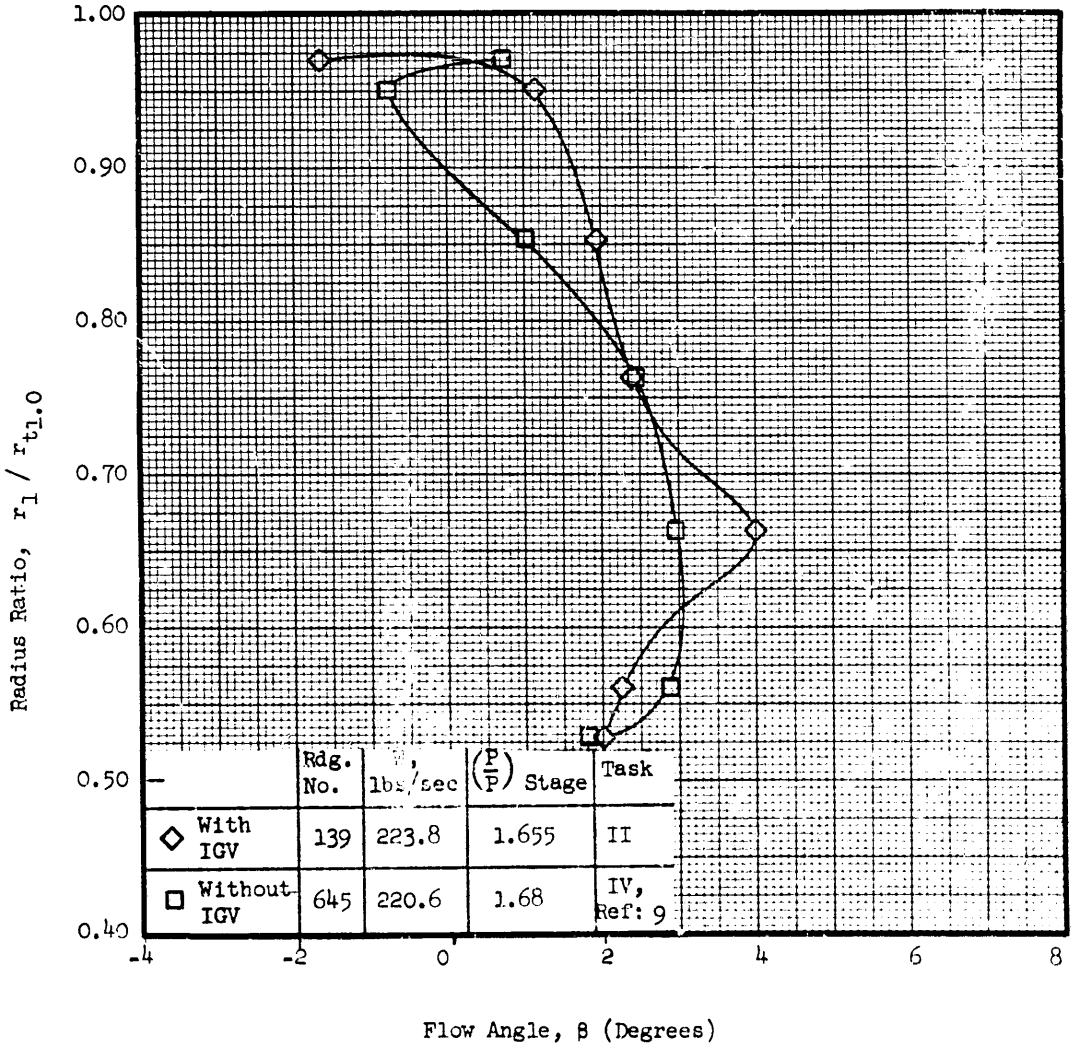

Figure 51. Radial Profiles of Task II Rotor Inlet Absolute Flow Angle with IGV at Nominal Setting and Without IGV; 100% Speed, Near Design Condition, Undistorted Inlet Flow.

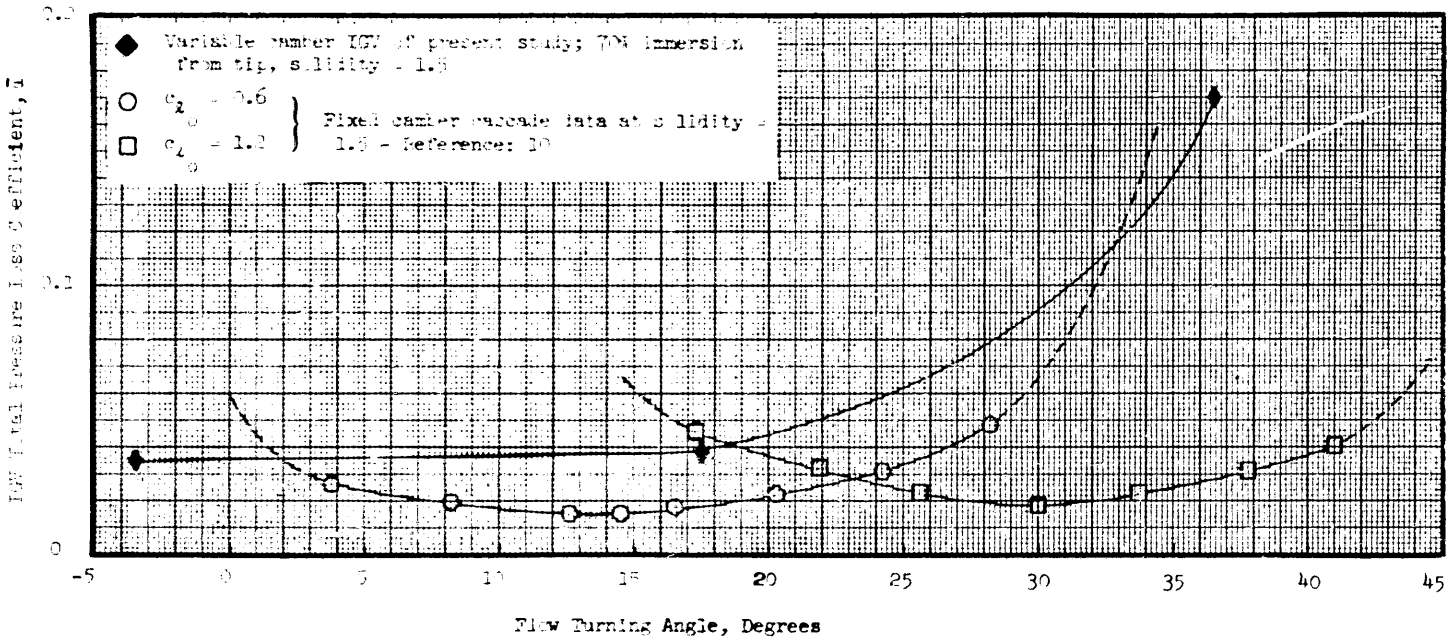

Figure 52. Comparison of Variable Geometry Inlet Guide Vane Total Pressure Loss Coefficient Data with those of Conventionally Cambered Guide Vane Airfoil Sections Having Equivalent Values of Row Solidity.

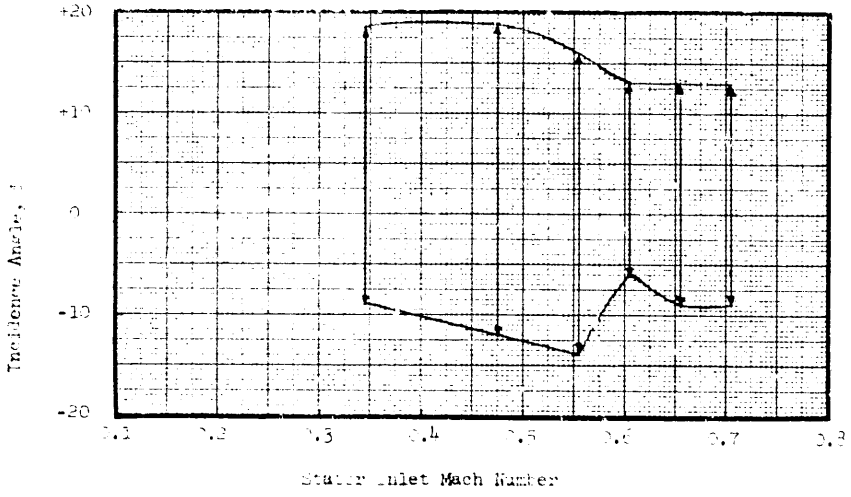

Figure 53 (b). Variation with Mach Number of Stator Incidence Angle Range for Twice Minimum Loss Condition at 50% Immersion from Tip, Undistorted Inlet Flow.

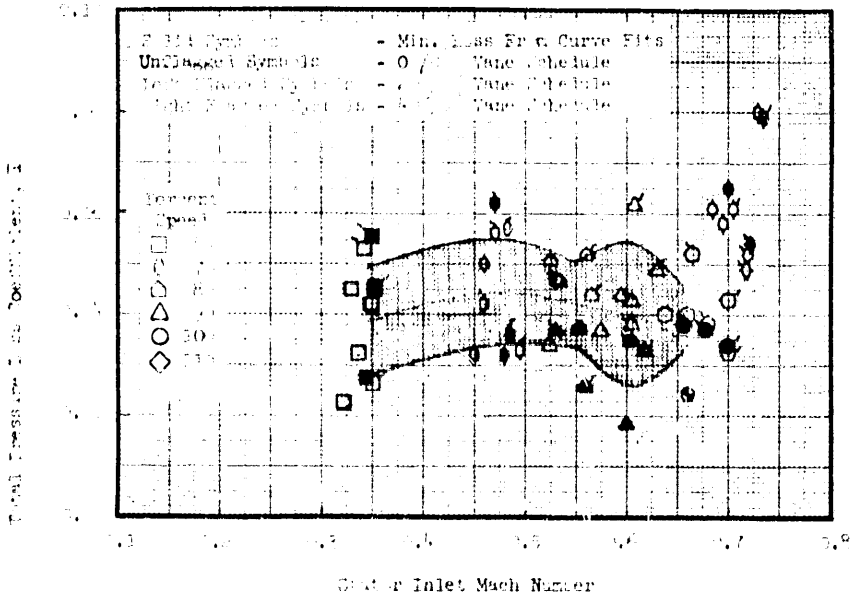

Figure 53 (a). Variation of Stator Minimum Loss Coefficient with Stator Inlet Mach Number at 50% Immersion from Tip, Undistorted Inlet Flow.

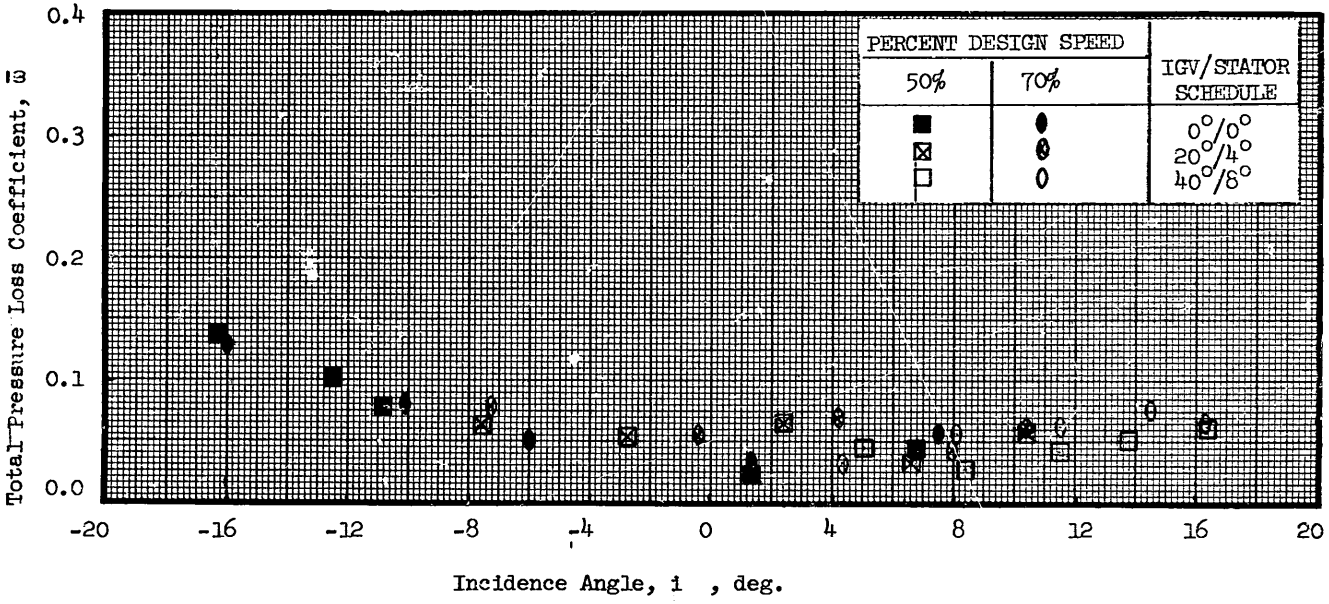

(a) 50% and 70% Design Speeds

Figure 54. Stator Blade Element Total Pressure Loss Coefficient Versus Stator Incidence Angle at 50% Immersion from Tip with Undistorted Inlet Flow, All Three Vane Schedules.

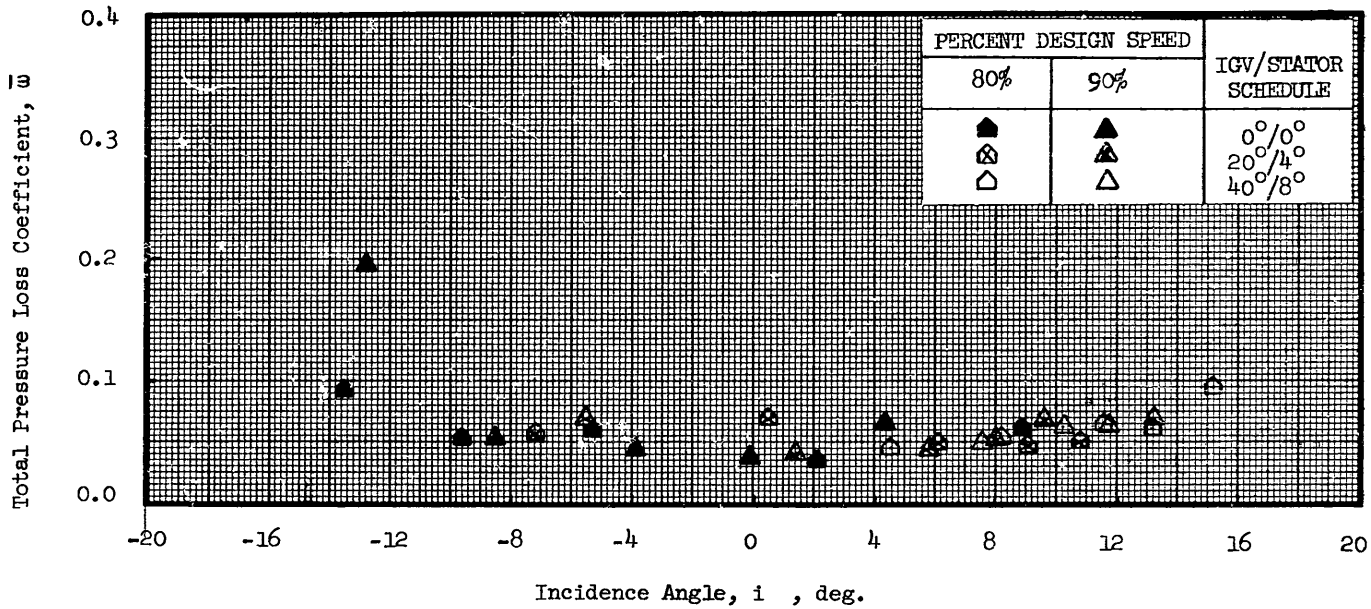

(b) 80% and 90% Design Speeds

Figure 54. Stator Blade Element Total Pressure Loss Coefficient Versus Stator Incidence Angle at 50% Immersion from Tip with Undistorted Inlet Flow, All Three Vane Schedules (Continued).

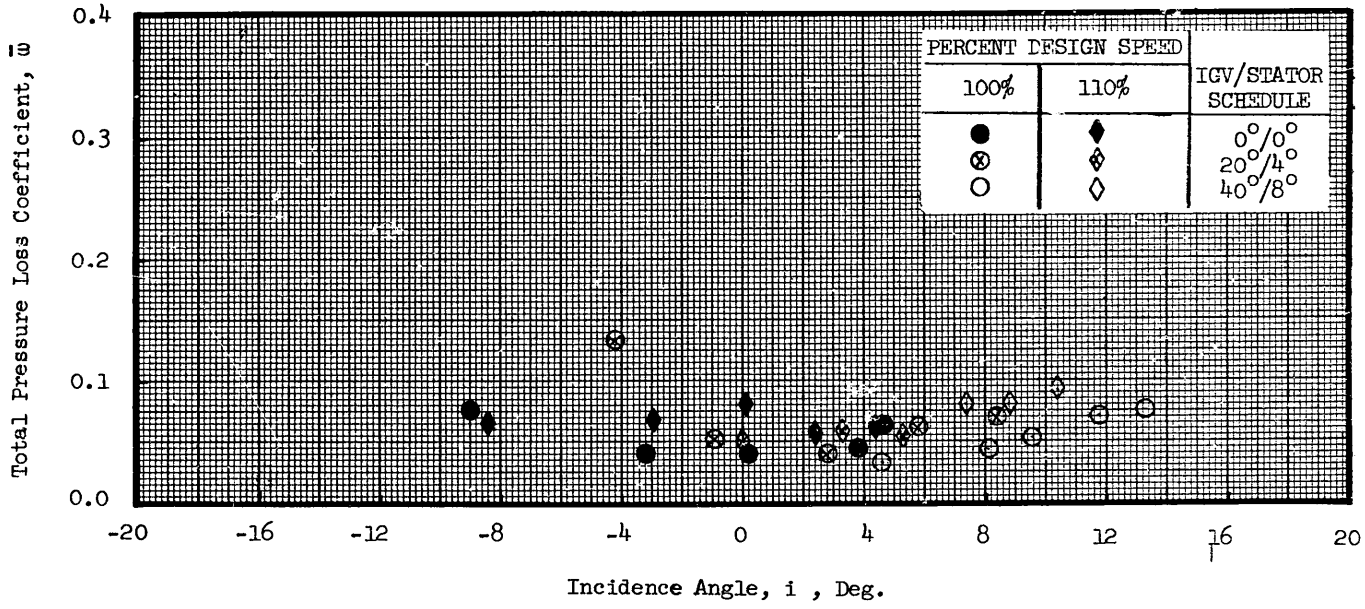

(c) 100% and 110% Design Speeds

Figure 54. Stator Blade Element Total Pressure Loss Coefficient Versus Stator Incidence Angle at 50% Immersion from Tip with Undistorted Inlet Flow, All Three Vane Schedules (Concluded).

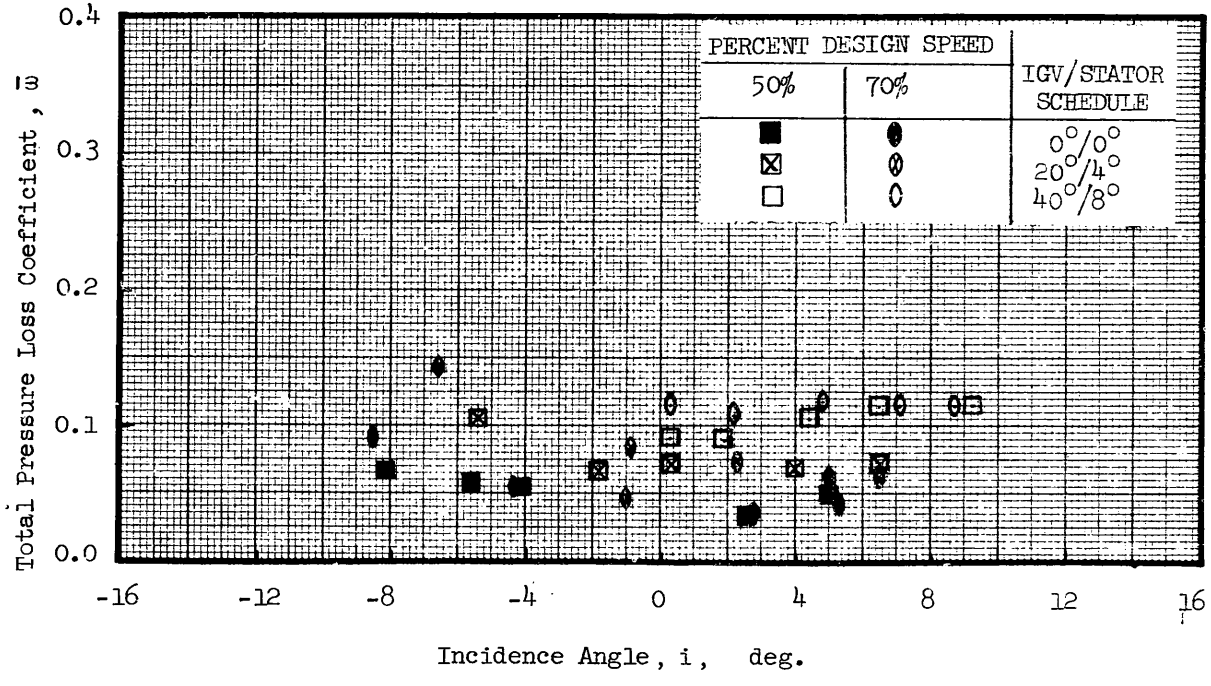

a. 50% and 70% Design Speeds

Figure 55. Stator Blade Element Total Pressure Loss Coefficient Versus Incidence Angle at 90% Immersion from Tip with Undistorted Inlet Flow, All Three Vane Schedules.

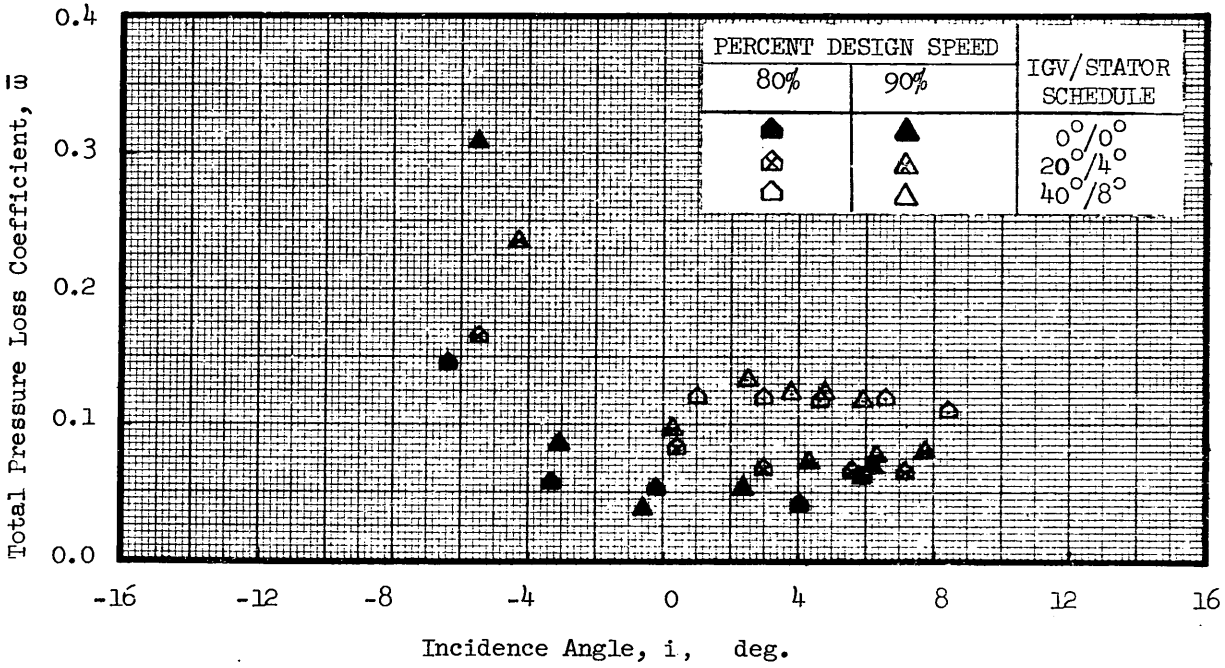

b. 80% and 90% Design Speeds

Figure 55. Stator Blade Element Total Pressure Loss Coefficient Versus Incidence Angle at 90% Immersion from Tip with Undistorted Inlet Flow, All Three Vane Schedules (Continued).

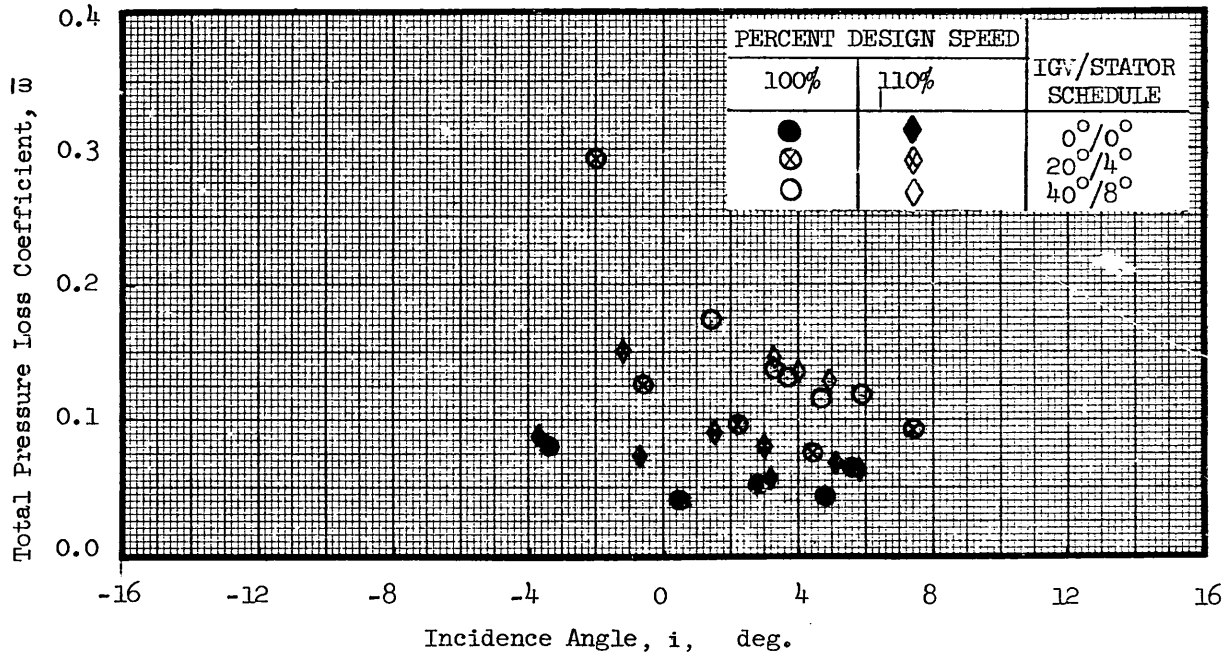

c. 100% and 110% Design Speeds

Figure 55. Stator Blade Element Total Pressure Loss Coefficient Versus Incidence Angle at 90% Immersion from Tip with Undistorted Inlet Flow, All Three Vane Schedules (Concluded).

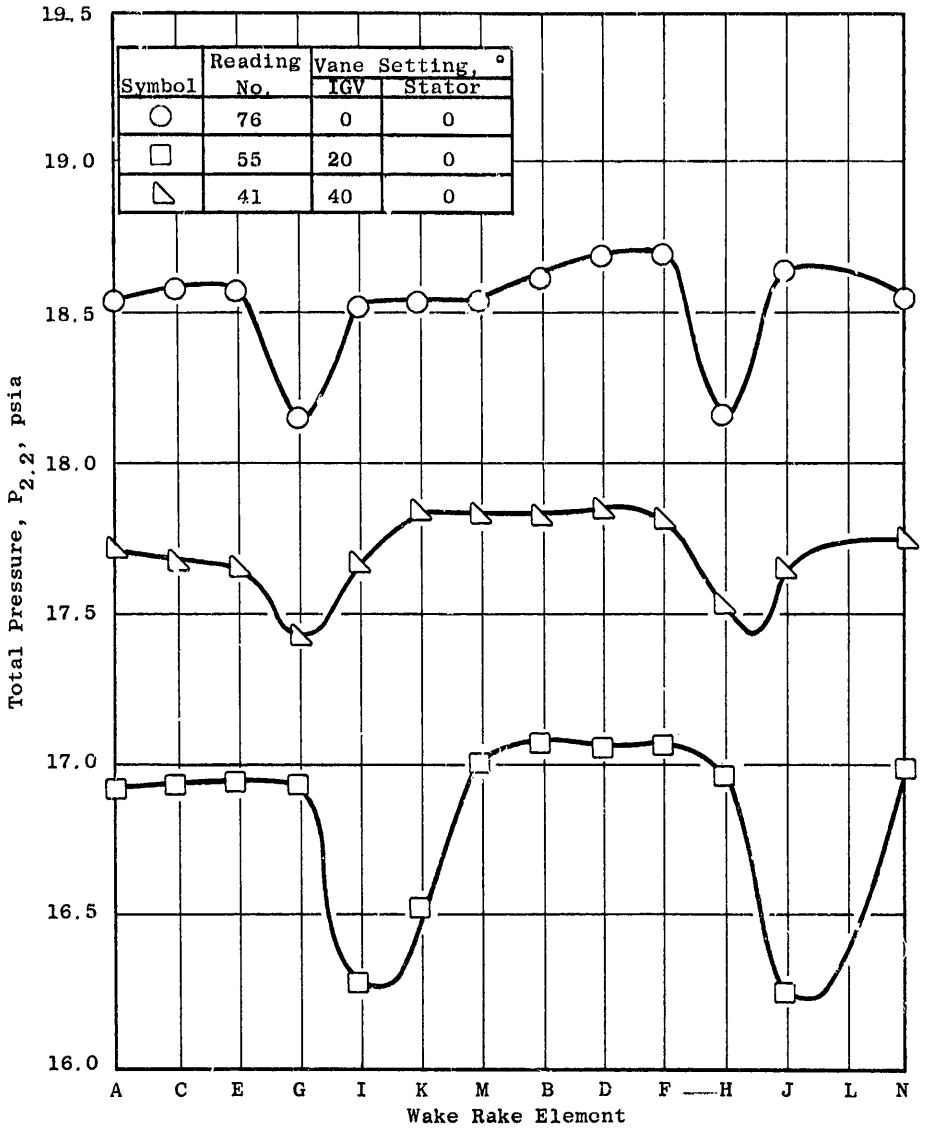

(a) 50% Immersion from Tip

Figure 56. Typical Stator Wake Profiles at 70% Speed, Constant Throttle Valve Setting with Undistorted Inlet Flow; IGV Setting Angles 0°, 20°, and 40°, Zero Stator Setting Angle.

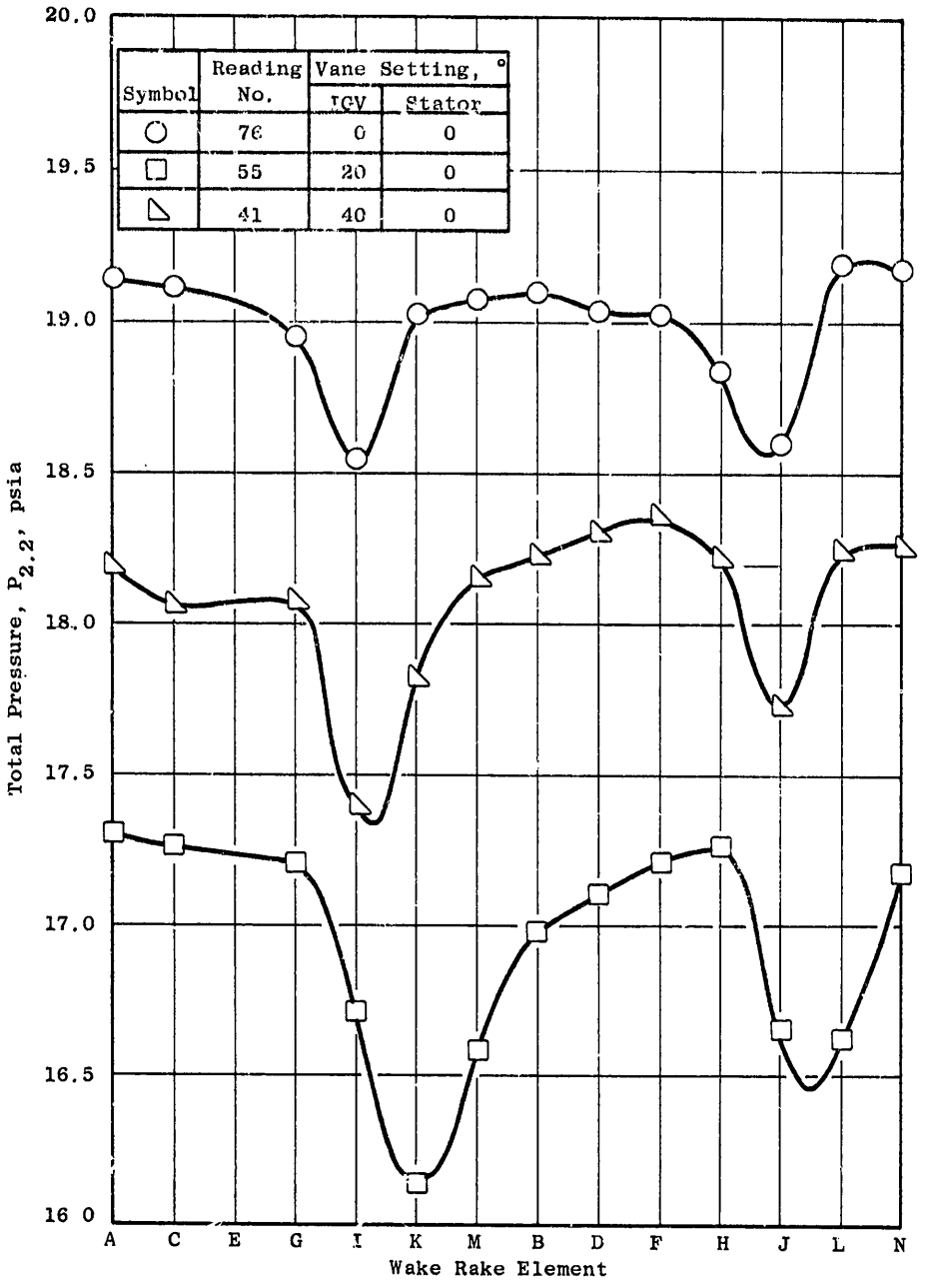

(b) 90% Immersion from Tip

Figure 56. Typical Stator Wake Profiles at 70% Speed, Constant Throttle Valve Setting with Undistorted Inlet Flow; IGV Setting Angles 0°, 20°, and 40°, Zero Stator Setting Angle (Concluded).

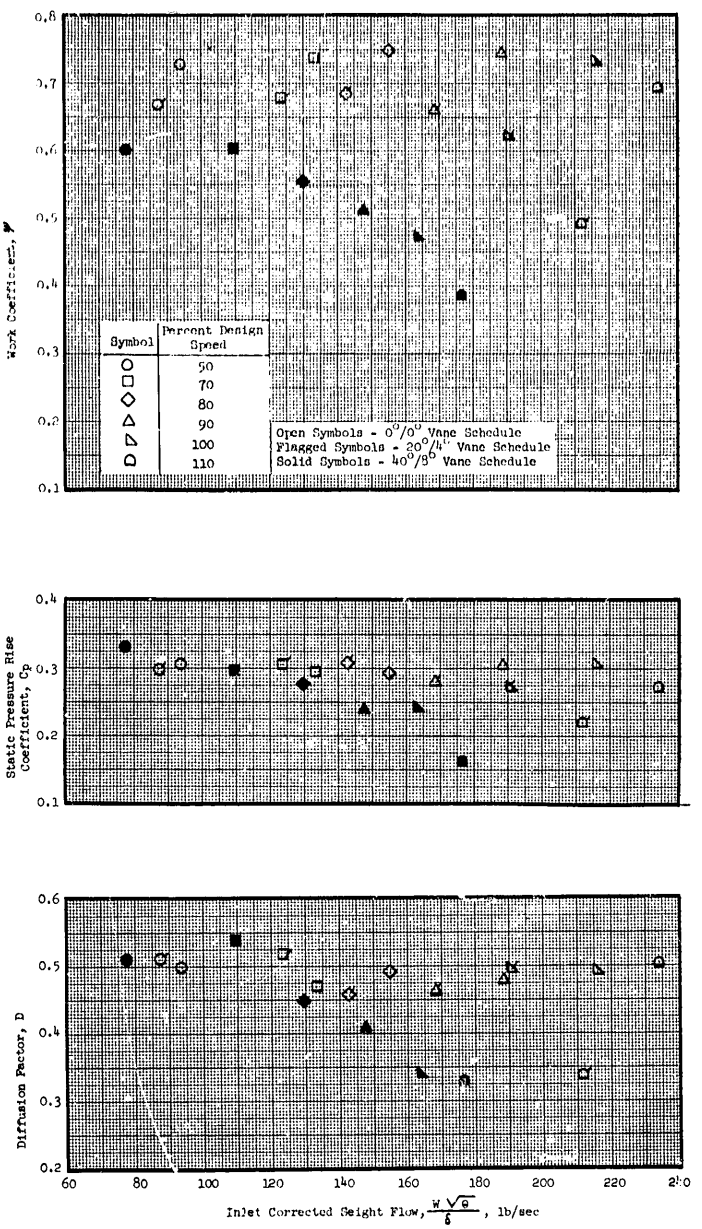

Figure 57 (a). Variation of Rotor Aerodynamic Loading Parameters with IGV/Stator Schedule and Tip Speed Near Stall in Undistorted Inlet Flow; 5% Immersion from Tip.

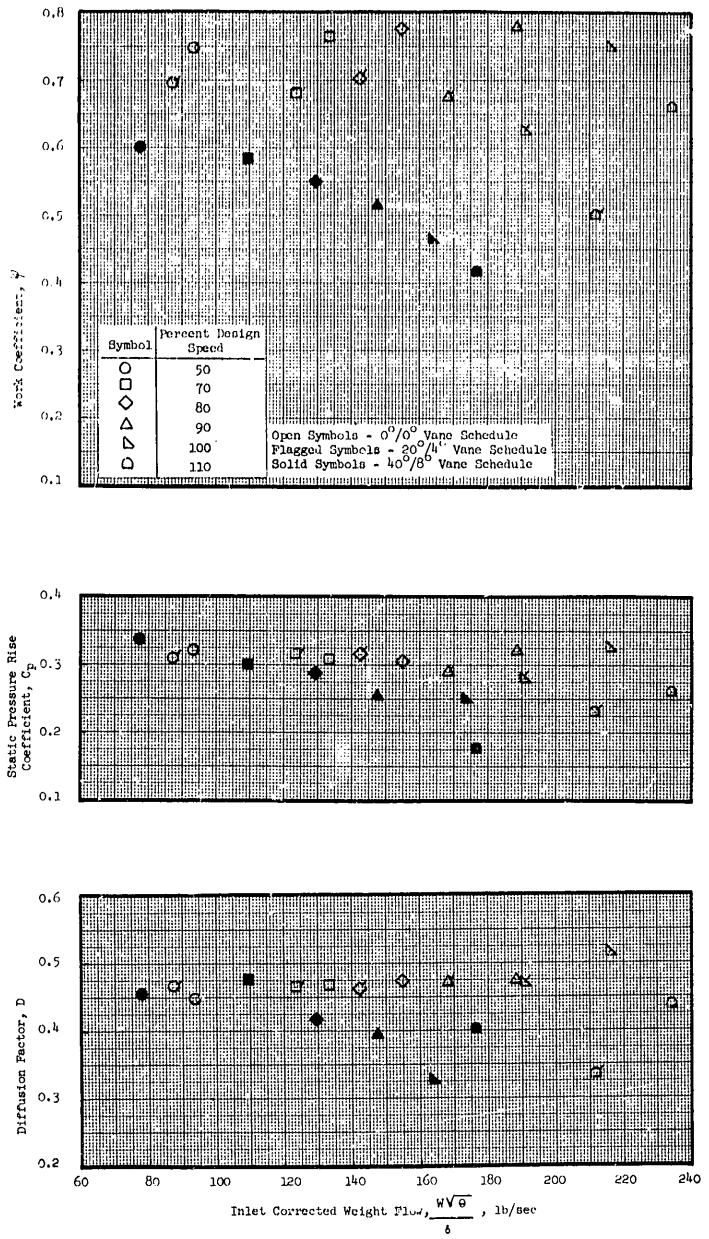

Figure 57 (b). Variation of Rotor Aerodynamic Loading Parameters with IGV/Stator Schedule and Tip Speed Near Stall in Undistorted Inlet Flow; 10% Immersion from Tip.

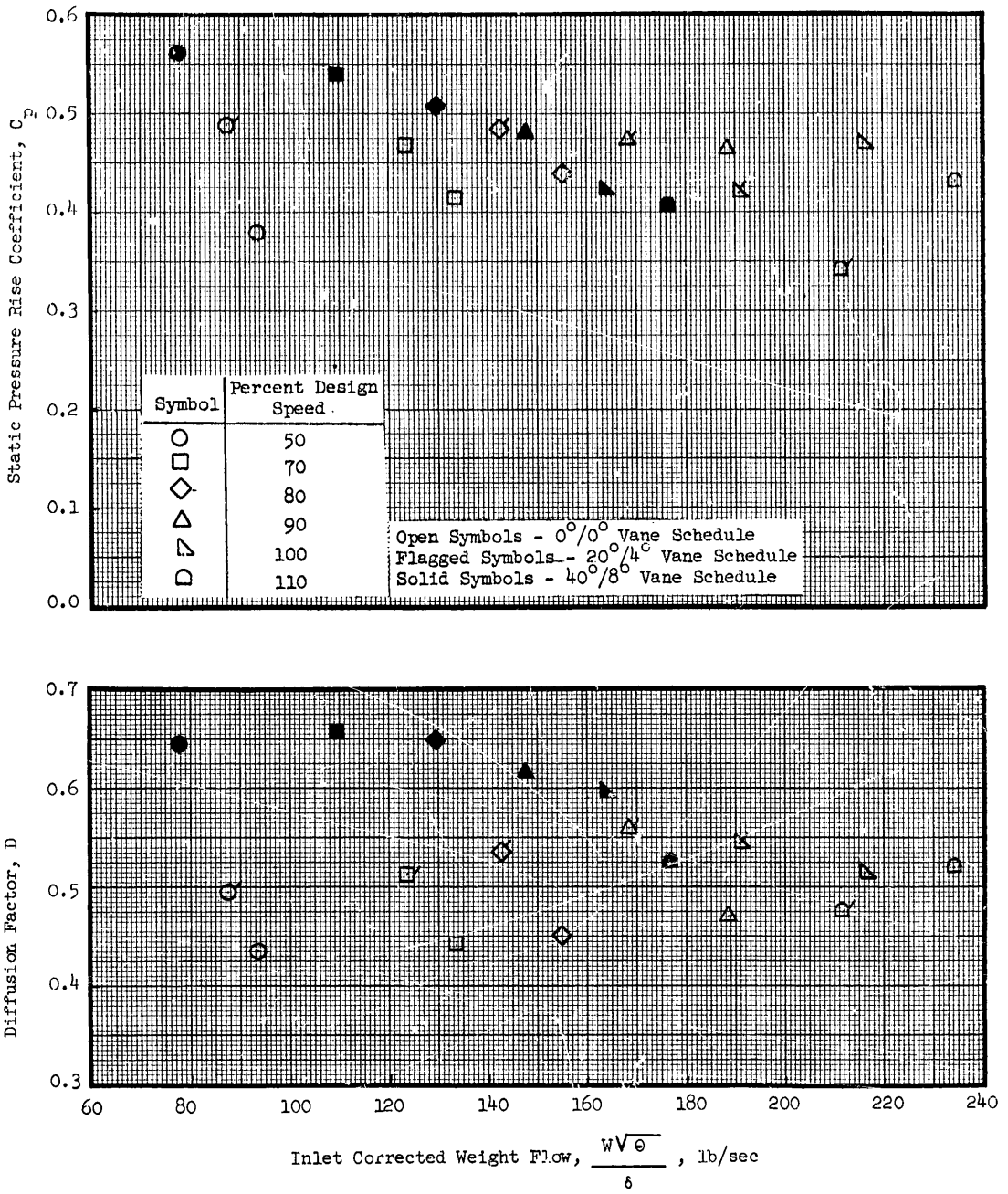

Figure 58 (a). Variation of Stator Aerodynamic Loading Parameters with IGV/Stator Schedule and Tip Speed Near Stall in Undistorted Inlet Flow; 90% Immersion from Tip.

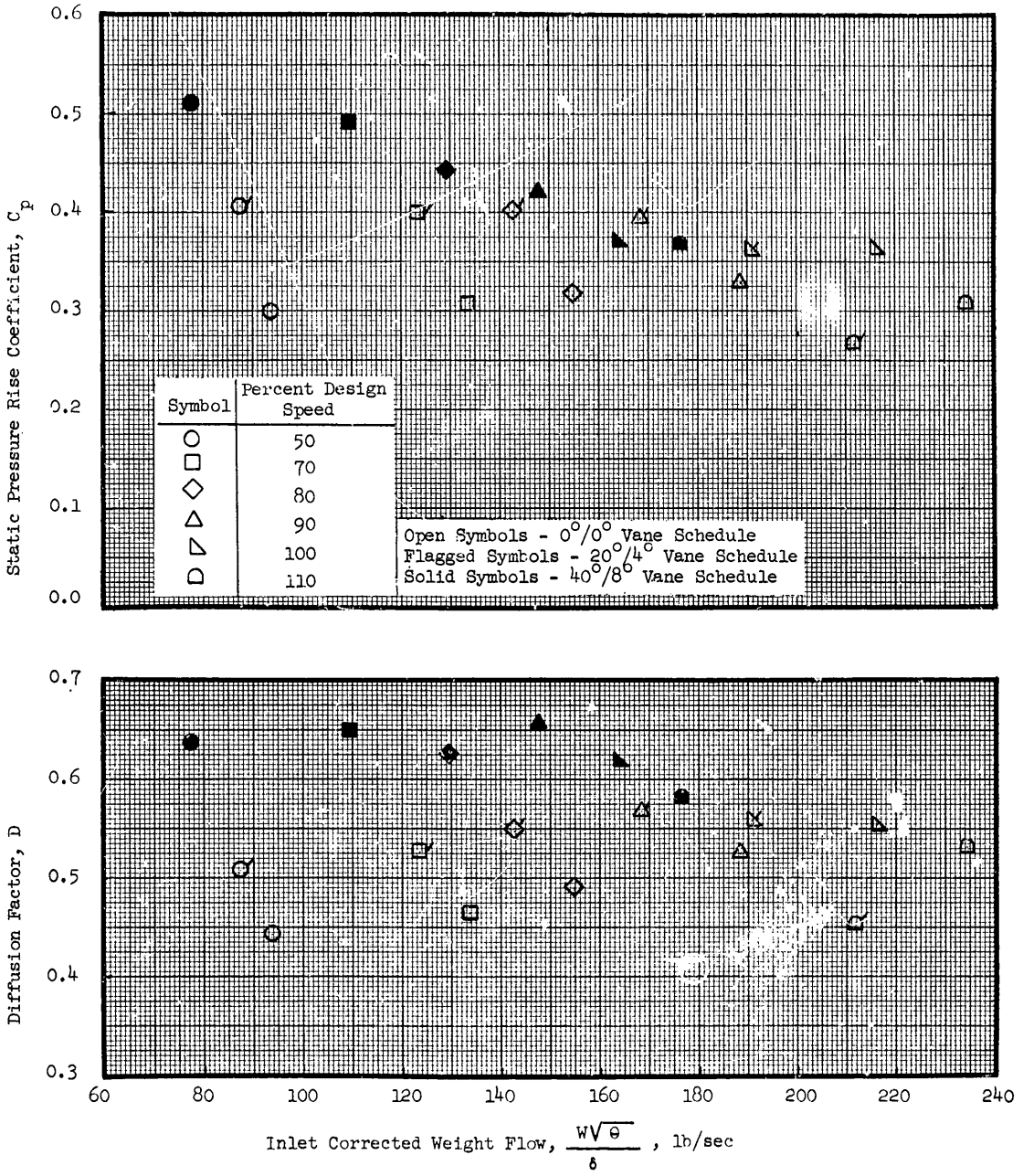

Figure 58 (b). Variation of Stator Aerodynamic Loading Parameters with IGV/Stator Schedule and Tip Speed Near Stall in Undistorted Inlet Flow; 95% Immersion from Tip.

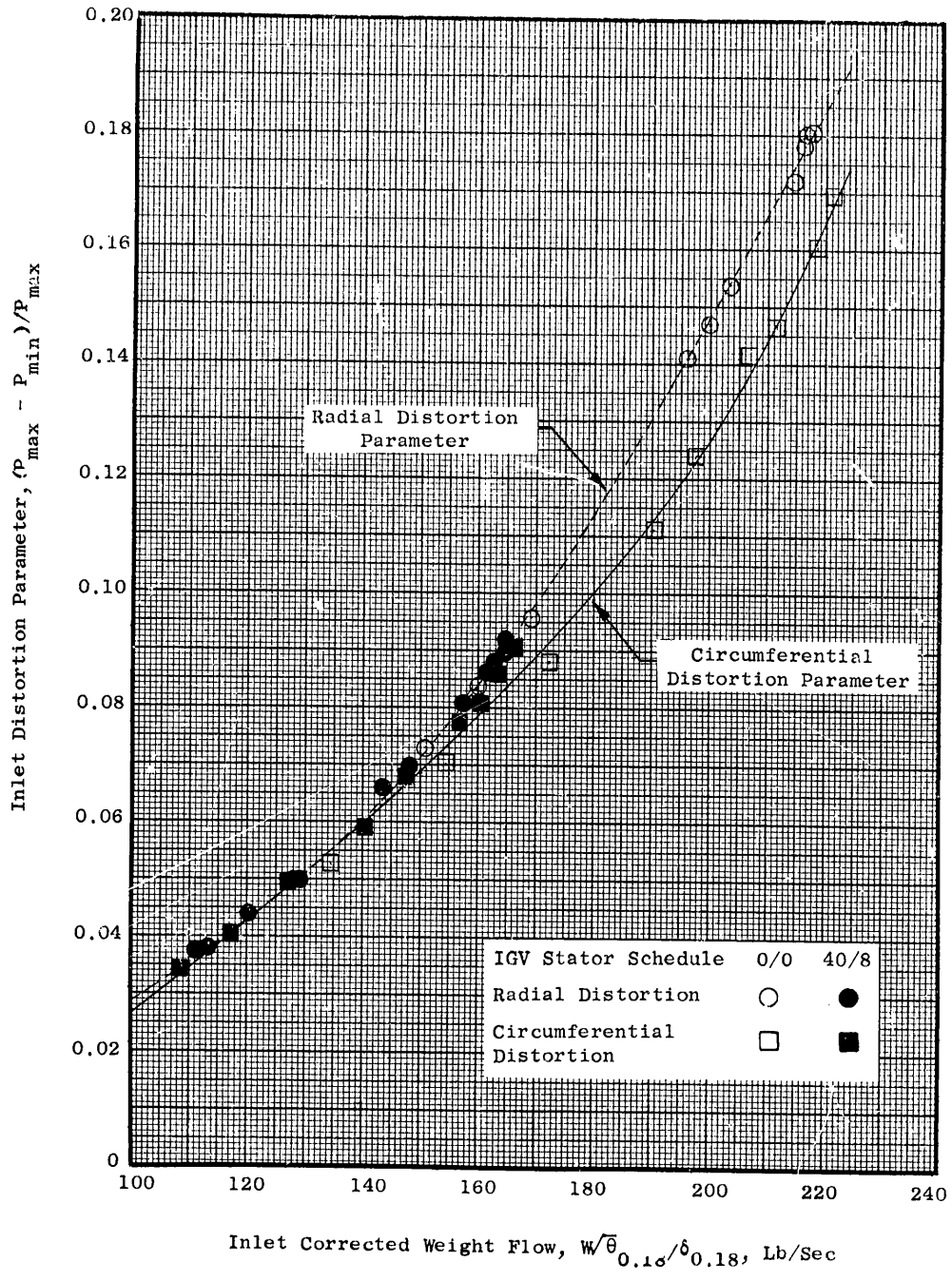

Figure 59. Variation of Distortion Parameter with Inlet Corrected Weight Flow for Radial and Circumferential Distortion.

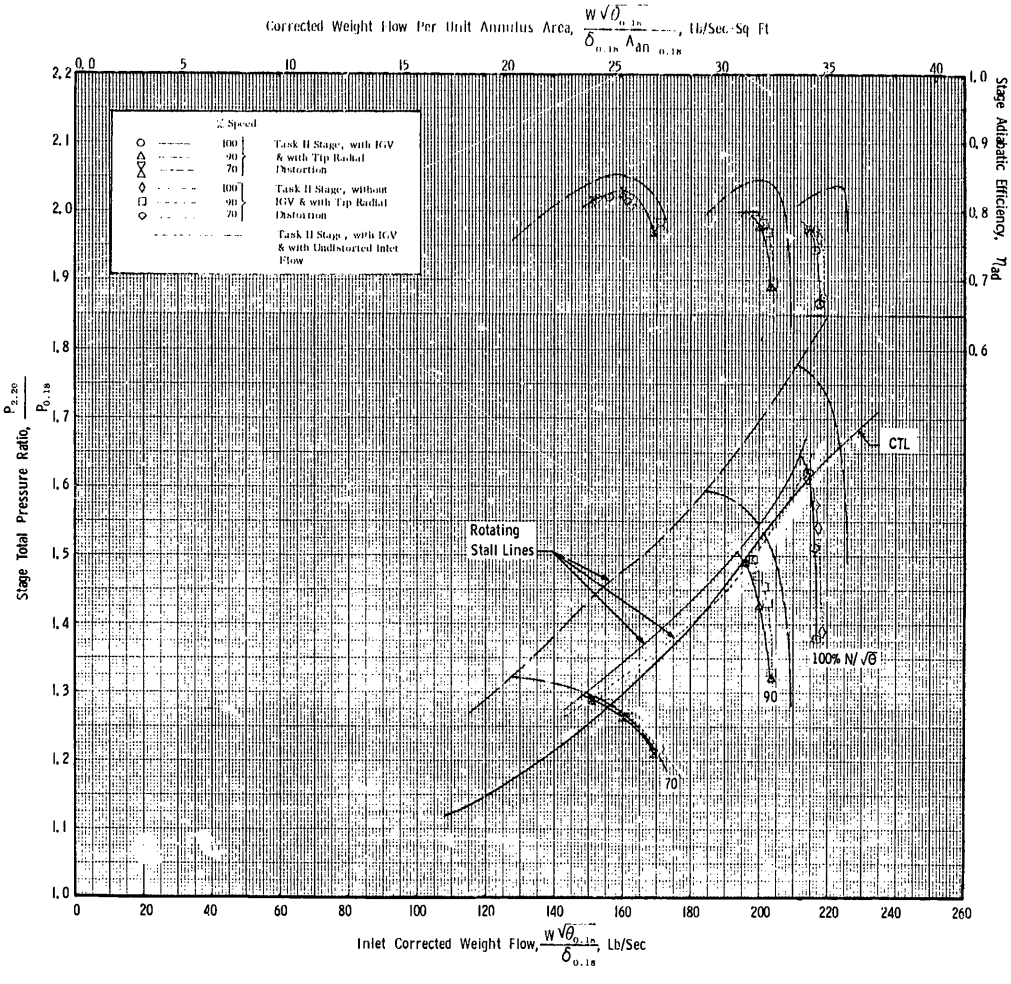

Figure 60. Task II Stage Performance Map with Tip-Radial Inlet Distortion for IGV/Stator Schedule 0°/0°.

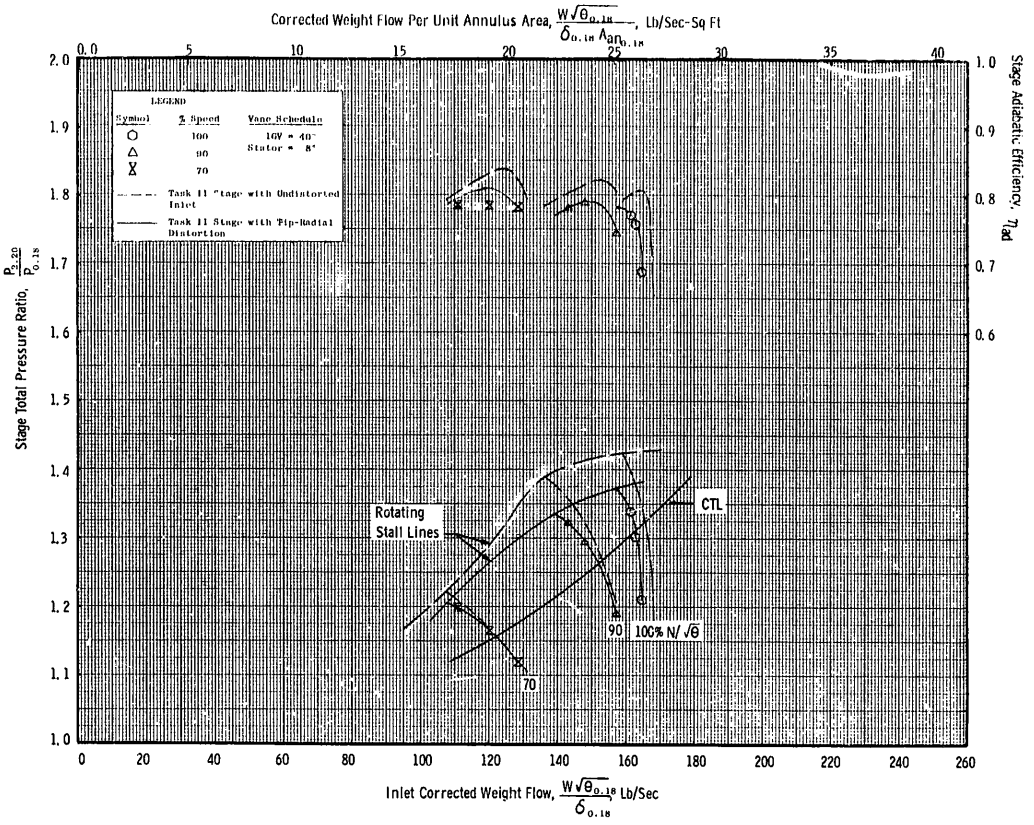

Figure 61. Task II Stage Performance Map with Tip-Radial Inlet Distortion for IGV/Stator Schedule 40°/8°.

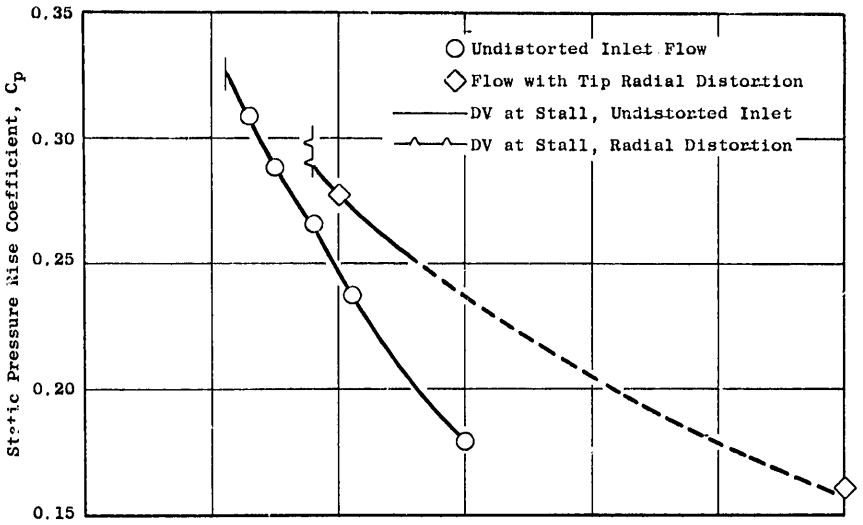

(b) Static Pressure Rise Coefficient

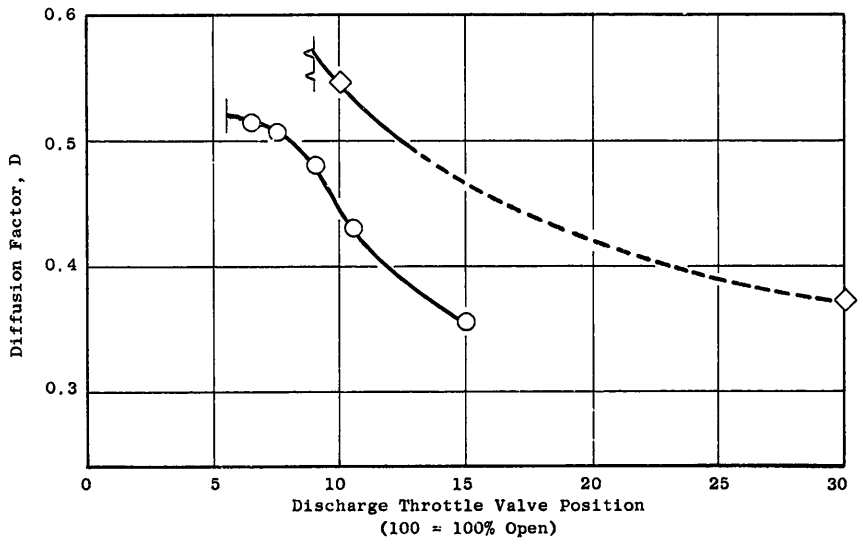

(a) Diffusion Factor

Figure 62. Variation of Rotor Blade Element Parameters with Throttle Valve Setting at 5% Immersion from Tip; 100% Speed, IGV/Stator Schedule 0°/0°, Undistorted Inlet Flow and Flow with Tip Radial Distortion.

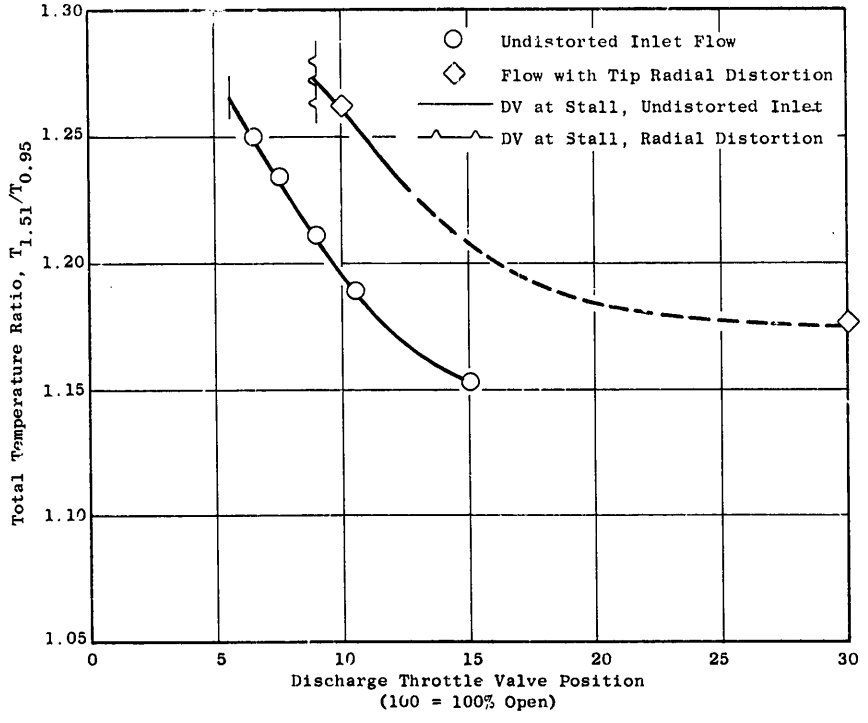

(c) Temperature Ratio

Figure 62. Variation of Rotor Blade Element Parameters with Throttle Valve Setting at 5% Immersion from Tip; 100% Speed, IGV/Stator Schedule 0°/0°, Undistorted Inlet Flow and Flow with Tip Radial Distortion (Continued).

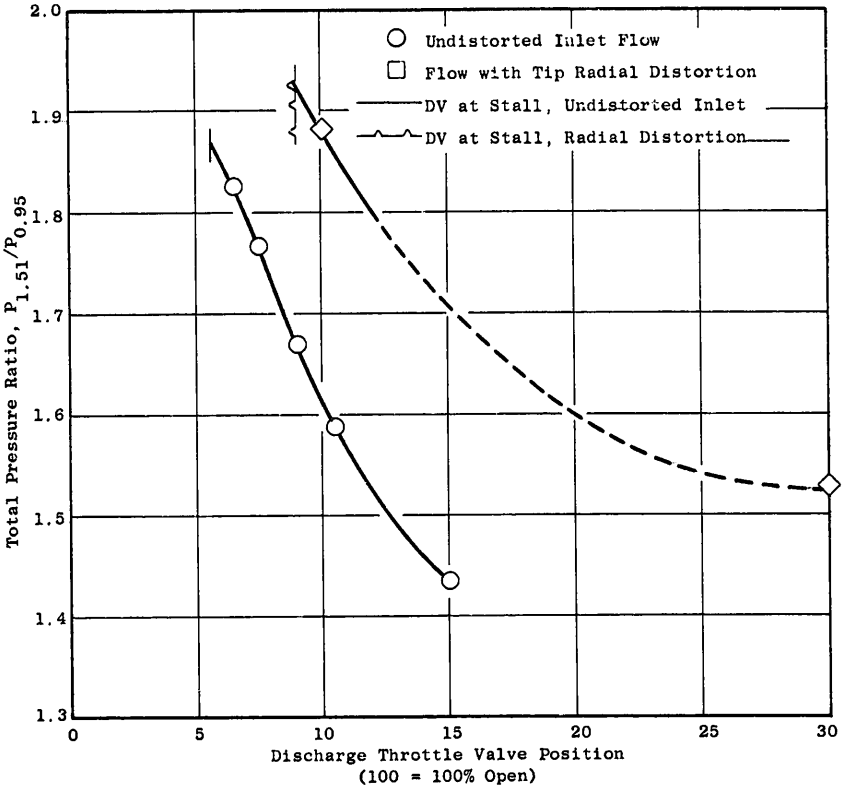

(d) Total Pressure Ratio

Figure 62. Variation of Rotor Blade Element Parameters with Throttle Valve Setting at 5% Immersion from Tip; 100% Speed, IGV/Stator Schedule 0°/0°, Undistorted Inlet Flow and Flow with Tip Radial Distortion (Concluded).

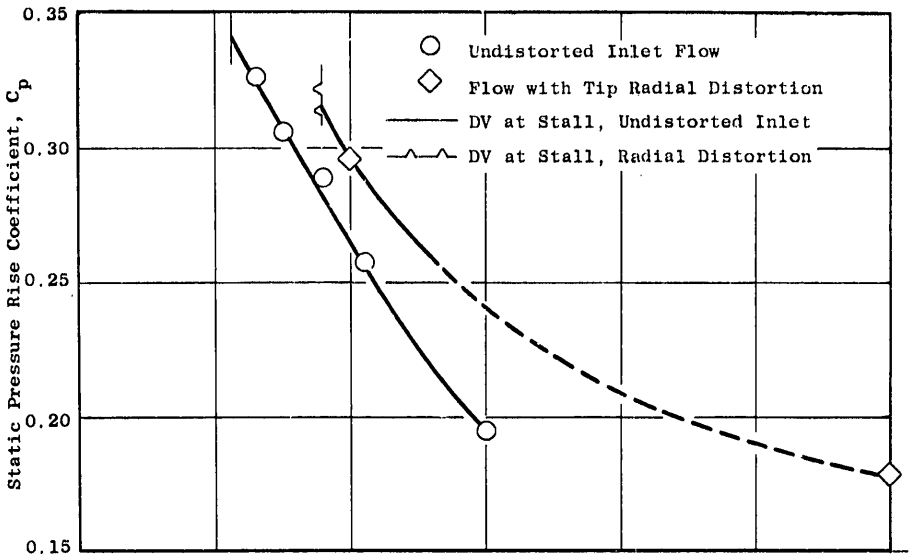

(b) Static Pressure Rise Coefficient, C_p

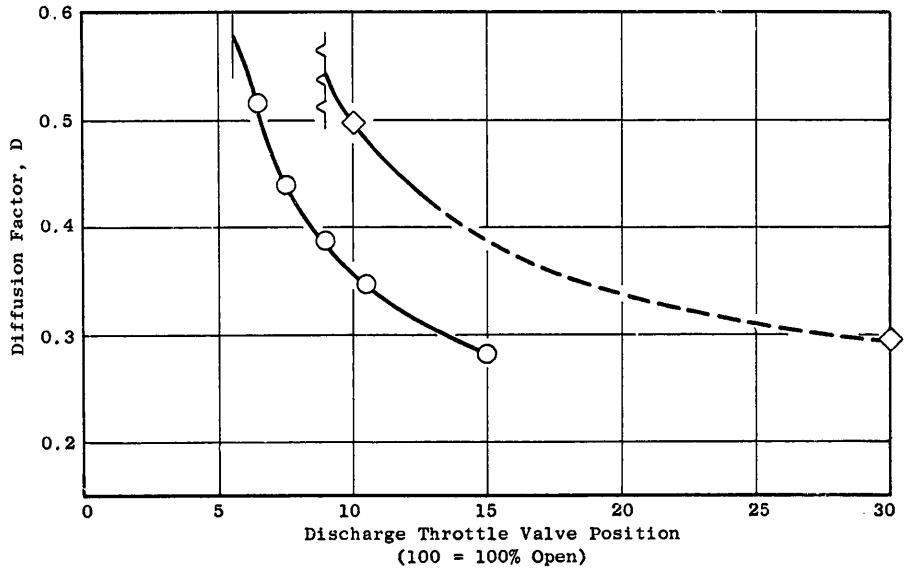

(a) Diffusion Factor, D

Figure 63. Variation of Rotor Blade Element Parameters with Throttle Valve Setting at 10% Immersion from Tip; 100% Speed, IGV/Stator Schedule 0°/0°, Undistorted Inlet Flow and Flow with Tip Radial Distortion.

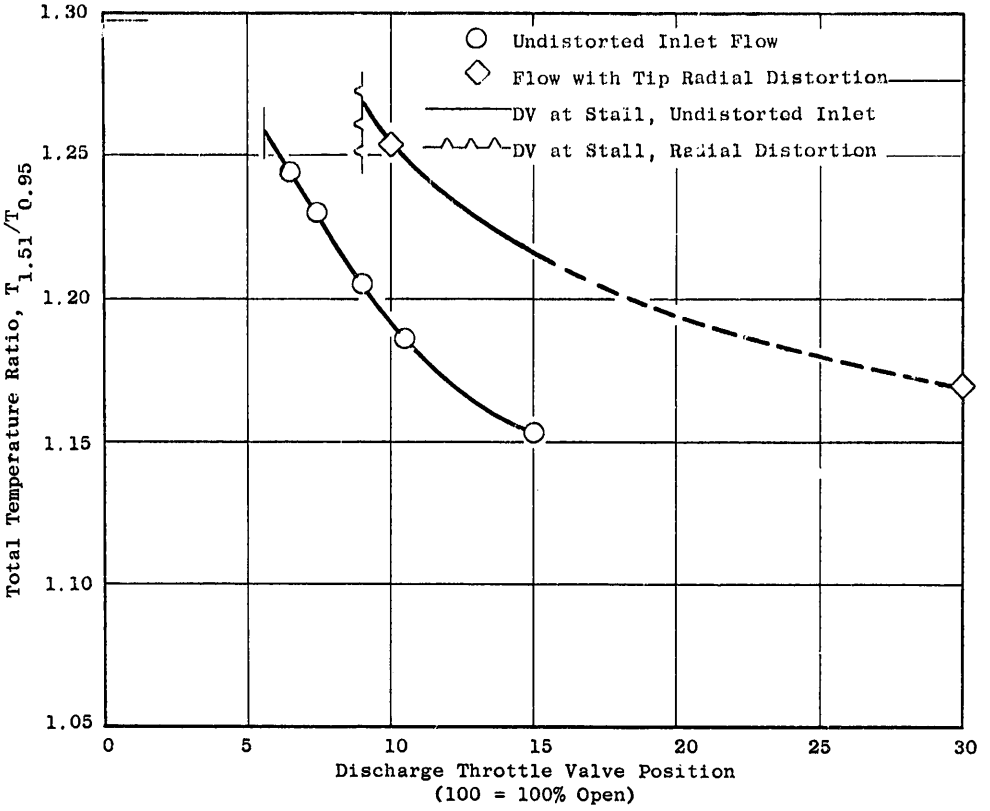

(c) Temperature Ratio, $T_{1.51}/T_{0.95}$

Figure 63. Variation of Rotor Blade Element Parameters with Throttle Valve Setting at 10% Immersion from Tip; 100% Speed, IGV/Stator Schedule 0°/0°, Undistorted Inlet Flow and Flow with Tip Radial Distortion (Continued).

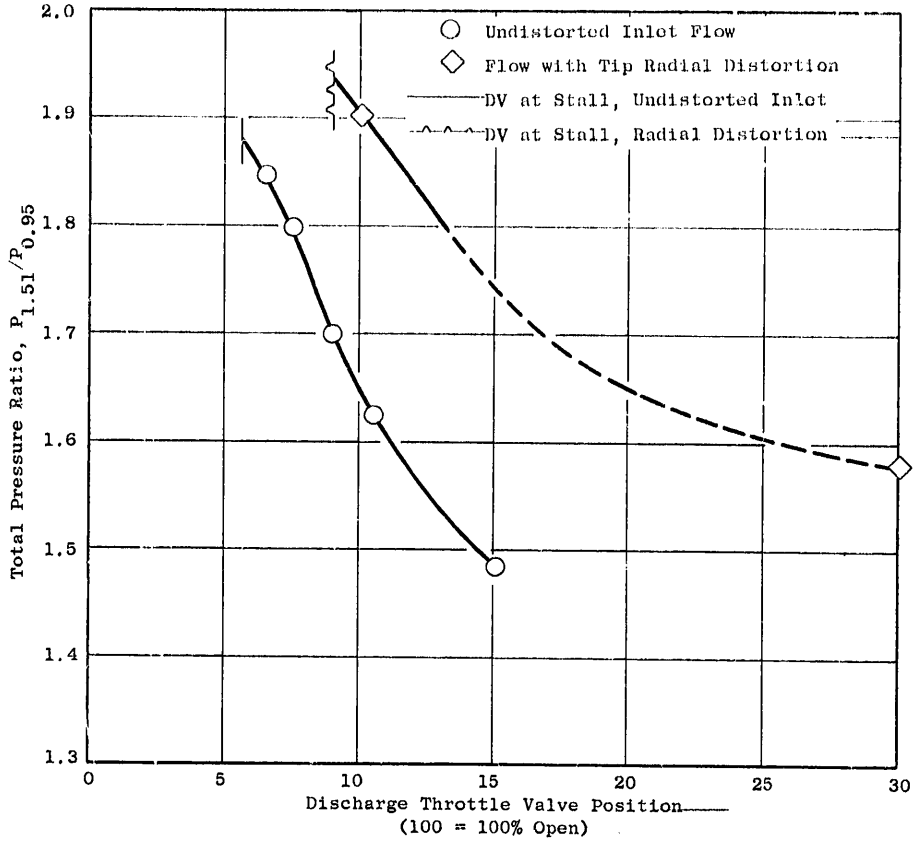

(d) Total Pressure Ratio, $P_{1.51}/P_{0.95}$

Figure 63. Variation of Rotor Blade Element Parameters with Throttle Valve Setting at 10% Immersion from Tip; 100% Speed, IGV/Stator Schedule 0°/0°, Undistorted Inlet Flow and Flow with Tip Radial Distortion (Concluded).

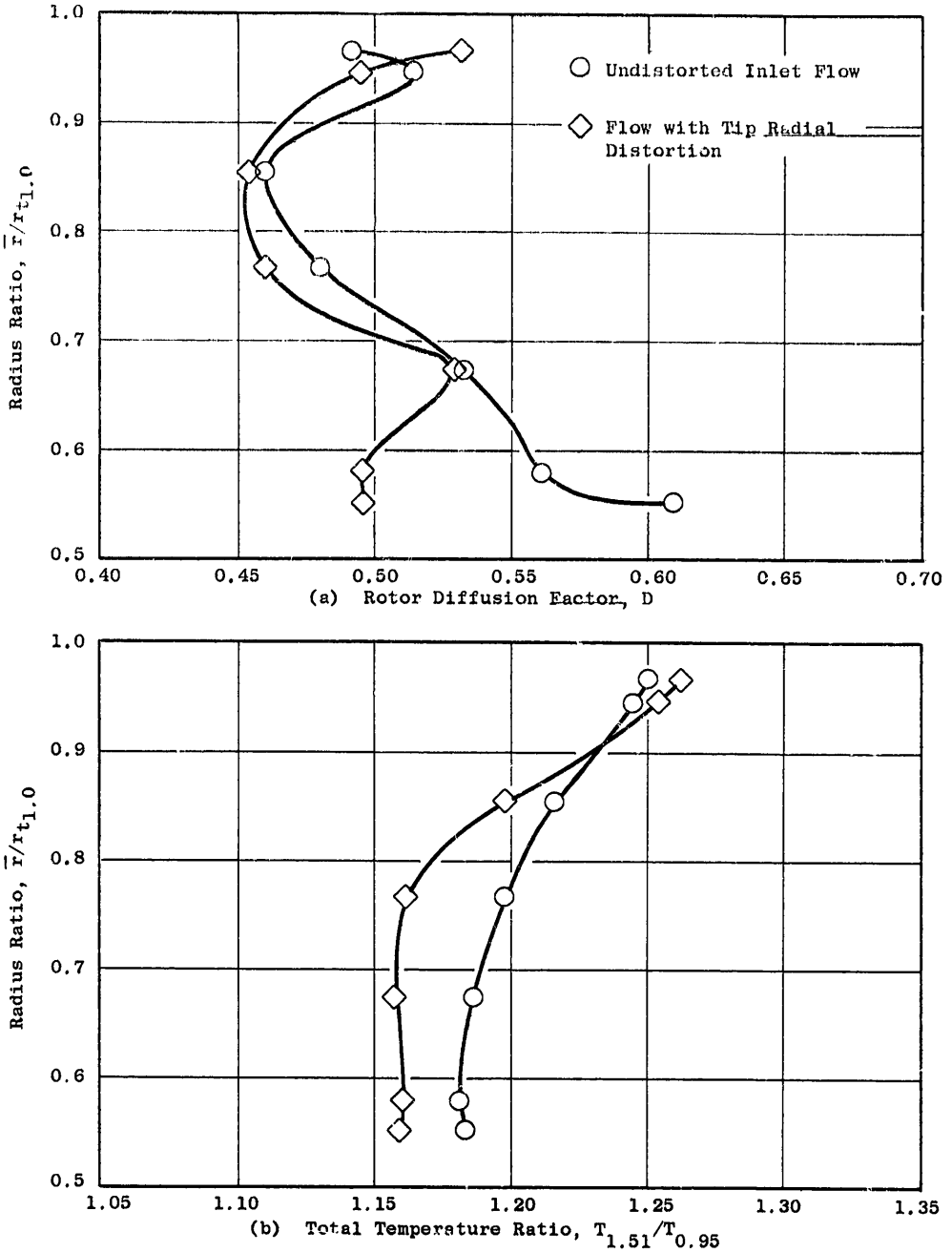

Figure 64. Comparison of Radial Profiles of Rotor Blade Element Parameters Between Undistorted Inlet Flow and Flow with Tip Radial Distortion; 100% Speed, Near Stall, IGV/Stator Schedule 0°/0°.

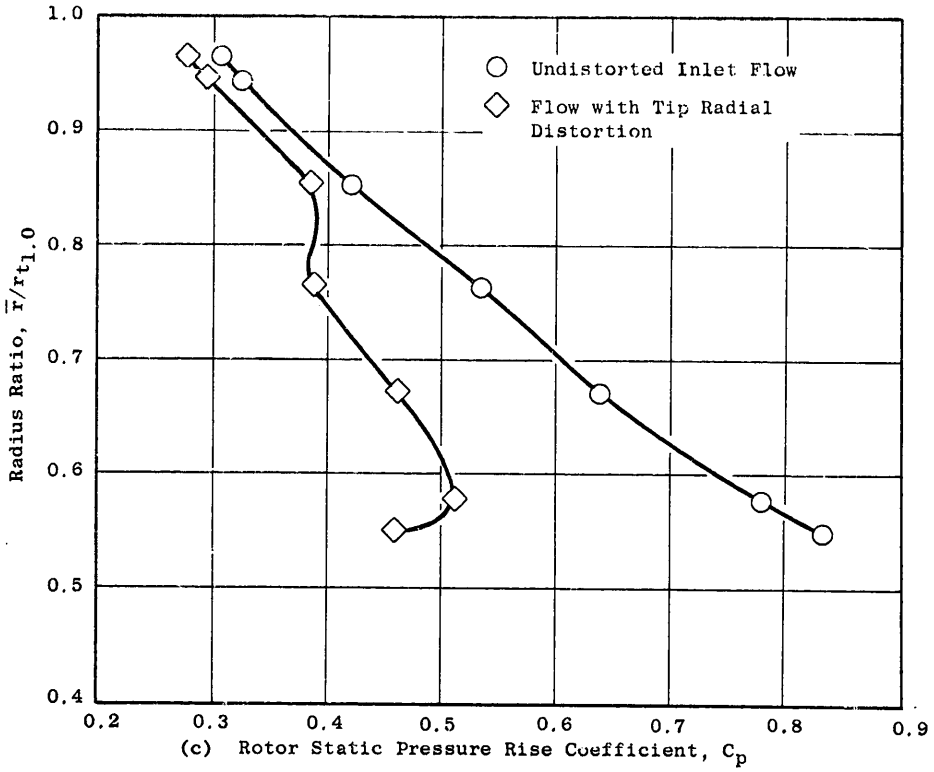

Figure 64. Comparison of Radial Profiles of Rotor Blade Element Parameters Between Undistorted Inlet Flow and Flow with Tip Radial Distortion; 100% Speed, Near Stall, IGV/Stator Schedule 0°/0° (Continued).

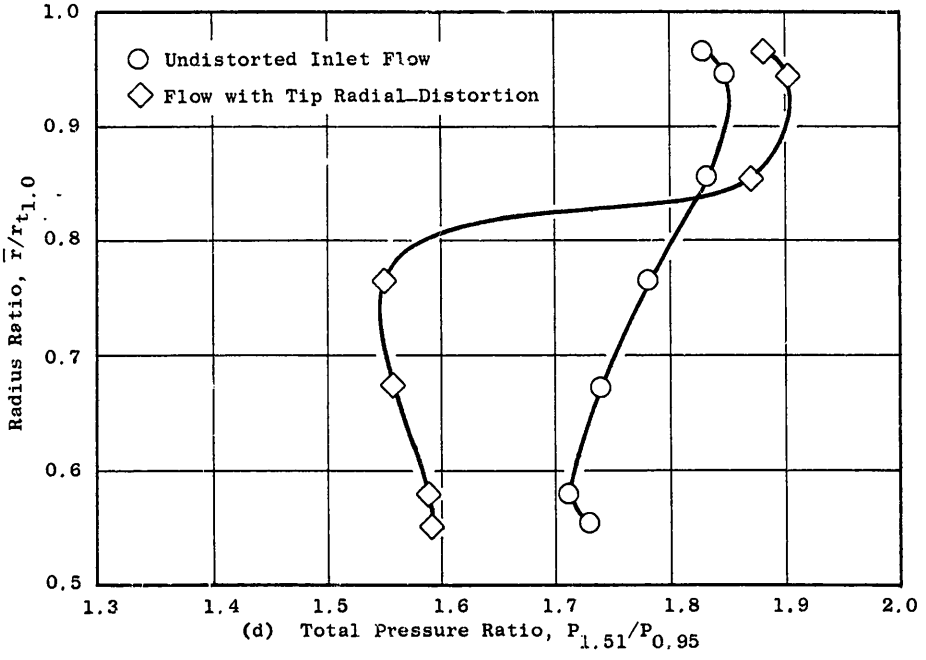

Figure 64. Comparison of Radial Profiles of Rotor Blade Element Parameters Between Undistorted Inlet Flow and Flow with Tip Radial Distortion; 100% Speed, Near Stall, IGV/Stator Schedule 0°/0° (Concluded).

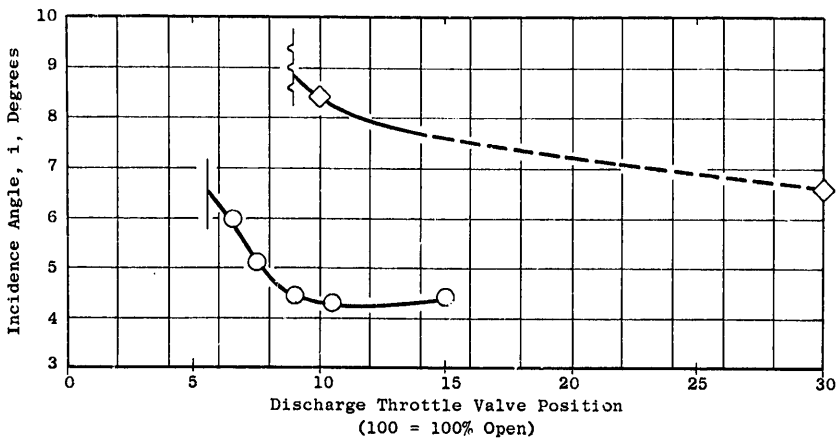

(b) 10% Immersion from Tip

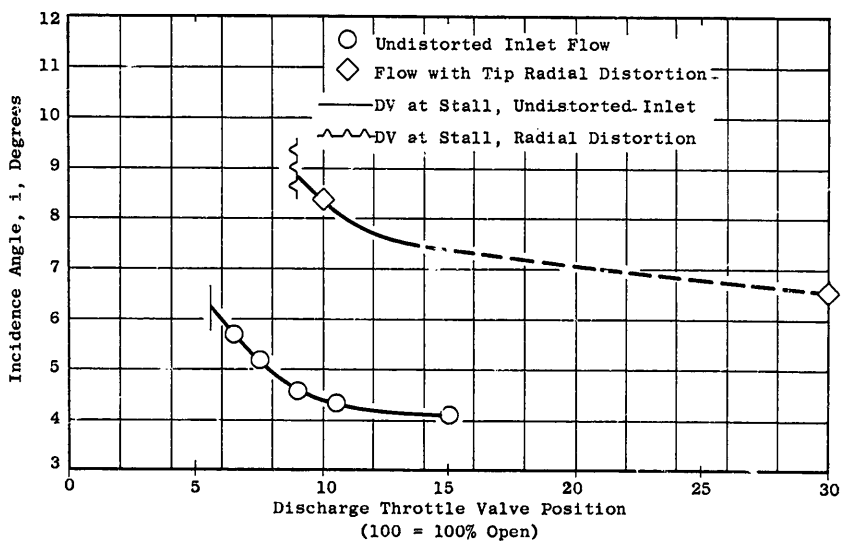

(a) 5% Immersion from Tip

Figure 65. Variation of Rotor Incidence Angle with Throttle Valve Setting; 100% Speed, IGV/Stator Schedule 0°/0°, Undistorted Inlet Flow and Flow with Tip Radial Distortion.

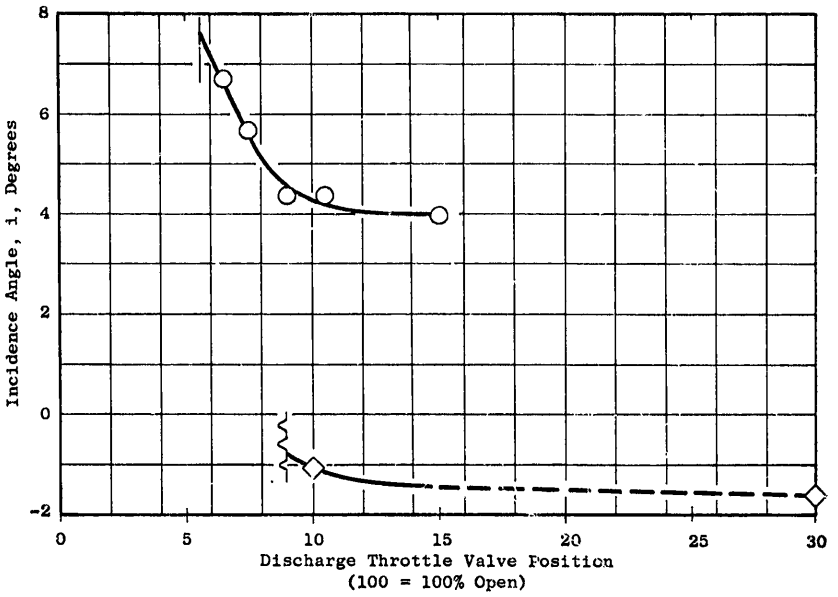

(d) 95% Immersion from Tip

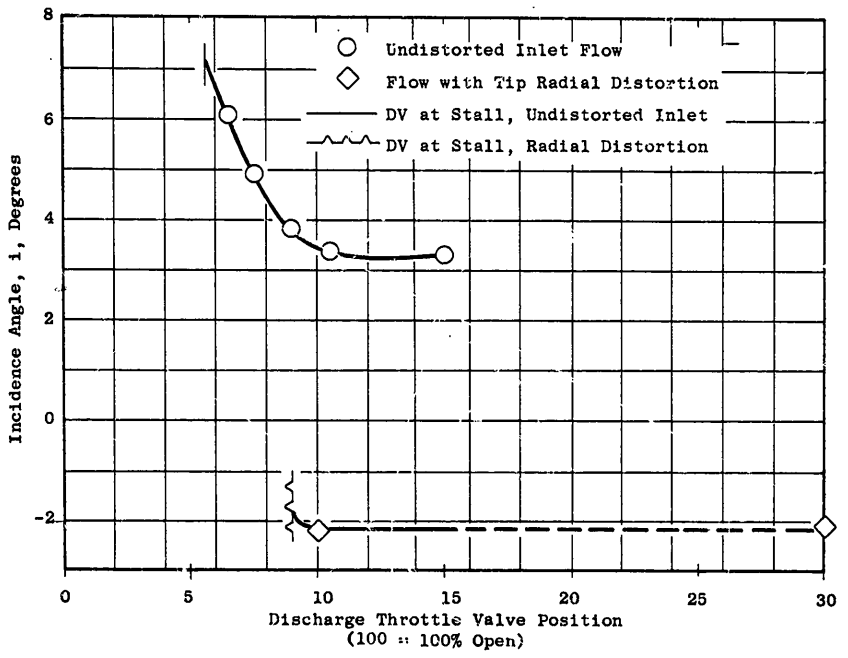

(c) 90% Immersion from Tip

Figure 65. Variation of Rotor Incidence Angle with Throttle Valve Setting, 100% Speed, IGV/Stator Schedule 0°/0°, Undistorted Inlet Flow and Flow with Tip Radial Distortion (Concluded).

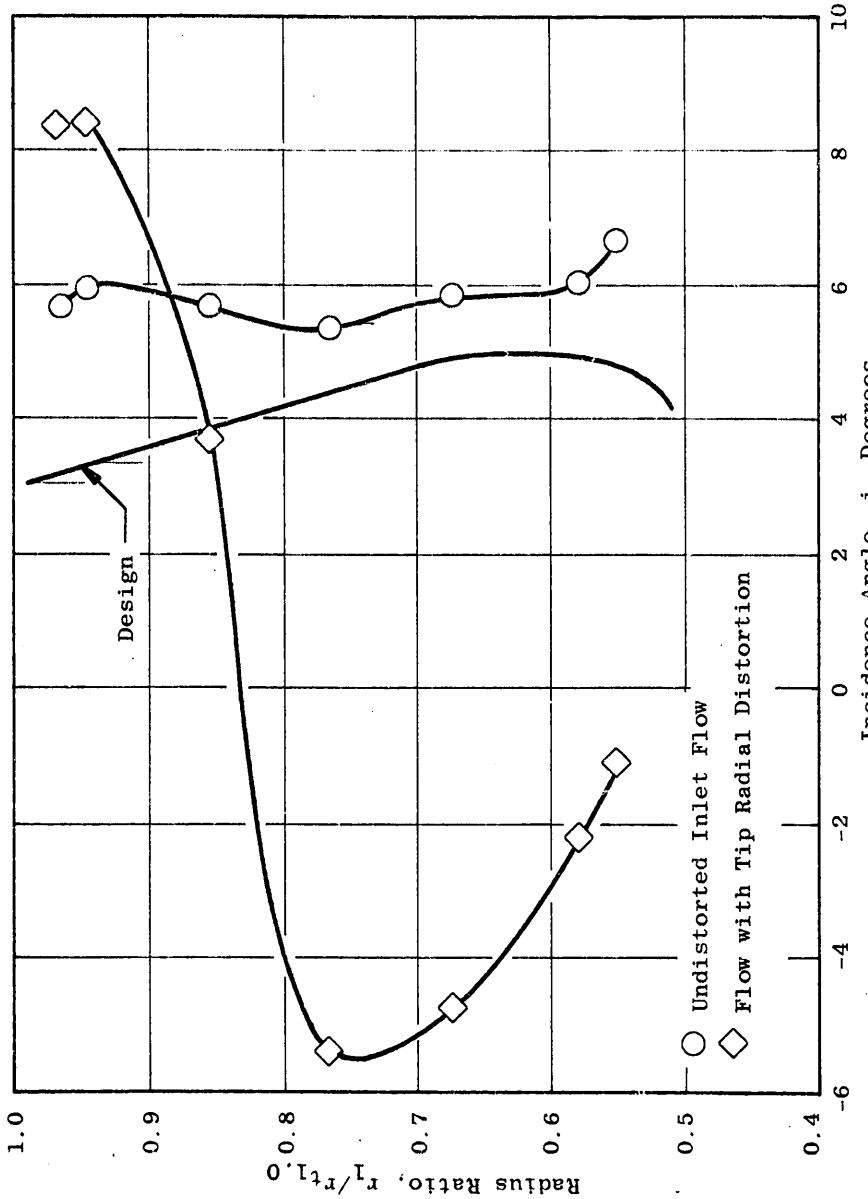

Figure 66. Comparison of Radial Profiles of Rotor Incidence Angle with Undistorted Inlet Flow and Flow with Tip Radial Distortion; 100% Speed, Near Stall; IGV/Stator Schedule 0°/0°.

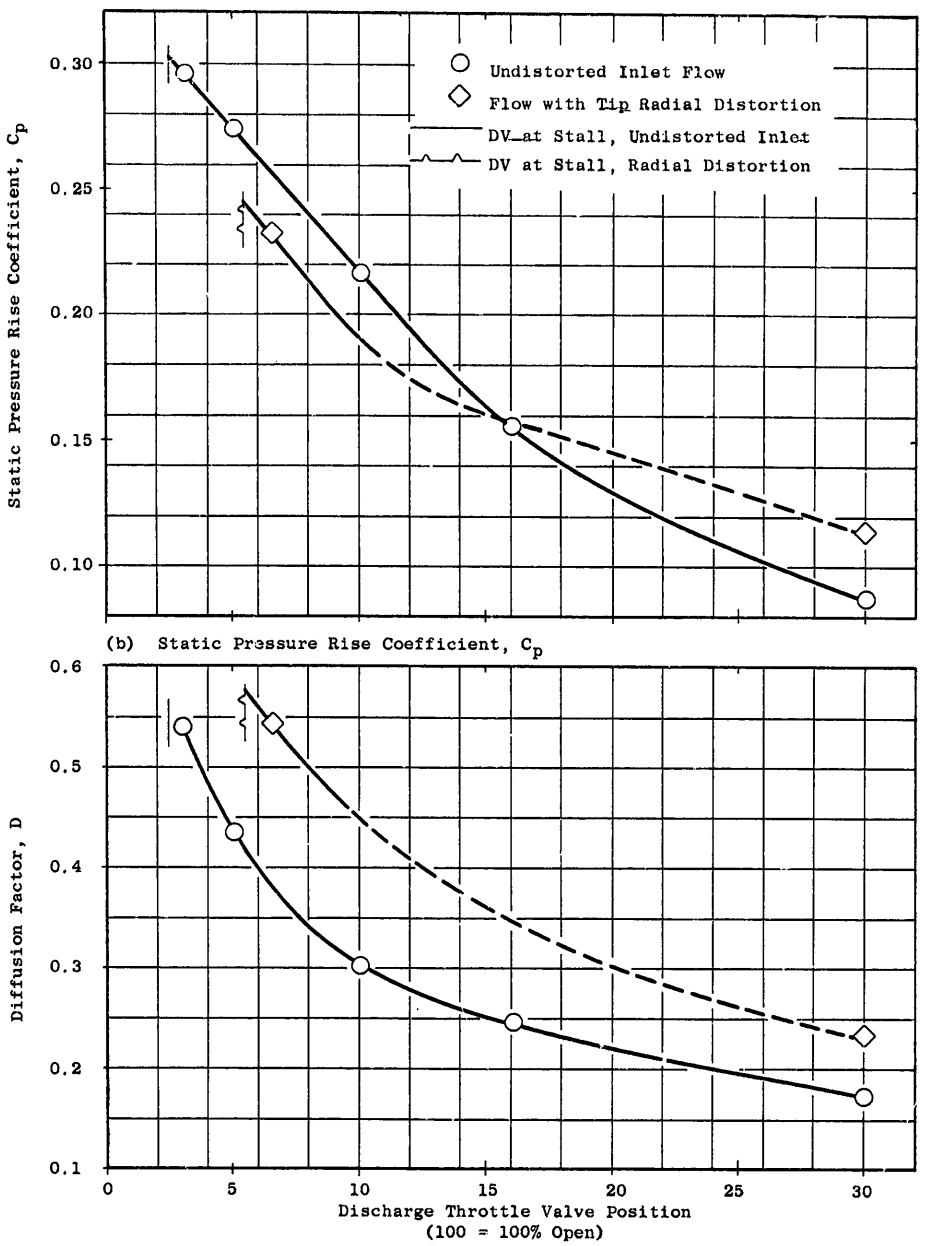

Figure 67. Variation of Rotor Blade Element Parameters with Throttle Valve Setting at 5% Immersion from Tip, 70% Speed, IGV/Stator Schedule 40°/8°, Undistorted Inlet Flow and Flow with Tip Radial Distortion.

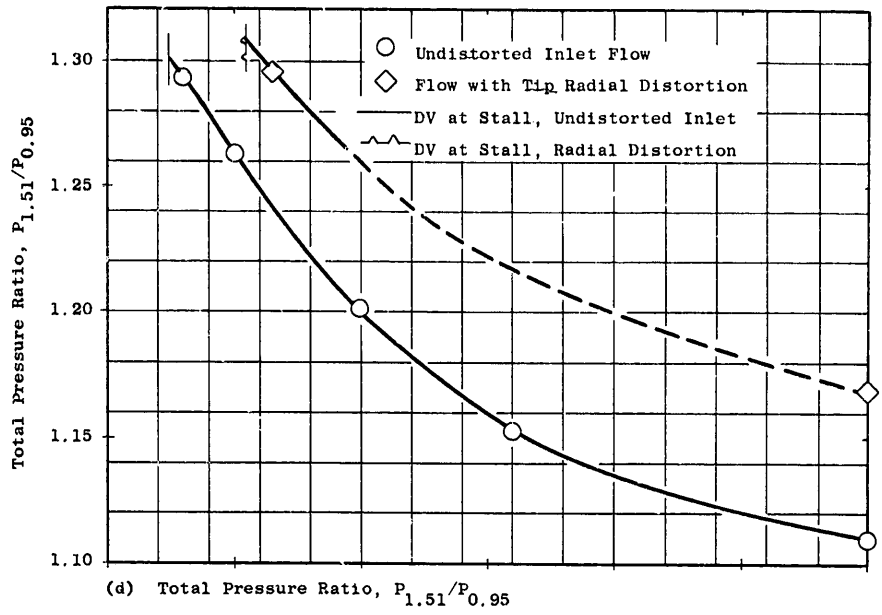

(d) Total Pressure Ratio, $P_{1.51}/P_{0.95}$

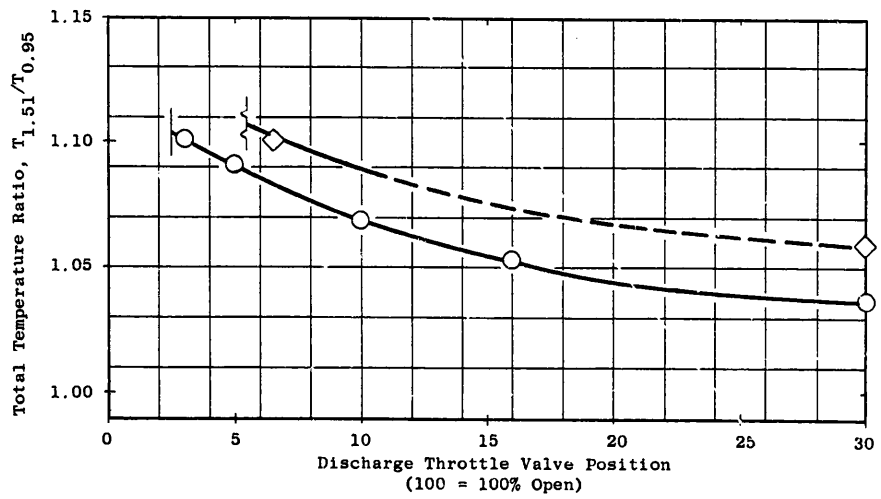

(c) Total Temperature Ratio, $T_{1.51}/T_{0.95}$

Figure 67. Variation of Rotor Blade Element Parameters with Throttle Valve Setting at 5% Immersion from Tip, 70% Speed, IGV/Stator Schedule 40°/8°, Undistorted Inlet Flow and Flow with Tip Radial Distortion (Concluded).

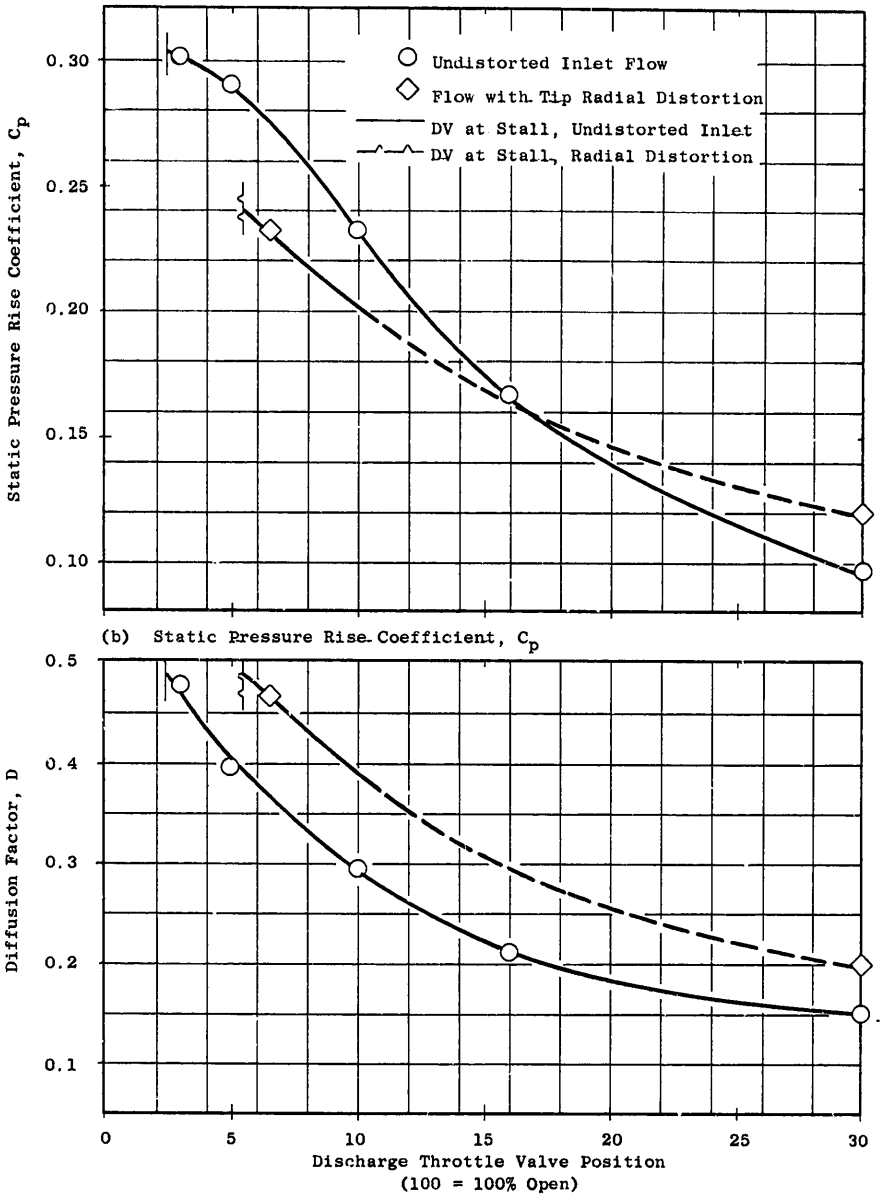

Figure 68. Variation of Rotor Blade Element Parameters with Throttle Valve Setting at 10% Immersion from Tip; 70% Speed, IGV/Stator Schedule 40°/8°, Undistorted Inlet Flow and Flow with Tip Radial Distortion.

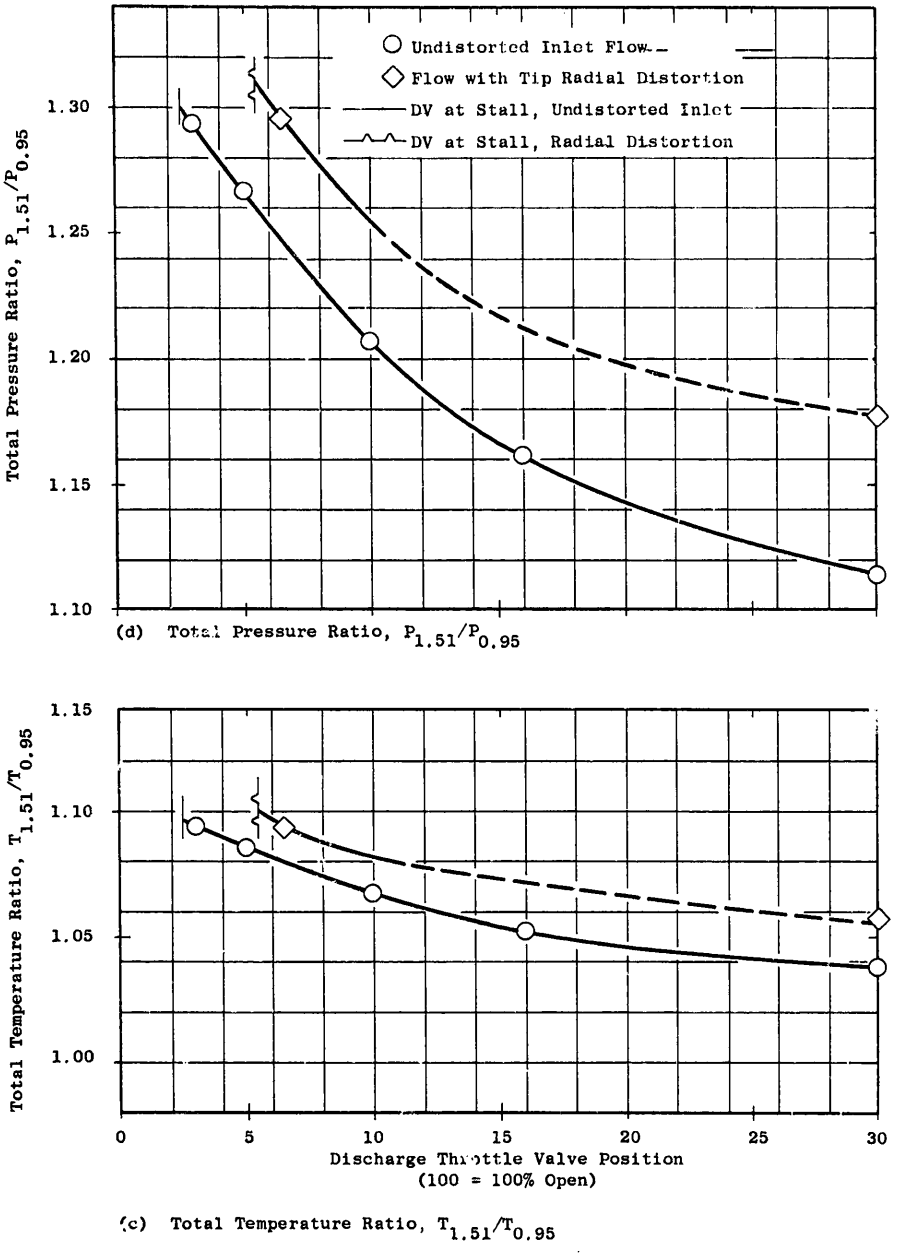

Figure 68. Variation of Rotor Blade Element Parameters with Throttle Valve Setting at 10% Immersion from Tip; 70% Speed, IGV/Stator Schedule 40°/8°, Undistorted Inlet Flow and Flow with Tip Radial Distortion (Concluded).

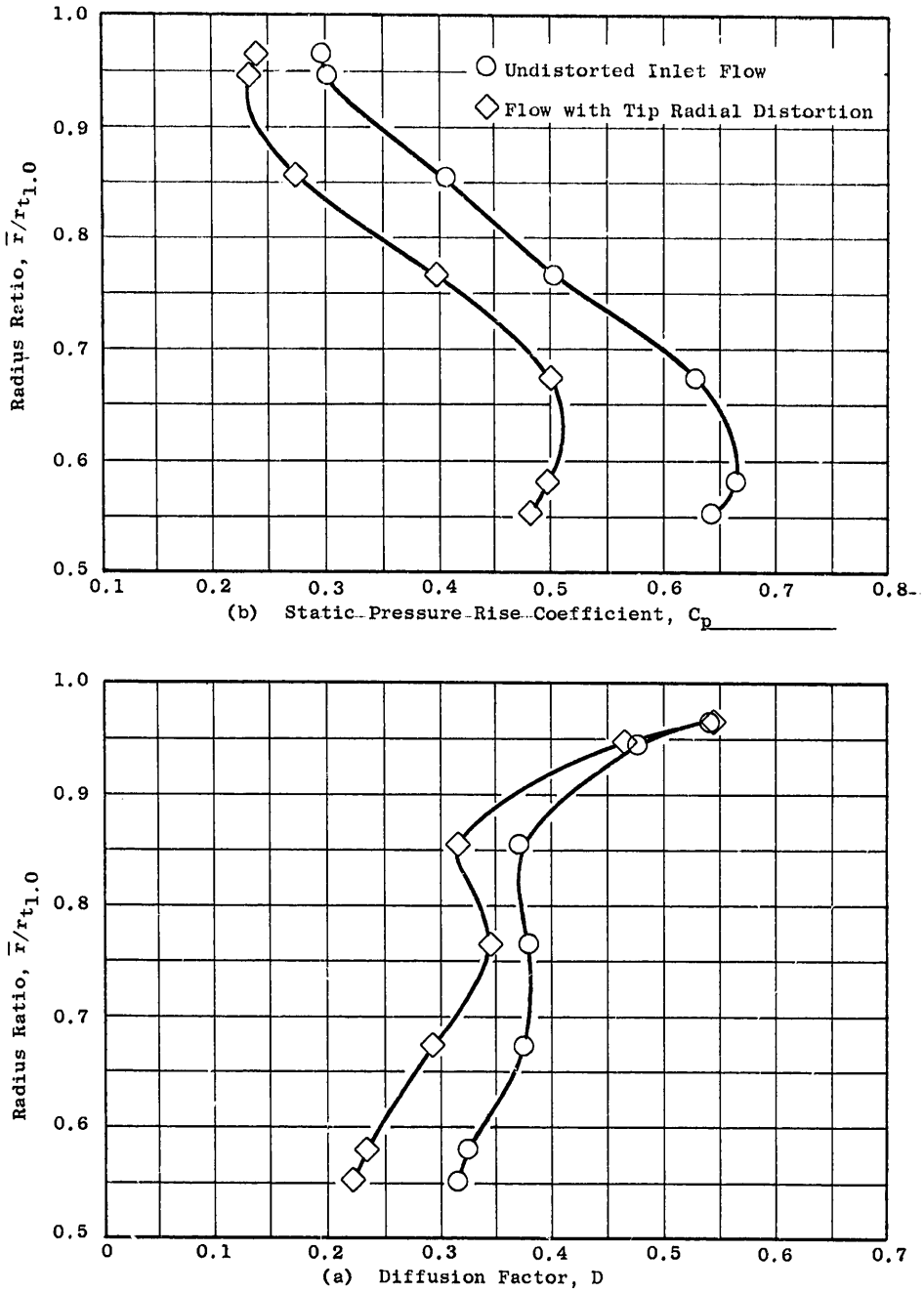

Figure 69. Comparison of Radial Profiles of Rotor Blade Element Parameters Between Undistorted Inlet Flow and Flow with Tip Radial Distortion; 70% Speed, Near Stall, IGV/Stator Schedule 40°/8°.

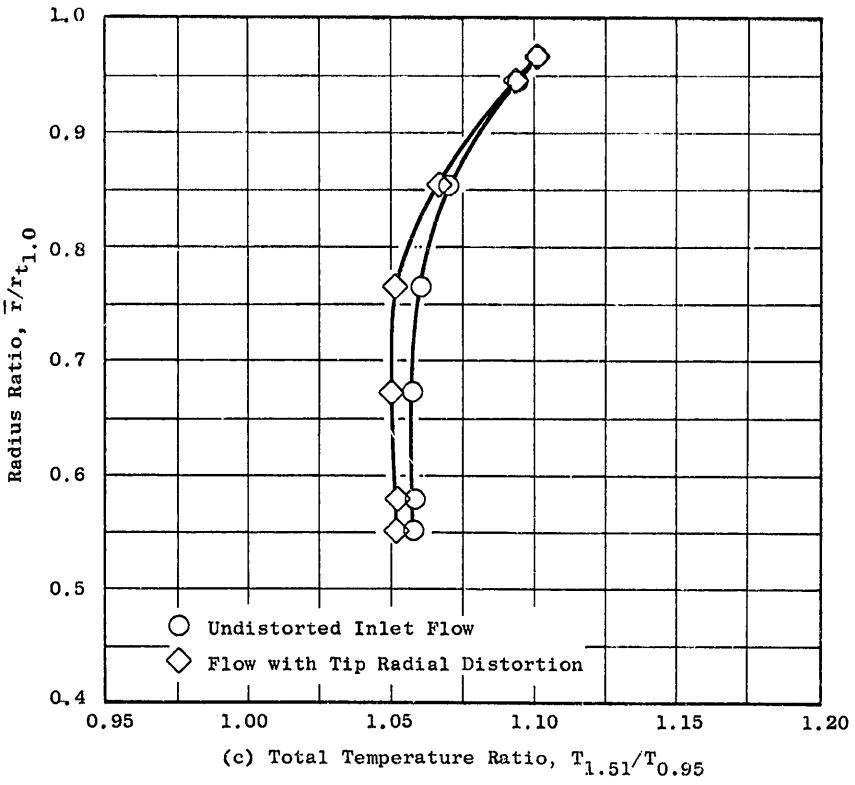

Figure 69. Comparison of Radial Profiles of Rotor Blade Element Parameters Between Undistorted Inlet Flow and Flow with Tip Radial Distortion; 70% Speed, Near Stall, IGV/Stator Schedule 40°/8° (Concluded).

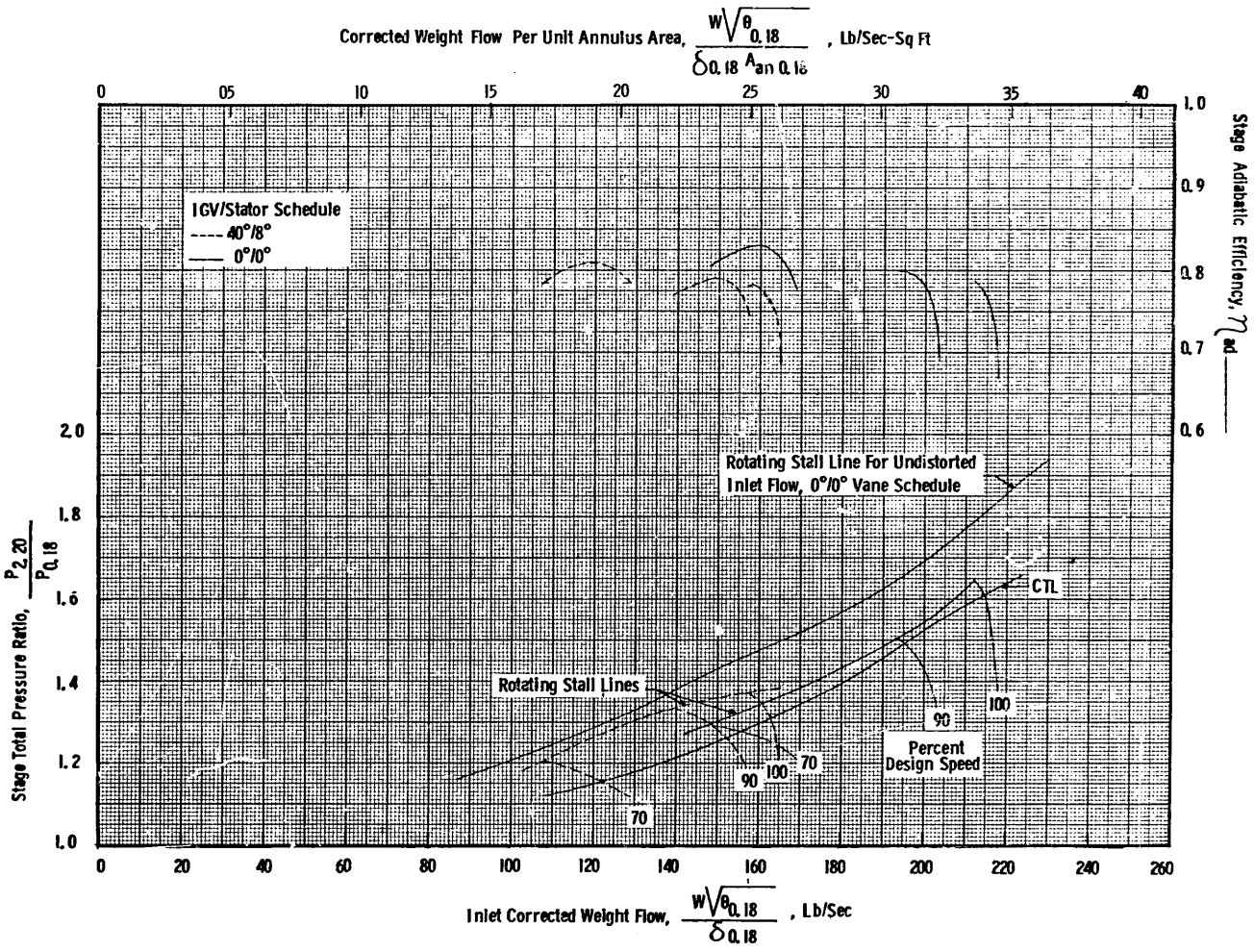

Figure 70. Consolidated Stage Performance Map for IGV/Stator Schedules 0°/0° and 40°/8°; Flow with with Tip Radial Distortion.

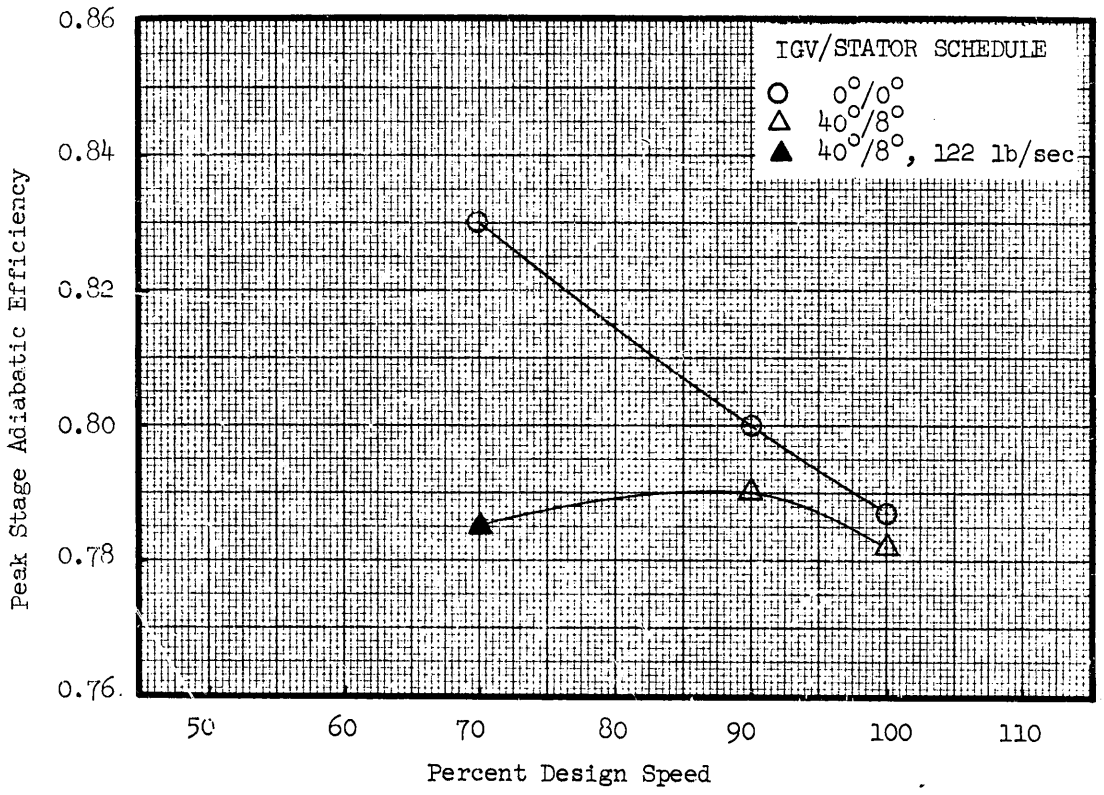

Figure 71(a). Variation of Stage Peak Efficiency with Rotor Speed and Vane Schedule: Flow with Tip Radial Distortion.

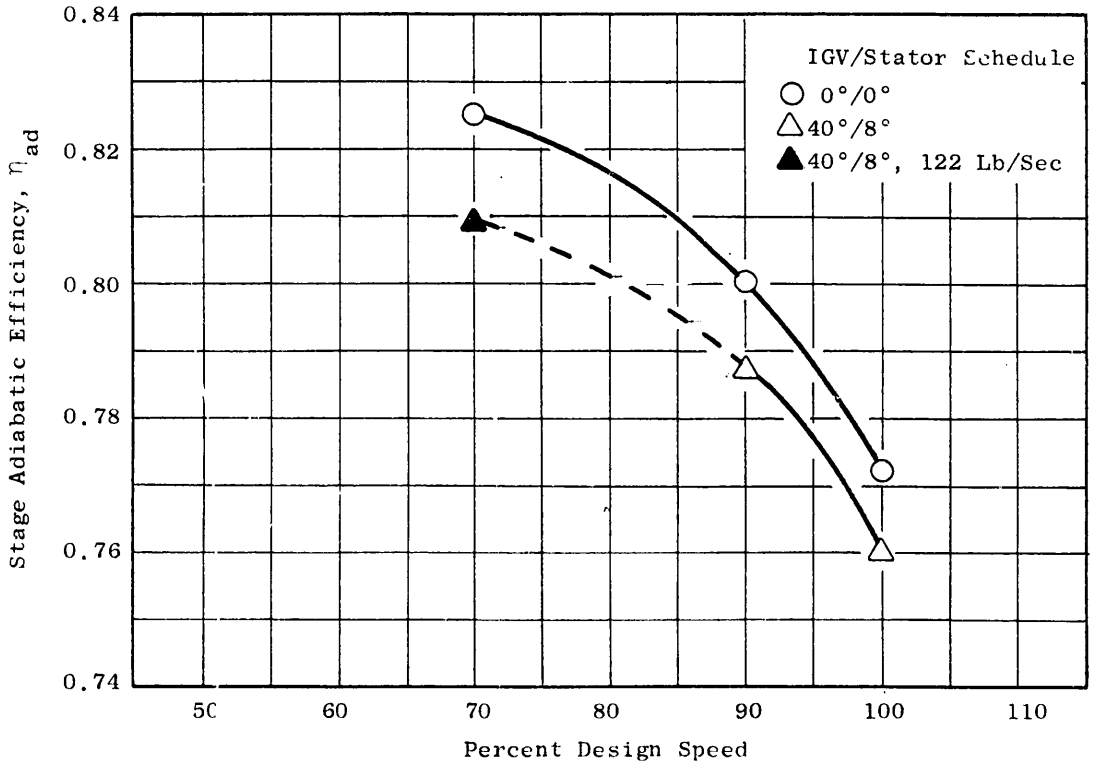

Figure 71(b). Variation of Stage Adiabatic Efficiency with Rotor Speed and Vane Schedule at the CTL Condition; Flow with the Tip Radial Distortion.

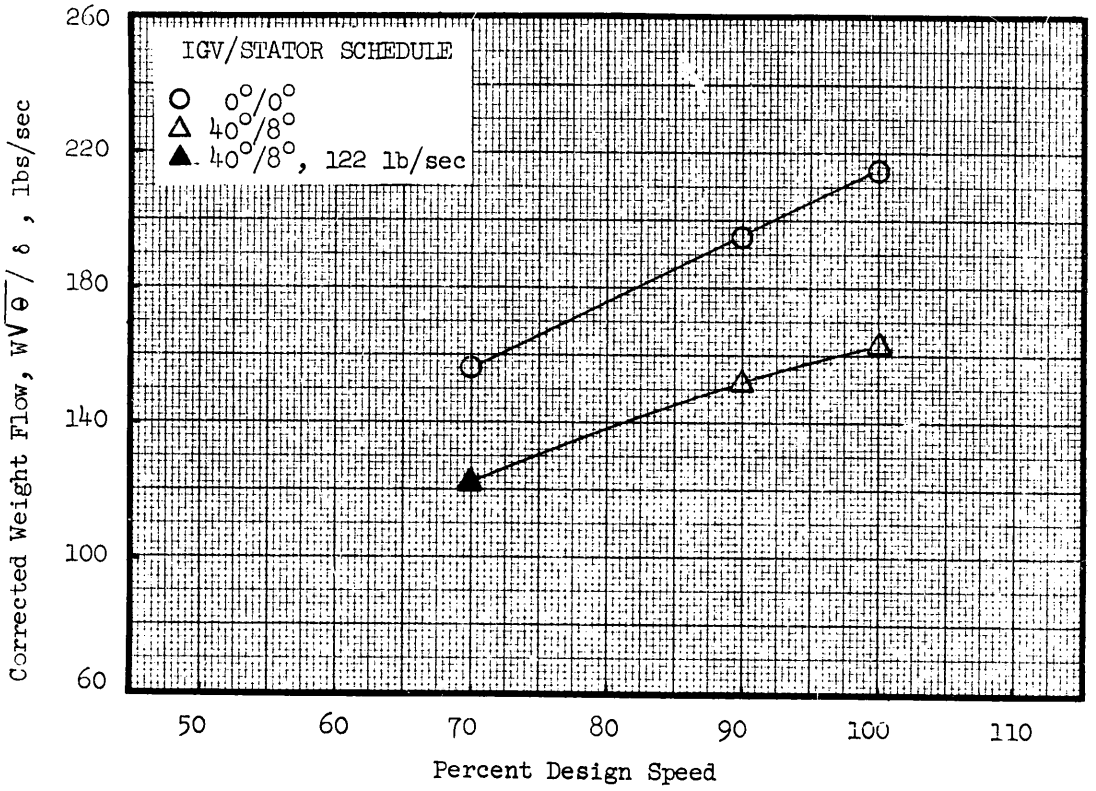

Figure 72. Variation of Stage Inlet Corrected Weight Flow with Rotor Speed and Vane Schedule at the CTL Condition; Flow with Tip Radial Distortion.

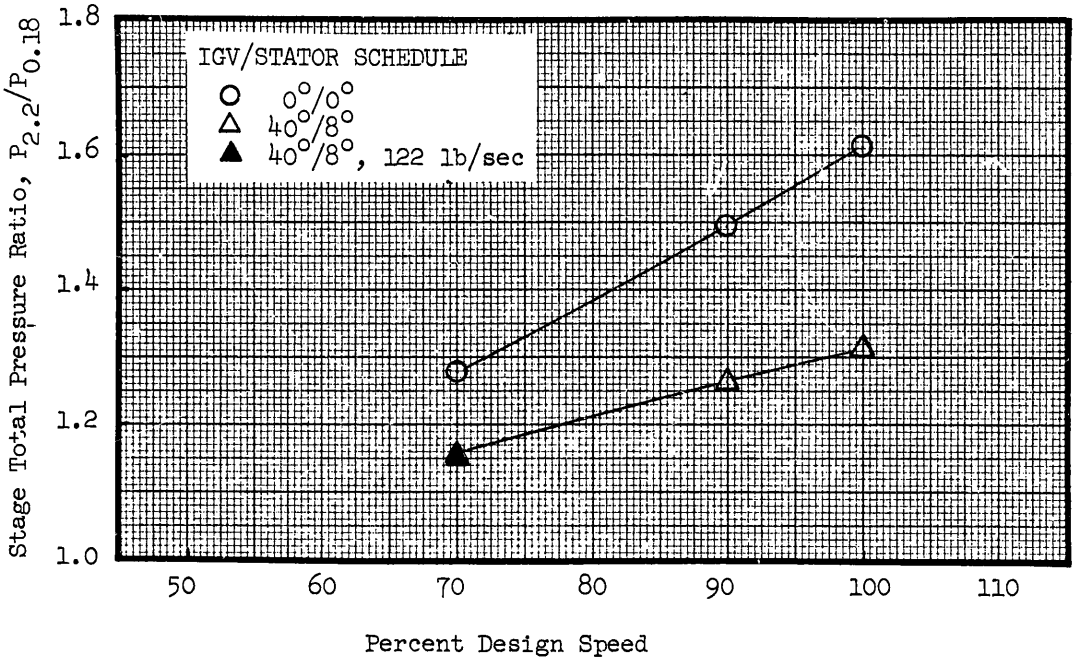

Figure 73. Variation of Stage Total Pressure Ratio with Rotor Speed and Vane Schedule at the CTL Condition; Flow with Tip Radial Distortion.

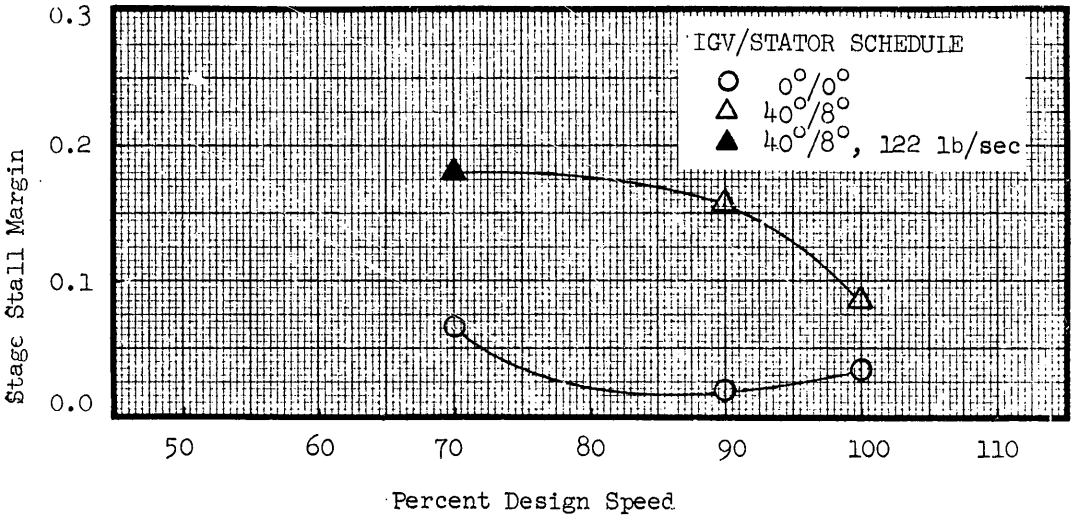

Figure 74. Variation of Stage Stall Margin with Rotor Speed and Vane Schedule at the CTL Condition; Flow with Tip Radial Distortion.

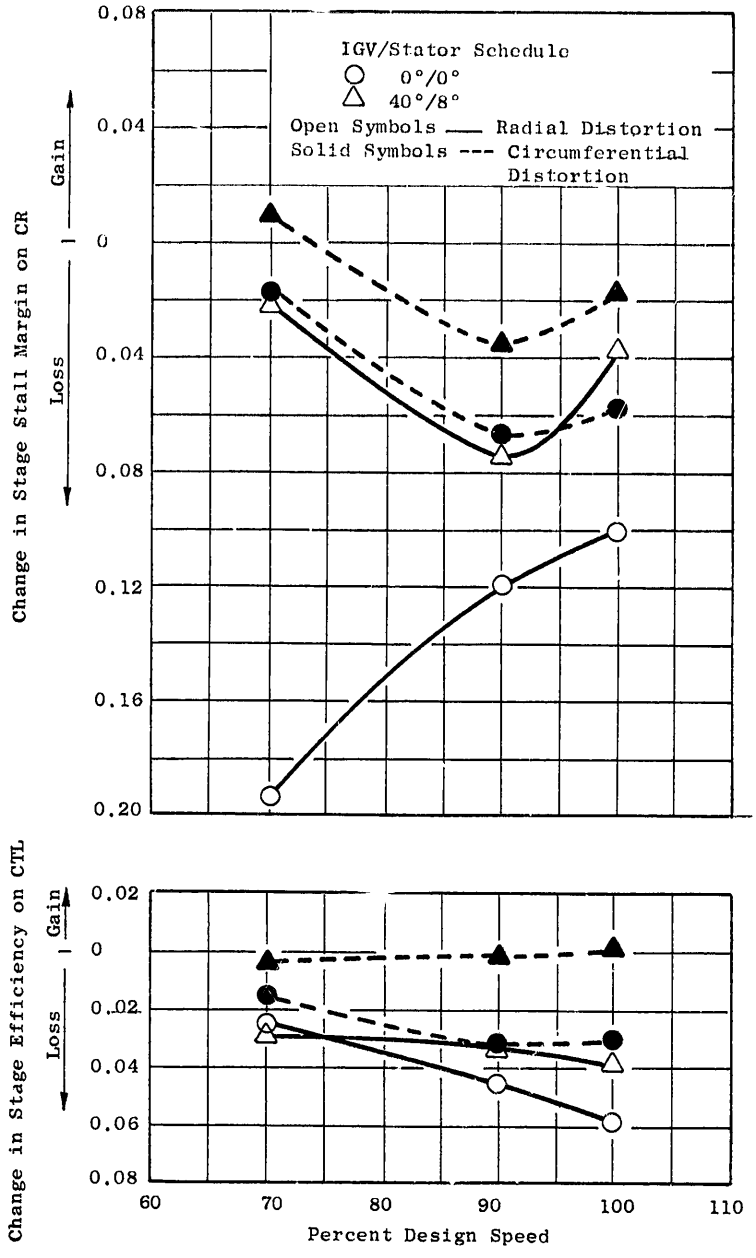

Figure 75. Variation with Rotor Speed and Vane Schedule of Differences in CTL Adiabatic Efficiency and CTL Stall Margin with Undistorted Inlet Flow and Distorted Inlet Flow.

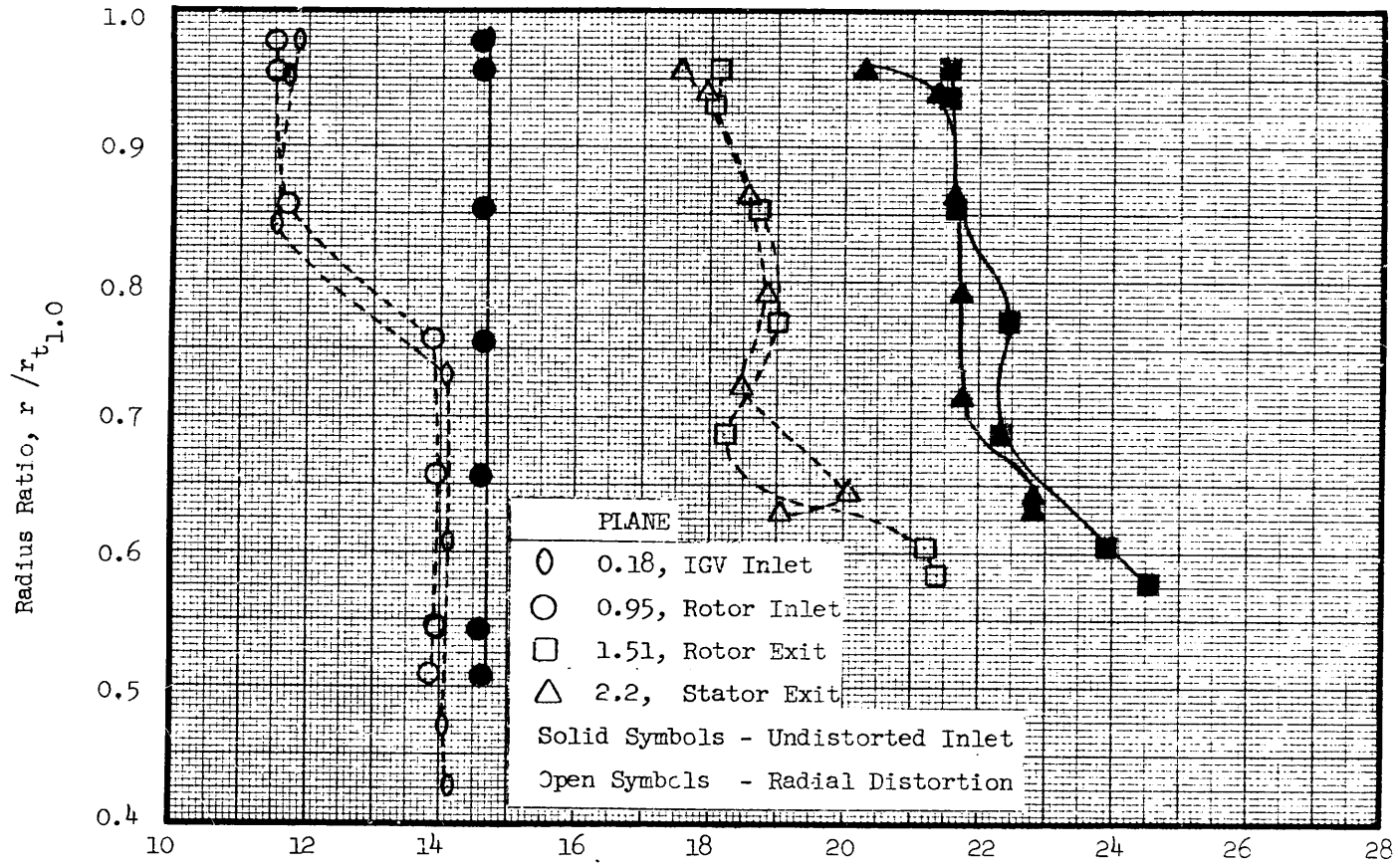

a. 100% Speed, Maximum Flow, IGV/Stator Schedule 0°/0°

Figure 76. Radial Profiles of Total Pressure at the Four Traverse Stations; Undistorted Inlet Flow and Flow with Tip Radial Distortion.

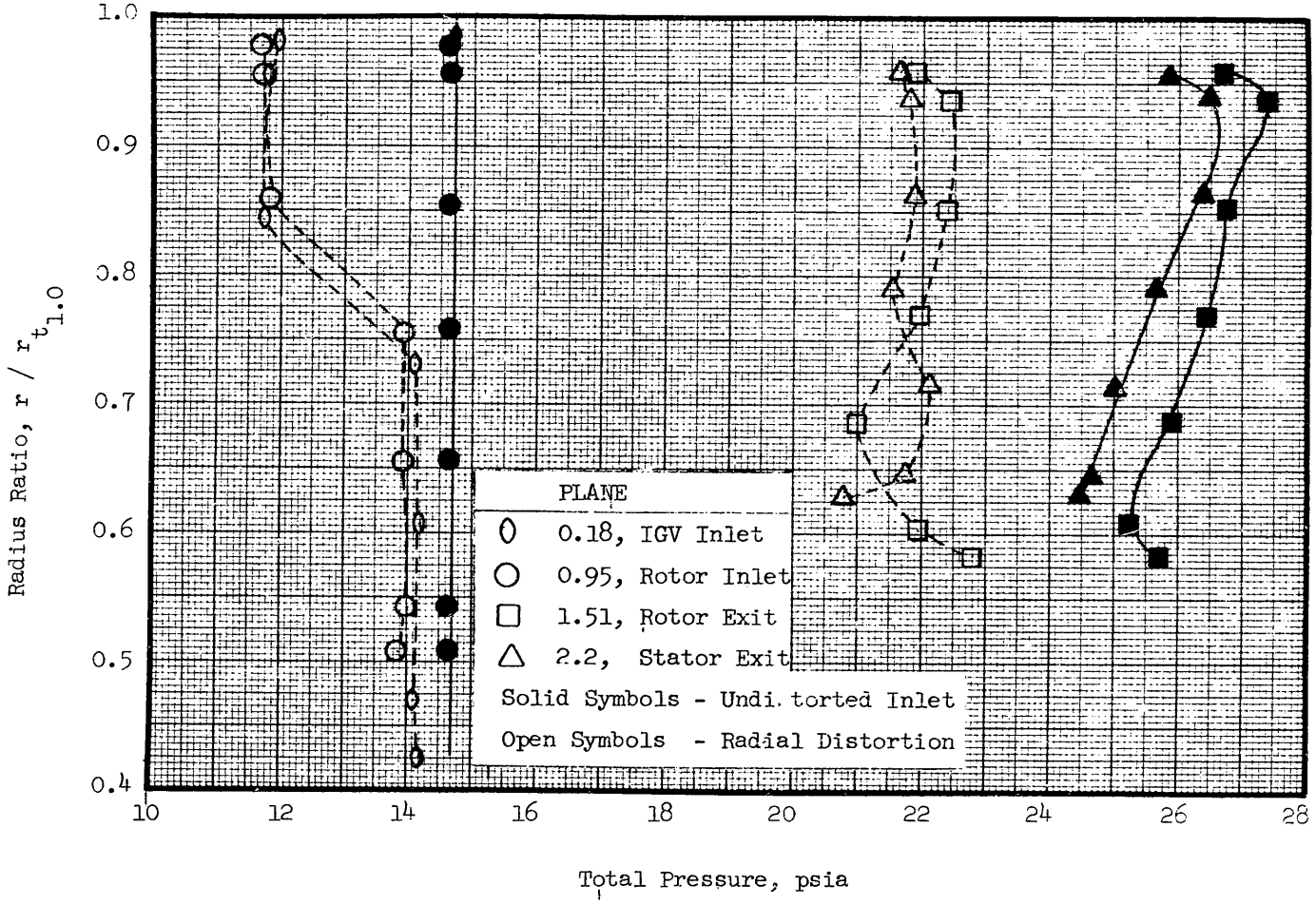

b. 100% Speed, Near Stall, IGV/Stator Schedule 0°/0°

Figure 76. Radial Profiles of Total Pressure at the Four Traverse Stations; Undistorted Inlet Flow and Flow with Tip Radial Distortion (Continued).

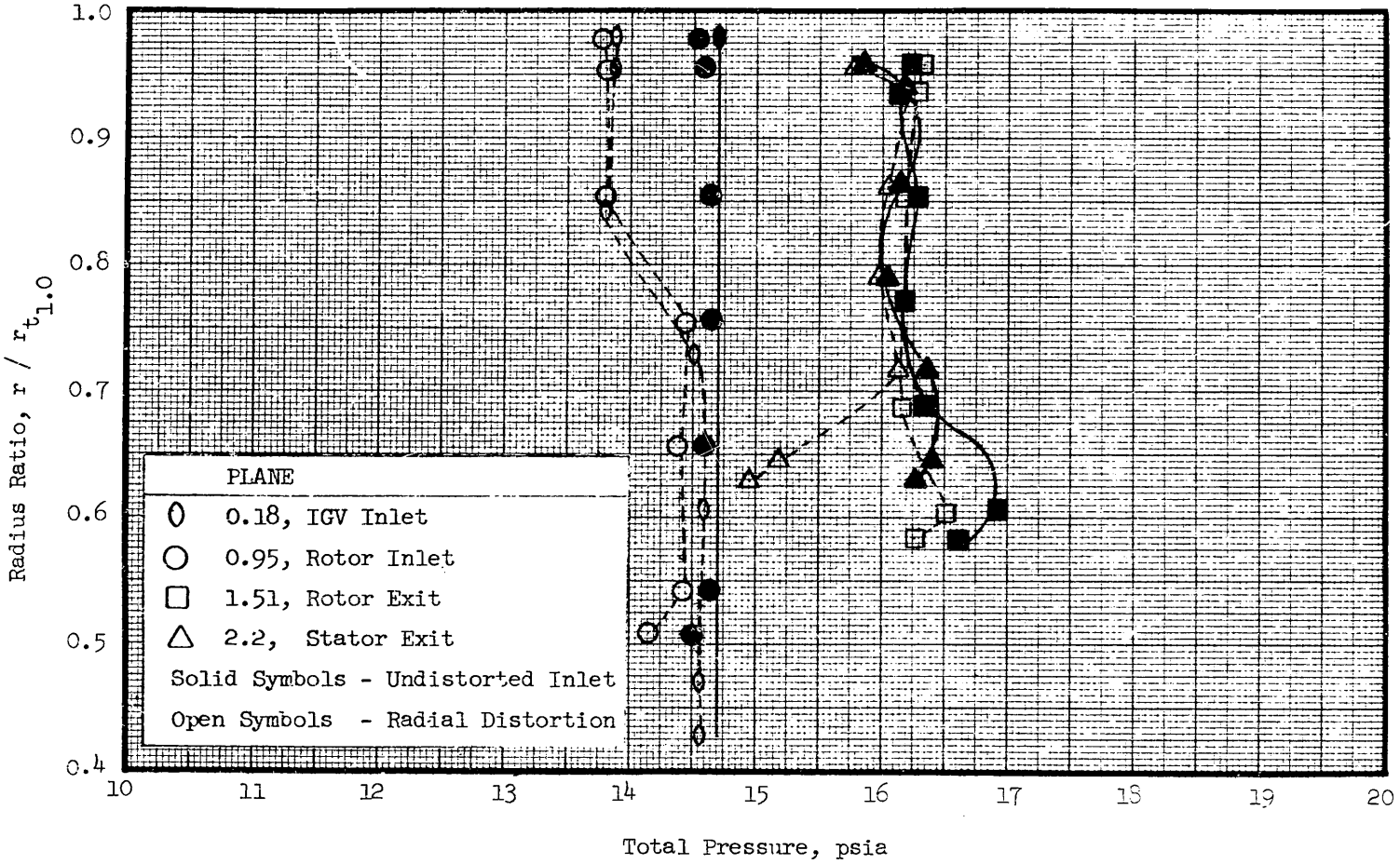

c. 70% Speed, Maximum Flow, IGV/Stator Schedule 40°/8°

Figure 76. Radial Profiles of Total Pressure at the Four Traverse Stations; Undistorted Inlet Flow and Flow with Tip Radial Distortion (Continued).

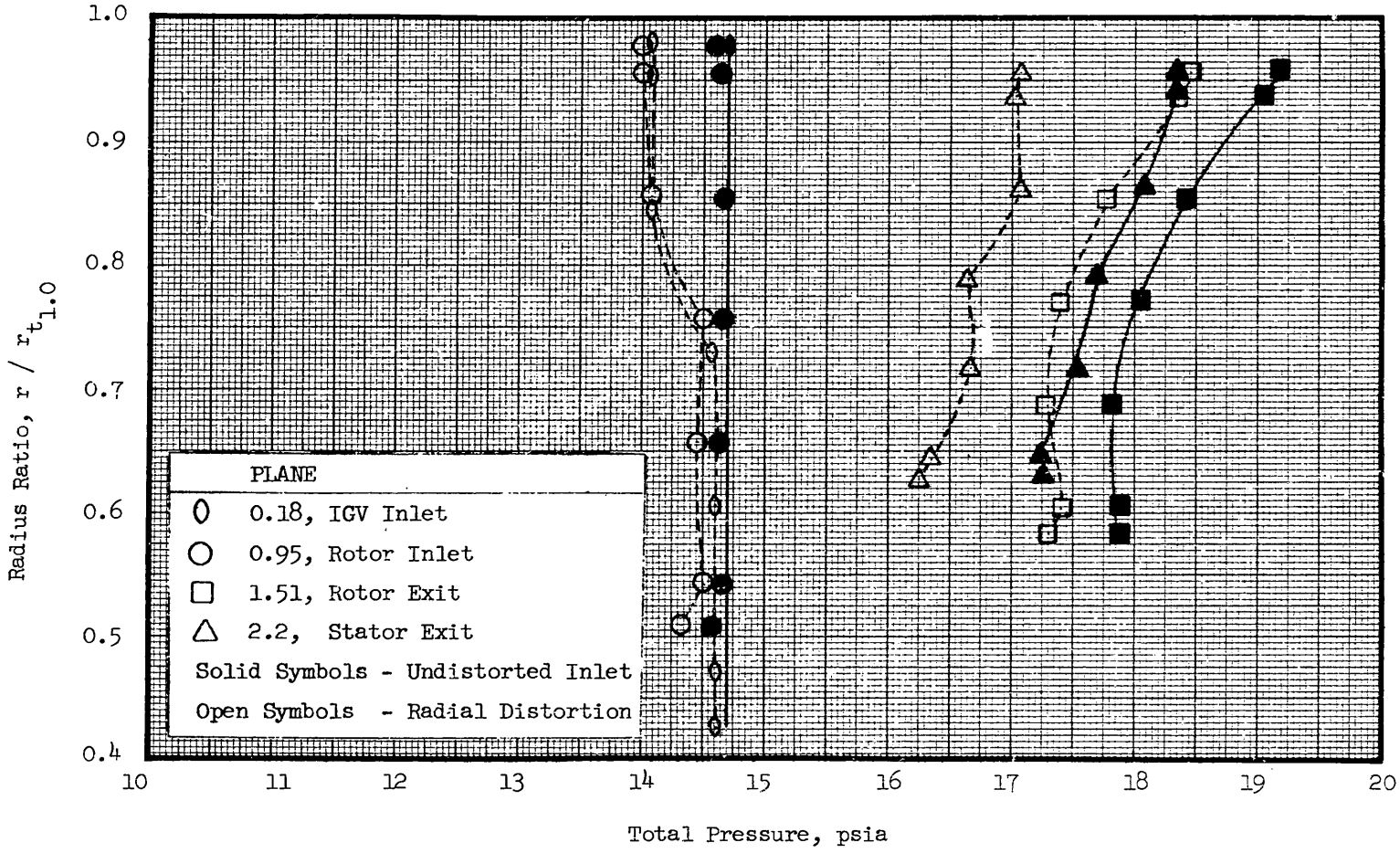

d. 70% Speed, Near Stall, IGV/Stator Schedule 40°/8°

Figure 76. Radial Profiles of Total Pressure at the Four Traverse Stations; Undistorted Inlet Flow and Flow with Tip Radial Distortion (Concluded).

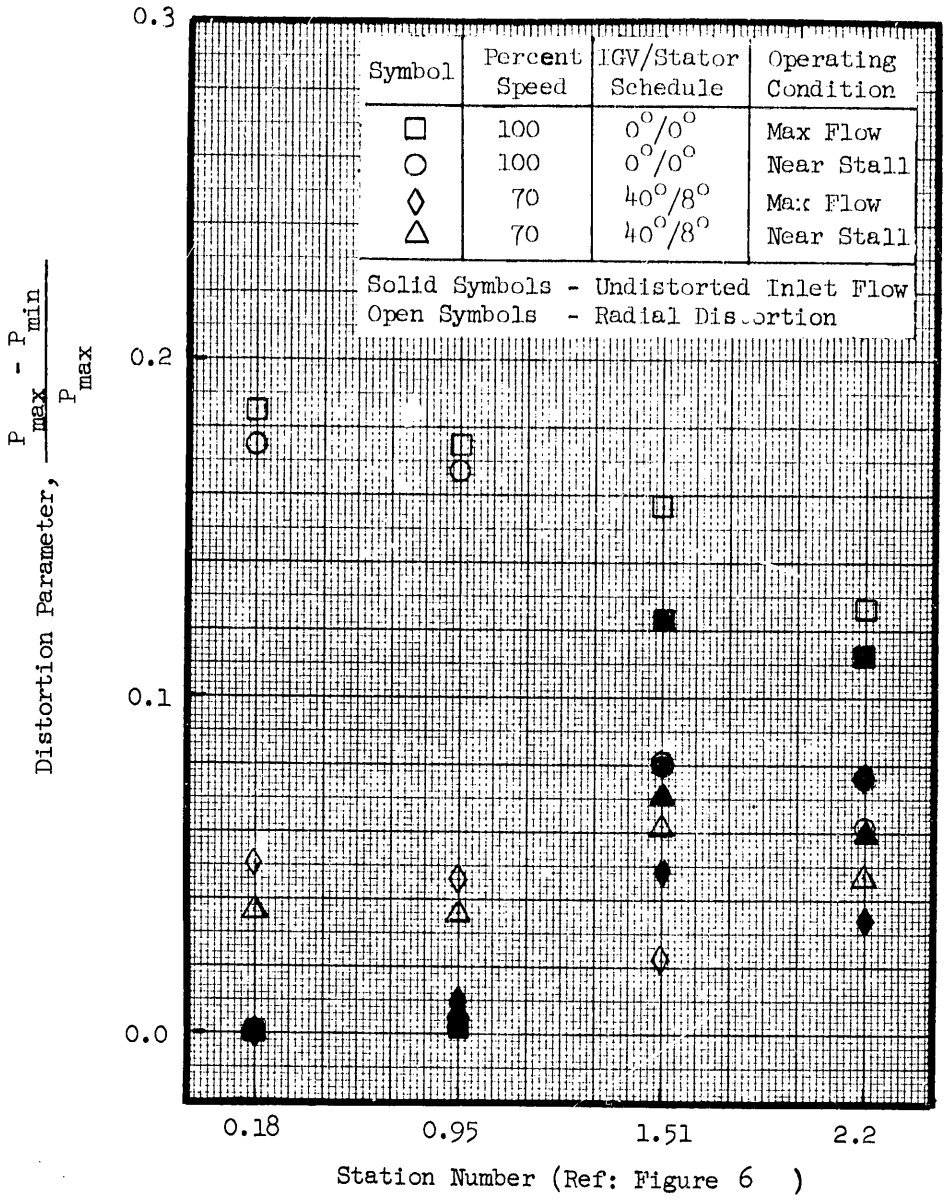

Figure 77. Distortion Parameter at the Four Axial Measurement Planes for Undistorted and Radially Distorted Inlet Flows.

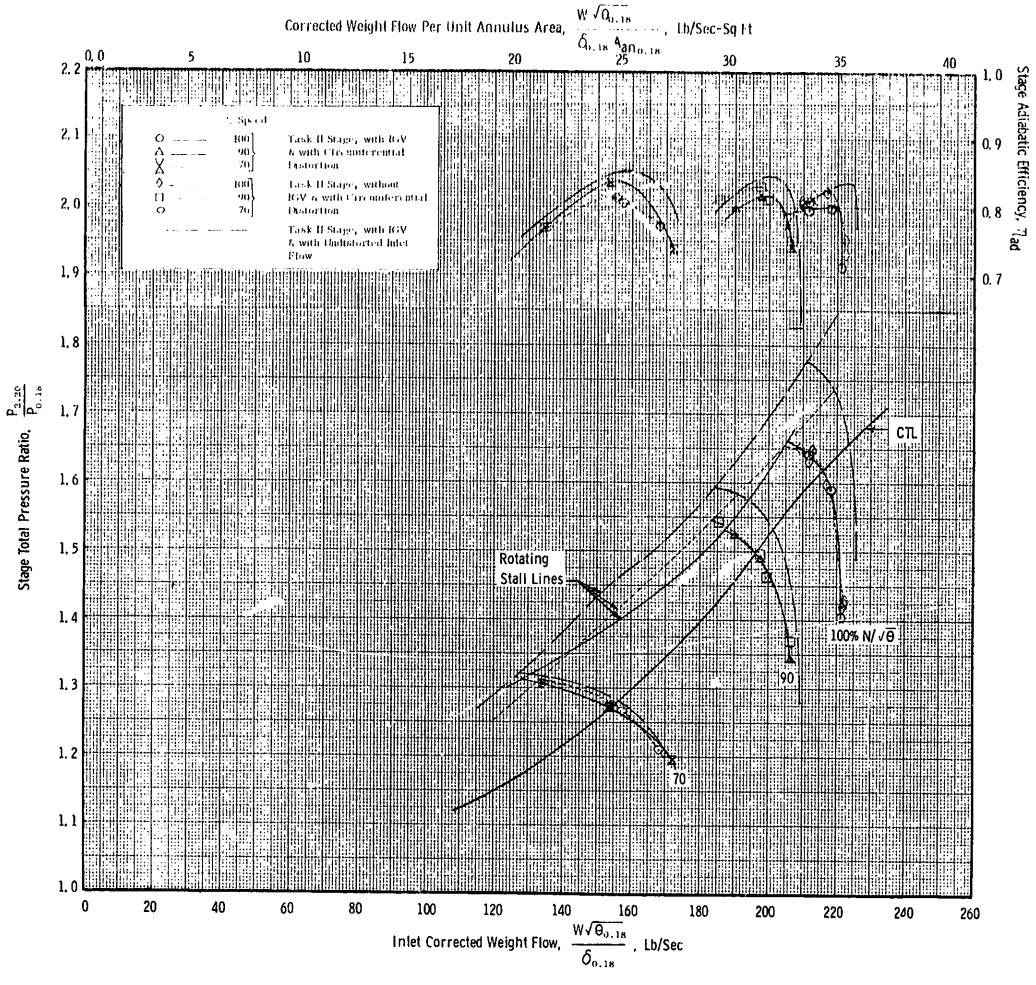

Figure 78. Stage Performance Map with Circumferential Inlet Distortion for IGV/Stator Schedule of 0°/0°.

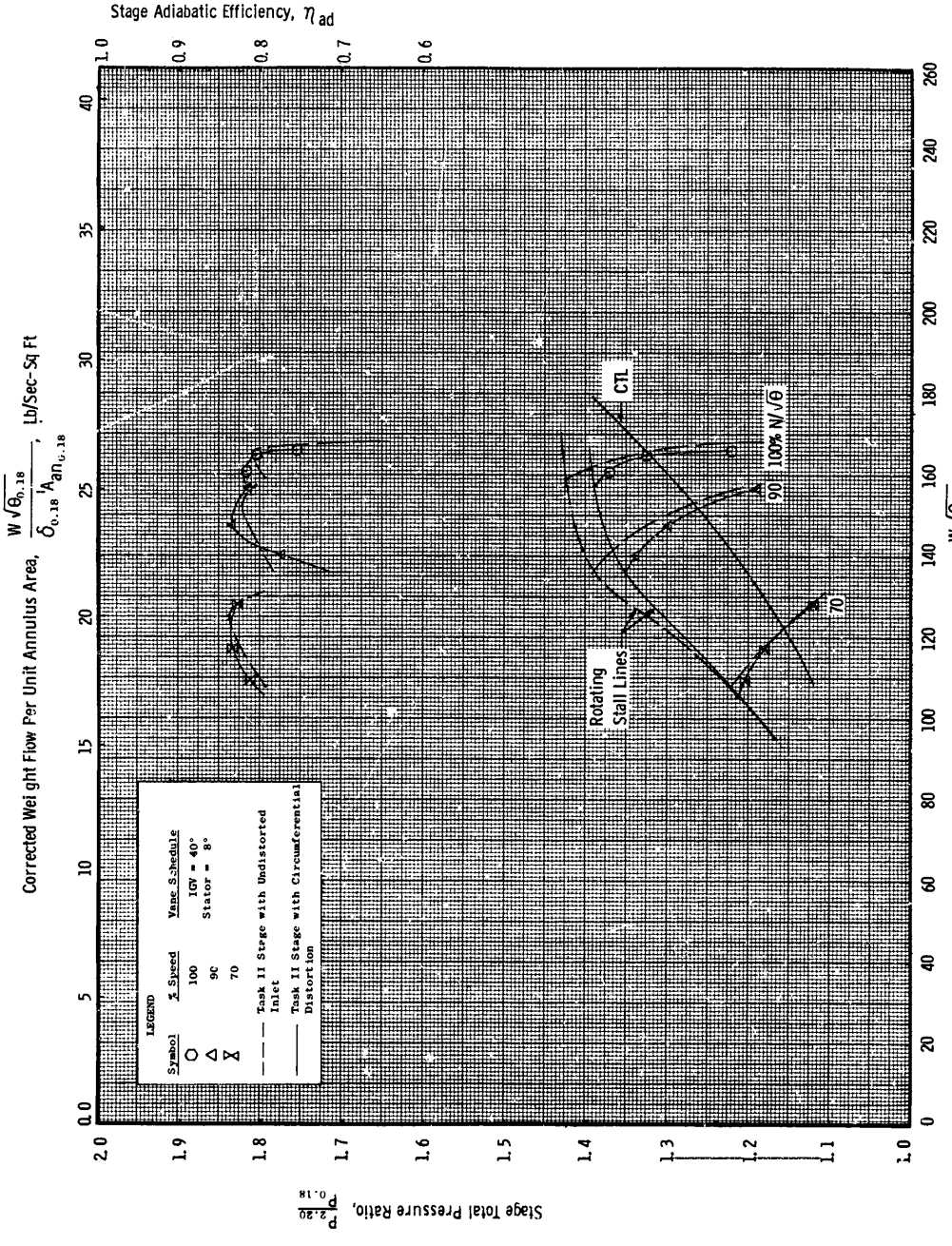

Figure 79. Stage Performance Map with Circumferential Inlet Distortion for IGV/Stator Schedule of 40°/8°.

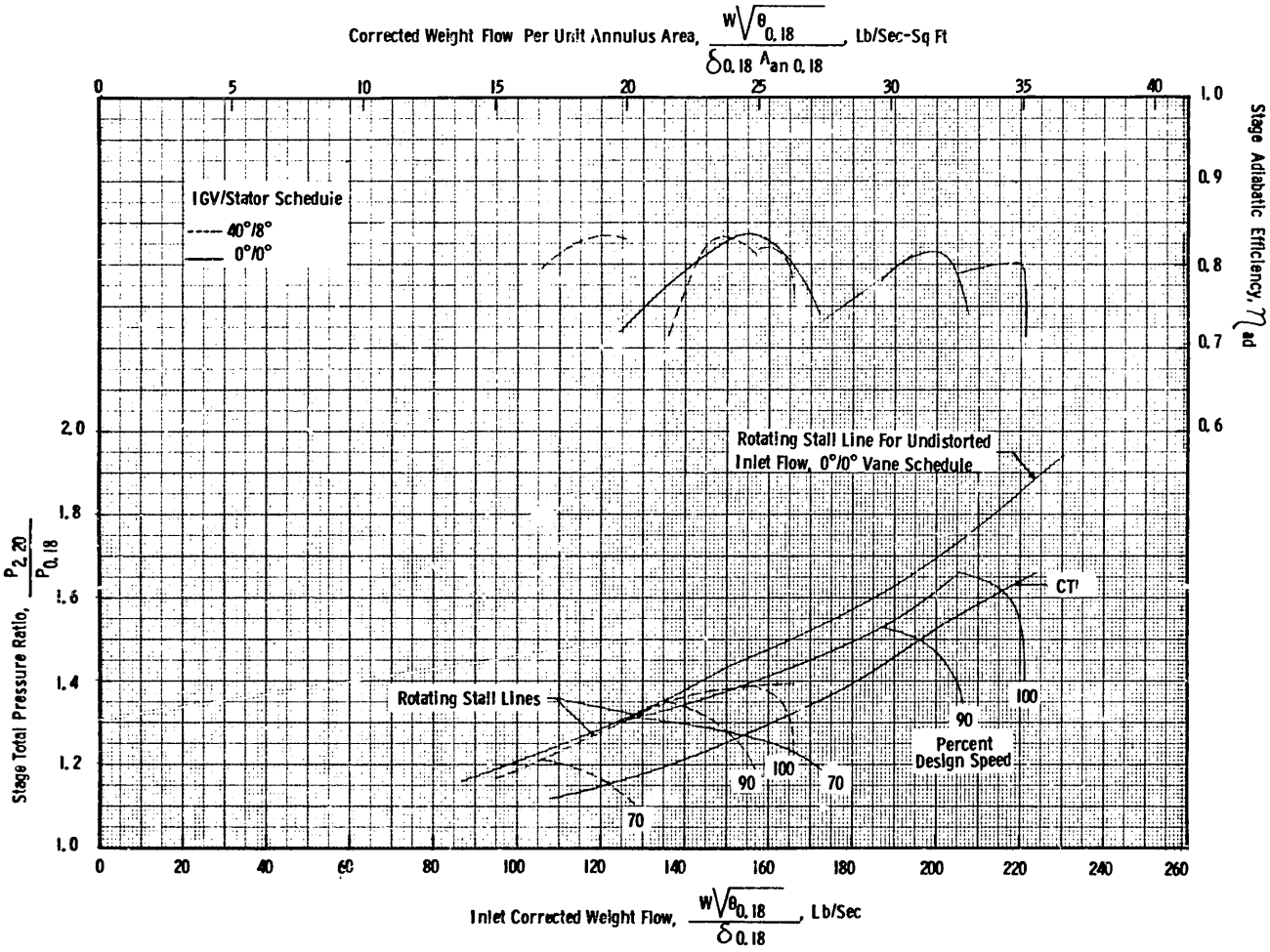

Figure 80. Consolidated Stage Performance for IGV/Stator Schedules 0°/0° and 40°/8°; Flow with Circumferential Inlet Distortion.

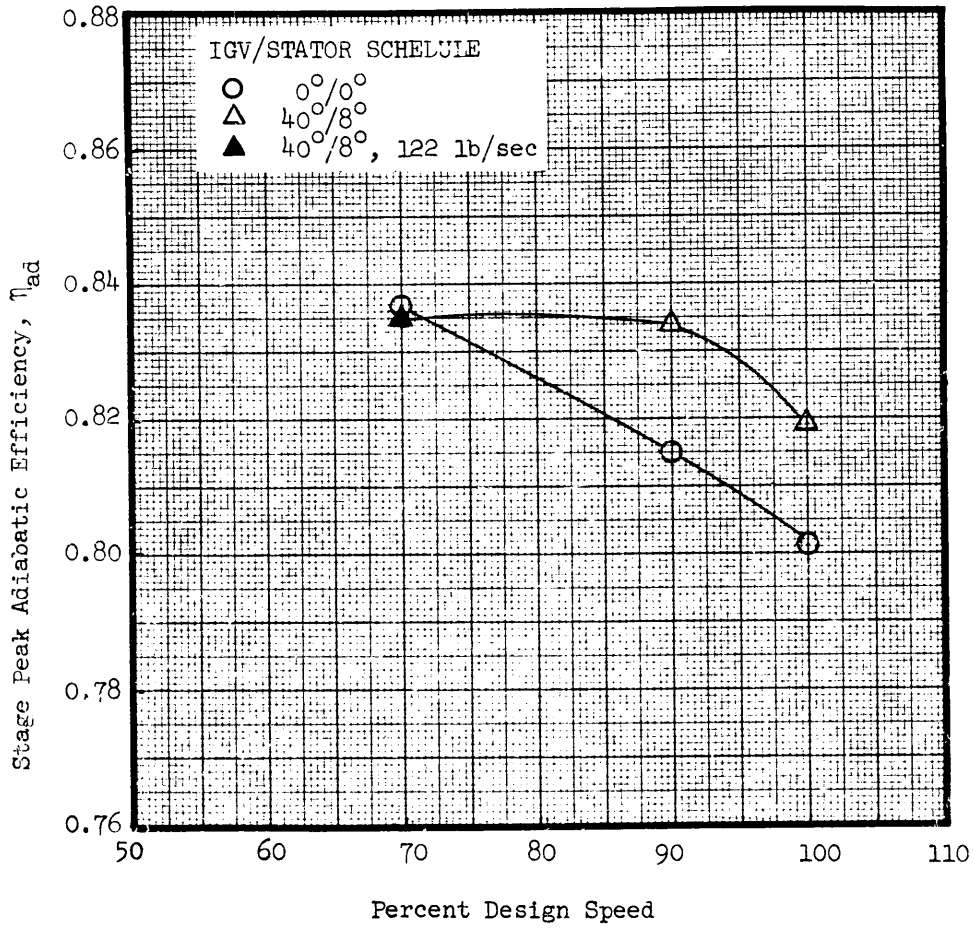

Figure 81(a). Variation of Stage Peak Adiabatic Efficiency with Rotor Speed and Vane Schedule; Flow with Circumferential Inlet Distortion.

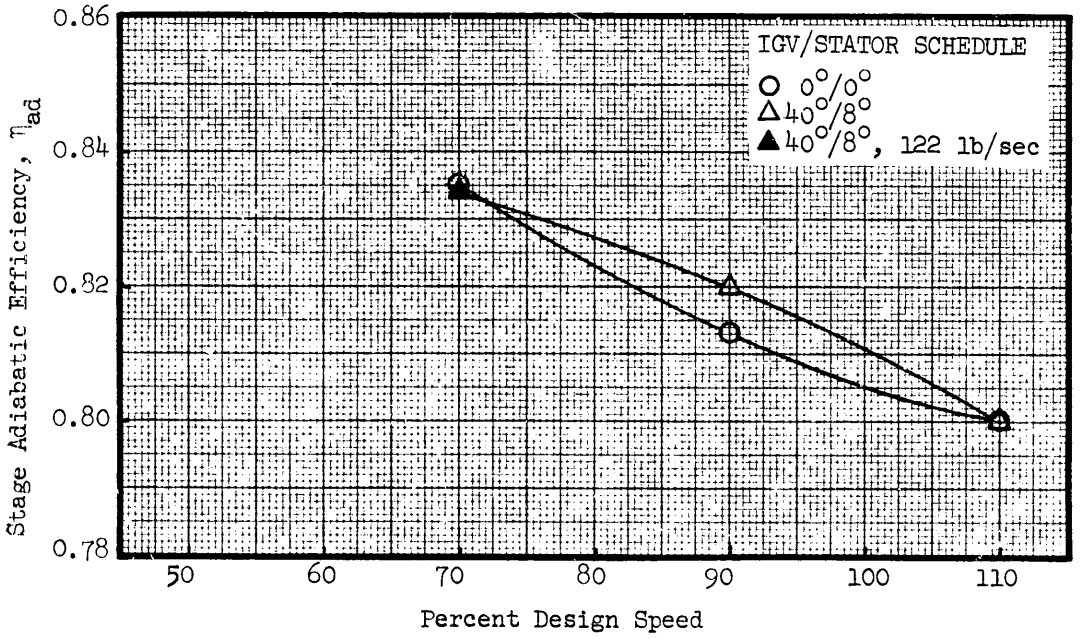

Figure 81(b). Variation of Stage Adiabatic Efficiency with Rotor Speed and Vane Schedule at the CTL Condition; Flow with Circumferential Inlet Distortion.

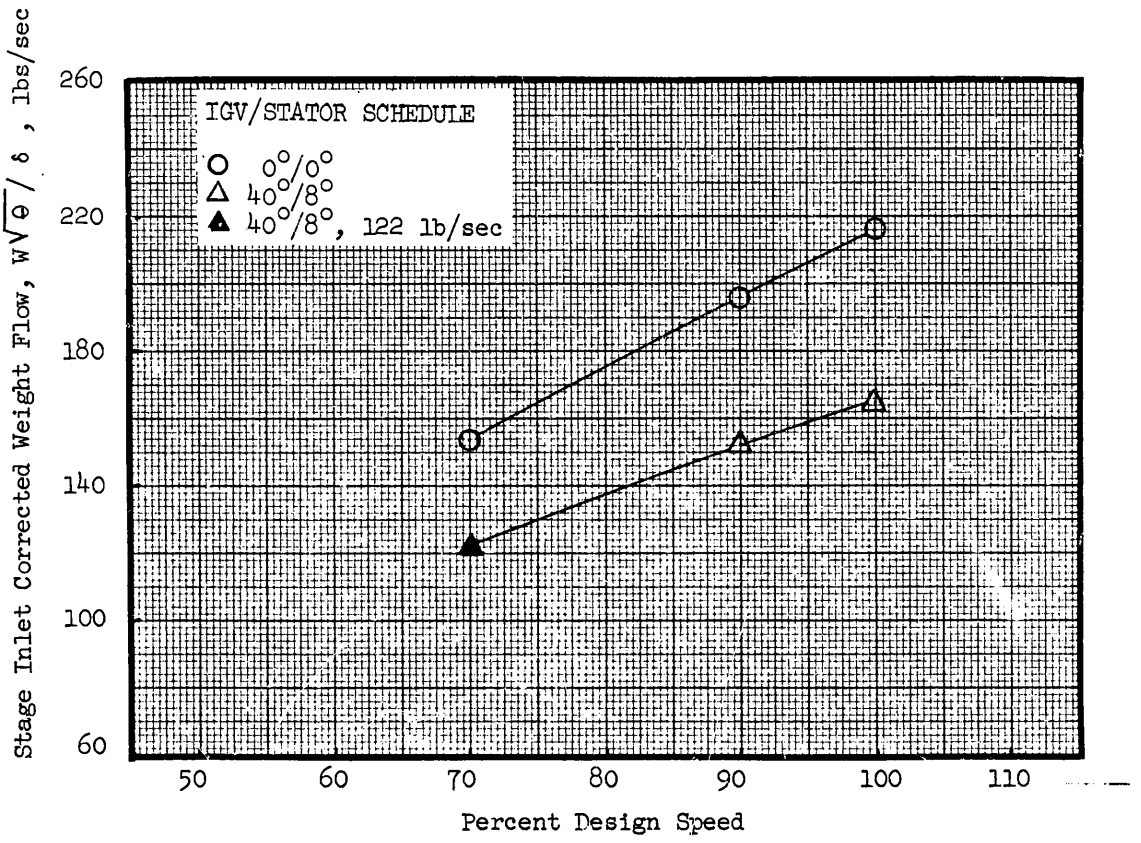

Figure 82. Variation of Stage Inlet Corrected Weight Flow at the CTL with Rotor Speed and Vane Schedule; Flow with Circumferential Inlet Distortion.

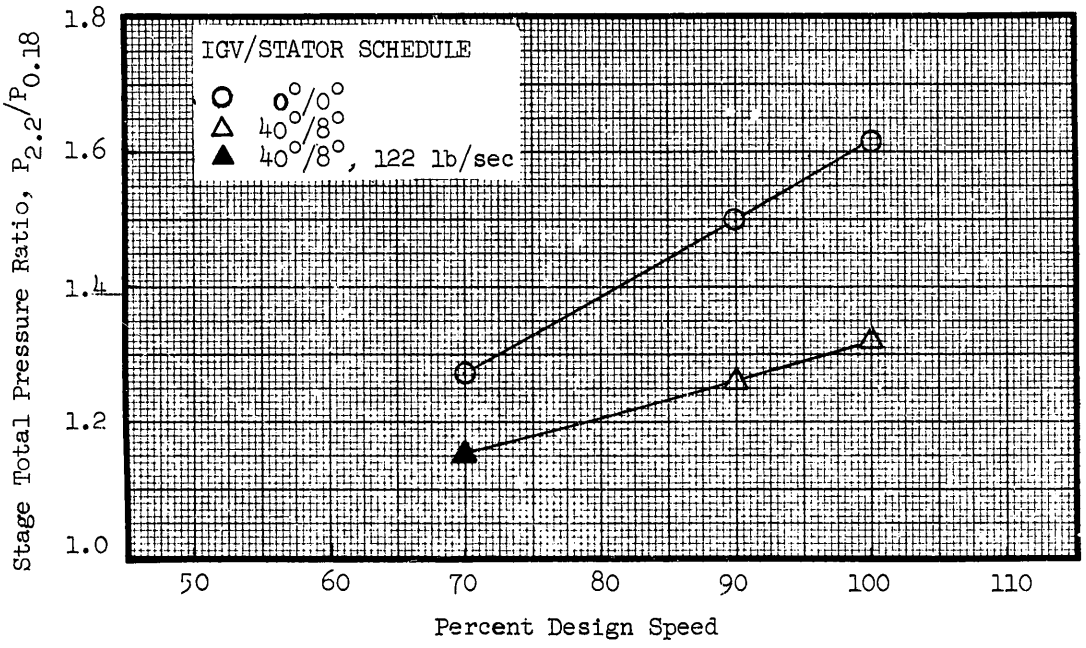

Figure 83. Variation of Stage Total Pressure Ratio at the CTL with Rotor Speed and Vane Schedule; Flow with Circumferential Inlet Distortion.

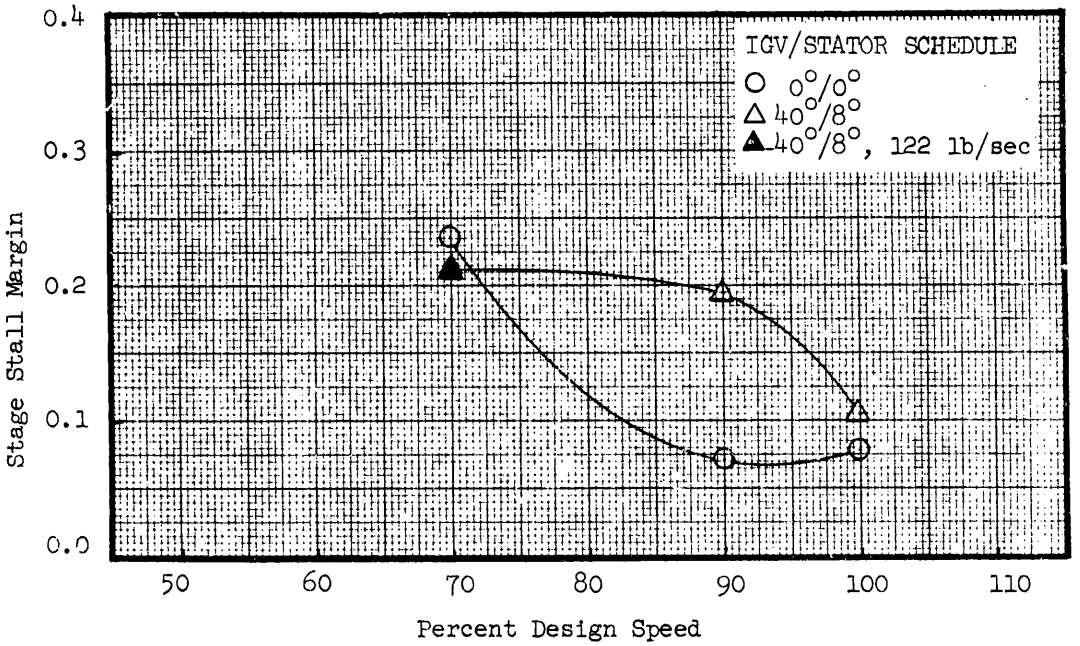

Figure 65. Variation of Stage Stall Margin at the CTL Condition with Rotor Speed and Vane Schedule; Flow with Circumferential Inlet Distortion.